University of Strathclyde

Department of

Electronic and Electrical Engineering

Photovoltaic System Design and Control

by

Nahla EzzEldin Zakzouk

B.Sc., M.Sc.

A thesis presented in fulfilment of the requirements for the degree of Doctor of Philosophy

2015

This thesis is the result of the author's original research. It has been composed by the author and has not been previously submitted for examination which has led to the award of a degree.

Signed: *Nahla EzzEldin Zakzouk* Date: August 2015

Acknowledgements

All praise to Allah for his guidance and blessing through this experience

I take this opportunity to express my sense of gratitude to my supervisors Prof. Barry W. Williams, Dr Derrick Holliday, and Prof. Ahmed Anas Elwogoud for their effective guidance, continuous encouragement and valuable advice throughout my PhD program.

Sincere thanks and deep appreciation to my supervisor and elder brother Dr. Ahmed Kadry Abdelsalam for his remarkable supervision and outstanding support.

I would also like to place my special thanks to Dr. Bader Nasser Alajami, Dr. Rania Assem, and eng. Mohamed Elsaharty for their great help and fruitful comments.

I am so grateful to my amazing figure Prof. Samah Elsafty, and my beloved colleagues eng. Rana Maher and eng. Mona Ibrahim for their emotional support.

Recognition is given to the academic members and technical staff at the Arab Academy for Science and technology for their support throughout my research period. Many thanks to Mr. Mohamed Samir for his effective assistance in making my experimental rig.

Finally, no words can express my gratefulness to my parents, husband and daughter for all the sacrifices they had to make and their support and patience during my study.

Dedication

To my family

You are my everything!

Table of Contents

Appendices

Abstract

Modern industrial society, increasing energy demands, and environmental issues have increased the need for new and clean renewable energy resources, among which photovoltaic energy has gained considerable interest. For best energy utilization, photovoltaic maximum power tracking and grid-integration aspects should be addressed.

Generally, variable-step, incremental conductance maximum power point tracking technique has the merits of good tracking accuracy and fast convergence speed. Yet, the division processes in its algorithm create a computational burden. Also the conventional variable step-size encounters steady-state power oscillation and dynamic problems, especially under sudden irradiance changes. In this thesis, a division-free incremental conductance algorithm is proposed for photovoltaic maximum power tracking. It features a modified variable step-size and a direct converter control scheme. The proposed tracking technique does not only have the merits of superior steady-state and transient performance but also offers simple implementation and control. Thus, it can be practically implemented using low-cost microcontrollers, reducing overall system cost.

Grid integration of photovoltaic systems using power electronic converters that vary in configurations, control loops and mandatory measured signals are investigated. A single-phase two-stage grid-interfaced photovoltaic system is presented in this thesis. It uses a boost chopper in the first stage for maximum power tracking and an H-bridge voltage source inverter in the second stage for grid interfacing. A novel DC-link voltage sensorless control technique is proposed for this topology. It eliminates the inverter outer DC-link voltage control loop, thus reducing system size, cost and control complexity. Additionally, system dynamics are enhanced during sudden changes.

Single-stage based grid-tied photovoltaic power converters receive attention due to their merits of reduced footprint and losses, but at the cost of a limited degree-of-freedom. In this thesis, a single-phase single-stage grid-tied photovoltaic system is proposed. It adopts a single transformerless current source inverter to achieve photovoltaic maximum power tacking, whilst satisfying grid interfacing requirements. A proportional-resonant controller, associated with harmonic compensator units, is proposed for the inverter in order to limit injected grid current harmonics. Thus, a lower-sized inductor can be used in the inverter DC-link which enhances efficiency without sacrificing system performance.

Simulation and experimental results validate all the proposed systems.

List of Symbols

a	Diode ideality constant	---
C_{dc}	VSI DC-link capacitor	F
C_f	CSI output filter capacitor	F
D	MPP converter duty ratio	---
D_{boost}	Boost chopper duty ratio	---
ΔD	Change in the MPP converter duty ratio	---
E	Error input to PV MPPT fuzzy controller	W/V
e	PV voltage error	V
e_{ig}	Grid current error	A
ΔE	Change in error input to PV MPPT fuzzy controller	W/V
Δe	Change in PV voltage error	V
f_{sw}, $f_{sw(b)}$	Switching frequency of the boost converter.	Hz
$f_{sw(i)}$	Inverter switching frequency	Hz
G	Actual irradiance acting on PV source	W/m^2
G_{boost}	Boost converter gain	---
G_{HC}	Harmonic compensator transfer function	---
G_n	Nominal irradiance acting on PV source, 1000 W/m^2	W/m^2
G_{PI}	PI controller transfer function	---
G_{PR}	PR controller transfer function	---
H	Order of grid current harmonic to be compensated	---
I, I_{PV}	PV output current	A
I_{Array}	PV array output current	A
I_{comp}	Compensating current rms value	A
I_d	Shockley diode current	A
I_{dc}	CSI DC-link current	A
I_{dcmax}	Maximum value of CSI DC-link current	A
I_{dcmin}	Minimum value of CSI DC-link current	A
I_{dcref}	CSI DC-link current reference	A
I_g	Grid current rms value	A
$I_{g(1)}$	rms of grid current fundamental frequency component	A
$\hat{I}_g$	Grid current amplitude	A
$\hat{I}_{gref}$	Reference grid current amplitude	A
I_{MPP}	PV current at MPP	A
$I_{MPP\text{-}e}$	Experimental PV current at MPP	A

I_{o1}	rms value of CSI fundamental output current	A
I_{pv}	Photovoltaic current generated by the incident light, acting on PV module	A
$I_{pv,cell}$	Photovoltaic current generated by the incident light, acting on PV cell	A
$I_{pv\text{-}n}$	Nominal Photovoltaic light-generated current	A
I_{SC}	PV module short-circuit current	A
$I_{SC\text{-}n}$	Nominal PV short-circuit current	A
$\hat{I}_{tri}$	Triangular carrier signal amplitude for CSI PWM	A
I_0	Saturation current of the PV module	A
$I_{0,cell}$	Diode reverse saturation current	A
i_c	Instantaneous current in CSI output filter capacitor	A
i_{ctrl}	CSI control signal	A
i_{comp}	Instantaneous compensating current	A
i_{dc}	Instantaneous values of the CSI DC-link current	A
i_g	Instantaneous grid current	A
i_i	Instantaneous input current to CSI	A
i_o	Instantaneous output current from CSI	A
$\Delta I, \Delta I_{PV}$	PV current change	A
ΔI_g	rms ripple component of the grid current	A
Δi_{dc}	DC-link current ripple amplitude at CSI DC-link	A
$\Delta i_{dcp\text{-}p}$	Peak to peak DC current ripple at CSI DC-link	A
Δi_L	Change in inductor current	A
K_I	Short circuit current/temperature coefficient	A/^{o}C
K_{I-i}	PI controller integral gain	---
K_{I-r}	PR controller resonant gain	---
$K_{(I-r)H}$	Cascaded PR controller individual resonant gain at harmonic order H	---
K_{P-i}	PI controller proportional gain	---
K_{P-r}	PR controller proportional gain	---
K_{PWMi}	CSI PWM gain	---
K_{PWMv}	VSI PWM gain	---
K_V	Open-circuit voltage/temperature coefficient	V/^{o}C
k	Boltzmann constant (1.3806503 × 10^{-23} J/˚K)	J/˚K
k_1	Ratio between V_{MPP} and V_{OC}	---
k_2	Ratio between I_{MPP} and I_{SC}	---

L, L_{boost}	Boost chopper inductance	H
L_{ac}	VSI output filter inductor	H
L_{dc}	CSI DC-link inductor	H
L_f	CSI output filter inductor	H
M	CSI modulation amplitude	---
m_a	VSI modulation index	---
N_{pp}	Number of the parallel strings in the PV array	---
N_s	Number of PV cells, connected in series, in a module	---
N_{ss}	Number of series PV modules in one PV string	---
N_1	Scaling factor of the conventional step-size, ΔD	---
N_2	Scaling factor of the conventional step-size, ΔV	---
N_3	Scaling factor of the proposed step-size, $\Delta D(proposed)$	---
P, P_{PV}	PV output power	W
P_{dc}	Input power to inverter DC-link	W
P_g	Average grid power	W
P_{MPP}, P_{mx}	Maximum PV output power	W
$P_{MPP\text{-}e}$	Experimental peak PV output power	W
p_{cap}	Instantaneous power in the VSI DC-link capacitor	W
$p_{conv-loss}$	Instantaneous inverter power losses	W
p_{inv}	Instantaneous power supplied to inverter	W
p_g	Instantaneous grid power	W
$\Delta P, \Delta P_{PV}$	PV power change	W
q	Electron charge ($1.60217646 \times 10^{-19}$ C)	C
R_s	PV module internal series resistance	Ω
R_{ss}	Series variable resistance of PV emulator	Ω
R_p	PV module parallel resistance	Ω
R_{p-min}	Minimum value of PV module parallel resistance	Ω
T	Actual PV cell temperature	°K
$THDi$	Grid current THD	%
T_n	Nominal PV cell temperature, 25°C	°K
$T_{sampling}$	Controller sampling time	s
$t_s, t_{settling}$	Settling time of system response	s
ΔT	Difference between actual and nominal temperatures	°K
V, V_{PV}	PV output voltage	V
V_{Array}	PV array output voltage	V
$V_{battery}$	Battery load voltage	V

V_{dc}	Average VSI DC-link voltage	V
V_{dcmax}	Maximum value of VSI DC-link voltage	V
V_{dcmin}	Minimum value of VSI DC-link voltage	V
V_{dcref}	VSI DC-link voltage reference	V
V_g	Grid voltage rms value	V
$\hat{V}_g$	Grid voltage amplitude	V
V_{MPP}	PV voltage at MPP	V
$V_{MPP\text{-}e}$	Experimental PV voltage at MPP	V
V_{OC}	PV module open-circuit voltage	V
$V_{OC\text{-}n}$	Nominal PV open-circuit voltage	V
V_{ref}	Reference PV voltage	V
V_t	PV thermal voltage	V
$V_{t\text{-}n}$	PV thermal voltage at the nominal temperature, 25^{o}C	V
$\hat{V}_{tri}$	Triangular carrier signal amplitude for VSI PWM	V
v_{ac}	Instantaneous voltage at CSI output	V
v_{ctrl}	VSI control signal	V
v_{dc}	Instantaneous values of the VSI DC-link voltage	V
v_{inv}	Instantaneous voltage at VSI output	V
v_L	Instantaneous voltage at CSI DC-link inductor	V
v_g	Instantaneous grid voltage	V
$\Delta V, \Delta V_{PV}$	PV voltage change	V
Δv_{dc}	DC-link voltage ripple amplitude at VSI DC-link	V
$\Delta v_{dcp\text{-}p}$	Peak to peak DC voltage ripple at VSI DC-link	V
x	Ratio between inductor reactance and capacitor reactance of the CSI output filter	---
ω	AC line angular frequency	rad/s
ω_{sw}	Inverter angular switching frequency	rad/s
ω_r	Angular resonant frequency of PR controller	rad/s
ϕ	Angle of CSI output current fundamental component	^{o}

List of Abbreviations

AC	Alternating current
AI	Artificial intelligence
ANFIS	Adaptive neuro-fuzzy inference system
ANN	Artificial neural network
A-Si	Amorphous silicon
B	Big
BOS	Balance-of-system
CdTe	Cadmium telluride
CIGS	Copper indium gallium di-selenite
CPR	Cascaded proportional resonant
CPRC	Conventional PR control
CPV	Concentrating photovoltaic
C-Si	Crystalline silicon
CSI	Current source inverter
CSP	Concentrated solar power
DC	Direct current
DER	Distributed energy resource
EPIA	European photovoltaic industry association
FFT	Fast Fourier transform
FL	Fuzzy logic
FOCV	Fractional Open Circuit Voltage
FSCC	Fractional Short Circuit Current
Ga-N	Gallium nitride
IEA	International Energy Agency
IEC	International Electro-technical Commission
IEEE	Institute of Electrical and Electronics Engineers
IGBT	Insulated gated bipolar transistor
Inc.Cond.	Incremental conductance
LCOE	Levelized cost of energy
LED	Light-emitting diode
Li-O	Lithium ion
M	Medium
MB	Medium big

MIC	Module integrated converter
MJ	Multi-junction
MPP	Maximum power point
MPPT	Maximum power point tracking
MS	Medium small
N	Negative
NB	Negative big
Ni-Cd	Nickel carbide
Ni-MH	Nickel metal hydride
NPWM	Nonlinear pulse width modulation
OC	Open-circuit
P	Positive
PAM	Pulse amplitude modulation
PB	Positive big
PCHC	Proposed cascaded harmonic compensator
PI	Proportional integral
PLL	Phase-locked loop
P&O	Perturb and observe
PR	Proportional resonant
PSO	Particle swarm optimization
PV	Photovoltaic
PWM	Pulse width modulation
SPWM	Sinusoidal pulse width modulation
RMS	Root-mean-square
S	Small
SC	Short-circuit
Si-C	Silicon carbide
SOC	State of charge
SPWM	Sinusoidal pulse width modulation
STC	Standard test conditions
TF	Thin film
THD	Total harmonic distortion
TS	Takagi–Sugeno
US	United States
VSI	Voltage source inverter
Z	Zero

Preface

As a result of fossil fuel resource depletion and associated environmental problems, renewable energy resource development is receiving increasing attention. Photovoltaic energy is considered a clean, sustainable, noiseless and maintenance-free resource. However, high fabrication cost and low conversion efficiency of photovoltaic systems in addition to their non-linear behaviour and dependency on environmental conditions are the main challenges facing their penetration into the energy market. In this research, possible solutions for stand-alone and grid-tied photovoltaic systems are proposed. The thesis is presented in seven chapters.

Chapter one gives an overview of photovoltaic energy with respect to its history, environmental impact, potential and industry. Photovoltaic system applications, efficiency, reliability and cost are also considered, followed by photovoltaic future prospects. A summary of the applicable grid codes and photovoltaic standards is presented. Finally, problem definition, thesis objectives and research methodology are presented.

Chapter two gives a description of the photovoltaic cell construction, photovoltaic effect and different combinations. The non-linear behaviour of photovoltaic modules is then demonstrated along with the development of a PV single-diode model. Finally, PV MPPT is discussed, with the commonly used MPPT techniques introduced.

In **chapter three**, off-grid photovoltaic system components and applications are presented followed by on-grid applications. An overview of different configurations of grid-tied photovoltaic inverters is presented. Power processing stages, required to transfer photovoltaic power to the grid, are then studied showing the features of each topology. Finally, common DC/AC inverter types, used in photovoltaic-grid interfacing, are presented.

Chapter four presents a stand-alone photovoltaic system which employs a DC/DC boost converter for tracking PV module maximum power. Different control schemes are investigated for the converter switching. The conventional variable-step incremental conductance technique is studied revealing its numerous division computations in addition to the degraded performance of its associated step-size. Then, a division-free incremental

conductance technique is proposed featuring a modified variable step and a direct converter control scheme. Simulation and experimental results are provided to verify the steady-state and transient performance of the proposed technique. The controller is then re-implemented using a low-cost microcontroller to establish its cost-effectiveness.

In **chapter five**, a single-phase two-stage grid-connected PV string is presented employing a boost chopper as the first stage, for maximum power tracking, and a voltage source inverter in the second stage to fulfil grid-interfacing requirements. First the inverter's conventional control loops are illustrated. Then, a novel sensorless technique is proposed to eliminate the inverter’s outer DC-link voltage control loop. Simulation and experimental results validate the proposed sensorless technique and confirm its enhanced dynamic performance under varying conditions.

In **chapter six**, a single-phase grid-tied photovoltaic system is developed employing a single-stage current source inverter. System modelling and parameter design are demonstrated along with illustration of the current source inverter modulating technique and control loops. A cascaded proportional resonant controller is used to mitigate injected grid current harmonics. This enables the use of a non-bulky DC-link inductor without degrading grid current quality. Simulation and experimental results are provided to validate the proposed system and confirm controller effectiveness.

Finally, **chapter seven** presents thesis general conclusions, the author's contribution, and suggestions for future research.

Chapter One

Introduction

Electrical power is considered the driving force for development, economic growth and modern industrial society. Consequently, electric energy consumption is dramatically increasing. The global energy demand is forecasted to grow by 37% by 2040 [1.1].

However, energy demand projections show that most of world's power generation depends on fossil fuels (coal, oil, and natural gas) [1.2]. Unfortunately, this is a non-sustainable source of energy that produces green house gases on combustion which are the main cause of air pollution, acid rain, climatic changes and global warming [1.3].

Consequently, sustainable and clean alternatives became a necessity drawing the world's attention to renewable energy resources. By the end of 2013, renewable energy sources were able to supply an estimated 22.1% of global electricity, with hydropower providing about 16.4%. By contrast, wind, bio-power and photovoltaic (PV) sources provide only 2.9%, 1.8% and 0.7% respectively. An estimated 0.4% was provided by power from geothermal, ocean and concentrated solar power (CSP) [1.4].

Among the latter, PV energy is a promising renewable energy source. Being a direct conversion system of sunlight to electric energy without the need of machinery or any moving devices, PV is a clean noiseless energy source with minimum maintenance costs. Moreover, it is a flexible modular source that is convenient for stand-alone applications in arid areas as well as distributed generation resources [1.5, 1.6].

1.1 Photovoltaic historical development

The PV effect was first discovered, in 1839, by the French scientist, Edmond Becquerel. In 1876, William Grylls Adams and his student, Richard Evans Day, discovered that an electrical current could be started in selenium by exposing it to light. In 1954, PV technology was born in the United States (US) when the silicon PV cell was developed at Bell Labs. The first PV application took place in 1958, in the form of a small (less than one Watt) array to power radios on a US space satellite. In the 1960s, PVs were successfully used in powering satellites [1.7, 1.8]. Since then, PV has become the key component of satellite systems, providing them with a maintenance-free power supply for years [1.7]. Moreover, the telecommunication revolution would never have evolved if not for PV powered satellites. As the price of PV cells continues to drop, they have become a cost-

effective solution for small-scale electrical demands located away from utility lines as well as being a good environmental option in domestic electricity micro-generation [1.9].

1.2 Environmental impact of photovoltaic energy

Generally, PV energy is a clean, silent, abundant, sustainable, and renewable source as well as inherently safer than any other traditional electricity generation system. Hence, it can solve many environmental problems created by traditional fossil fuels. During PV system operation, there is zero release of greenhouse emissions and it does not contribute to global warming [1.9]. However, large-scale PV power plants are being developed at a rapid rate, which cause some environmental problems that should be addressed regarding land use intensity, and impact on wild life [1.10].

1.3 Photovoltaic potential and market development

PV power use has grown significantly as a source of renewable energy during the past decade. From 2003 to 2013, global PV cumulative installed capacity has grown at an average rate of 49% per year, as shown in Figure 1.1 [1.11]. In 2013, around 38 GW of new PV capacity was installed in about 30 countries bringing the total global capacity to over 138.9 GW [1.11]. Although Europe is still the world's leading region in terms of cumulative installed capacity, with about 81.5 GW in 2013, Asian countries contributions are growing fast, with 40.6 GW currently installed [1.12].

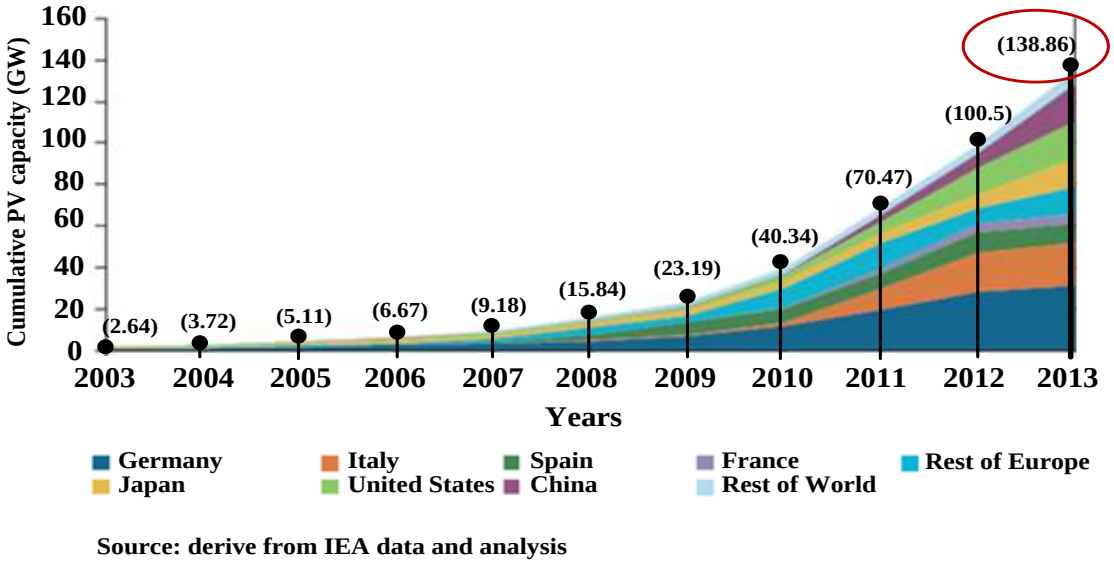

Figure 1.1. Global cumulative growth of PV capacity in IEA countries [1.11].

The great progress in global PV market and installation, shown in Figure 1.1, can be related to a number of factors which mainly include the rapid reductions in PV modules and systems' costs. The latter results from improvements in PV technology, scaling up of manufacturing and mass production of associated components such as power electronic converters and controllers. Moreover, the ease of installation of PV panels at the domestic level has encouraged the "feed in tariff" policy where PV power suppliers are paid a cost-based price for the PV power they generate which in turn increases investments in PV applications [1.11].

1.4 Photovoltaic industry and manufacturing technology

The main PV cell technologies are shown in Figure 1.2. They include crystalline silicon (C-Si), whether single or multi-crystalline, and thin films (TF) [1.9]. The latter includes amorphous silicon (A-Si), cadmium telluride (CdTe), and alloys of copper indium gallium di-selenite (CIGS). Other cell technologies include multi-junction dye-sensitized, and organic cells [1.9]. C-Si modules currently dominate the PV market with around 90% share. TF now represents less than 10% of the market [1.4]. Lately, progress has been made with respect to PV manufacturing that specific materials' (silicon, metal pastes, etc.) cost, and amount of labour have all been significantly reduced. This manufacturing industry has witnessed a dramatic shift, from Europe; particularly Germany to Asia; mostly China and Taiwan [1.11].

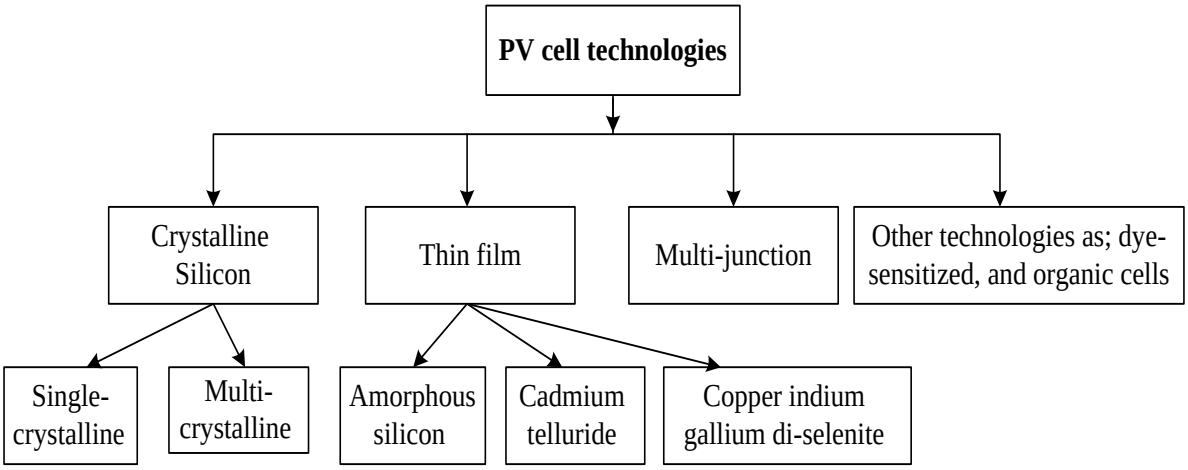

Figure 1.2. PV cell technologies.

1.5 Photovoltaic system specification

A PV system consists of one or several PV modules, connected to either an electricity network (grid-connected) or to a group of loads (off-grid) through power electronic converters. PV system applications, efficiency, reliability and cost are now discussed.

1.5.1 Applications

PV applications include off-grid and grid-tied systems as shown in Figure 1.3. The latter supply the utility network with PV power at all scales, from a few kW to hundreds of MW. Whereas, the former can be even smaller, providing power for urban areas far from a utility [1.13]. Grid-tied PV applications include de-centralized systems, occupying about 60% of the global market, as well as centralized systems representing close to 40%. Off-grid systems account for less than 1% of the PV market [1.11].

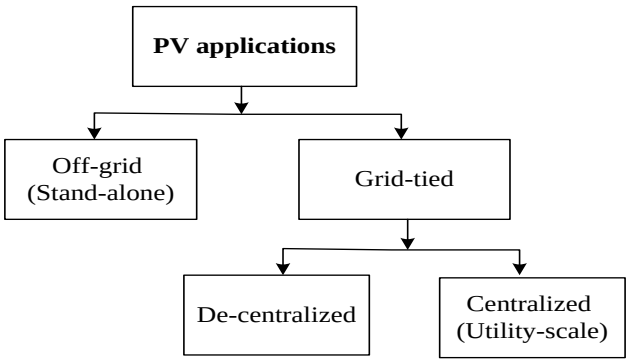

Figure 1.3. PV application classification.

i. Off-grid PV systems

PV systems offer longer service life with minimum maintenance costs. Moreover, they are simple to design, easily mounted and expanded. Hence, they can be operated in remote or isolated areas where utility power is unavailable or costly [1.13]. A storage battery is usually required to provide energy during low-sunlight periods. Off-grid PV applications mainly appear in power sources for remote buildings, urban home systems, water pumping, transportation, mobile applications, communications, and satellites [1.14]. In 2013, estimates showed that 500 MW of off-grid applications were installed in China, 28 MW in Australia and 14.1 MW in Japan [1.13].

ii. On-grid PV systems

PV sources are increasingly being connected to utility grids for best utilization of their produced electric power as well as their ability to be installed in the distribution level close to loads to decrease transmission costs [1.15]. In grid-connected PV systems, a DC/AC

inverter is used to interface the PV source with its DC output source to the AC utility [1.16, 1.17]. Several configurations for grid-tied PV inverters have been developed [1.18]. Grid-connected PV applications include centralized (utility-scale) power plants which are ground mounted as well as decentralized PV systems which are used by customers to generate their own power and usually are roof-mounted [1.13]. Currently, a 550 MW centralized PV plant is the world largest farm, located in California [1.19] while the world's largest rooftop PV system is located in Belgium, with a total capacity of 40 MW [1.20].

1.5.2 Efficiency

PV system efficiency depends on its major components which are the PV panels, PV power electronic-based converter and its associate controller.

PV cell conversion efficiency varies from one cell technology to another. Table 1.1 shows the conversion efficiencies of different PV cell technologies [1.21, 1.22]. Multi-junction cells show the highest efficiency but at the cost of higher price.

Table 1.1. Conversion efficiency of different PV cell technologies

PV cell technology		**Average Conversion efficiency (%)**
Multi-junction	3-junction	38.6
	4-junction	45.1
	5-junction	45.1
	6-junction	47.7
Silicon	Crystalline	25.6
	Multi-crystalline	20.8
Thin Film	CdTe	21
	CIGS	20.5
	A-Si	13.4
Dye-sensitized		11.9
Organic		11

Considering PV inverters, their losses have reduced due to the intensive related research, and recently show efficiency values above 97% and even more for central inverters (which may reach 98% efficiency) [1.23]. However, converter efficiency is expected to achieve higher values when silicon carbide (Si-C) and gallium nitride (Ga-N) semiconductors devices become economically viable [1.5].

The PV converter controller impacts on PV system efficiency. PV module non-linear characteristics and their dependency on atmospheric temperature and irradiance level greatly affect PV system efficiency [1.24]. To overcome these limitations, controlled PV operation at its peak power is a must. Thus, various maximum power point tracking (MPPT) techniques have been presented for PV applications [1.25].

1.5.3 Reliability

For assessing the entire PV system reliability, the system components are not equally evaluated. Encountering no noise or moving parts, PV modules have proven to be reliable maintenance-free source, comprising 1% of the energy loss due to underperformance from all causes [1.26]. Often module failures are caused by external causes, such as incorrect handling and mounting. PV modules are usually guaranteed for a lifetime of 25 years at a minimum 80% of their rated output, and sometimes for 30 years at 70% [1.11].

But the PV converter is assumed to fail, more frequently and is responsible for more losses, than any other system component [1.26]. Hence, studies are carried out to enhance inverters reliability [1.27]. Protection devices must be carefully selected to prevent any failure of the power circuit.

An associated battery storage device is an option for better grid reliability in the case of grid-tied PV systems and is mandatory in the case of critical loads. Battery life-time varies depending on the type and operating regime but is typically between 5 and 10 years [1.2].

1.5.4 Price and investment costs

The PV system is considered economically viable on the long run. It has the merits of long life-time, as well as flexibility at the installation location. Moreover, the emergence of the global PV market has coincided with rapid reductions in the costs of PV modules and systems resulting from improvements in PV technology and the scaling up of manufacturing.

In 2012, PV module prices, in mature markets, were reduced to one fifth their values in 2008 while PV system prices were reduced to one third. In 2013 and 2014, module prices more or less stabilized. PV modules' production in China has stimulated competition and reduced prices. In the first half of 2014, Chinese Tier 1 module was sold at 0.59-0.60 USD/W in China, and 0.67-0.79 USD/W in other countries. On the other hand, German modules were sold at 0.95 USD/W [1.11].

However, the entire PV systems' prices range more widely than those of PV modules since they involve the PV source itself along with the applied power electronic converter and other BOS components. Small systems, such as rooftop systems, are usually more expensive than larger ones, especially ground-based utility-scale systems. Moreover, prices vary significantly among countries for similar system types. Most of this gap comes from differences in “soft costs”, which include customer acquisition, permitting, inspection and interconnection, installation labour, and financing costs, especially for small system. In 2013, China showed the lowest PV systems' prices; 1.5, 1.4, and 1.4 USD/W for residential, commercial and utility-scale PV systems respectively [1.11].

Considering the levelized cost of energy (LCOE) from PV systems, it is rapidly approaching the level of generation costs from conventional alternatives with increased restrictions. In 2014, feed-in tariff paid for electricity, from large-scale PV installations in Germany, fell to 9 ct/kWh from over 40 ct/kWh, for installations connected in 2005. Even lower prices have been reported in sunnier regions of the world. A power purchase agreement for a 200 MW-solar farm in Dubai was recently signed for 5 ct/kWh [1.28].

Finally, regarding renewable energy investment costs, PV power was the leading sector in terms of money committed during 2013. It received 53% (113.7 billion USD) of the total new investment in renewable power and fuels [1.29].

1.6 Photovoltaic future outlook

For PV future growth, PV industry associations, like the European photovoltaic industry association (EPIA), and the International Energy Agency (IEA), have taken different supportive steps and present different future plans. For the EPIA low-high scenario, global PV cumulative installed capacity in 2018 will reach 321.4-430.3 GW compared to the 138.9 GW achieved at 2013 [1.12]. The IEA estimates that the cumulative installed PV global capacity can reach 465 GW to 515 GW by 2020 [1.11]. PV power will soon be considered the cheapest form of electricity in many regions. Depending on annual irradiance level, power costs of 4-6 ct/kWh are expected in Europe by 2025 [1.28].

1.7 Grid codes required for PV-grid interface

For PV integration with the main grid and surrounding micro grids, many aspects have to be investigated in the fields of power electronics and power quality to make its interface a reality. Hence, many organizations are working towards imposing grid requirement standards that can be adapted by different countries for PV-grid interface such as; the

Institute of Electrical and Electronics Engineers (IEEE) and the International Electro-technical Commission (IEC) [1.30]. Examples of IEEE and IEC PV standards are IEEE-1547 and IEC61727 respectively. IEEE 1547 provides specifications for grid-interface of distributed generation systems [1.31] while IEC 61727 defines utility-connection criteria for PV systems [1.32]. When the PV inverter is grid connected, these standards (summarized in Table 1.2) must be complied with [1.30].

Table 1.2. Summary of PV-related standards [1.30]

Standard / **Parameter**	**IEC 61727**	**IEEE 1547**
Supply voltage level for normal operation, Voltage range (V)	196-253	97-121
Frequency deviations for normal operation (Hz)	50 ± 1	59.3 < f < 60.5
Total harmonic distortion (THD)	5%	5%
Power factor	More than 0.9 (lagging) for 50% of rated power	----------
DC offset	< 1% of the rated root-mean-square (RMS) current	< 0.5% of the rated RMS current

1.8 Problem definition

This thesis is involved with investigating a complete PV system, shown in Figure 1.4, starting from the PV side with its MPPT issue to the grid side with the interface requirements.

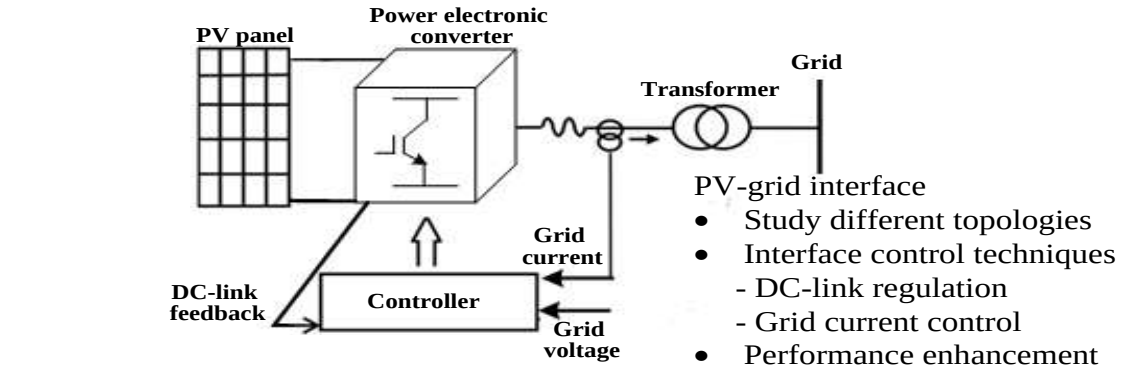

Figure 1.4. The main research points addressed in this thesis.

1.9 Thesis objective

The main objective of this research is to find solutions to some PV system associated problems which are MPPT and grid interface issues. Regarding the former, the submitted thesis aims at finding a low-cost efficient MPPT technique convenient for stand-alone and grid-tied PV systems. This MPPT technique should feature reduced implementation complexity along with minimal steady-state power oscillations around the MPP and fast dynamic response under varying atmospheric conditions. Considering grid-tied PV systems, the thesis targets the study of single-phase two-stage and single-stage topologies. In both cases, the control loops required for PV-grid interfacing are addressed, along with enhancements to the studied system's performance.

1.10 Research methodology

This thesis includes: (i) the study of a stand-alone PV system to address the MPPT problem and (ii) two grid-tied systems to address grid interface requirements. The latter, includes two-stage and single-stage PV systems. The research methodology is:

1.10.1 Stand-alone PV system with a battery load

- Investigate different schemes controlling the applied DC/DC converter's switching.
- Study a conventional MPPT technique showing its limitations.
- Introduce a low-cost MPPT technique featuring simple implementation, with superior steady-state and transient performance during irradiance changes.

1.10.2 Grid-tied PV systems

Two PV grid-connected topologies are presented in this thesis to achieve the following objectives

i. Single-phase, two-stage grid-tied PV system employing a boost chopper followed by a voltage source inverter (VSI)

- Study conventional control loops for this topology.
- Introduce a sensorless control technique and compare it with the conventional one.

ii. Single-phase, single-stage grid-tied PV system applying a current source inverter (CSI)

- Apply a single CSI stage, to perform MPPT and PV-grid interfacing.
- Model and design of the presented system.
- Investigate a high performance grid current controller that achieves minimised grid. current harmonics with reduced low-valued DC-link inductor.

References

[1.1] International Energy Agency (IEA), "World Energy Outlook 2014: Executive Summary", 2014.

[1.2] B. K. Bose, "Global Energy Scenario and Impact of Power Electronics in 21st Century", IEEE Trans. Industrial Electronics, Vol. 60, No. 7, 2013. pp. 2638-2651.

[1.3] B. K. Bose, "Global Warming: Energy, Environmental Pollution, and the Impact of Power Electronics", IEEE Industrial Electronics Magazine, Vol. 4, No. 1, 2010, pp. 6–17.

[1.4] Renewable Energy Policy Network for the 21st century (REN21), "RENEWABLES 2014: GLOBAL STATUS REPORT", 2014.

[1.5] M. Liserre, T. Sauter, and J. Y. Hung, "Future Energy Systems: Integrating Renewable Energy Sources into the Smart Power Grid through Industrial Electronics", IEEE Industrial Electronics Magazine, Vol. 4, No.1, March 2010, pp.18-37.

[1.6] J. M. Guerrero, et al., "Distributed Generation: Toward a New Energy Paradigm", IEEE Industrial Electronics Magazine, Vol. 4, No.1, March 2010, pp.52-64.

[1.7] John Perlin, "A History of Photovoltaics", 2008.
Available:
http://www.usc.edu/org/edisonchallenge/2008/ws1/AHistoryof Photovoltaics.pdf

[1.8] US Department of Energy, "The History of Solar".
Available: https://www1.eere.energy.gov/solar/pdfs/solar_timeline.pdf

[1.9] M. Hosenuzzaman, et al., "Global Prospects, Progress, Policies, and Environmental Impact of Solar Photovoltaic Power Generation", Renewable and Sustainable Energy Reviews, Vol. 41, 2015, pp. 284–297.

[1.10] D. Turney, and V. Fthenakis, "Environmental Impacts from the Installation and Operation of Large-scale Solar Power Plants", Renewable and Sustainable Energy Reviews, Vol. 15, No. 6, 2011, pp.3261-3270.

[1.11] International Energy Agency (IEA), "Technology Roadmap: Solar Photovoltaic Energy", 2014.

[1.12] European Photovoltaic Industry Association (EPIA), "GLOBAL MARKET OUTLOOK: For Photovoltaics 2014-2018", 2014.

[1.13] International Energy Agency (IEA), "TRENDS 2014 IN PHOTOVOLTAIC APPLICATIONS: Survey Report of Selected IEA Countries between 1992 and 2013", 2014.

[1.14] North Carolina Solar Center, "Photovoltaic Applications", 2002. Available: http://infohouse.p2ric.org/ref/49/48007.pdf

[1.15] National Renewable Energy Laboratory (NREL), "Energy Analysis: Solar Power and the Electric Grid", 2010.

[1.16] F. Blaabjerg, et al, " Overview of Control and Grid Synchronization for Distributed Power Generation Systems", IEEE Trans. Industrial Electronics, Vol. 53, No. 5, October 2006, pp. 1398-1409.

[1.17] M. A. Eltawil, and Z. Zhao, " Grid-connected Photovoltaic Power Systems: Technical and Potential Problems—A Review", Renewable and Sustainable Energy Reviews, Vol. 14, No. 1, January 2010, pp. 112–129.

[1.18] S. B. Kjaer, J. K. Pedersen, and F. Blaabjerg," A Review of Single-phase Grid-connected Inverters for Photovoltaic Modules", IEEE Trans. Industry Applications, Vol. 41, No. 5, 2005, pp.1292-1306.

[1.19] PV Power plants 2014: Industry guide, 2014. Available: http://www.pv-power-plants.com/industry/falling-prices-new-markets

[1.20] Trinasolar, "World's Largest Rooftop PV System: Antwerp, Belgium". Available: http://www.trinasolar.com/downloads/us/casestudy_Antwerp_40MW_WW.pdf

[1.21] Martin A. G., et al, "Solar Cell Efficiency Tables (version 45)", Progress in Photovoltaics: Research and Applications, Vol. 23, No.1, 2015, pp. 1–9.

[1.22] R. R. King et al, "Solar Cell Generations Over 40% Efficiency", Progress in Photovoltaics: Research and Applications, Vol. 20, No.6, 2012, pp. 801–815.

[1.23] S. Kouro et al, "Grid-Connected Photovoltaic Systems: An Overview of Recent Research and Emerging PV Converter Technology", IEEE Industrial Electronics Magazine, Vol. 9, No. 1, March 2015, pp. 47–61.

[1.24] D.P. Hohm and M. E. Ropp, "Comparative Study of Maximum Power Point Tracking Algorithms", Progress in Photovoltaics: Research and Applications, Vol. 11, No.1, 2003, pp. 47–62.

[1.25] T. Esram, and P.L. Chapman, "Comparison of Photovoltaic Array Maximum Power Point Tracking Techniques," IEEE Trans. Energy Conversion, Vol. 22, No. 2, June 2007, pp. 439-449.

[1.26] A. Golnas, "PV System Reliability: An Operator's Perspective", IEEE Journal of Photovoltaics, Vol. 3, No. 1, January 2013, pp. 416-421.

[1.27] Bin Gu, et al, "High Reliability and Efficiency Single-Phase Transformerless Inverter for Grid-Connected Photovoltaic Systems", IEEE Trans. Power Electronics, Vol. 28, No. 5, May 2013, pp. 2235- 2245.

[1.28] Fraunhofer ISE, "Current and Future Cost of Photovoltaics: Long-term Scenarios for Market Development, System Prices and LCOE of Utility-Scale PV Systems", 2015.

[1.29] FS– UNEP Collaborating Centre for Climate & Sustainable Energy Finance, "GLOBAL TRENDS IN RENEWABLE ENERGY INVESTMENT 2014", 2014.

[1.30] Seddik Bacha, et al, "Photovoltaics in Microgrids: An Overview of Grid Integration and Energy Management Aspects", IEEE Industrial Electronics Magazine, Vol. 9, No. 1, March 2015, pp. 33-46.

[1.31] "Standard Voltages", IEC Std. 60038, 2002.

[1.32] "IEEE Standard for Interconnecting Distributed Resources with Electric Power Systems", IEEE Std. 1547-2003, 2003, pp. 1–16.

Chapter Two

Photovoltaic System Components and Operation

In this chapter, several facts regarding PV sources are presented; starting from the PV cell construction and combinations to form a PV field. Then, PV module' electrical characteristics are discussed followed by the development of an enhanced PV single-diode model. Finally, the PV maximum power point tracking (MPPT) aspect is discussed along with an explanation of the most common MPPT algorithms.

2.1 PV cell fabrication and arrangements

A PV field consists of a number of PV arrays grouped together as shown in Figure 2.1. The PV array itself is a group of series-parallel connected modules in which the key component is the solar cell [2.1]

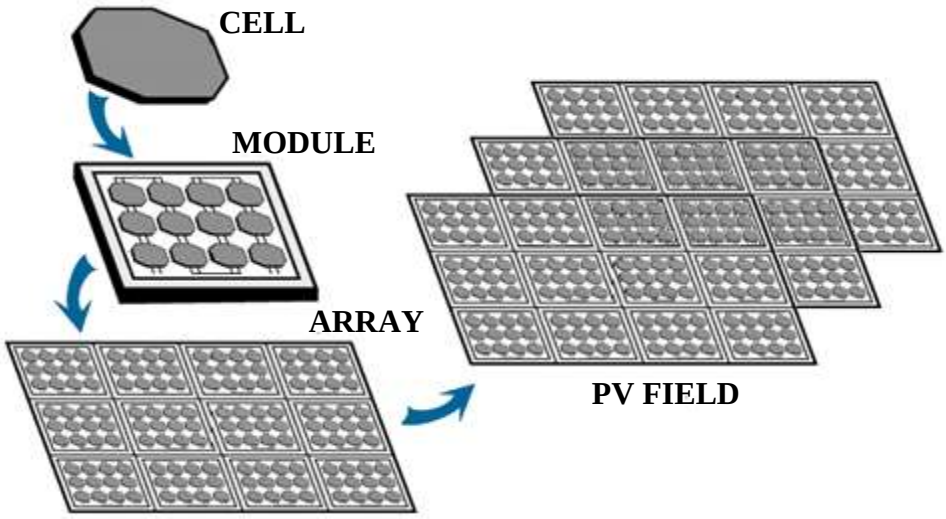

Figure 2.1. PV cell arrangements.

2.1.1 PV cell fabrication

Generally, silicon is the semi-conductor material from which PV cells are made [2.2]. The manufacturing process creates an n-type emitter, p-type base, and charge-separating junction (p-n junction). It also deposits an anti-reflective coating, and adds metal contacts (front and back contacts) [2.3]. The purpose of the top contacts is to collect current from the emitter and to pass this current, through a metal top grid, to an external circuit. The anti-reflection coating minimizes light reflection from the PV cell, thus increasing its output power. Cells are then grouped into modules, with transparent glass for the front

side, a weatherproof material for the back side and usually a surrounding frame [2.2]. The PV cell effect and its components are demonstrated in Figure 2.2.

As shown in Figure 2.2, PV cells are made up of at least 2 semi-conductor layers; the p-type layer containing positive charge (holes) and the n-type layer with a negative charge (electrons). During junction formation, electrons move from the n-type silicon into the p-type, as they will be attracted to the nearby holes, while holes move in the opposite direction. These neutralising charge movements build up a fixed potential barrier, at the junction between the n-type and p-type layers, opposing any further movement of free carriers and creating a state of equilibrium in the form of an electric field [2.4]. As a PV cell is exposed to sun irradiance, many of the sunlight photons are reflected, pass right through, or are absorbed by the PV cell. When enough photons are absorbed by the PV cell negative layer, electrons will gain high energy and will be knocked out of a molecular lattice, leaving ‘free electron’ and ‘hole’ pairs. These pairs of covalent opposite electrical charge carriers are separated by the p-n junction and diffuse, in the electric field into two different directions [2.3, 2.4]. Electrons move to the n-type layer and holes go to the p-type layer. Hence, a voltage will be created on the junction driving a current through an external circuit connecting the two layer contacts [2.4].

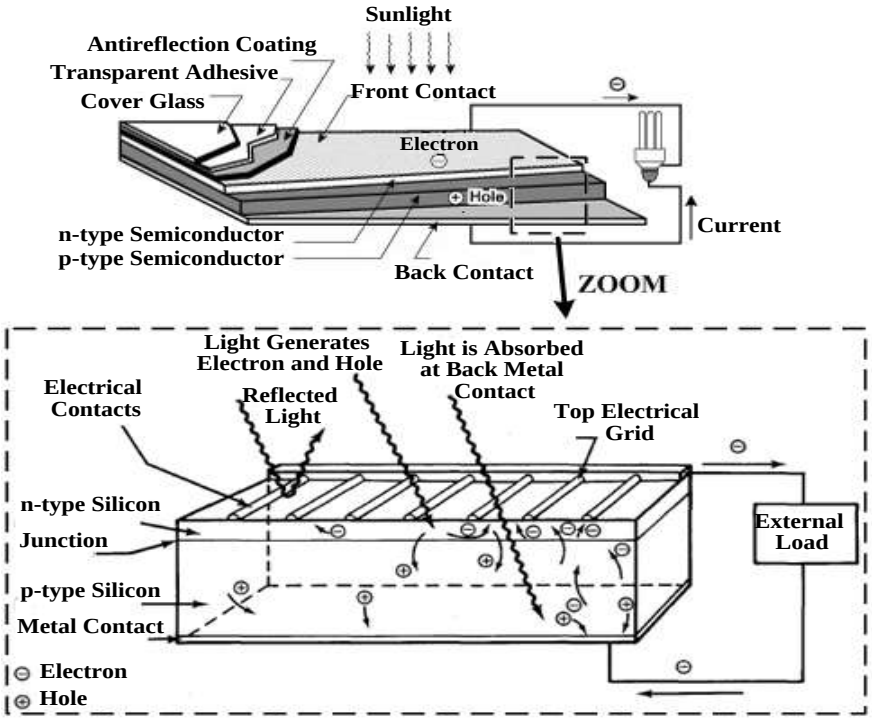

Figure 2.2. PV cell construction and operation [2.3].

This ‘photoelectric effect’ has most commonly been generated with materials such as crystalline silicon (C-Si) and a range of thin-film (TF) semiconductors. In addition, several emerging PV cell technologies may be technically and economically competitive in the future [2.5]. The performance of a PV cell is expressed in terms of its ‘energy conversion efficiency’, that is, the efficiency in converting the energy in sunlight into electricity. This efficiency depends on the length and intensity of sun- light falling on the system, and the type and quality of PV cell materials.

A summary of different PV cell technologies follows, along with their relative applications and conversion efficiency [2.2, 2.5-7]:

Crystalline Silicon (C-Si): These technologies constitute about 90% of the current PV market [2.2, 2.3, and 2.5]. There are two general types of crystalline or wafer-based silicon PV cells; viz., mono-crystalline and multi-crystalline. Mono-crystalline semiconductor wafers are cut from single-crystal silicon ingots whereas multi-crystalline semiconductor wafers are cut from directionally solidified blocks or grown in thin sheets. Mono-crystalline ingots are more difficult, energy intensive, and expensive to grow than simple blocks of multi-crystalline silicon [2.2]. However, the former produces higher efficiency, over 25%, thus can be applied in terrestrial and space applications [2.5]. Multi-crystalline cells, applied in terrestrial uses, show efficiency of more than 20% [2.6].

Thin Film (TF): This technology is mainly in the form of thin films of semiconductor materials on a solid backing material. The semiconductor layer is only a few microns (smaller than 10 mm) thick, which is about 100 times thinner than current C-Si cells [2.2]. Most thin films are direct band gap semiconductors, which means they are able to absorb the energy contained in sunlight with a much thinner layer than indirect band gap semiconductors like traditional C-Si PV [2.2]. Being deposited on a stainless steel substrate, thin film PV cells allow the creation of a flexible PV module, thus lowering the manufacturing cost by the high throughput deposition process and lower material cost. The most common thin-film semiconductor materials are amorphous silicon (A-Si), cadmium telluride (CdTe), and alloys of copper indium gallium di-selenite (CIGS) with cell efficiencies 13.5%, 21% and 20.5%, respectively [2.6]. Generally thin film cells are used for terrestrial applications where the lowest efficiency A-Si is specifically used for low power applications such as calculators and garden lights [2.5].

Concentrating photovoltaic (CPV): This technology uses mirrors or lenses to concentrate sunlight onto high-efficiency silicon or multi-junction (MJ) PV cells. MJ cells are capable of much high efficiencies (about 45%) compared to single-junction silicon cells in which the silicon wafers do not absorb all the light energy [2.7]. MJ cells have several wafer pairs (p-n junctions) above or below where each junction is tuned to a different wavelength of light using different doping chemicals. Therefore, the MJ solar cell can absorb more energy from the light, increasing cell efficiency [2.2]. However, this higher efficiency comes at higher manufacturing cost, thus they are mainly applied for space purposes rather than terrestrial applications [2.5].

A number of other PV technologies - frequently referred to as third-generation PV - are being developed [2.2]. Dye-sensitized PV cells use dye molecules absorbed onto a nano-structured substrate and immersed in a liquid or gel electrolyte to absorb solar radiation and have demonstrated laboratory efficiencies as high as 11.9% [2.6]. Organic PV cells, based on polymers or small molecules with semiconductor properties, have demonstrated laboratory cell efficiencies of about 11% [2.6]. These newly developed cells, being inexpensive solutions, are generally used in terrestrial applications [2.5]. However, there are significant challenges to their commercialization due to the stability of their materials against oxygen and water ingress [2.2]. This limits their lifetime from a few hundred hours to 2 years. Also, organic and dye-sensitized PV cells use dyes that have shown degradation in the case of long time exposure to direct sunlight.

2.1.2 PV module combinations

Generally, each individual PV cell produces only 1-2 Watts [2.1, 2.3]. To increase their power output, cells are combined in series in a package called a PV module. The choice of connecting the cells in series comes from the fact that their operating voltage is few hundreds of mV, while the current they generate at high irradiation is of some amperes (being area dependant). As a consequence, the cells series connection leads to PV modules working at few tens of volts and several amperes [2.1]. These modules are then wired in serial and/or parallel connection with one another, into what is called a PV array, to create the voltage and amperage output required in the power processing system. In PV power fields, PV arrays are grouped to reach the power level required by the PV plant.

Regarding PV module efficiency, commercial crystalline-silicon modules have shown improved average efficiency in the last years, reaching 23% [2.6]. Non-standard cell architectures tend to use high-quality mono-crystalline wafers and more sophisticated processing to achieve higher module efficiencies. Thin film modules have lower efficiencies, about 12% for A-Si, 16% for CIGS, and 17.5% for CdTe [2.6]. CdTe-based PV has experienced significantly higher market growth during the last decade than the other thin-film PV technologies [2.2]. CPV modules offer the highest efficiencies which vary from 25% to 35% [2.8].

2.2 PV electrical characteristics

In order to study PV electrical characteristics, PV characteristics equations are first demonstrated, and then the PV module's *I-V* curve is presented focusing on its operating points.

2.2.1 PV *I-V* characteristic equations

For simplicity, the PV single diode model, shown in Figure 2.3, is studied in this work. This model offers a good compromise between simplicity and accuracy [2.9-11]. *I-V* characteristic equations for single diode PV devices are illustrated as follows:

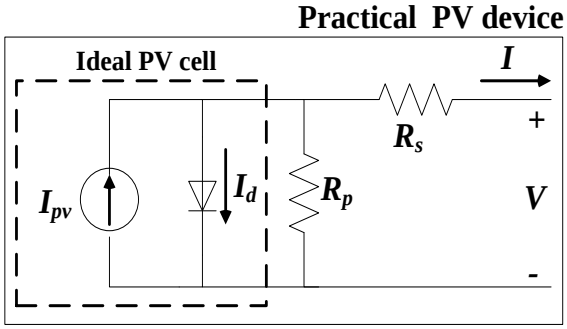

Figure 2.3. PV device single diode model [2.11].

i. Ideal PV cell I-V equation

The equivalent circuit of the ideal PV cell consists of a photocurrent source and a diode as shown in Figure 2.3. The basic equation from the theory of semiconductors [2.12] that mathematically describes the *I–V* characteristic of the ideal PV cell is:

$$I = I_{pv,cell} - \underbrace{I_{0,cell}\left[\exp\left(\frac{qV}{akT}\right) - 1\right]}_{I_d} \tag{2.1}$$

where $I_{pv,cell}$ is the current generated by the incident light (it is directly proportional to the sun radiation), I_d is the Shockley diode current equation, $I_{0,cell}$ is the reverse saturation or leakage current of the diode, q is the electron charge ($1.60217646 \times 10^{-19}$ C), k is the Boltzmann constant ($1.3806503 \times 10^{-23}$ J/K), T (in K) is the temperature of the *p–n* junction, and a is the diode ideality constant.

ii. Practical PV module I-V equation

The basic equation (2.1) of the elementary PV cell does not represent the *I–V* characteristic of a practical PV module. A PV module is composed of several similar PV cells connected in series, thus the observation of the characteristics at the terminals of the module requires the inclusion of additional parameters to the basic equation which results in (2.2) [2.12]. Equation (2.2) describes the single-diode model of the practical PV device presented in Figure 2.3.

$$I = I_{pv} - I_0 \left[\exp\left(\frac{V + R_s I}{V_t a}\right) - 1\right] - \frac{V + R_s I}{R_p} \tag{2.2}$$

where V and I are the PV module output voltage and current respectively. I_{pv} is the photovoltaic current which is generated by the incident light (directly proportional to the sun irradiance) and I_0 is the saturation current of the PV module. R_s and R_p are the internal series and parallel resistances of the module respectively, as shown in fig 2.3. Finally, V_t, which is equal to $\frac{N_s kT}{q}$, is the PV thermal voltage with N_s PV cells connected in series.

iii. PV array I-V equation

A PV array consists of a group of series-parallel connected PV modules as shown in Figure 2.4 to obtain the desired voltage and current. The size of the PV array varies from a single PV module to any number of modules. Hence, PV array output voltage and current can be calculated from equations (2.3) and (2.4) respectively [2.1].

$$I_{Array} = N_{pp} \times I \tag{2.3}$$

$$V_{Array} = N_{ss} \times V \tag{2.4}$$

where I_{Array} is the PV array output current, and I is the PV module output current, calculated using eq. (2.2). V_{Array} is the PV array output voltage, and V is the PV module output voltage. N_{pp} is the number of the parallel strings in the PV array, and N_{ss} is the number of series PV modules in one PV string. In the PV array, the number of PV modules in each string should be identical to get equal parallel voltages.

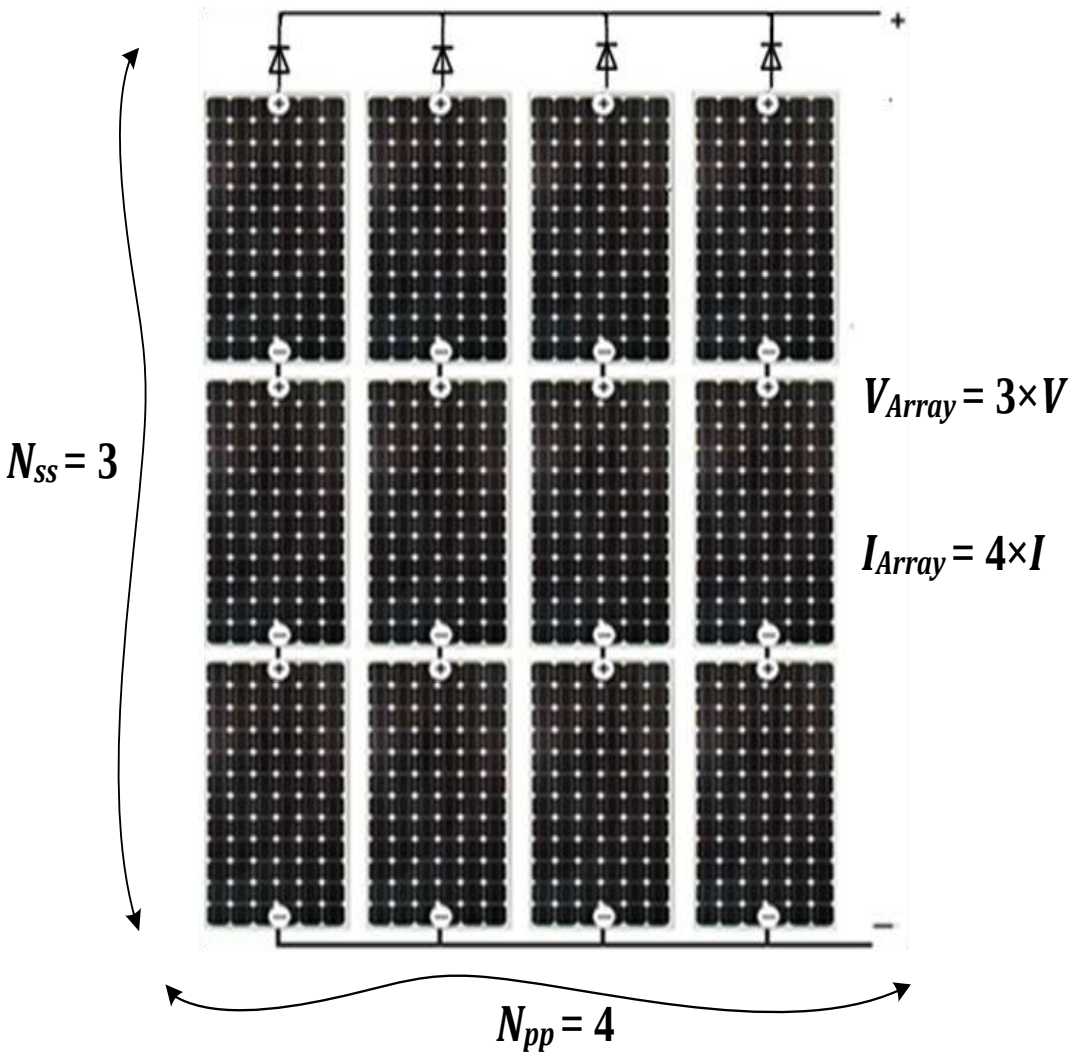

Figure 2.4. PV array configuration.

2.2.2 *I-V* characteristic curve of PV modules

Equation (2.2) shows that a PV device has a non-linear *I-V* characteristics curve as shown in Figure 2.5. This curve depends on the internal characteristics of the device (R_s , R_p) and on external influences, such as the cell temperature level and sun irradiance [2.11]. The amount of incident light directly affects the generation of charge carriers, and consequently, the current generated by the device. There are three specific operating points on the PV *I-V* curve, as follows [2.1]:

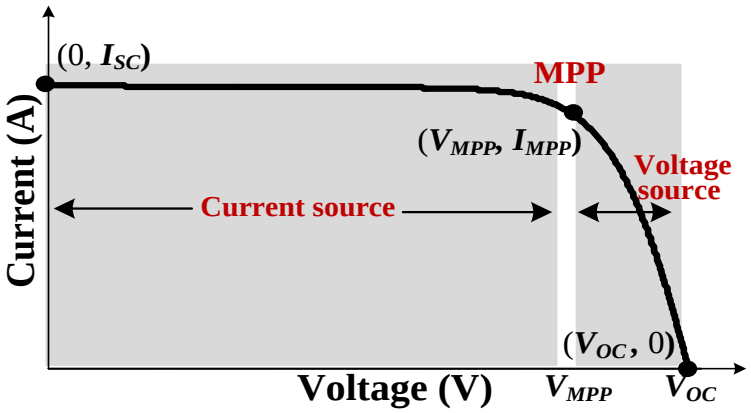

Figure 2.5. PV module *I-V* characteristic curve at a given irradiance and cell temperature.

- The short-circuit (SC) condition, characterized by zero voltage at the PV module terminals and the short-circuit current I_{SC}.
- The open-circuit (OC) condition, characterized by zero current flowing from the PV panel terminals and an open-circuit voltage V_{OC}.
- The maximum power point (MPP), at which the current is I_{MPP}, the voltage is V_{MPP}. The resulting power P_{MPP}, equal to $V_{MPP} \times I_{MPP}$, is the maximum PV power that can be delivered for the given environmental conditions.

It can be concluded, from Figure 2.5, that although electric sources are generally classified as current or voltage sources, practical PV modules present a hybrid behaviour [2.11]. It may be a current or voltage source depending on the operating point. In the region left of the MPP, the PV current is almost constant and the PV module can be approximated as a constant current source. Right of the MPP, the PV current begins a sharp decline and the PV module can be approximated as a constant voltage source.

The practical PV device has series resistance R_s whose influence is dominant when the device operates in the voltage source region and a parallel resistance R_p dominant in the current source region of operation [2.11]. The R_s resistance is the sum of several device structural resistances such as the contact resistance of the metal base with the p semiconductor layer, the resistances of the p and n bodies, the contact resistance of the n layer with the top metal grid, and the metal grid resistance [2.13]. The R_p resistance exists mainly due to the leakage current of the *p–n* junction and depends on the fabrication method of the PV cell.

2.3 Developing a mathematical model for PV modules

Manufacturers of PV panels, instead of the *I–V* equation, provide only a few experimental data about electrical and thermal characteristics. PV module datasheets provide basically the following information: the nominal open-circuit voltage ($V_{OC\text{-}n}$), the nominal short-circuit current ($I_{SC\text{-}n}$), the experimental voltage at the MPP ($V_{MPP\text{-}e}$), the experimental current at the MPP ($I_{MPP\text{-}e}$), the open-circuit voltage/temperature coefficient (K_V), the short circuit current/temperature coefficient (K_I), and the maximum experimental peak output power ($P_{MPP\text{-}e}$) [2.11]. These PV specifications are given by manufacturers under specific nominal operating conditions, which are universally defined as standard test conditions (STC). Such conditions are defined by the cell temperature = 25 ℃, irradiation level = 1000 W/m^2, and the air mass value = 1.5. The latter gives a measure of the effect of the air mass, between a surface and the sun, on the spectral distribution and intensity of sunlight. The path length of the solar radiation through the atmosphere affects the light deviation and absorption [2.1, 2.11].

Basically, the latter is all the information that can be found in PV panel datasheets. Unfortunately, other parameters required for adjusting PV array models is not given, such as the diode ideality constant, the light-generated current, and the diode reverse saturation current, and the series and shunt resistances.

To solve the latter, [2.11] developed a method for the mathematical modelling of PV modules and determining the unknown parameters of the single-diode model equation of a practical PV module. Thus, this method fits the mathematical *I–V* equation to the experimental specific points of the *I–V* curve of the practical module. This occurs using the nominal specifications found in the panel datasheet without the need to guess or estimate any other parameters, except the diode constant *a*. The simplicity of the method presented in [2.11] for adjusting PV parameters make the proposed model ideal for power electronics designers who are looking for an easy and effective model for the simulation of PV devices with power converters.

2.3.1 Calculating PV unknown parameters

Parameters of the single-diode model shown in eq. (2.2), which are not found in PV datasheets, can be computed as follows [2.11]:

i. Diode ideality constant

The value a expresses the degree of diode ideality and it may be arbitrarily chosen. This constant affects the curvature of the *I–V* curve and varying a slightly improves the model accuracy [2.11]. It usually ranges from 1 to 1.5 [2.9].

ii. Light-generated current

Because, in practical devices, the series resistance is low and the parallel resistance is high, the nominal light-generated current ($I_{pv\text{-}n}$) at STC is generally assumed to be equal the nominal short circuit current ($I_{SC\text{-}n}$) given in PV datasheets. However, for improving the PV model, [2.11] proposes the calculation of $I_{pv\text{-}n}$ using (2.5) where the values of R_s and R_p are calculated by an iterative method presented at the end of this subsection.

$$I_{pv-n} = \frac{R_p + R_s}{R_p} I_{SC-n} \tag{2.5}$$

The light-generated current of the PV device (I_{pv}) depends linearly on the solar irradiation and is also influenced by temperature [2.10, 2.11], as shown in (2.6);

$$I_{pv} = (I_{pv-n} + K_I \Delta T) \frac{G}{G_n} \tag{2.6}$$

where $\Delta T = T - T_n$ (T and T_n are the actual and nominal temperatures, K, respectively), G (W/m^2) is the irradiation on the device surface, and G_n is the nominal irradiation.

iii. Diode saturation current

The nominal diode saturation current is computed from (2.7) as follows [2.11]:

$$I_{0-n} = \frac{I_{SC-n}}{\exp\left(\frac{V_{OC-n}}{V_{t-n} a}\right) - 1} \tag{2.7}$$

where V_{t-n} is the thermal voltage of N_s series-connected cells at the nominal temperature, 25^{o}C.

In order to show the strong dependence of the saturation current (I_0) on temperature, [2.11] proposes (2.8) which is obtained from (2.7) by including the practical current and voltage coefficients K_I and K_V. Hence, for a wide range of temperature variations, the best match between the model open-circuit voltages and the experimental data is achieved as well as the best possible *I–V* curve fitting.

$$I_0 = \frac{I_{SC-n} + K_I \Delta T}{\exp\left(\frac{V_{OC-n} + K_V \Delta T}{V_t a}\right) - 1} \tag{2.8}$$

iv. Series and shunt resistances

A method for adjusting R_s and R_p is given in [2.11], based on the fact that there is a pair of resistances that guarantees that the maximum power (P_{MPP}), computed by $V_{MPP} \times I_{MPP}$ from the *I–V* model equation (2.2), is equal to the maximum experimental power from the datasheet ($P_{MPP\text{-}e}$). Hence, the relation between R_s and R_p, can be found by making $P_{MPP} = P_{MPP\text{-}e}$ and solving the resulting equation for R_s:

$$P_{MPP} = V_{MPP}\left\{I_{pv} - I_0\left[\exp\left(\frac{q}{kT}\frac{V_{MPP} + R_s I_{MPP}}{N_s a}\right) - 1\right] - \frac{V_{MPP} + R_s I_{MPP}}{R_p}\right\} \tag{2.9}$$

$$= P_{MPP-e}$$

$$R_p = \frac{V_{MPP}(V_{MPP} + R_s I_{MPP})}{\left\{V_{MPP} I_{pv} - V_{MPP} I_0 \exp\left(\frac{q}{kT}\frac{V_{MPP} + R_s I_{MPP}}{N_s a}\right) + V_{MPP} I_0 - P_{MPP-e}\right\}} \tag{2.10}$$

Hence, to find the value of R_s (thence R_p) that makes the peak of the mathematical *P–V* curve coincide with the experimental peak power, an iterative process is proposed in [2.11] where *R*s is slowly incremented starting from $R_s = 0$. Thus, several values of R_s and R_p are calculated for adjusting the *I–V* curve to cross the desired experimental maximum power point at (V_{MPP}, I_{MPP}).

However, initial guesses for R_s and R_p are necessary before the iterative process starts. The initial value of R_s is zero while that of R_p may be given by (2.11). The latter determines the minimum value of R_p which is the slope of the line segment between the short-circuit and the maximum-power operating points [2.11];

$$R_{p-min} = \frac{V_{MPP}}{I_{SC-n} - I_{MPP}} - \frac{V_{OC-n} - V_{MPP}}{I_{MPP}} \tag{2.11}$$

The iterative method, proposed in [2.11] to calculate the series and shunt resistances and adjust the *I-V* model, is shown in Figure 2.6.

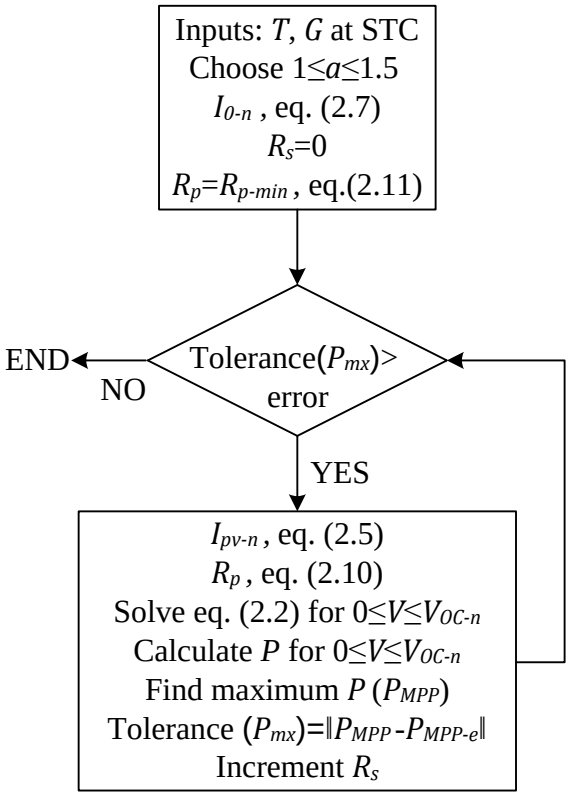

Figure 2.6. Flowchart of the iterative method applied for finding R_s and R_p [2.11].

2.3.2 Steps for adjusting the PV model (an illustrative example)

The main steps of adjusting a PV model, as proposed in [2.11], are verified using the illustrative example given in this subsection. A KD135SX_UPU PV module, with the datasheet shown in Table 2.1, is considered and its characteristic curves are plotted for different environmental conditions. The related MATLAB-file programs to achieve the latter are shown in Appendix D.1. The curves fitting steps can be summarised as follows;

1. The diode ideality constant (a) is selected in the range $1 \leq a \leq 1.5$. In the considered case, a is chosen to be 1.25.
2. R_s and R_p are calculated using the iterative method shown in Figure 2.6. The resistance iterative values result in the *I-V* and *P-V* curves shown in Figure 2.7. The *P-V* curve peak point coincides with the experimental peak power (135 W). In the considered case, the resistances are found to be; R_s=0.18Ω and R_p=63Ω, for a peak power tolerance of 0.1 W.
3. Input the current irradiance level and cell temperature
4. Calculate the nominal light-generated current ($I_{pv\text{-}n}$) using eq. (2.5)
5. Calculate the light-generated current at the considered conditions (I_{pv}) using eq. (2.6)
6. Calculate the diode saturation current at the considered conditions (I_0) using eq. (2.8)

7. Obtain the open-circuit voltage at considered environmental conditions from;

$$V_{OC} = V_{OC-n} + K_V \Delta T \tag{2.12}$$

8. Solve eq. (2.2), for $0 \leq V \leq V_{OC}$

9. Calculate P, for $0 \leq V \leq V_{OC}$

10. Plot I-V and P-V curves, for $0 \leq V \leq V_{OC}$

Table 2.1. KD135SX_UPU module specifications at standard test conditions

Nominal Short Circuit Current ($I_{SC\text{-}n}$)	8.37	A
Nominal Open Circuit Voltage ($V_{OC\text{-}n}$)	22.1	V
Maximum Power Current ($I_{MPP\text{-}e}$)	7.63	A
Maximum Power Voltage ($V_{MPP\text{-}e}$)	17.7	V
Maximum Output Power ($P_{MPP\text{-}e}$)	135	W
Temperature Coefficient of I_{SC} (K_I)	$5.02e^{-3}$	$A/^oC$
Temperature Coefficient of V_{OC} (K_V)	$-8e^{-2}$	$V/^oC$
Series Cells (N_s)	36	----

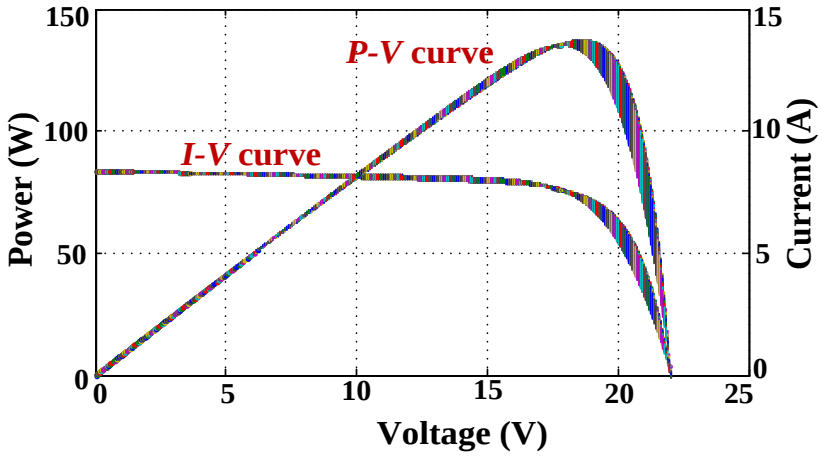

Figure 2.7. KD135SX_UPU module I-V and P-V curves plotted using the iterative method.

In order to demonstrate the strong dependence of PV module performance on temperature and irradiance level, the KD135SX_UPU PV module I-V and P-V curves are plotted, using R_s and R_p values of 0.18Ω and 63Ω respectively, for different environmental conditions as shown in Figure 2.8. From Figure 2.8 parts (a) and (b), there is a single MPP for a certain irradiance level and cell temperature. As the PV module characteristic curve shifts with changing irradiance or cell temperature, this MPP moves. As shown in Figure 2.8(a), the PV module short-circuit current is linearly dependent on the irradiance level unlike the open-circuit voltage which almost independent of it. As shown in Figure 2.8 (b),

cell temperature significantly affects the open-circuit voltage value whereas it has a negligible effect on the short circuit current value [2.1].

It is worth noting that once thermal stability occurs, the cell temperature usually changes quite slowly and almost fixed with respect to the variation in the irradiation level during the day [2.1].

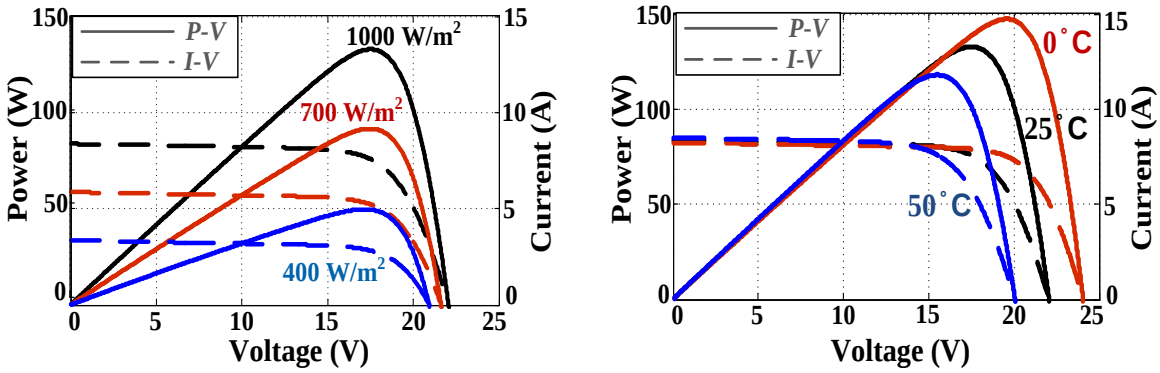

(a) (b)

Figure 2.8. *P-V* and *I-V* curves of KD135SX_UPU PV module (a) under three irradiance levels at 25℃ and (b) for three different cell temperatures during irradiance of 1000 W/m^2.

2.4 Photovoltaic maximum power point tracking issue

As previously discussed, a PV module, under uniform irradiance level and cell temperature, has a non-linear *I–V* and *P-V* characteristic curve on which there is a single optimal operating point, called the maximum power point (MPP). At this point, the module produces maximum output power. However, for a PV module directly connected to a DC load (a so-called 'direct-coupled' system), as shown in Figure 2.9 (a), the system's operating point 'A' is at the intersection of the PV module *I–V* curve and the load line as shown in Figure 2.9 (c). In general, this operating point is not at the module's MPP. Thus, in a direct-coupled system, the module must usually be oversized to ensure that the load power requirements can be supplied. This leads to an overly expensive impractical system [2.14].

To overcome this problem, a switched-mode power electronic converter, called a "maximum power point tracker", must be placed between the PV terminals and the load, as shown in Figure 2.9 (b), to maintain the PV array's operating point at the MPP [2.14, 2.15]. As shown in Figure 2.9 (c), left of the MPP, in the current source region, the slope of the *P-V* curve is positive while right ot the MPP, in the voltage source region, the slope is negative. At the MPP, the *P-V* curve slope equals to zero.

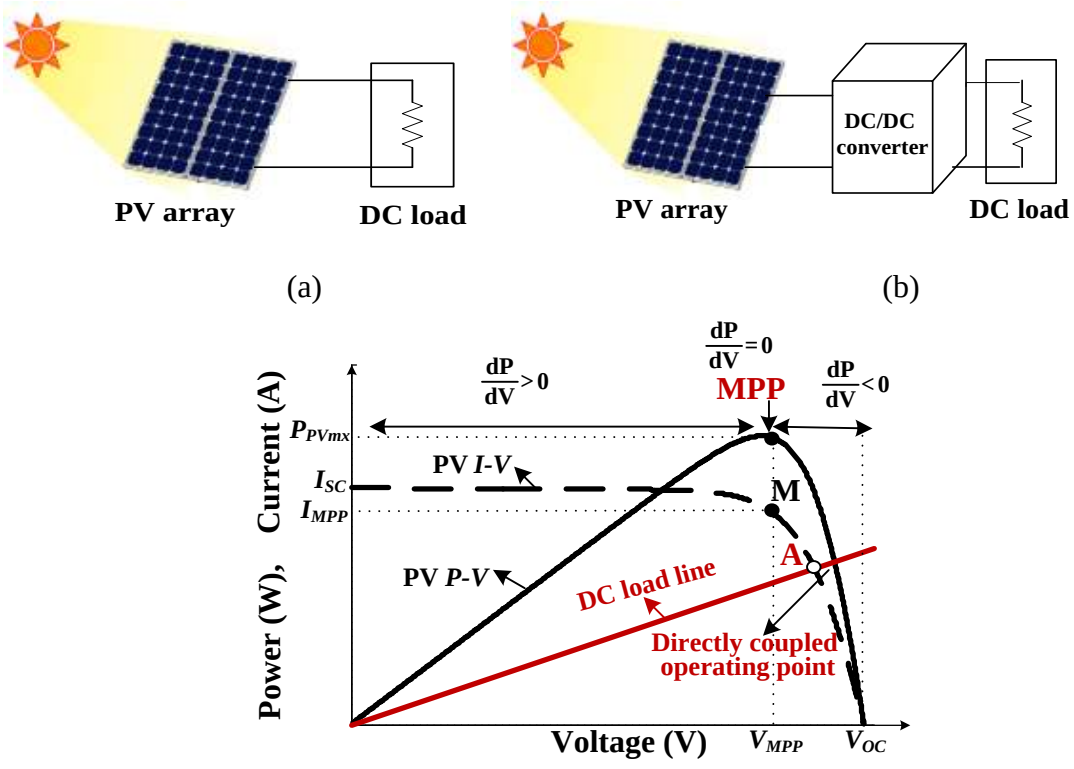

Figure 2.9. A PV module coupled to a DC load (a) without a MPP tracker, (b) via a MPP tracker, and (c) *I-V* and *P-V* curves of the system.

This MPP varies depending on the angle of sunlight, the surface of the panel, irradiance level and cell temperature. Hence, continuous tracking of the MPP becomes mandatory to maximize PV efficiency [2.15]. Moreover, in the case of partial shading [2.16], the PV module's characteristic curve may have multiple local peaks, but overall there is still only one MPP as shown in Figure 2.10. Hence, many studies have been carried out to solve problems of partial shading and detect the global MPP [2.17, 2.18].

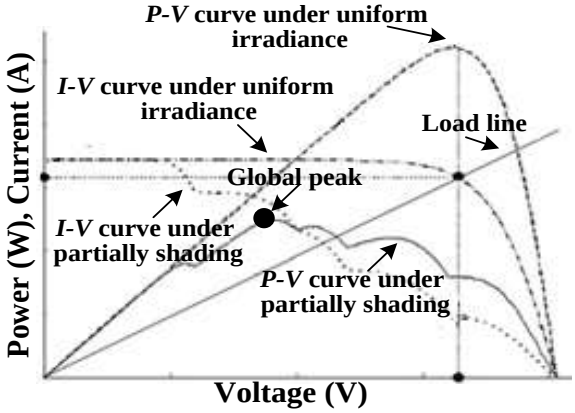

Figure 2.10. *I-V* and *P-V* curves of PV module under partial shading conditions.

2.5 Photovoltaic maximum power point tracking techniques

Various MPPT techniques have been presented in the literature [2.19-25]. Commonly applied MPPT methods include search algorithms such as perturb and observe (P&O) and incremental conductance (Inc.Cond.) algorithms. Also, there are module-based techniques such as fractional open-circuit voltage (V_{OC}) and fractional short-circuit current (I_{SC}). Different artificial intelligence techniques, such as fuzzy logic (FL), and artificial neural networks (ANN) techniques, are widely applied in the MPPT process, for their efficient performance under non-uniform and partially shading conditions.

2.5.1. Considered MPPT techniques' scheme and characteristics

The control scheme, advantages, limitations and advances of each of the considered MPPT techniques are discussed in details

i. Perturb and observe (P&O) technique

P&O technique involves a perturbation in the operating voltage of the PV array until reaching the MPP [2.21].

Control Scheme

On the *P-V* curve, shown in Figure 2.9, incrementing (decrementing) the PV voltage, increases (decreases) the power when operating on the current source region and decreases (increases) the power when operating on voltage source region. Therefore, if there is an increase in power, the subsequent perturbation should be kept the same to reach the MPP and if there is a decrease in power, the perturbation should be reversed. The process is repeated periodically until the MPP is reached. The system then oscillates around the MPP. The flowchart of P&O algorithm is shown in Figure 2.11

Advantages and Limitations

The P&O algorithm has the merits of simple structure, low cost and implementation ease with simple analogue circuitry or a low-cost microcontroller. It generally gives satisfactory performance with convenient efficiency. However, it has some limitations that reduce the tracking efficiency. It cannot be determined when the MPP tracker has actually reached the MPP; instead, it oscillates around the MPP. The oscillation can be minimized by reducing the perturbation step size. However, a smaller perturbation size slows down the MPPT. Furthermore, it may show degraded performance at low irradiance levels with

flattened *P–V* curves [2.19] and it can even fail under rapid atmospheric changes or partially shading conditions [2.19, 2.21]

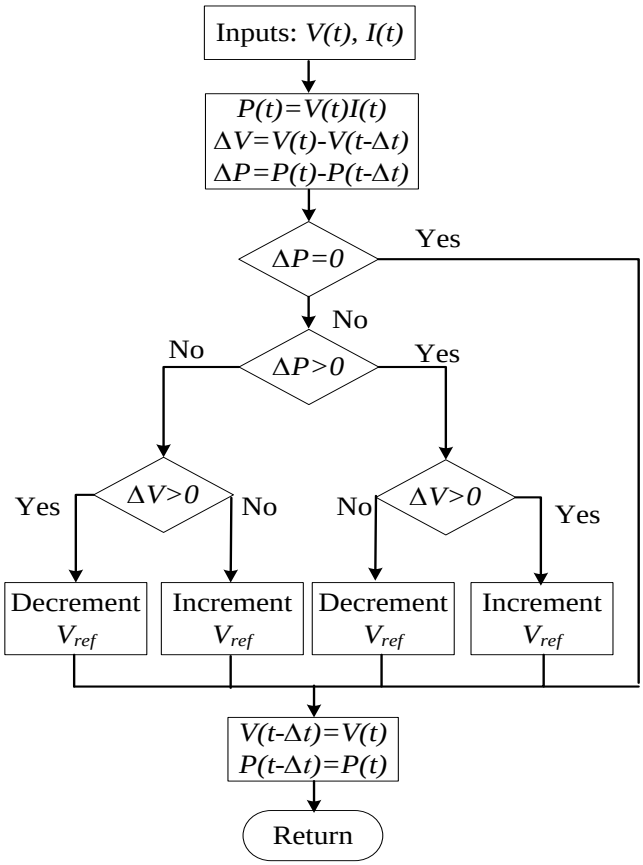

Figure 2.11. Flowchart of the P&O algorithm.

Modifications and advances

The oscillations encountered by the P&O technique can be minimized by reducing the perturbation step size. However, a smaller perturbation size slows down the MPPT. A solution to this conflicting situation is to have a variable perturbation size that gets smaller towards the MPP, thus compromising the aims of speed and accuracy as proposed in [2.26-28]. In [2.29], the PV array current is estimated from the PV array voltage, eliminating the need for a current sensor. A PI controller is utilized, in [2.30], as the adaptive perturb value generator for the reference array voltage. Finally, [2.31] proposes a zero-oscillation adaptive-step P&O technique to enhance P&O steady-state and transient performance.

ii. Incremental conductance (Inc.Cond.) technique

In this algorithm, the MPP is tracked by matching the PV array incremental conductance with the effective instantaneous conductance of the converter reflected across the module terminals [2.20].

Control scheme

The incremental conductance algorithm is derived by differentiating the PV array power with respect to voltage and setting the result to zero.

$$\frac{dP}{dV} = \frac{d(IV)}{dV} = I + V\frac{dI}{dV} = 0 \qquad \text{at MPP} \tag{2.13}$$

Thus, the slope of the array *P*-*V* curve is zero at the MPP, positive on the left of the MPP, and negative on the right [2.21]. Hence

$$\frac{dP}{dV} = 0 \qquad \text{at MPP} \tag{2.14}$$

$$\frac{dP}{dV} > 0 \qquad \text{left to MPP} \tag{2.15}$$

$$\frac{dP}{dV} < 0 \qquad \text{right to MPP} \tag{2.16}$$

Since

$$\frac{dP}{dV} = \frac{d(IV)}{dV} = I + V\frac{dI}{dV} \cong I + V\frac{\Delta I}{\Delta V} \tag{2.17}$$

Then

$$\frac{\Delta I}{\Delta V} = -\frac{I}{V} \qquad \text{at MPP} \tag{2.18}$$

$$\frac{\Delta I}{\Delta V} > -\frac{I}{V} \qquad \text{left to MPP} \tag{2.19}$$

$$\frac{\Delta I}{\Delta V} < -\frac{I}{V} \qquad \text{right to MPP} \tag{2.20}$$

The MPP can thus be tracked by comparing the instantaneous conductance (*I*/*V*) to the incremental conductance (Δ*I*/Δ*V*) and accordingly the voltage perturbation sign is determined until reaching the MPP. However, if the irradiance increases (decreases), that is, the PV current increases (decreases), the MPP moves to the right (left) with respect to PV voltage. To compensate for this movement, the MPPT must increase (decrease) the PV operating voltage. Hence, this algorithm can determine the direction to reach the MPP. The flowchart of the Inc.Cond. algorithm is shown in Figure 2.12.

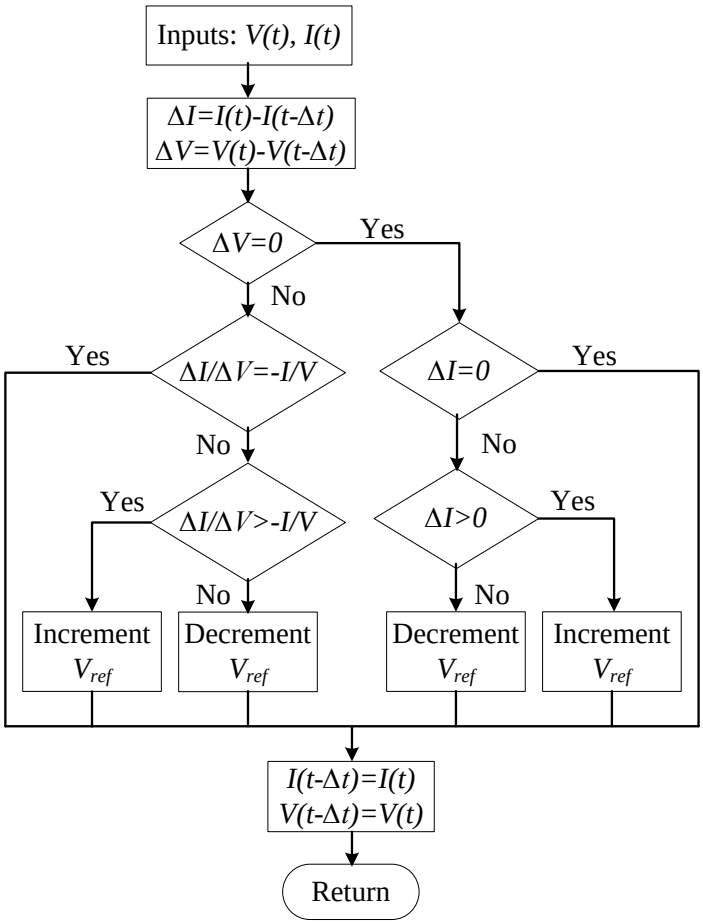

Figure 2.12. Flowchart of Inc.Cond. algorithm [2.21].

Advantages and Limitations

The main advantage of the Inc.Cond. technique, over the P&O algorithm, is that it can actually calculate the direction in which to perturb the array's operating point to reach the MPP [2.19]. Thus, it shows better accuracy, less oscillations and better performance especially under varying conditions. However, Inc.Cond. algorithm requires differentiation, division circuitry and a relatively complex decision making process. Therefore it requires a more complex microcontroller with higher cost, more memory and high sampling compliance [2.19, 2.23]. Moreover, there is still a tradeoff when considering the accuracy of this algorithm and tracking speed based on the associated step-size. Because of some factors such as measurement error and noise, the condition that ($\Delta I/\Delta V$) and ($-I/V$) exactly equal would never be satisfied and they will be within a small range of each other. However, at low irradiances, in the region near the MPP, this range will be approximately satisfied, and the algorithm gets 'stuck' at an operating voltage that is not exactly the V_{MPP} [2.19].

Modifications and advances

The Inc.Cond. technique applied variable step sizes, in [2.32-33], which are automatically tuned according to the inherent PV array characteristics. In [2.34], a MPPT technique is presented that functions either as a power increment algorithm or Inc.Cond. algorithm according to a threshold-tracking zone in order to improve the tracking behaviour. Two fixed step sizes are applied in [2.35]; the higher step size is used when the system operates far from the MPP, whereas the step size is decreased for the area around the MPP

iii. Fractional Open Circuit Voltage (FOCV) / Fractional Short Circuit Current (FSCC)

The open circuit voltage method is based on the fact that the ratio of the MPP PV voltage (V_{MPP}) to open circuit voltage (V_{OC}) is nearly constant independent of any external conditions (varying irradiance or temperature). Similarly, the near-linear relationship between the MPP array current (I_{MPP}) and the short circuit current (Isc), under varying irradiance and temperature levels, has given rise to the short circuit current method.

Control scheme

Under varying weather conditions;

$$V_{MPP} \approx k_1 V_{OC} \tag{2.21}$$

$$I_{MPP} \approx k_2 I_{SC} \tag{2.22}$$

Since k_1 is dependent on the characteristics of the PV array being used, it usually has to be computed beforehand by empirically determining V_{MPP} and V_{OC} for the specific PV array at different irradiance and temperature levels. Similarly, k_2 has to be determined according to the PV array in use. Usually k_1 ranges between 0.71 and 0.78 and k_2 ranges between 0.78 and 0. 92 [2.21]. Once V_{MPP} (I_{MPP}) has been approximated, closed-loop control on the array power converter can be used to reach this desired voltage (current).

Advantages and limitations

The linear current function used by the FSCC technique is a more accurate approximation than the linear voltage function of the FOCV technique. However, the latter is normally favoured as it shows better overall performance regarding cost, efficiency, and noise [2.36] and measuring I_{SC} during operation is problematic [2.19].

Generally FOCV method requires only one voltage sensor and can be readily implemented using analogue hardware or low-cost microcontrollers [2.24], thus it is

considered the lowest-cost MPPT technique. In low irradiance conditions, it is generally more effective than either the P&O or Inc. Cond. methods. Due to this characteristic, the FOCV method is often combined with other MPPT techniques [2.37]. But this method has some limitations. The MPPT tracking efficiency may decrease due to the temporary loss of power resulting from the momentarily isolation of the MPP converter from the PV array to measure V_{OC}. The latter is repeated periodically until the MPP is reached [2.21]. Also, this method may show low accuracy because V_{OC} is affected by PV cell temperature and the ratio k_1 varies by as much as 8% (absolute) over the entire range of atmospheric conditions [2.19]. Finally, k_1 is not valid in the presence of partial shading (which causes multiple local maxima) of the PV array [2.21].

Modifications and advances

In [2.38], a boost converter is used, where the switch in the converter is used to short the PV array for measuring I_{SC}. In [2.39], V_{oc} is determined using a diode mounted at the back of the array (such that it is at the same temperature as the array). A constant current is fed into the diode and the resulting voltage across the diode is used as the array's V_{oc} which is then utilized in tracking V_{MPP}. A hybrid method is applied in [2.40-42], where [2.40] applies FOCV in the starting process to reach a working point near the maximum power point in a short time and then the Inc.Cond. with variable step-size is used to track the maximum power point. A combination of FOCV and P&O algorithms is proposed in [2.41, 2.42] gaining the advantages of both methods.

iv. Artificial intelligence (AI) Based MPPT Algorithms

Recently fuzzy logic (FL) and artificial neural networks (ANN), known as artificial intelligence (AI) techniques, have been used widely in the MPPT process, particularly under non-uniform and partially shading conditions [2.25].

Control scheme

1. Fuzzy logic (FL)

Fuzzy logic control generally consists of three stages, as shown in Figure 2.13, which are; fuzzification, rule base table, and de-fuzzification.

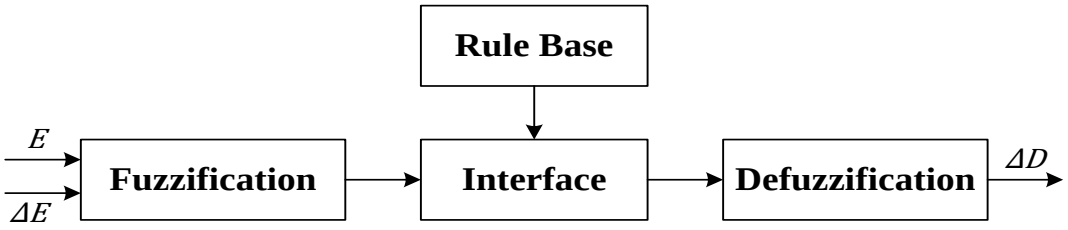

Figure 2.13. PV MPPT fuzzy logic controller [2.25].

During **fuzzification**, numerical input variables are converted into linguistic variables based on input membership functions. The inputs to a MPPT fuzzy logic controller are usually the error E and the change in error ΔE. Since $dP/dV=0$ at the MPP, E and ΔE can be approximated as [2.43, 2.44]:

$$E(k) = \frac{P(k) - P(k-1)}{V(k) - V(k-1)} \quad or \quad \frac{P(k) - P(k-1)}{I(k) - I(k-1)} \tag{2.23}$$

$$\Delta E(k) = E(k) - E(k-1) \tag{2.24}$$

After the fuzzification stage, the fuzzy logic controller output, which is typically a change in the power converter duty ratio (ΔD) can be looked up in a **rule base matrix** like that shown Table 2.2 [2.44] which is dedicated to the boost converter.

Finally, in the defuzzification stage, the fuzzy logic output is converted from a linguistic variable to a numerical variable using a membership function. The membership functions of the inputs and output are shown in Figure 2.14 [2.44]. In this case, five fuzzy levels are used: NB (negative big), N (negative), Z (zero), P (positive), and PB (positive big).

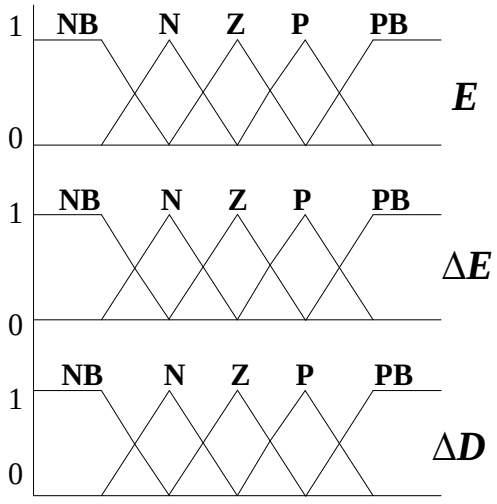

Figure 2.14: Membership function for FL inputs and outputs [2.44].

Table 2.2. Fuzzy-rule of the FL controller [2.44]

ΔE / E	**NB**	**N**	**Z**	**P**	**PB**
NB	Z	Z	NB	NB	NB
N	Z	Z	N	N	N
Z	N	Z	Z	Z	P
P	P	P	P	Z	Z
PB	PB	PB	PB	Z	Z

2. Artificial Neural network (ANN)

Neural networks commonly have three layers: input, hidden, and output layers as shown in Figure 2.15. The number of nodes in each layer varies and is user-dependent. The input variables can be PV array parameters like V_{OC} and I_{SC}, atmospheric data like irradiance and temperature, or any combination of these. The output is usually one or several reference signal(s) like a duty cycle used to drive the power converter to operate at the MPP [2.25]. How close the operating point gets to the MPP depends on the algorithms used by the hidden layer and how well the neural network has been trained. The links between the nodes are all weighted. To accurately identify the MPP, these weights have to be carefully determined through a training process, where the PV array is tested and the patterns between the input(s) and output(s) of the neural network are recorded [2.21].

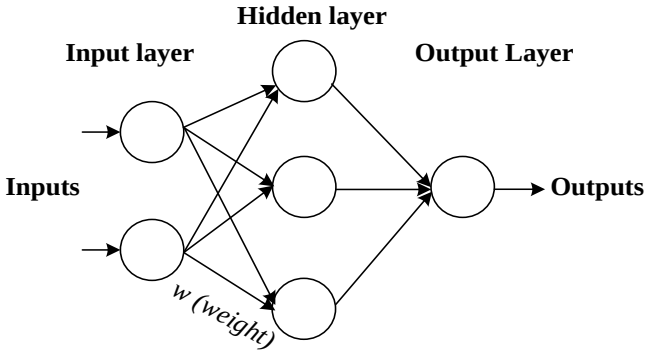

Figure 2.15. Example of a neural network [2.21].

Advantages and limitations

AI techniques show the fastest convergence speed to the MPP and highest accuracy under varying environmental conditions (especially instantaneous climate changes and partial shading) [2.21, 2.25]**.** However, they feature high algorithm complexity and require high-end performance, costly controllers. Their effectiveness and systems accuracy depend

on the knowledge of the user or control engineer in choosing the right algorithm parameters.

Modifications and advances

A sensorless FL-based MPPT control scheme is developed in [2.45] where only the load current is fed back and controlled for MPPT performance, resulting in simplification of control circuit and algorithm. In [2.46] an adaptive MPPT method is proposed based on FL control, featuring automatic parameter tuning to the employed step change. In [2.47], an ANN-based MPPT technique is proposed which utilizes two cascaded ANNs to minimize the number of training sets. Based on the slope of power versus voltage, a novel MPPT algorithm using a neural network compensator is proposed in [2.48] to avoid the power oscillation problem and effects of uncertain parameters in PV arrays. Some researches use an adaptive neuro-fuzzy inference system (ANFIS) which combines neural network and fuzzy logic to overcome drawbacks of each techniques [2.49, 2.50]. In [2.51], an intelligent approach to MPPT is applied using an ANN estimator and a FL controller. Finally, simple search algorithms, such as P&O and Inc.Cond. methods, are combined with AI to enhance their performance [2.52-55].

2.5.2 Comparison between the considered MPPT techniques

Various MPPT techniques differ in hardware complexity, tracking accuracy, convergence speed, dynamic response under sudden environmental changes, required sensors' number, and dependency on PV module parameters. Considering such factors, Table 2.3 compares the presented MPPT methods [2.15, 2.20, 2.21, and 2.23];

Regarding **implementation complexity,** P&O and fractional V_{OC} methods can be simply implemented using analogue circuits or with low cost microcontrollers. However, Inc.Cond. requires differentiation, division circuitry and a relatively complex decision making process, and therefore requires a more complex microcontroller with more memory. Also for fractional I_{SC}, measuring the short circuit current during operation is problematic. Artificial Intelligence algorithms are the most complex and require high performance controllers.

Considering **tracking speed**, P&O and Inc.Cond. methods with large step size are the slowest. This is why associated variable-steps are considered which get smaller towards the MPP, speeding up the tracking process. The fractional V_{OC} method is faster than the

latter. However, artificial intelligence methods are better as they employ larger correction steps to track the MPP.

The **tracking accuracy** is an important factor affecting the MPPT process. P&O and Inc.Cond. methods track the MPP accurately, though with large oscillation around the MPP, with a fixed step-size. Generally, the fractional V_{OC} method performs well at stable environmental conditions with reasonable accuracy. However, it shows inaccurate tracking under varying environmental conditions, increasing the power ripple around the MPP. Artificial intelligence techniques, when precisely settled, give accurate results with reduced oscillation around the MPP.

A merit of P&O and Inc.Cond. methods is not being **PV module dependent**. Hence, they can be applied to any PV array without knowledge of its configuration and parameter values. This is not the case with the other methods, which depend on PV array parameters.

The **number of sensors** required to implement a MPPT algorithm differs from one technique to another. Generally, it is easier and more reliable to measure voltage than current. Current sensors are usually expensive. Usually the P&O and Inc.Cond. methods require two sensors, for voltage and current measurement. Fractional V_{OC} method requires only one voltage sensor while for fractional $I_{SC,}$ only a current sensor is required. For artificial intelligence techniques, the number of required sensors depends on the algorithm input parameters.

The technique **response under varying conditions** significantly affects the decision process. Generally, Inc.Cond. method shows more accuracy and faster response than the P&O method, especially with environmental changes. Fractional V_{OC} may fail under partial shading. Artificial intelligence algorithms show fast response and accurate tracking under varying conditions.

Finally, regarding **MPPT technique cost**, this depends on the actual implementation details. Analogue implementation of the algorithm is generally cheaper than digital implementation. Eliminating current sensors considerably reduces costs.

However, the choice of a MPPT scheme is mainly application specific [2.21]. For example, space satellites and orbital stations involve a MPP tracker that does not require periodic tuning and is capable of continuously tracking the true MPP in minimum time. In this case, modified P&O, and modified Inc.Cond. are appropriate. PV systems for street lighting are used for charging batteries during the day. Thus, they do not need strict

constraints, but easy and cheap implementation is more important, making fractional V_{OC} or I_{SC} viable. Solar vehicles generally require fast convergence to the MPP, so fuzzy logic control and neural networks are good options in this case. Artificial intelligence algorithms are now attractive in very large, high-power PV applications, due to their high accuracy and efficiency.

Table 2.3. Comparison between commonly applied MPPT techniques [2.19-21]

MPPT Technique	**P&O**	**Inc.Cond.**	**Fractional V_{OC} (I_{SC})**	**Artificial Intelligence**
Implementation complexity	Low	Medium	Low (Medium)	High
Analogue or digital	Both	Digital	Both	Digital
Tracking speed	Varies	Varies	Medium	Fast
Accuracy (True MPPT)	Yes	Yes	No	Yes
Maximum power oscillations	Varies	Varies	Large	Small
PV array dependent	No	No	Yes	Yes
Periodic tuning	No	No	Yes	Yes
Sensed parameters	V, I	V, I	V (I)	Varies
Response to environmental changes	shows problems with varying conditions and low irradiance levels	More accurate and faster than P&O under varying conditions, but may show inaccuracy at low irradiance levels	May fail under partial shading conditions	Shows fast response and accurate tracking under varying environmental conditions.
Tracking efficiency over a period of time	97%	97%	93%	99%

2.6 Summary

In this chapter, PV cell construction and its photovoltaic effect were demonstrated along with cell combinations to form a PV module, array, and field. PV module non-linear electrical characteristics were described, followed by the main steps required to develop a PV single diode model. The PV MPPT issue was then illustrated together with its commonly applied algorithms. Control schemes, characteristics and modifications regarding each of these MPPT algorithms were compared.

References

[2.1] N. Femia, et al, Power Electronics and Control Techniques for Maximum Energy Harvesting in Photovoltaic Systems: Taylor & Francis Group, 2013.

[2.2] U.S. Department of Energy, "SunShot Vision Study- Photovoltaics: Technologies, Cost, and Performance ", 2012.

[2.3] SOLAR IN DEPTH [Online]. Available: http://solarcellcentral.com/solar_page.html

[2.4] P. Hersch, and K. Zweibel, Basic Photovoltaic Principles and Methods: Technical Information Office, Solar Energy Research Institute, U.S. Department of Energy, 1982.

[2.5] M. Hosenuzzaman, et al., "Global Prospects, Progress, Policies, and Environmental Impact of Solar Photovoltaic Power Generation", Renewable and Sustainable Energy Reviews, Vol. 41, 2015, pp. 284–297.

[2.6] Martin A. G., et al, "Solar Cell Efficiency Tables (version 45)", Progress in Photovoltaics: Research and Applications, Vol. 23, No.1, 2015, pp. 1–9.

[2.7] R. R. King et al, "Solar Cell Generations Over 40% Efficiency", Progress in Photovoltaics: Research and Applications, Vol. 20, No.6, 2012, pp. 801–815.

[2.8] International Energy Agency (IEA), "Technology Roadmap: Solar Photovoltaic Energy", 2014.

[2.9] C. Carrero, J. Amador, and S. Arnaltes, "A Single Procedure for Helping PV Designers to Select Silicon PV Module and Evaluate the Loss Resistances," Renewable Energy, Vol. 32, No. 15, 2007, pp. 2579–2589.

[2.10] D. Sera, R. Teodorescu, and P. Rodriguez, "PV Panel Model Based on Datasheet Values," in Proc. IEEE International Symposium Industrial Electronics (ISIE), 2007, pp. 2392–2396.

[2.11] M. Villalva, J. Gazoli, and E. Filho, "Comprehensive approach to modeling and Simulation of Photo-voltaic Arrays", IEEE Trans. Power Electronics, Vol. 24, no. 5, May 2009, pp.1198-1208.

[2.12] H. S. Rauschenbach, Solar Cell Array Design Handbook: Van Nostrand Reinhold, 1980.

[2.13] F. Lasnier and T. G. Ang, Photovoltaic Engineering Handbook. New York: Adam Hilger, 1990.

[2.14] P. Meshram, and U. B. Mujumdar, "Design and Development of MPPT based Converter for Efficient Solar Power Conversion," IJAIS Proceedings on 2nd National Conference on Innovative Paradigms in Engineering and Technology, pp. 35-39, 2013

[2.15] N. Onat, "Recent Developments in Maximum Power Point Tracking Technologies for Photovoltaic Systems", International Journal of Photo-energy, Vol. 2010, 2010, pp1-11.

[2.16] H. Patel and V. Agarwal," Maximum Power Point Tracking Scheme for PV Systems Operating Under Partially Shaded Conditions", IEEE Trans. Industrial Electronics, Vol. 55, NO. 4, 2008, pp.1689- 1698.

[2.17] E. Koutroulis, and F. Blaabjerg, "A New Technique for Tracking the Global Maximum Power Point of PV Arrays Operating Under Partial-Shading Conditions", IEEE Journal of Photovoltaics, Vol. 2, No. 2, 2012, pp.184-190.

[2.18] K. Chen, et al, "An Improved MPPT Controller for Photovoltaic System Under Partial Shading Condition", IEEE Trans. Sustainable Energy, Vol. 5, No. 3, July 2014, pp. 978-985.

[2.19] D.P. Hohm and M. E. Ropp, "Comparative Study of Maximum Power Point Tracking Algorithms", Progress in Photovoltaics: Research and Applications, Vol. 11, No. 1, 2003, pp. 47- 62.

[2.20] S. Jain, and V. Agarwal, "Comparison of the Performance of Maximum Power Point Tracking Schemes Applied to Single-stage Grid-connected Photovoltaic Systems," IET Electric Power Applications, Vol. 1, No. 5, 2007, pp. 753-762.

[2.21] T. Esram, P. L. Chapman, "Comparison of Photovoltaic Array Maximum Power Point Tracking Techniques," IEEE Trans. Energy Conversion, Vol. 22, No. 2, June 2007, pp. 439-449.

[2.22] A. N. A. Ali, et al, "A Survey of Maximum PPT Techniques of PV Systems", in Proc. IEEE Energy tech Conference, May 2012, pp. 1-17.

[2.23] B. Subudhi, and R. Pradhan, "A Comparative Study on Maximum Power Point Tracking Techniques for Photovoltaic Power Systems", IEEE Trans. Sustainable Energy, Vol. 4, No. 1, Jan. 2013, pp. 89-98.

[2.24] M. Gomes de Brito, et al, "Evaluation of the Main MPPT Techniques for Photovoltaic Applications", IEEE Trans. Industrial Electronics, Vol. 60, No. 3, March 2013, pp. 1156-1167.

[2.25] V. P, and M. A. Mathews, "Modelling and Analysis of Artificial Intelligence Based MPPT Techniques for PV Applications", in Proc. IEEE International Conference on Advances in Green Energy (ICAGE), December 2014, pp. 56-65.

[2.26] A. Pandey, N. Dasgupta, and A.K. Mukerjee, "High-Performance Algorithms for Drift Avoidance and Fast Tracking in Solar MPPT System", IEEE Trans. Energy Conversion, Vol. 23, No.2, June 2008, pp. 681-689.

[2.27] L. Piegari, and R. Rizzo, "Adaptive Perturb and Observe Algorithm for Photovoltaic Maximum Power Point Tracking", IET Renewable Power Generation, Vol. 4, No. 4, 2010, pp. 317–328.

[2.28] F. Aashoor, and F. Robinson, "A Variable Step Size Perturb and Observe Algorithm for Photovoltaic Maximum Power Point Tracking", in Proc. IEEE Universities Power Engineering Conference (UPEC), 2012.

[2.29] N. Kasa, T. Iida, and L. Chen, "Flyback Inverter Controlled by Sensor less Current MPPT for Photovoltaic Power System", IEEE Trans. Industrial Electronics, Vol. 52, No. 4, August 2005, pp. 1145–1152.

[2.30] A. Abdelsalam, et al, "High Performance Adaptive Perturb and Observe MPPT Technique for Photovoltaic-based Microgrids", IEEE Trans. Power Electronics, Vol. 26, No. 4, April 2011, pp. 1010 – 1021.

[2.31] F. Paz, and M. Ordonez, "Zero Oscillation and Irradiance Slope Tracking for Photovoltaic MPPT", IEEE Trans. Industrial Electronics, Vol. 61, No. 11, November 2014, pp. 6138- 6147.

[2.32] F. Liu, et al, "A Variable Step Size INC MPPT Method for PV Systems," IEEE Trans. Industrial Electronics, Vol. 55, No.7, July 2008, pp.2622-2628.

[2.33] Q. Mei, et al, "A Novel Improved Variable Step-Size Incremental-Resistance MPPT Method for PV Systems," IEEE Trans. on Industrial Electronics, Vol.58, No.6, June 2011, pp.2427-2434.

[2.34] [2.34] G. Hsieh, et al, "Photovoltaic Power-Increment-Aided Incremental-Conductance MPPT With Two-Phased Tracking", IEEE Trans. Power Electronics, Vol. 28, No. 6, June 2013, pp. 2895-2911.

[2.35] R. Faraji, et al, "FPGA-based Real Time Incremental Conductance Maximum Power Point Tracking Controller for Photovoltaic Systems", IET Power Electronics, 2014, Vol. 7, No. 5, pp. 1294–1304.

[2.36] M. A. S. Masoum, H. Dehbonei, and E. F. Fuchs, "Theoretical and Experimental Analyses of Photovoltaic Systems With Voltage- and Current-Based Maximum Power-Point Tracking", IEEE Trans. Energy Conversion, Vol. 17, No. 4, 2002, pp 514-522.

[2.37] G. J. Yu, et al, "A Novel Two-mode MPPT Control Algorithm Based on Comparative Study of Existing Algorithms," in Proc. IEEE Photovoltaic Specialists Conference, 2002, pp. 1531-1534.

[2.38] S. Yuvarajan and S. Xu, "Photo-voltaic Power Converter with a Simple Maximum-Power-Point-Tracker", in Proc. IEEE International Symposium on Circuits and Systems, 2003, pp. 399-402.

[2.39] K. Kobayashi, H. Matsuo, and Y. Sekine, "An Excellent Operating Point Tracker of the Solar-Cell Power Supply System", IEEE Trans. Industrial Electronics, Vol. 53, No. 2, 2006, pp. 495–499.

[2.40] Z. Yan, et al, "Study on Realizing MPPT by Improved Incremental Conductance Method with Variable Step-size," in Proc. IEEE Conference on Industrial Electronics and Applications (ICIEA), June 2008, pp.547-550.

[2.41] J. Baek, et al, "Development of Novel MPPT Algorithm of PV System Considering Radiation Variation", in Proc. International Conference on Control Automation and Systems (ICCAS), October 2010, pp.1235-1241.

[2.42] F. Zhang, et al, "Adaptive Hybrid Maximum Power Point Tracking Method for a Photovoltaic System", IEEE Trans. Energy Conversion, Vol. 28, No. 2, June 2013, pp. 353-360.

[2.43] N. Khaehintung, et al, "RISC Microcontroller Built-in Fuzzy Logic Controller of Maximum Power Point Tracking for Solar-Powered Light-Flasher Applications," in Proc. IEEE Conference on Industrial Electronics Society, 2004, pp. 2673–2678.

[2.44] C. Won, et al, "A New Maximum Power Point Tracker of Photovoltaic Arrays using Fuzzy Controller," in Proc. IEEE Power Electronics Specialists Conference (PESC), 1994, pp. 396–403.

[2.45] S. Kim, et al "An Effective POS MPPT Control Method for PV Power Generation System," in Proc. International Conference on Electrical Machines and Systems (ICEMS) 2009, pp.1-6.

[2.46] J. Qiufeng, L. Sujuan, and Y. Hai-zhu, "Maximum Power Point Tracking in Photovoltaic System by Using Fuzzy Algorithm", in Proc. IEEE International Conference on Intelligent Computing and Cognitive Informatics,2010, pp.267-270

[2.47] L. M. Elobaid, A. K. Abdelsalam, and E. E. Zakzouk, "Artificial Neural Network Based Maximum Power Point Tracking Technique for PV Systems", in Proc. IEEE Conference on Industrial Electronics Society (IECON), 2012, pp. 937-942.

[2.48] M. Tsai, et al, "A Novel MPPT Control Design for PV Modules Using Neural Network Compensator", in Proc. IEEE International Symposium on Industrial Electronics (ISIE), 2012, pp. 1742 – 1747.

[2.49] H. Afghoul, et al, "Tracking the Maximum Power from a PV Panels Using of Neuro-fuzzy Controller", in Proc. IEEE International Symposium on Industrial Electronics (ISIE), 2013, pp. 1-6.

[2.50] A. Chikh, and A. Chandra, "An Optimal Maximum Power Point Tracking Algorithm for PV Systems with Climatic Parameters Estimation", IEEE Trans. Sustainable Energy, Vol. 6, No. 2, April 2015, pp. 644-652.

[2.51] B. Bendib, et al, "An Intelligent MPPT Approach Based on Neural-network Voltage Estimator and Fuzzy Controller, Applied to a Stand-alone PV System", in Proc. IEEE International Symposium on Industrial Electronics (ISIE), 2014, pp. 404-409.

[2.52] M. C. Di Piazza, et al, "A Growing Neural Gas Network Based MPPT Technique for Multi-string PV Plants," in Proc. IEEE International Symposium on Industrial Electronics (ISIE), 2010, pp.544-549.

[2.53] A. Al Nabulsi and R. Dhaouadi, "Efficiency Optimization of a DSP-Based Standalone PV System Using Fuzzy Logic and Dual-MPPT Control", IEEE Trans. Industrial Informatics, Vol. 8, No. 3, August 2012, pp. 573-584.

[2.54] P. C. Sekhar, and S. Mishra, "Takagi–Sugeno Fuzzy-based Incremental Conductance Algorithm for Maximum Power Point tracking of a Photovoltaic Generating System", IET Renewable Power Generation, Vol. 8, No. 8, 2014, pp. 900–914.

[2.55] M. A. Zainuri, *et al*, "Development of Adaptive Perturb and Observe-fuzzy Control Maximum Power Point Tracking for Photovoltaic Boost dc–dc Converter", IET Renewable Power Generation, Vol. 8, No. 2, 2014, pp. 183–194.

Chapter Three

PV System Configurations

Photovoltaic systems are solar energy systems which can supply power starting from a micro scale to large PV plants of hundreds of MW. A PV system is made up of a PV device and the balance-of-system (BOS) equipment which comprise the remaining components and procedures for a complete PV system production. This includes combiner boxes (junction boxes), charge controllers and storage batteries for stand-alone PV systems, inverters for grid-connected systems or systems supplying AC loads, mounting structures, wiring, switchgear and fuses, surge arrestors, earth-fault protection devices and so forth. The BOS may account for up to half the capital cost of a PV system (for small systems) and most of the maintenance costs [3.1].

PV systems are used in a variety of applications which can be grouped into two categories: stand-alone (off-grid) systems and grid-tied (on-grid) PV systems [3.2, 3.3]. The former supplies power directly to electrical equipment while the latter feeds energy into the public electricity grid.

In this chapter, the main components and applications of stand-alone and grid-tied PV systems are discussed. This is followed by a review on different grid-tied PV inverters in terms of their configurations, power processing stages, and common types.

3.1 Stand-alone PV systems

In many remote locations, the cost of running a line extension, at $15,000 to $20,000, or more, per mile, is not economical. With conventional fossil fuel generators, the cost of fuel transport is often higher than the cost of the fuel itself. Conventional fuel generators also need significant maintenance, making stand-alone PV systems a cost effective solution in many instances, especially in locations far from the utility [3.2].

3.1.1 System components

As shown in Figure 3.1 (a), most off-grid PV systems consist of PV modules, a charge controller and storage batteries to supply power to DC loads. If the system has to supply power to AC loads, an inverter is needed to convert the DC power into AC power [3.1].

Storage batteries are essential for stand-alone PV systems as electricity generation is not constant and is not controllable (it depends on solar irradiance). With storage batteries,

electricity generated by PV panels can be stored and used to power the electrical loads when the sunshine is insufficient (at night or on cloudy days). Although convenient with high cycle efficiency (typically 90%), battery storage is possibly expensive (typically > $0.1/kWh) [3.4]. Hence, it has to be properly selected and managed to increase its life-time. There is different battery types used in PV systems. Lead-acid batteries, in particular the deep-cycle battery is the most popular type as it offers high rates of charge and discharge [3.1, 3.4]. However, the major problem of lead acid batteries is ageing that is, the increase in the battery internal resistance with age commonly shortens its service life. Another problem caused by the use of lead acid batteries is the potential environmental hazard caused by lead upon disposal [3.1]. The lead acid battery is most recycled item in the world. Recently, other types of batteries such as nickel carbide (Ni-Cd), nickel metal hydride (Ni-MH), Lithium ion (Li-O), and flow batteries (such as vanadium redox) are finding favour [3.4]. Nickel and Li-O batteries have the advantage that they cannot be over-charged or deep-discharged, however they are considerably more expensive. Flow batteries show fast response and can be more economical in large-scale storage [3.4]. Battery lifetime varies depending on the operating profile, but it is typically between 5 and 10 years. In PV systems, the storage capacities of battery systems are generally in the range of 0.1kWh to 100kWh [3.1].

A charge controller is a device used in standalone PV systems for regulating the current flowing from the PV array to the storage batteries. It maintains the battery at the highest possible state of charge (SOC) and provides the user with the required quantity of electricity while protecting the battery from deep discharge or overcharge [3.1]. A MPP charge controller incorporates a DC/DC converter such that the PV panel can operate at V_{MPP} in order to deliver maximum output power at the corresponding solar irradiance [3.1].

3.1.2 Off-grid applications

There are numerous applications for stand-alone PV systems, categorized as [3.2, 3.3]:

Pico PV systems utilize a small PV panel of only a few watts to provide a number of services such as phone charging, powering a radio or a small computer and lighting. In the latter, efficient lights (mostly LEDs) altogether with sophisticated charge controllers and efficient batteries are applied [3.5].

Off-grid domestic systems provide electricity to households and villages in remote areas that are not connected to the utility electricity network. They provide electricity for

lighting, refrigeration, radios, televisions, flashlights, outdoor lights, security systems and even small-scale air conditioners [3.6]. Generally, off-grid PV domestic systems offer an economic alternative to electricity distribution network extension at distances of more than 1 or 2 km from existing power lines [3.3].

Off-grid non-domestic installations provide power for a wide range of applications, such as telecommunication [3.7], mobile applications [3.8], water pumping [3.9], transportation [3.10], cathodic protection, vaccine refrigeration, navigational aids and satellite systems. These are applications where small amounts of electricity have a high value, thus making PV commercially cost competitive with other small generating sources.

Hybrid systems combine the advantages of PV and diesel generator in small distributed hybrid generation systems for rural electrification to address the needs of remote communities [3.11]. This, in turn, limits fuel price increases, reduces operating cost and offers higher service quality than traditional single-source generation systems.

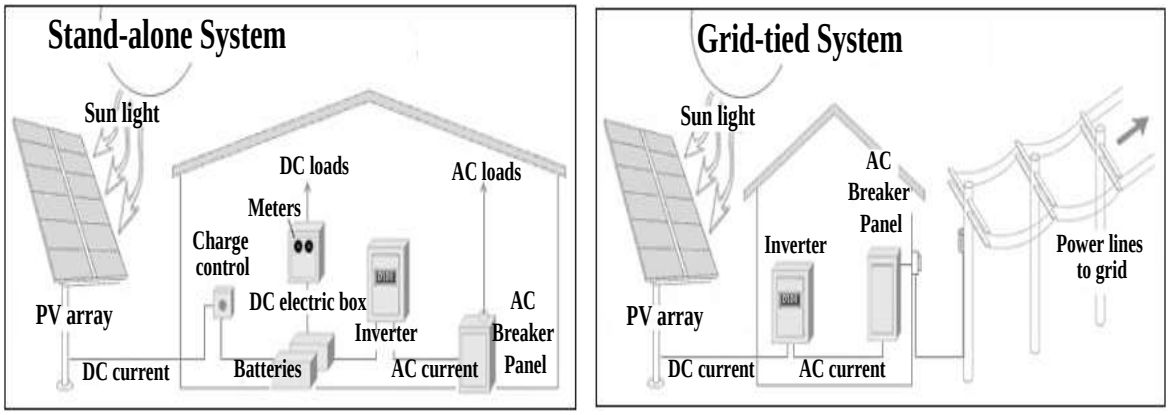

(a) (b)

Figure 3.1. PV applications: (a) stand-alone systems and (b) grid-tied systems.

3.2 Grid-connected PV systems

Common distributed energy resources (DERs), particularly PV sources, are increasingly being connected to utility grids for best utilization of their produced electric power. Grid-tied PV systems are becoming economically interesting as they supply the maximum extracted PV power into the grid without the need of battery back-up as well as their ability to be installed in the distribution level close to loads to decrease transmission costs [3.12].

As shown in Figure 3.1 (b), the main component of grid-connected PV systems is the DC/AC inverter required to convert electricity from direct current (DC) as produced by the PV panel to alternating current (AC) which is then supplied to the electricity network.

Grid-tied PV inverter configurations as well as PV-grid interfacing topologies are discussed in the third section of this chapter. Grid-connected PV applications mainly include [3.2, 3.3]:

Grid-connected centralized systems that perform the functions of centralized power stations that is, supplying bulk power rather than being associated with a particular electricity customer. These systems are typically ground-mounted and function independent of any nearby development [3.3].

Grid-connected decentralized (distributed) PV systems which are installed to provide power to a grid-connected customer or directly to a certain part of the electricity distribution network configured to power a number of customers. These systems are usually integrated into the customer's electricity meter and mounted on the roof-top of residential, commercial or industrial buildings or simply in the built environment on motorways [3.3]. They provide power to common loads or sell it back to the utility when more electricity is generated than is used by the PV system. However, when the electricity need is more than the PV system can generate, the necessary power is bought from the local power company**.** An attractive merit in such systems is their ability to supply power, instead of the utility, during peak demand hours, which usually coincide with peak sunlight hours [3.2].

This explains the concept of 'net metering tariffs' which enables customers to use the electricity they generate in excess of their consumption at certain times to offset their use of electricity from the grid at other times [3.13]. The latter reduces electrical bills as customers use electric power they generated and in addition they can export electricity into the grid [3.14]. Hence, these tariffs are designed to encourage distributed renewable generation, that is, the generation of small amounts of electricity at the point of ultimate use, rather than the generation of large amounts at a central location [3.13]. This in turn encourage consumers to generate their own power and make their homes and business environmentally friendly and fuel efficient.

3.3 Grid-tied PV inverters

For successful interfacing of a PV source to the grid, requirements of MPPT, DC/AC conversion, and PV voltage level transformation if required, are mandatory [3.15-17]. These tasks can be achieved using power electronic converters of varying configurations and interfacing topologies [3.15, 3.16].

3.3.1. Configurations of grid-tied PV inverters

Five PV inverter families arise to achieve PV-grid interface [3.15, 3.18-22]: 1) central inverters; 2) string inverters; 3) multi-string inverters; 4) ac-module inverters; and 5) cascaded inverters. Configurations of these inverter technologies are shown in Figure 3.2.

The central inverter, which is considered an old technology, interfaces a large number of PV modules to the grid as shown in Figure 3.2 (a). These modules are divided into series connections (called a string), each generating a sufficiently high voltage to avoid further amplification. These series connections are then connected in parallel, through string diodes, in order to reach high power levels. The resulting PV array is connected to the grid through a single DC/AC inverter. However, this inverter technology includes several limitations, such as high-voltage DC cables between the PV modules and the inverter, power losses due to the centralized MPPT, mismatch losses between the PV modules, losses in the string diodes, and a non-flexibility as mass production benefits can not be reached [3.18, 3.19].

Hence, new inverter topologies were introduced to minimize these drawbacks. The string inverter, shown in Figure 3.2 (b), is a reduced version of the centralized inverter. In this topology, a single string of PV modules is connected to the inverter and the PV system can be expanded by adding additional strings with their associated inverters, hence enhancing system flexibility [3.22]. Moreover, the MPP of each PV string is separately tracked, mitigating centralized MPPT losses and the extra losses associated with string diodes. This increases the overall efficiency compared to the centralized inverter, and reduces inverter cost, due to mass production [3.15, 3.19]. The input voltage may be high enough to avoid voltage amplification, however for using fewer PV modules in series, a DC/DC converter [3.20] or line-frequency transformer is used for voltage amplification which in turn increases system losses [3.19].

The multi-string inverter depicted in Figure 3.2 (c) is a further development of the string inverter, where several strings are interfaced with their own DC/DC converter to a common DC/AC inverter. Hence, it still has the advantage of individually controlling every string,while utilizing a single DC/AC inverter which decreases system size, cost and losses [3.15, 3.19]. Further enlargements are achieved by plugging a new string with a DC/DC converter into the existing platform, enhancing system flexibility and efficiency.

Although the string and multi-string topologies have their merits, limited modularity exists as the whole string is operated at a single maximum power point (MPP). The latter may cause PV module mismatch due to manufacturing tolerances or non optimal conditions such as partial shading, or alignment at different angles. Hence, the module integrated converter (MIC) topology, shown in Figure 3.2 (d), developed where a single PV module is integrated with an inverter into one unit regarded as a PV AC module connected in parallel to the grid [3.18]. This eliminates mismatch losses between PV modules and supports optimal adjustment between the PV module and the inverter. Due to its modular structure, the AC module is considered a 'plug and play' user-friendly device that allows the PV system to be easily expanded. Its mass production results in low manufacturing cost and low retail price. However, the necessary voltage amplification may reduce the overall efficiency and increases the price per watt, because of more complex circuit topologies [3.19].

Finally, the fifth category is the cascaded inverters which consist of several PV converters connected in series [3.20, 3.21]. Thus, the high power and/or high voltage from the combination of the multiple modules favour this topology in medium and large grid-connected PV systems. There are two types of cascaded converters [3.21]. Figure 3.2 (e) shows a cascaded DC/DC converter connection of PV modules where each module has its own DC/DC converter, and the modules with their associated converters are connected in series to create a high dc voltage, which is then provided to a simple DC/AC inverter. This approach offers the advantages of individual module MPPT, yet at less cost and more efficiency than AC module inverters. However, there are two power conversion stages in this configuration. The other cascaded inverter type is shown in Figure 3.2 (f), where each PV module is connected to its own DC/AC inverter, and those inverters are then placed in series to reach a high-voltage level. This cascaded inverter maintains the benefits of separate MPPT per PV module and removes the need for two power conversion stages featured in the other cascaded DC/DC converter configuration, which further improves the overall efficiency [3.21].

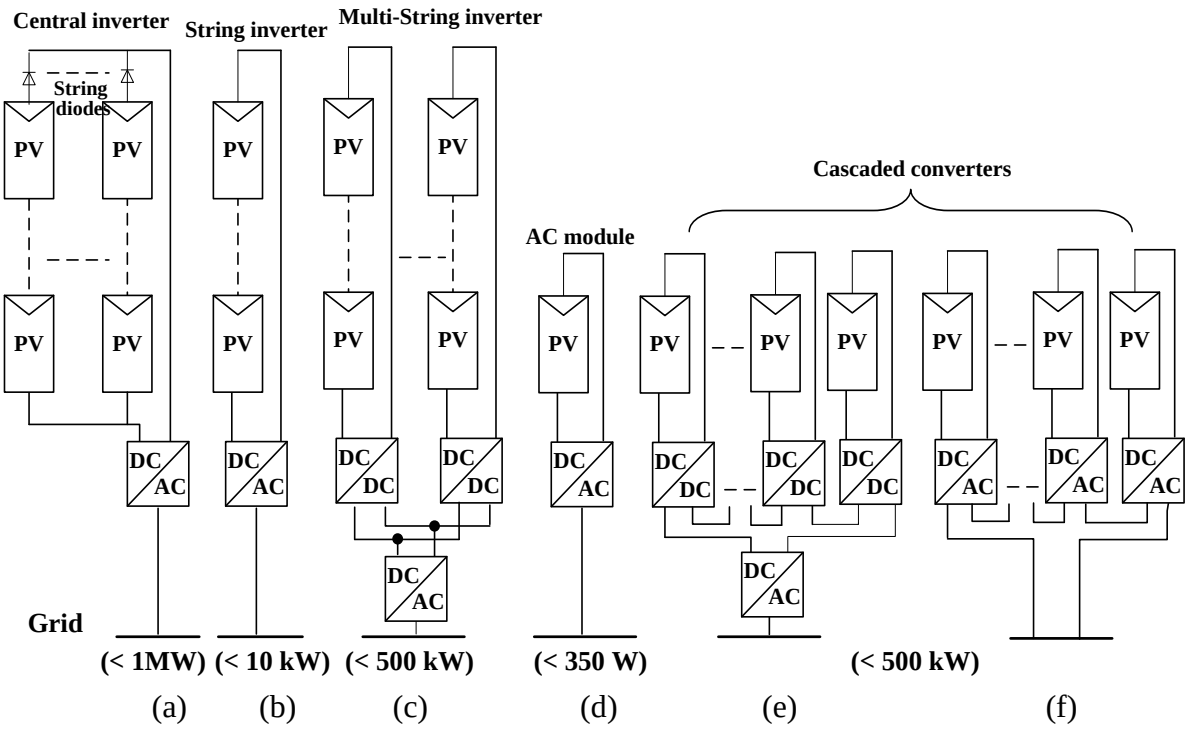

Figure 3.2. Different grid-tied PV configurations: (a) central inverter, (b) string inverter, (c) multi-string inverter, (d) AC module, (e) and (f) cascaded inverters [3.19, 3.21].

3.3.2. Power processing stages

For successful interfacing between a PV source and the grid, a number of requirements arise [3.23, 3.24]. First, PV MPPT is mandatory to maximize PV system efficiency. Inverter DC-link regulation and grid current control are essential to transfer the maximum PV power to the grid and achieve the required interface. Voltage level transformation, depending on the available PV voltage, may also be a requirement. In order to achieve the previous tasks, two types of power processing stages exist which are single-stage and two-stage topologies [3.19, 3.25] as shown in Figure 3.3.

In the **two-stage topology** [3.26, 3.27] shown in Figure 3.3 (a), two conversion stages are used. The first is a DC-DC converter to change the voltage level and in some cases provide galvanic isolation [3.19]. Also this converter decouples the energy change between the PV array and the DC link capacitor and performs the MPPT function. The second stage employs a DC/AC inverter to transfer PV power to the electric grid. In the **single-stage topology** [3.28, 3.29] shown in Figure 3.3 (b), a single DC/AC inverter stage is used between the PV and the grid, thus reducing system footprint and increasing its efficiency.

However, this inverter is responsible for performing all the functions of MPPT, grid current control and voltage amplification (if necessary).

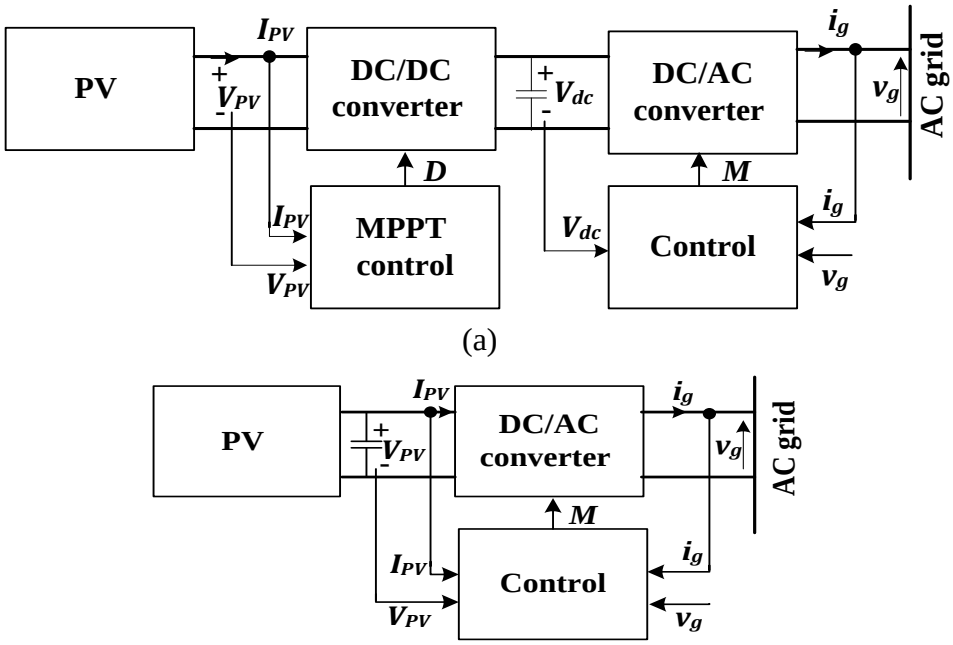

Figure 3.3. Types of power conversion stages for grid-connected PV systems: (a) two-stage and (b) single-stage.

For low-power (<10 kW) applications, DERs are usually connected to the AC grid through a single-phase inverter at a voltage level of 110/220V [3.30]. However, for single-phase systems, a main factor affecting the previous topologies design is the effect of AC grid power oscillation on the PV source.

For active power generated to a single-phase grid, the instantaneous grid power pulsates at a frequency twice that of the grid frequency. Processing of such power by DC/AC converters, such as voltage source inverters (VSIs) or current source inverters (CSIs), results in low frequency ripple of voltage (current) at the VSI (CSI) DC-link [3.31, 3.32].

This is demonstrated by following the equations and Figure 3.4.

For grid current i_g, which is in phase with the grid voltage v_g, the instantaneous value of power injected into the grid p_g is obtained mathematically as follows;

$$v_g = \hat{V}_g \sin \omega t \tag{3.1}$$

$$i_g = \hat{I}_g \sin \omega t \tag{3.2}$$

$$p_g = v_g i_g = \hat{V}_g \hat{I}_g \sin^2 \omega t = ½ \hat{V}_g \hat{I}_g (1 - \cos(2\omega t)) = P_g (1 - \cos(2\omega t)) \tag{3.3}$$

where $\hat{V}_g$ is the grid voltage amplitude, $\hat{I}_g$ is the injected grid current amplitude, P_g is the average value of the active power injected into the grid, and ω is the AC line angular frequency in rad/s.

Power from the PV array (P_{PV}) is constant under a constant irradiance. By neglecting system losses, the PV output power is equal to the average part of the grid power as shown in (3.4)

$$P_{PV} = \frac{1}{2\pi}\int_0^{2\pi} p_g d\omega t = P_g \tag{3.4}$$

The resulting grid power pulsations at double the line frequency ($P_g \cos 2\omega t$) goes back to the inverter DC-link resulting in second order harmonic components in the current and voltage waveforms at the inverter DC-link as shown in Figure 3.4 [3.32]. Energy storage devices at the inverter DC-link (DC-link capacitor for a VSI and DC-link inductor in case of a CSI) act as a buffer these pulsations. However, for low capacitor or inductor values, the ripples reach the PV source resulting in large PV voltage and current ripple. This in turn enlarges the PV power oscillation around the MPP as shown in Figure 3.5, decreasing the extracted PV power and degrading the tracking efficiency in addition to introducing low order harmonics in grid current [3.33, 3.34].

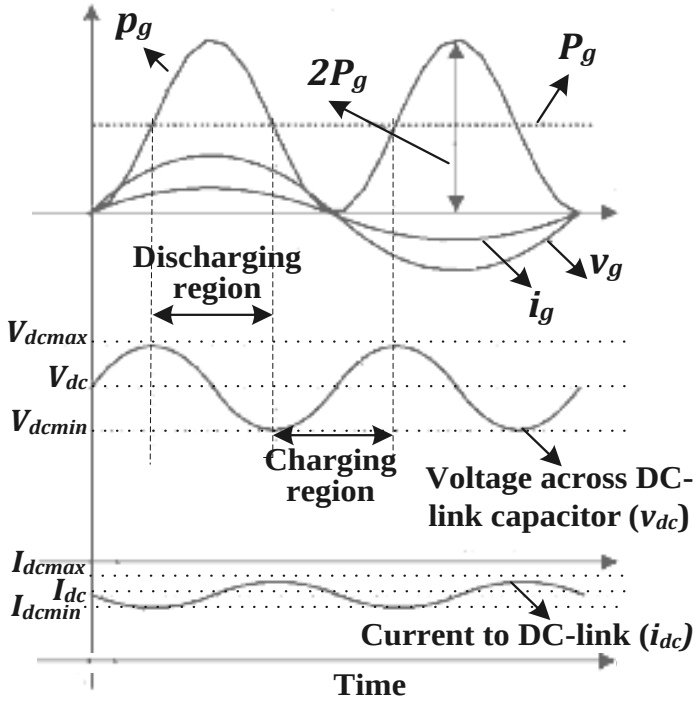

Figure 3.4. Effect of single-phase grid power oscillation on inverter DC-link voltage and current waveforms in case of VSI [3.32].

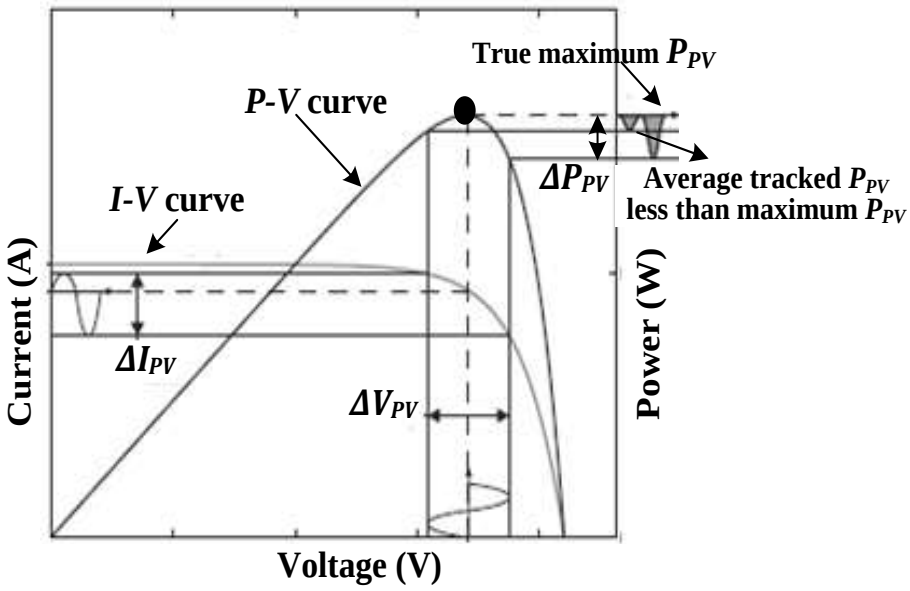

Figure 3.5. Effect of the inverter DC-link ripples on PV voltage, current and power [3.34].

Hence, the interference of such oscillation with the PV source should be avoided. In the two stage- topology, the power decoupling DC/DC stage added between the PV source and the DC/AC inverter stage has the merit of decoupling the PV module from the output inverter. This allows the use of small size energy storage device at inverter DC-link [3.35, 3.36]. Consequently, the inverter DC-bus ripple, resulting from the double line-frequency, has limited impact on the PV source. Moreover, it boosts the PV voltage level thus expanding its operating range and increasing flexibility for the number of PV modules used in each string [3.19]. However, this topology suffers from higher part count, reduced efficiency, lower reliability, higher cost, and larger size when compared to its alternative; the single-stage topology [3.37].

The latter, involving a single conversion stage, encounters minimum system component count thus increasing conversion efficiency, system reliability and reduce size and cost. However, in such a topology, since a single inverter achieves both the MPPT and interface functions, it must be properly designed and controlled. This in turn adds to system control complexity and limits the system degree-of-freedom. Moreover, in order to limit DC-link ripple propagation to the PV output power, a large capacitor (inductor) at the VSI (CSI) DC-link must be used for decoupling and buffering purposes [3.34, 3.36]. Large DC-link electrolytic capacitors increase inverter size and cost and are the limiting factor of the

inverter lifetime and system reliability [3.38] while large DC-link inductors are bulky, lossy and add to system cost and size.

3.3.3 Interfacing DC/AC inverter types

In grid-connected PV systems, various DC/AC inverter types can be used, in either the single-stage or two-stage topologies, in order to transfer the DC PV power to the AC grid. Power loss occurs during the DC to AC conversion process. The conversion efficiencies of inverters of different designs are generally in the range of 85% to 95% [3.1]. An inverter of good conversion efficiency should be used to reduce energy loss. Also, AC generation quality (such as the harmonic contents, voltage and frequency stability) and protection features (such as short-circuit/ open-circuit protection, and overload protection) should also be considered when choosing an inverter [3.15]. In this section, the commonly employed DC/AC inverters in PV applications are presented.

i. Voltage source inverter (VSI)

The conventional VSI is widely used in two-stage [3.39, 3.40] and single-stage [3.41, 3.42] grid-connected PV applications because of its simplicity and availability. However, in the single-stage topology, a PV array with a high DC voltage output is required; otherwise a step-up transformer is needed. A line-frequency transformer is regarded as a poor component due to increased losses, size, weight, and price. Moreover, as explained in the previous section, for such a topology a large electrolytic capacitor should be placed on the inverter DC-link to buffer low-frequency DC-link voltage ripple. Since large electrolytic capacitors degrade inverter lifetime, they should be replaced with film or ceramic capacitors to increase system reliability, but at the cost of higher price [3.19]

ii. Current source inverter

Although the current source inverter (CSI) has not been extensively applied for grid-connected renewable energy systems, it is considered a viable alternative in grid-interfaced PV systems with two-stage [3.43] and single-stage [3.44] topologies. However, for single-stage topologies, CSIs are highly competitive to VSIs for the following reasons [3.44];

- The DC input current is continuous which is important for PV application.
- They have inherent voltage boosting capability which allows a low-voltage PV source to be grid interfaced without the need of a step up transformer or an additional voltage boosting stage.

- System lifetime and reliability are increased by replacing the shunt large input electrolytic capacitor with a series input inductor.
- They have the ability of near sinusoidal, high quality voltage generation as well as an inherent short-circuit protection capability provided by the DC inductor.

However, for single-phase single-stage applications, grid power fluctuations cause second-order even harmonics at the CSI DC-side as explained. Thus, MPPT performance is degraded and PV lifetime is reduced. Also, odd order harmonics are generated on the grid side [3.45]. Therefore, eliminating DC-side even harmonics is essential in PV applications, when utilizing this inverter.

Moreover, the CSI has some limitations, compared to the VSI. It has a lower power density due to the bulky inductor at its DC side encountring higher losses in its internal resistance (2-4%) while internal resistance losses of the VSI DC-link capacitor is about (0.5%) [3.46]. Furthermore, the CSI may show more conduction losses due to its high input DC current and pulsed output AC current.

iii. Cascaded multilevel inverters

Cascaded multilevel inverters are considered a good option for PV-grid interface applications since separate DC voltage sources are available [3.20, 3.21, and 3.47]. The separate DC links in the multilevel inverter make independent voltage control possible. As a result, individual MPPT control in each PV module can be achieved, hence the energy harvested from PV panels can be maximized. The modularity and low cost of multilevel converters make them a prime candidate for the next generation of efficient, robust, and reliable grid connected solar power electronics [3.21].

3.4 Summary

In this chapter, different stand-alone and grid-tied PV applications have been discussed. A review of different grid-tied PV inverter configurations was presented. The centralized inverter technology included many shortcomings for which the string topology arose. A natural development was to add more strings, thus the multi-string inverters can to light. Another trend seen in this field is the development of the AC module and then cascaded inverters. This review was followed by the power processing stages and common types of DC/AC inverters required to achieve the PV-grid interface.

References

[3.1] EMSD HK RE NET-Solar Solar Photovoltaic Technology Outline. Available: http://re.emsd.gov.hk/english/solar/solar_ph/solar_ph_to.html

[3.2] North Carolina Solar Center, "Photovoltaic Applications", 2002. Available: http://infohouse.p2ric.org/ref/49/48007.pdf

[3.3] International Energy Agency (IEA), "TRENDS 2014 IN PHOTOVOLTAIC APPLICATIONS: Survey Report of Selected IEA Countries between 1992 and 2013", 2014.

[3.4] B. K. Bose, "Global Energy Scenario and Impact of Power Electronics in 21st Century", IEEE Trans. Industrial Electronics, Vol. 60, No. 7, July 2013. pp. 2638-2651.

[3.5] Y. Ai, T. Liu, and S. Wang, "Design and Implementation of a Novel High-Performance Stand-alone Photovoltaic LED Lighting System," in Proc. IEEE Asia-Pacific Power and Energy Engineering Conference (APPEEC), 2010, pp.1-4.

[3.6] K. Chao, and C. Huang, "Bidirectional DC–DC Soft-switching Converter for Stand-alone Photovoltaic Power Generation Systems", IET Power Electronics, Vol. 7, No. 6, 2014, pp. 1557–1565.

[3.7] E. Kaplani, "Design and Performance Considerations in Standalone PV Powered Telecommunication Systems", IEEE Latin America Trans., Vol. 10, No. 3, April 2012, pp.1723-1729.

[3.8] A. Ridge, G. Amaratunga, "Photovoltaic Maximum Power Point Tracking for Mobile Applications," Electronics Letters, Vol. 46, No. 22, 2010, pp.1520-1521.

[3.9] J. Caracas, et al, "Implementation of a High-Efficiency, High-Lifetime, and Low-Cost Converter for an Autonomous Photovoltaic Water Pumping System", IEEE Trans. Industry Applications, Vol. 50, No. 1, 2014, pp. 631-641.

[3.10] P. Wolfs, and Q. Li, "A Current-Sensor-Free Incremental Conductance Single Cell MPPT for High Performance Vehicle Solar Arrays", in Proc. IEEE Power Electronics Specialists Conference (PESC), 2006, pp.1-7.

[3.11] M. Datta, et al, "A Frequency-Control Approach by Photovoltaic Generator in a PV–Diesel Hybrid Power System," IEEE Trans. Energy Conversion, Vol.26, No.2, June 2011, pp.559-571.

[3.12] National Renewable Energy Laboratory (NREL), "Energy Analysis: Solar Power and the Electric Grid", 2010

[3.13] U.S. Energy Information Administration, "Today in Energy", [Online]. Available: http://www.eia.gov/todayinenergy/detail.cfm?id=6190

[3.14] "Feed-in Tarrifs", [Online]. Available: http://www.fitariffs.co.uk/FITs/

[3.15] E. Cadaval, et al, " Grid-connected Photovoltaic Generation Plants: Components and Operation," IEEE Industrial Electronics Magazine, Vol.7, No.3,2013, pp.6-20.

[3.16] S. Kouro et al, "Grid-Connected Photovoltaic Systems: An Overview of Recent Research and Emerging PV Converter Technology", IEEE Industrial Electronics Magazine, Vol. 9, No. 1, March 2015, pp. 47–61.

[3.17] E. Romero-Ca Daval, et al, "Grid-Connected Photovoltaic Plants: An Alternative Energy Source, Replacing Conventional Sources", IEEE Industrial Electronics Magazine, Vol. 9, No. 1, March 2015, pp. 18-32.

[3.18] M. Calais, et al, "Inverters for Single-phase Grid Connected Photovoltaic Systems-An overview," in Proc. IEEE Power Electronics Specialists Conference (PESC), 2002, pp. 1995–2000.

[3.19] S. Kjaer, J. Pedersen, and F. Blaabjerg, "A Review of Single-Phase Grid-Connected Inverters for Photovoltaic Modules", IEEE Trans. Industry Applications, Vol. 41, No. 5, 2005, pp. 1292-1306.

[3.20] C. Meza, et al, "Inverter Configurations Comparative for Residential PV-Grid Connected Systems", in Proc. IEEE Industrial Electronics Conference (IECON), 2006, pp. 4361-4366.

[3.21] B. Xiao, "Modular Cascaded H-Bridge Multilevel PV Inverter With Distributed MPPT for Grid-Connected Applications", IEEE Trans. Industry Applications, Vol. 51, No. 2, 2015, pp. 1722-1731.

[3.22] J. Myrzik and M. Calais, “String and Module Integrated Inverters for Single-phase Grid-connected Photovoltaic Systems - A Review”, in Proc. IEEE Bologna PowerTech Conf. Vol. 2, June 2003.

[3.23] F. Blaabjerg, et al, " Overview of Control and Grid Synchronization for Distributed Power Generation Systems", IEEE Trans. Industrial Electronics, Vol. 53, No. 5, October 2006, pp. 1398-1409.

[3.24] M. Eltawil, and Z. Zhao, " Grid-connected Photovoltaic Power Systems: Technical and Potential Problems—A Review", Renewable and Sustainable Energy Reviews, Vol. 14, No. 1, January 2010, pp. 112–129.

[3.25] F. Blaabjerg, Z. Chen, and S. Kjaer, "Power Electronics as Efficient Interface in Dispersed Power Generation Systems", IEEE Trans. on Power Electronics, Vol. 19, No. 5, Sept. 2004, pp. 1184-1194.

[3.26] M. Ahmed, M. Orabi, and O. AbdelRahim, "Two-stage Micro-grid Inverter with High-voltage Gain for Photovoltaic Applications", IET Power Electronics, Vol. 6, No. 9, 2013, pp. 1812–1821.

[3.27] Y. Du, et al, "Closed-Form Solution of Time-Varying Model and Its Applications for Output Current Harmonics in Two-Stage PV Inverter", IEEE Trans. Sustainable Energy, Vol. 6, No. 1, January 2015, pp. 142-150.

[3.28] S. Jain, and V. Agarwal, "A Single-Stage Grid Connected Inverter Topology for Solar PV Systems with Maximum Power Point Tracking", IEEE Trans. Power Electronics, Vol. 22, No. 5, September 2007, pp. 1928-1940.

[3.29] R. Mastromauro, M. Liserre, and A. Dell'Aquila, "Control Issues in Single-Stage Photovoltaic Systems: MPPT, Current and Voltage Control", IEEE Trans. Industrial Informatics, Vol. 8, no. 2, May 2012, pp. 241-254.

[3.30] S. Chowdhury, S. Chowdhury and P. Crossley, Microgrids and Active Distribution Networks, IET Renewable Energy Series 6, Institution of Engineering and Technology, 2009.

[3.31] B. Ho, and H. Chung, "An Integrated Inverter with Maximum Power Tracking for Grid-Connected PV Systems", IEEE Trans. Power Electronics, Vol. 20, No. 4, 2005, pp. 953 – 962.

[3.32] S. Jain and V. Agarwal, "Comparison of the Performance of Maximum Power Point Tracking Schemes Applied to Single-stage Grid-connected Photovoltaic Systems", IET Electric Power Applications, Vol. 1, No. 5, 2007, pp. 753–762.

[3.33] C. Bush, B. Wang, "A Single-Phase Current Source Solar Inverter with Reduced-Size DC Link", in Proc. IEEE Energy Conversion Congress and Exposition, (ECCE) 2009, pp. 54-59.

[3.34] M. Vitorino, "Compensation of DC Link Oscillation in Single-Phase VSI and CSI Converters for Photovoltaic Grid Connection", in Proc. IEEE Energy Conversion Congress and Exposition (ECCE), 2011, September 2011, pp. 2007-2014.

[3.35] T. Shimizu, K. Wada, and N. Nakamura, "Flyback-type Single-phase Utility Interactive Inverter with Power Pulsation Decoupling on the DC Input for an AC Photovoltaic Module System", IEEE Trans. Power Electronics, Vol. 21, No. 5, Sept 2006, pp. 1264–1272.

[3.36] H. Hu, et al, "A Review of Power Decoupling Techniques for Micro Inverters with Three Different Decoupling Capacitor Locations in PV Systems," IEEE Trans. on Power Electronics, Vol. 28, No. 6, June 2013, pp. 2711-2726.

[3.37] T. Wu, et al, "Power Loss Comparison of Single- and Two-stage Grid-connected Photovoltaic Systems", IEEE Trans. on Energy Conversion, Vol. 26, No. 2, June 2011, pp. 707-715.

[3.38] Y. Chen, C. Chang, and H. Wu, "DC-Link Capacitor Selections for the Single-phase Grid-connected PV System", in Proc. IEEE International Power Electronics and Drive Systems Conf. (PEDS), 2009, pp. 72 – 77.

[3.39] B. Yang, et al, "Design and Analysis of a Grid-Connected Photovoltaic Power System", IEEE Trans. Power Electronics, Vol. 25, No. 4, April 2010, pp. 992-1000.

[3.40] S. Samerchur, et al, "Power Control of Single-Phase Voltage Source Inverter for Grid-Connected Photovoltaic Systems", in Proc. IEEE Power Systems Conference and Exposition (PSCE), March 2011, pp. 1-6.

[3.41] M. Ropp, and S. Gonzalez, "Development of a MATLAB/Simulink Model of a Single-Phase Grid-Connected Photovoltaic System", IEEE Trans. Energy Conversion, Vol. 24, No. 1, 2009, pp. 195-202.

[3.42] R. Gonzalez, et al, "Transformerless Inverter for Single-Phase Photovoltaic Systems", IEEE Trans. Power Electronics, Vol. 22, No. 2, 2007, pp. 693-697.

[3.43] F. Tofoli, et al, "A Low Cost Single-phase Grid-connected Photovoltaic System with Reduced Complexity", in Proc. IEEE Power Electronics Conference (COBEP), 2009, pp. 1033-1038.

[3.44] B. N. Alajmi, et al, "Single-Phase Single-Stage Transformer less Grid-Connected PV System", IEEE Trans. Power Electronics, Vol. 28, No. 6, 2013, pp. 2664-2676.

[3.45] R. Li, H. Chung, and T. Chan, "An Active Modulation Technique for Single-Phase Grid-Connected CSI", IEEE Trans. Power Electronics, Vol. 22, No. 4, July 2007, pp. 1373-1382.

[3.46] E. Wiechmann, et al, "On the Efficiency of Voltage Source and Current Source Inverters for High-power Drives," IEEE Trans. Industrial Electronics, Vol. 55, No. 4, April 2008, pp. 1771-1782.

[3.47] E. Villanueva, *et al*, "Control of a Single-Phase Cascaded H-Bridge Multilevel Inverter for Grid-Connected Photovoltaic Systems", IEEE Trans. Industrial Electronics, Vol. 56, No. 11, November 2009, pp. 4399-4406.

Chapter Four

A Modified Incremental Conductance Technique for Photovoltaic Maximum Power Point Tracking

Owing to the non-linear behaviour and dependency of PV characteristics on the atmospheric temperature and irradiance levels, PV MPPT is mandatory to maximize PV system efficiency [4.1]. The performance of any PV MPPT technique and its implementation complexity depend mainly on the applied converter control scheme, MPPT algorithm structure, and the nature of the adopted step-size.

In this chapter, three converter control schemes are presented which are: direct generation of the appropriate duty-ratio to the MPPT converter, closed loop converter control scheme using conventional proportional-integral (PI) control, and then using adaptive fuzzy–tuned PI control. Among the latter, the direct-control scheme is the simplest however at the cost of high power oscillation around the MPP.

Considering MPPT techniques, the variable-step incremental conductance (Inc.Cond.) method has merits of good tracking accuracy and fast convergence speed. But it lacks implementation simplicity due to the mathematical division computations involved in its algorithm structure. Also, the conventional variable step-size, based on the division of PV power change by PV voltage change, encounters steady-state power oscillation and dynamic problems, especially under sudden irradiance changes.

This chapter presents a stand-alone PV system employing a boost DC/DC converter for tracking PV module maximum power. A modification is proposed to the conventional MPPT Inc.Cond. algorithm to eliminate the division computations involved in its structure. This results in technique simplification enabling its implementation in low-cost microcontrollers, to cut down system cost. Additionally, a modified variable step method is proposed which depends solely on PV power change. This improves system transient performance and yields minimal power oscillation. In turn, a direct converter control scheme becomes convenient since adopting the proposed variable step limits the sustained power oscillation encountered by this scheme. Hence, control complexity is minimized, with enhanced system performance.

Simulation results validate the superior performance of the proposed technique. Then, a system employing a TI 32-bit DSP TMS320F28335, is implemented to experimentally

validate the proposed technique during stable and changing environmental conditions. Finally, the algorithm is implemented in a low-cost 8-bit Atmega328 microcontroller on ARDUINO Uno board, to substantiate the proposed technique's cost-effectiveness.

4.1 System under investigation

The considered stand-alone PV system consists of a KD135SX_UPU PV module, a DC/DC boost converter, and a 3×12 V battery load as shown in Figure 4.1.

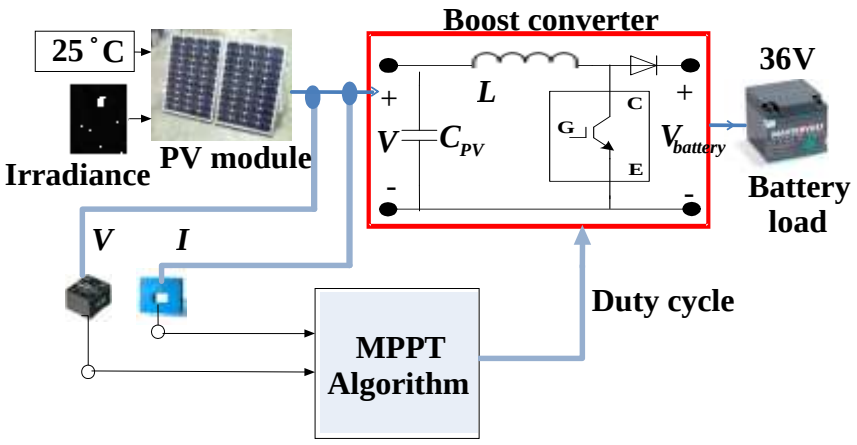

Figure 4.1. Stand-alone PV system under consideration.

4.1.1 DC/DC boost converter

The design of the boost converter, shown in Figure 4.1, in the continuous conduction mode can be summarized as follows [4.2]:

$$V = V_{battery}(1 - D) \tag{4.1}$$

$$\Delta i_L = \frac{VD}{Lf_{sw}} \tag{4.2}$$

$$\Delta V = \frac{VD}{8LC_{PV}{f_{sw}}^2} \tag{4.3}$$

where V and ΔV are the PV output voltage and its ripples respectively, $V_{battery}$ is the battery load voltage and D is the duty ratio determined by the applied MPPT algorithm to control the boost chopper switching. Δi_L is the change in inductor current, L is the chopper inductance, C_{PV} is the PV capacitor and f_{sw} is the chopper switching frequency. The DC/DC boost converter parameters are:

- Chopper inductance (L): 2.3 mH, for Δi_L = 3.5%.
- PV capacitor (C_{PV}): 100µF, for ΔV = 0.12%.
- Switching frequency (f_{sw}): 15 kHz.

4.1.2 MPPT algorithm

The non-linear *P-V* characteristics and their variation with changing irradiance levels, as shown in Figure 4.2, make PV MPPT a necessity. This is achieved using a MPPT algorithm which controls the switching of the converter between the PV module and the load to ensure that the PV panel maximum power is extracted. The performance of any MPPT technique and its implementation complexity depend mainly on the applied MPPT algorithm structure with its associated step-size [4.3-6], in addition to the nature of the employed control scheme generating the converter duty-ratio.

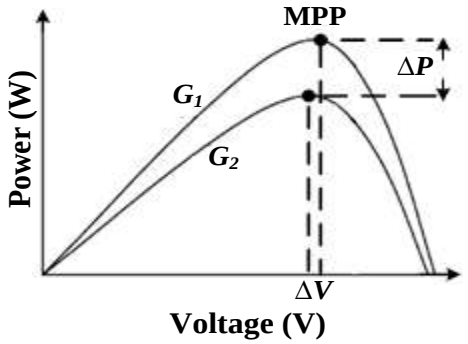

Figure 4.2. *P-V* characteristics of PV module under two irradiance levels (G_1 and G_2).

4.2 Converter control schemes

Three different schemes are investigated in this section to control the switching of the DC/DC boost converter.

4.2.1 Direct duty ratio generation scheme

In this scheme, the MPPT algorithm directly generates the converter reference duty ratio, without any closed loop control as shown in Figure 4.3 (a). It has the advantages of simple realization and easy implementation, but suffers from high steady-state power oscillation around the MPP [4.7].

4.2.2 Closed-loop control with classical PI control

Closed loop control exhibits fast dynamic performance with less steady-state power oscillation when compared to those experienced by the previous scheme [4.8]. A classical PI controller is the most popular tool in closed loop control systems, due to its simple architecture and ability to improve both the transient response and steady-state error. Hence, in this control scheme, the reference PV module MPP voltage is determined using

the MPPT technique and a classical PI controller is employed to force the PV voltage to track this reference, as shown in figure 4.3 (b).

The PI controller gains are designed using the Ziegler-Nichols technique and remain fixed under varying operating conditions. The PI controller's output signal is shown in (4.3).

$$u(k) = K_P e(k) + K_I \sum_{i=0}^{k} e(i) \tag{4.4}$$

where u is the signal produced by the PI controller to generate the appropriate converter switch duty ratio, K_P and K_I are the proportional and integral gains respectively, and the error e is the difference between the reference and the actual PV voltage.

However, PV MPPT techniques, applying classical PI controllers, may incur degraded performance under sudden changes as their gains are not self tuned during operation [4.9].

4.2.3 Closed-loop control with adaptive fuzzy-tuned PI control

For nonlinear systems with unpredictable parameter variations, it is necessary to use adaptive controllers whose parameters are automatically adjusted during changes [4.10]. Hence, a fuzzy-tuned PI controller is applied, however at the cost of increased controller complexity. Its gains (K_P and K_I) are continuously tuned using a fuzzy tuner [4.11, 4.12] as shown in Figure 4.3 (c) to respond quickly to sudden irradiance changes.

The input variables to the fuzzy tuner are the error (e) and the change in error (Δe) where the error is the difference between the reference PV module voltage, which is determined by the MPPT algorithm, and the actual PV voltage. These input variables pass through the fuzzification interface and consequently change to linguistic variables. Then, a rule base that holds the decision-making logic is used to determine the linguistic fuzzy output (K_P, K_I). Finally, a defuzzification stage converts the fuzzy output into signals to be sent out. The fuzzy sets of the input and output variables are shown in Figure 4.3 (d) [4.12].

The inputs linguistic variable levels are assigned as: negative big (NB), negative (N), zero (Z), positive (P), and positive big (PB) while those of the outputs are assigned as small (S), medium small (MS), medium (M), medium big (MB), and big (B). A Mamdani fuzzy model is used where the linguistic levels as well as the inputs and outputs ranges, are chosen according to the MPPT system characteristics and specifications. Finally, the rule

base, shown in Table 4.1, is applied using a set of linguistic IF-THEN rules, built with the help of the designer knowledge and experience [4.12].

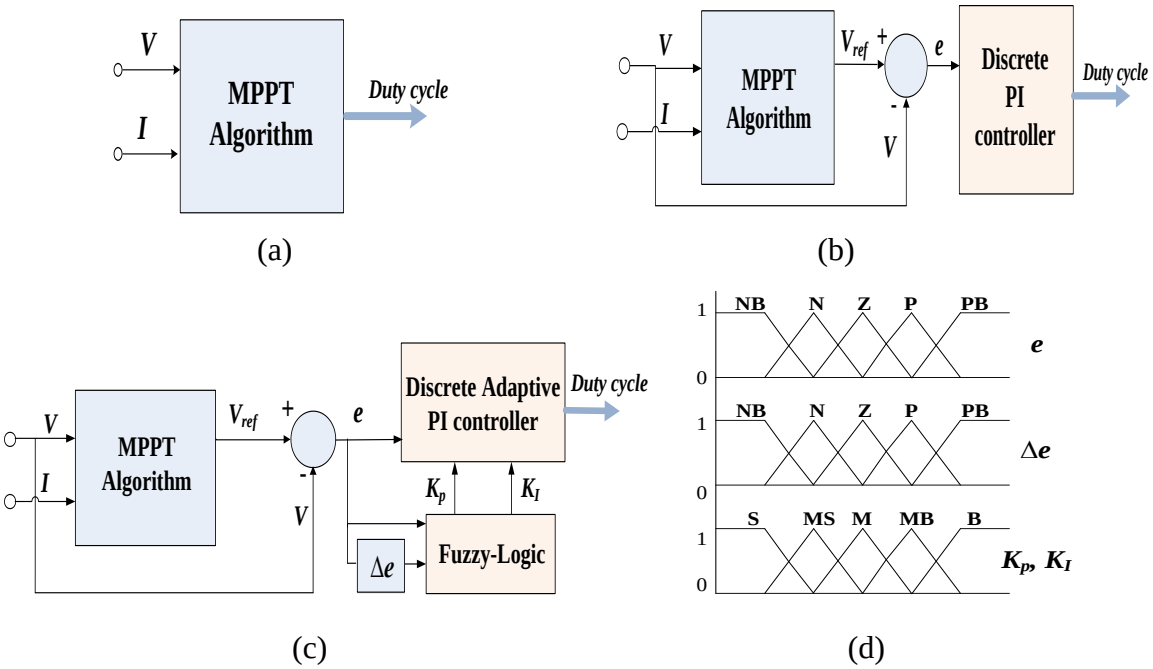

Figure 4.3. Different converter control schemes: (a) direct control, (b) closed-loop with classical PI controller, (c) closed-loop with adaptive fuzzy-tuned PI controller, and (d) inputs and outputs fuzzy sets of the fuzzy tuner.

Table 4.1. Fuzzy tuner rules [4.12]

e \ Δ*e*	**NB**	**N**	**Z**	**P**	**PB**
NB	S	S	MS	MS	M
N	S	MS	MS	M	MB
Z	MS	MS	M	MB	MB
P	MS	M	MB	MB	B
PB	M	MB	MB	B	B

4.3 Conventional variable-step incremental conductance technique

The most commonly used MPPT algorithms are perturb and observe (P&O) and incremental conductance (Inc.Cond.) [4.13, 4.14]. The P&O algorithm is widely used in PV stand-alone systems for its simple implementation [4.15-18]. In such PV systems, MPPT algorithms are preferably realized using low-cost microcontrollers to cut down the entire system cost. Thus, the P&O, being a division-free algorithm, is a convenient choice for controller implemented. Inc.Cond. is more complex in structure than P&O as it uses many mathematical divisions which increase the computational burden [4.3, 4.5].

However, P&O can easily lead to erroneous judgment and oscillation around the maximum power point (MPP) which results in power loss [4.19]. Whereas Inc.Cond. can accurately track the MPP, with less steady-state oscillation and faster response during changes, thus increasing the tracking efficiency [4.20-24]. Hence, the Inc.Cond. technique is a better candidate, especially during rapidly varying environmental conditions, so is considered henceforth in this thesis.

4.3.1 Conventional algorithm structure

As discussed in chapter two, the Inc.Cond. algorithm compares the instantaneous conductance (I/V) to the incremental conductance ($\Delta I/\Delta V$) and accordingly the voltage perturbation sign is determined, until reaching the MPP as shown in Figure 4.4 [4.4].

$$\frac{\Delta I}{\Delta V} = -\frac{I}{V} \qquad \text{at MPP} \tag{4.5}$$

$$\frac{\Delta I}{\Delta V} > -\frac{I}{V} \qquad \text{left to MPP} \tag{4.6}$$

$$\frac{\Delta I}{\Delta V} < -\frac{I}{V} \qquad \text{right to MPP} \tag{4.7}$$

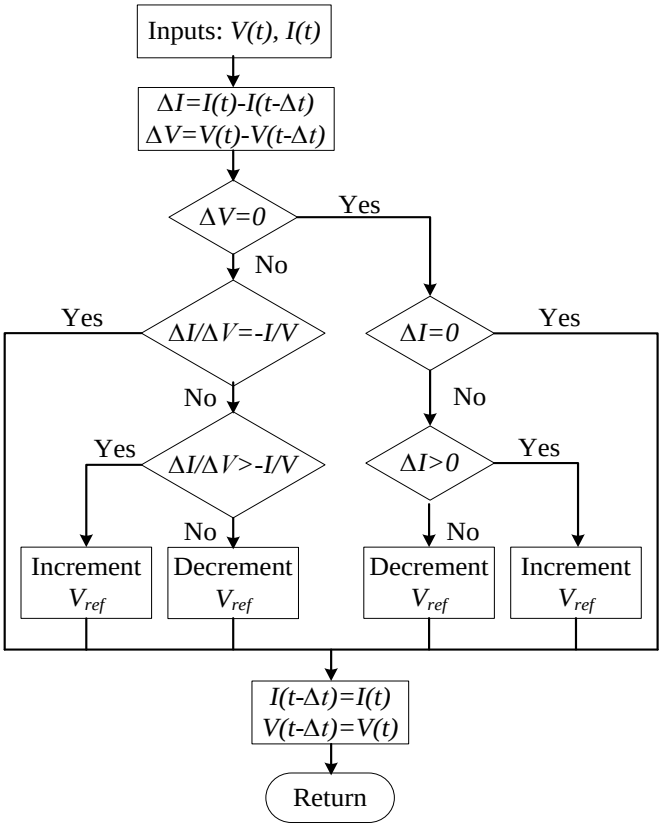

Figure 4.4. Conventional Inc.Cond. algorithm flowchart.

However, as shown in Figure 4.4, the conventional Inc.Cond. algorithm features several division calculations and a relatively complex decision making process. This in turn necessitates a more powerful microcontroller [4.22], for practical implementation, featuring a higher clock frequency and floating point calculation capability. This decreases the possibility of achieving a low cost system solution.

4.3.2 Conventional variable step-size

For a fixed-step Inc.Cond. algorithm, a smaller step-size slows down MPPT while a larger one increases the steady-state oscillation around the MPP. A solution to this conflicting situation is to have a variable step-size that gets smaller towards the MPP [4.25-31]. This improves the technique performance and solves the trade-off between tracking accuracy and convergence speed.

The conventional variable step-size depends on PV power change divided by PV voltage change ($\Delta P/\Delta V$) [4.26]. For a direct control scheme which directly controls converter switching, the considered step is the change in the converter duty ratio (ΔD) as shown in (4.7). But in the closed loop control scheme that controls PV voltage, the considered variable-step is the PV voltage change (ΔV) shown in (4.8);

$$\Delta D = N_1 \left|\frac{\Delta P}{\Delta V}\right| \tag{4.8}$$

$$\Delta V = N_2 \left|\frac{\Delta P}{\Delta V}\right| \tag{4.9}$$

where

$$\Delta P = P(k) - P(k-1) \tag{4.10}$$

$$\Delta V = V(k) - V(k-1) \tag{4.11}$$

$$\Delta D = D(k) - D(k-1) \tag{4.12}$$

and N_1 is the scaling factor which is tuned at the design stage to adjust the conventional step-size (ΔD) to compromise between tracking accuracy and its convergence speed while N_2 is the scaling factor of the step-size (ΔV).

However, the conventional variable step-size, being dependent on the division of PV power change by PV voltage change ($\Delta P/\Delta V$), can affect MPPT performance due to this step size digression, particularly under sudden irradiance changes [4.32, 4.33].

4.4 Modified variable-step incremental conductance technique applying direct converter control

In this research, an enhancement is introduced into the structure of the conventional Inc.Cond. algorithm to eliminate division computation and simplify its implementation. Also the conventional variable step is modified to improve its performance. This proposed variable-step division-free technique directly generates the converter duty-ratio, minimizing system control complexity. High steady-state power oscillation, generated from direct control scheme, are expected to be minimized by the enhanced performance of the proposed step-size.

4.4.1 Proposed division-free algorithm

A modification is introduced to the Inc.Cond. algorithm in order to eliminate all division computations in the algorithm. Using (4.4-6), the following modifications can be implemented:

$$\frac{\Delta I}{\Delta V} + \frac{I}{V} = 0 \qquad \text{at MPP} \tag{4.13}$$

$$\frac{\Delta I}{\Delta V} + \frac{I}{V} > 0 \qquad \text{left to MPP} \tag{4.14}$$

$$\frac{\Delta I}{\Delta V} + \frac{I}{V} < 0 \qquad \text{right to MPP} \tag{4.15}$$

Unifying the denominators in (4.12-14) to ($V \times \Delta V$), this denominator can be eliminated from the first equation as it equals zero whereas only V is eliminated from the denominator of the other two equations as it is always positive and its sign does not affect these equations. Thus equations (4.15-17) result:

$$(V \times \Delta I) + (I \times \Delta V) = 0 \qquad \text{at MPP} \tag{4.16}$$

$$\frac{(V \times \Delta I) + (I \times \Delta V)}{\Delta V} > 0 \qquad \text{left to MPP} \tag{4.17}$$

$$\frac{(V \times \Delta I) + (I \times \Delta V)}{\Delta V} < 0 \qquad \text{right to MPP} \tag{4.18}$$

Finally, in order to eliminate the division operations, the three Inc.Cond. algorithm rules can be rewritten as follows:

$$(V \times \Delta I) + (I \times \Delta V) = 0 \qquad \text{at MPP} \tag{4.19}$$

$$(V \times \Delta I) + (I \times \Delta V) > 0 \quad \&\& \quad \Delta V > 0 \qquad \text{left to MPP} \tag{4.20}$$

$$(V \times \Delta I) + (I \times \Delta V) > 0 \quad \&\& \quad \Delta V < 0 \qquad \text{right to MPP} \tag{4.21}$$

$$(V \times \Delta I) + (I \times \Delta V) < 0 \quad \&\& \quad \Delta V > 0 \qquad \text{right to MPP} \tag{4.22}$$

$$(V \times \Delta I) + (I \times \Delta V) < 0 \quad \&\& \quad \Delta V < 0 \qquad \text{left to MPP} \tag{4.23}$$

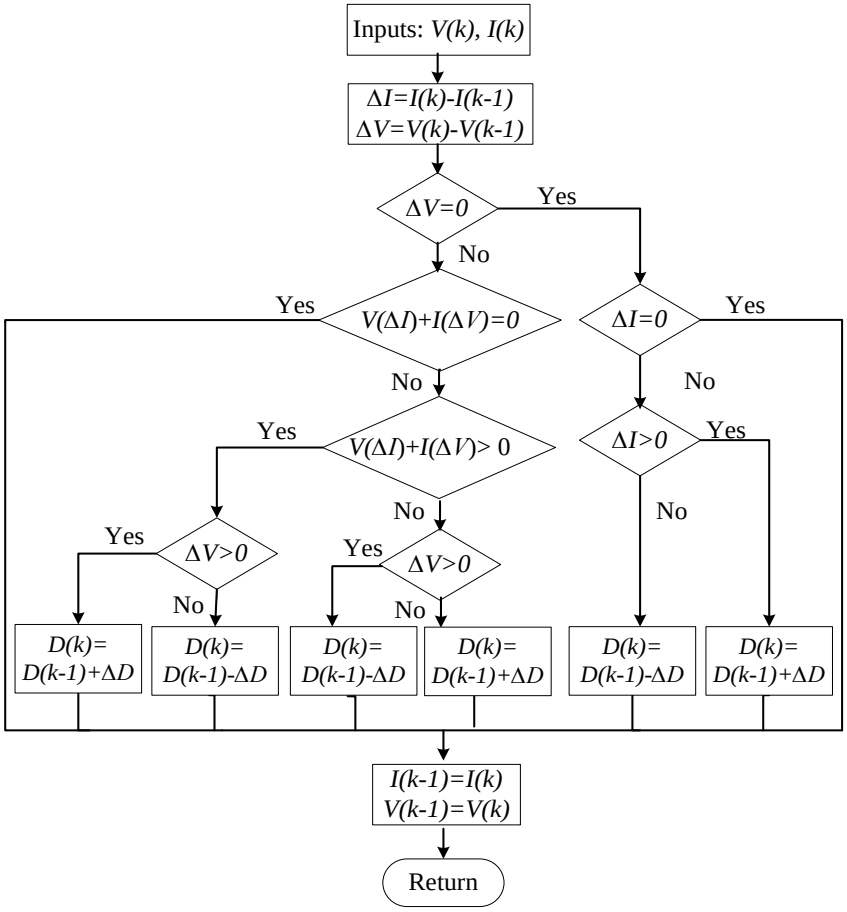

Figure 4.5. Proposed division-free Inc.Cond. algorithm flowchart.

The flowchart of the proposed algorithm is shown in Figure 4.5 where the removal of all division computation in the algorithm is compensated by applying arithmetic/logic mathematical operations. Now, algorithm structure complexity is minimized which in turn reduces processing real-time and enables the algorithm to be implemented in low cost microcontrollers.

4.4.2 Proposed variable step-size

The conventional step-sizes presented in (4.7) and (4.8), being dependant on the change of the PV power with respect to PV voltage change, exhibit dynamic performance deterioration during sudden irradiance changes. Furthermore, steady-state power oscillation noticeably arises around the MPP. This can be explained as follows.

i. During stable environmental conditions

Because of unavoidable factors such as measurement error, ripple and noise, the condition that ($\Delta I/\Delta V$) and (- I/V) be exactly equal can never be satisfied. Thus, the operating point does not settle exactly at the MPP. Instead, it oscillates around the MPP, changing the sign of the increment after each ΔP measurement [4.19, 4.23]. From Figure 4.2, in the regions at the MPP and close to it (constant voltage region), the change in PV voltage (ΔV) is small resulting in large $\Delta P/\Delta V$ steps. Although, these large step-sizes increase the tracking speed at start of PV operation, they enlarge the steady-state power oscillation, affecting PV system accuracy which in turn decreases tracking efficiency.

ii. During varying irradiance conditions

The conventional variable step method may show poor transient performance during sudden irradiance changes. As shown in Figure 4.2, when the irradiance changes from G_1 to G_2, there is a considerable power change (ΔP) while the PV voltage change (ΔV) is relatively small. Since the step-size depends on $\Delta P/\Delta V$, this will result in a large converter duty ratio change (ΔD) thus shifting the operating point far away from the new MPP. Noticeable transient decrease in the PV power occurs and the algorithm takes time to reach the new MPP. Consequently, the transient power loss increases, decreasing tracking efficiency.

In order to overcome this, a variable step-size is proposed which depends only on PV power change (ΔP). The proposed step size is used by the MPPT algorithm to directly control converter switching, thus it represent the change in the converter duty ratio as shown in (4.23);

$$\Delta D(proposed) = N_3|\Delta P| \tag{4.24}$$

where N_3 is the scaling factor which is tuned at the design stage to adjust the proposed step-size to compromise between tracking accuracy and convergence speed.

From the PV module *P-V* curve, the change in PV power (ΔP) is small around the MPP and large away from it. Thus, the proposed step-size, which depends on ΔP, will be large away from the MPP and decreases around the MPP to compromise between steady-state power oscillation and tracking speed. Unlike the conventional variable step which depends on the two ripple parameters (ΔP and ΔV) and their division, the proposed variable step depends solely on ΔP. Removing the division by ΔV, from the step-size calculation,

simplifies the algorithm and eliminates large step-size variations that occur at small PV voltage changes. Although this may slow down the tracking process at the start of operation, it minimizes the steady-state power oscillation around the MPP thus improving tracking accuracy and efficiency. Also it reduces the operating point shift away from the MPP during sudden irradiance changes, resulting in better transient performance with fast dynamic response and less transient power loss.

For further explanation, an illustrative example is shown in Figure 4.6. When the irradiance decreases from G_1 to G_2, the operating point shifts from 'A' to 'B', resulting in considerable PV power change (ΔP) due to PV current change (ΔI) while ΔV is almost zero. In order to reach the new MPP 'M', the MPPT algorithm must decrement the duty ratio D. Hence, algorithm performance is affected by the variable step adopted to achieve this decrement.

- For the conventional $\Delta P/\Delta V$ dependent step, a near zero ΔV results in a large step-size that significantly decrements D and shifts the operation to point 'C'. Hence, a noticeable transient power loss occurs and the algorithm takes longer to reach the new MPP 'M'.
- For the proposed ΔP based step, a large step-size is avoided and D is decremented to shift the operating point to 'D' which is close to the MPP 'M'. This will hasten the tracking process and reduce transient power loss.

In summary, the proposed variable step-size can effectively improve MPPT dynamics during sudden changes and limit steady-state power oscillation around the MPP. This enables direct converter control thus minimizing control complexity.

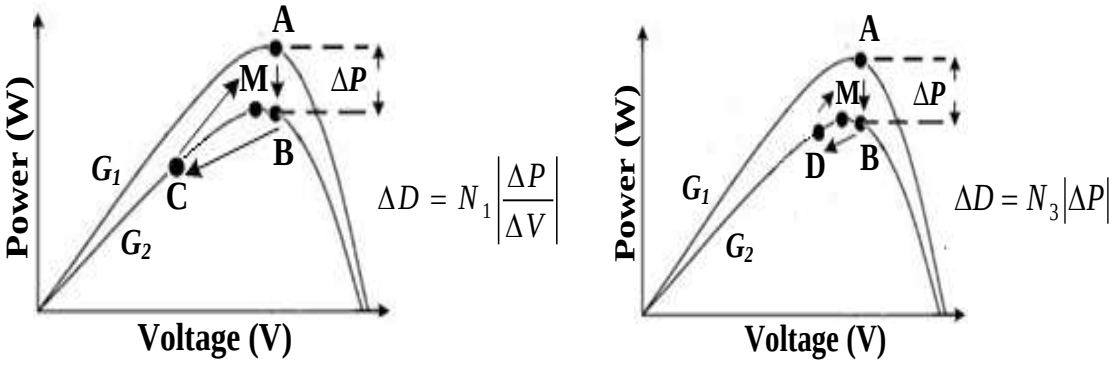

Figure 4.6. MPPT algorithm performance, at irradiance change, adopting (a) conventional $\Delta P/\Delta V$ based variable step and (b) proposed ΔP based variable step.

4.5 Simulation results

Simulation is used to compare the steady-state and transient performance of four MPPT models under irradiance level step changes (from 1000W/m^2 to 400W/m^2 at t=0.2s then from 400W/m^2 to 700W/m^2 at 0.4s). The first three models employ conventional variable-step Inc.Cond. technique (division-included Inc.Cond. algorithm associated with $\Delta P/\Delta V$ based variable step), in three different converter control schemes. The first MPPT model directly controls converter switching while the second and third models apply closed loop control using classical and fuzzy-tuned PI controllers respectively. The last MPPT model employs the proposed variable-step Inc.Cond. technique (division-free Inc.Cond. algorithm applying ΔP based variable step) to directly generate the converter duty-ratio.

Figure 4.7 shows the four MPPT models performance during the first and second simulated step changes while Table 4.2 gives their steady-state and transient performance parameters. Under varying irradiance conditions, all the models successfully track the MPP yet with different levels of tracking accuracy, convergence speed and transient undershoot.

As shown in Figure 4.7 parts (a) and (b), the direct control model with the conventional Inc.Cond. technique (Model I) gives the highest steady-state power oscillation at the MPP. Using a classical PI controller in closed-loop control (Model II) reduces steady-state power oscillation as shown in Figure 4.7 parts (c) and (d). However, it exhibits poor transient performance (slow tracking speed and largest undershoot) during sudden changes. To overcome this, the fuzzy tuned PI controller is adopted in Model III which compromises between steady-state power oscillation and tracking convergence speed, as shown in Figure 4.7 parts (e) and (f). It shows less undershoot than that produced by the previous two models which decreases its transient power loss. Finally, Figure 4.7 parts (g) and (h) show that steady-state and transient performance of the proposed model, which applies the proposed step-size, out-performs that of the other models during the two step irradiance changes.

The elimination of division by ΔV in the proposed step-size has limited the large increase in the step thus minimizing the steady-state power oscillation around the MPP. It shows the fastest dynamic response as well as the lowest undershoot during transients. The proposed model has the simplest implementation due to division elimination as well as the least complex control scheme as it directly generates the converter duty ratio. Thus, the proposed model effectiveness is established.

MODEL I: Direct Converter Control with Conventional Inc.Cond.

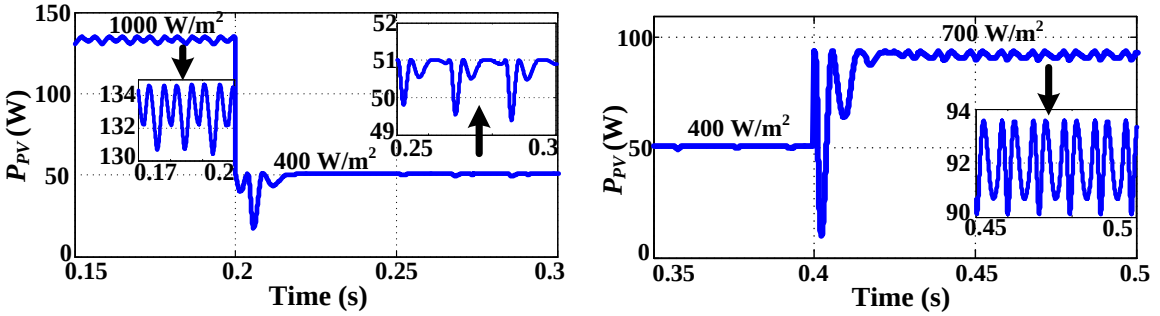

(a) (b)

MODEL II: Classical PI- based Closed Loop Control with Conventional Inc.Cond.

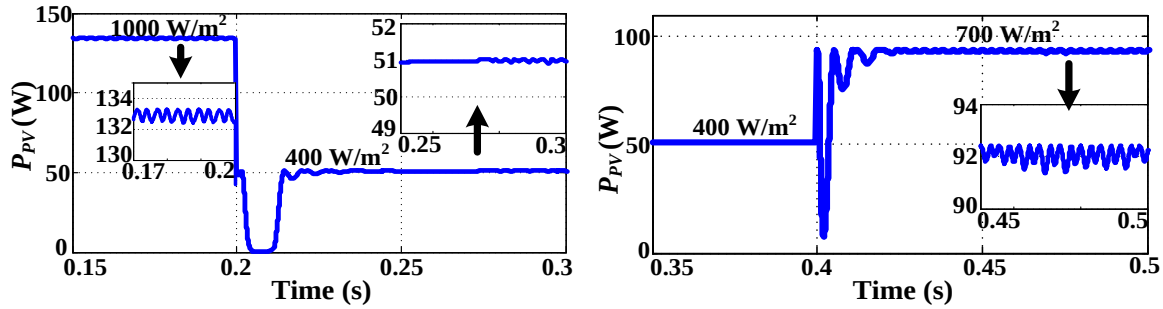

(c) (d)

MODEL III: Fuzzy-tuned PI-based Closed Loop Control with Conventional Inc.Cond.

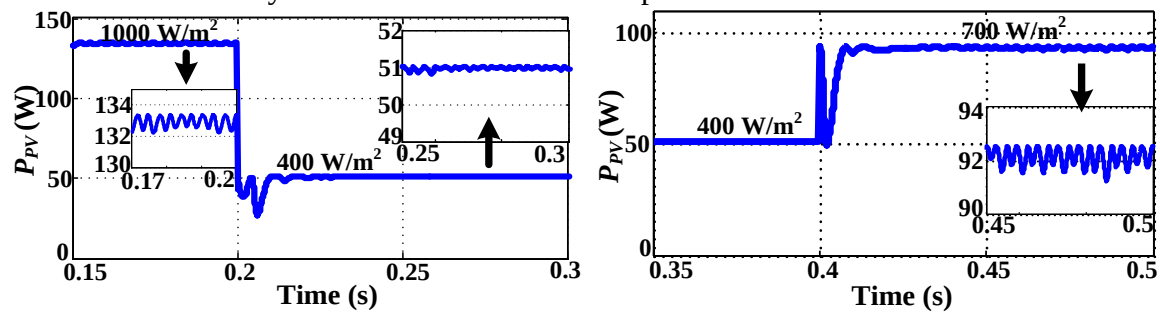

(e) (f)

Proposed model: Direct Converter Control with Proposed Inc.Cond.

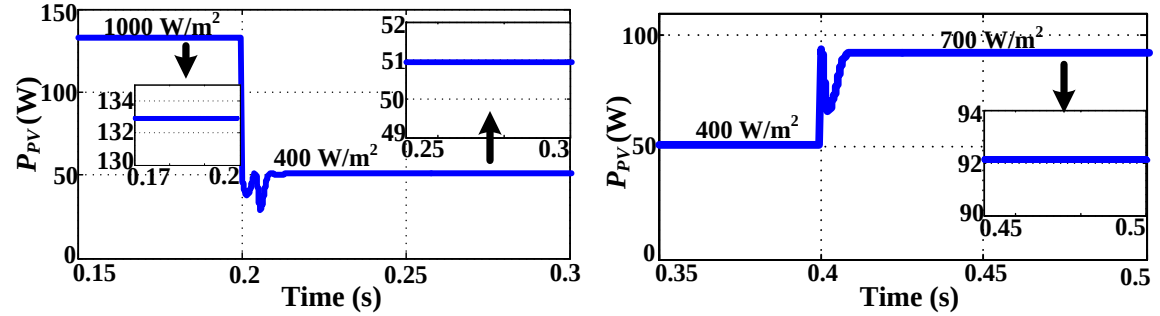

(g) (h)

Figure 4.7. PV Power acquired by (a, b) Model I, (c, d) Model II, (e, f) Model III, and (g, h) proposed model.

Table 4.2. Performance parameters of the four considered MPPT models under two step changes in irradiance

Irradiance (W/m^2)	**Model**	**Transient**		**Steady-state**
		% Power Undershoot	***Settling Time* (s)**	***Oscillations at MPP* (W)**
First step change (1000 to 400)	Model 1	66.63	0.021	1.5
	Model 2	100	0.035	0.11
	Model 3	46.42	0.017	0.1
	Proposed	**43.67**	**0.014**	**0.0025**
Second step change (400 to700)	Model 1	89.35	0.022	3.5
	Model 2	91.47	0.021	0.85
	Model 3	46.2	0.02	1
	Proposed	**28.5**	**0.01**	**0.022**

Finally, Table 4.3 summarizes the differences between the four considered MPPT models in terms of implementation complexity, control scheme, and performance at sudden irradiance changes.

Table 4.3. Comparison between the four considered MPPT models

Models / **Point of comparison**	**MODEL I**	**MODEL II**	**MODEL III**	**Proposed**
MPPT algorithm	Variable-step Inc.Cond. (conventional)	Variable-step Inc.Cond (conventional)	Variable-step Inc.Cond (conventional)	**Variable-step Inc.Cond (Modified)**
Division computations	Present	Present	Present	**Eliminated**
Variable step-size	$\Delta P/\Delta V$-based	$\Delta P/\Delta V$-based	$\Delta P/\Delta V$-based	**ΔP-based**
Control nature	Direct Control	Closed-loop	Closed-loop	**Direct Control**
Controller	Open loop	Classical PI	Fuzzy-tuned PI	**Open loop**
Complexity	Low	High	Highest	**Least**
Ability to compromise between steady-state power oscillation, tracking speed and transient under shoot during sudden changes	Low	Low	High	**Highest**

From the tables, the first and proposed MPPT models have minimal control complexity as both apply direct converter control without any closed-loop controllers. Hence, they will be considered through the remainder of this chapter. However, the proposed model shows further simplification in its implementation due to division elimination from its algorithm structure, enabling it to be effectively-implemented by low-cost microcontrollers. It gives the best steady-state and transient performance at sudden changes owing to the proposed ΔP based-step.

For further clarification on the superiority of the proposed step-size tracking performance on the PV module *P-V* curves, the 3-D figures (Figure 4.8 parts (a) and (b)) are presented. They illustrate the PV power, achieved by the conventional and proposed step-sizes, versus PV voltage and time, during the considered step irradiance changes. The proposed ΔP-based step almost eliminated the steady-state power oscillation around the MPP of each *P-V* curve relative to its irradiance level. It shows a faster response during irradiance changes with less power undershoot. Considering Table 4.2, the MPP tracking time, acquired by the proposed step-size (applied in proposed model), is reduced by 33.3% and 54.55% of that achieved by the conventional step-size (applied in Model I), at the first and the second step changes respectively. The proposed step succeeds in reducing the power undershoot, during the two step changes, by almost 23% and 60.85% of the maximum tracked PV power at 400 W/m^2 and 700 W/m^2 respectively, compared to those achieved with the conventional step-size.

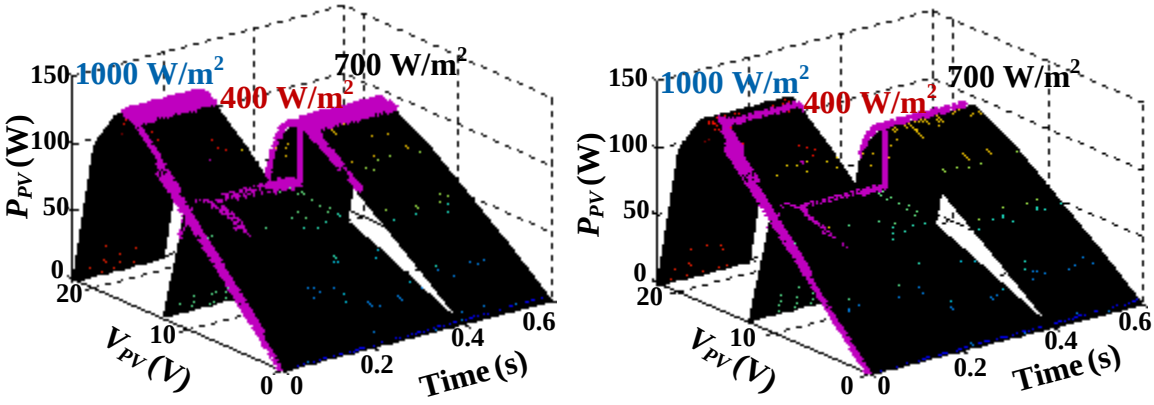

Figure 4.8. Power tracking nature on module *P-V* curves for (a) conventional technique adopting $\Delta P/\Delta V$ step and (b) proposed division-free technique with ΔP step, when both applying direct converter control.

4.6. Experimental results

Due to their simple control structure, both being directly control converter switching, the first and the proposed MPPT simulation models are considered for practical implementation. The former applies the conventional variable-step Inc.Cond. technique (division-included Inc.Cond. algorithm associated with $\Delta P/\Delta V$ based variable step). The latter employs the proposed variable-step Inc.Cond. technique (division-free Inc.Cond. algorithm applying ΔP based variable step). First, a TI 32-bit DSP TMS320F28335 is implemented to verify the better performance of the proposed ΔP-based variable step during stable and changing environmental conditions. Then, an ARDUINO Uno board, based on low-cost 8-bit Atmega328 microcontroller, is employed. This verifies the proposed technique's cost-effectiveness, being a division-free algorithm efficiently implemented in low-cost micro-controllers.

Both processors' features are shown in Appendix C.1.2 while MATLAB programs implementing the considered algorithms are presented in Appendix D.2.1 and D.3. In all cases the converter was operated at 15 kHz switching frequency.

4.6.1 Experimental implementation using TI 32-bit DSP TMS320F28335

Experimentally DSP TMS320F28335 is used to established the real-time implementation validity of the proposed division-free IncCond. algorithm. The experimentation focuses on the impact of the proposed ΔP-based variable step on the system performance and its superiority to the conventional $\Delta P/\Delta V$-based step-size. This is carried out during fixed and changing environmental conditions.

i. Stable environmental conditions

First, the performance of both the conventional and proposed variable-step Inc.Cond. techniques, are tested under fixed environmental conditions (800 W/m^2 and 23° C). A KD135SX_UPU PV panel is employed. Figure 4.9 (a) shows the performance of the conventional technique employing $\Delta P/\Delta V$-based variable step-size while Figure 4.9 (b) shows that of the proposed division-free technique applying ΔP-based step. The proposed step-size minimizes the steady-state oscillation around the MPP, thus maximizing tracking accuracy.

Conventional $\Delta P/\Delta V$-based step-size **Proposed ΔP-based step-size**

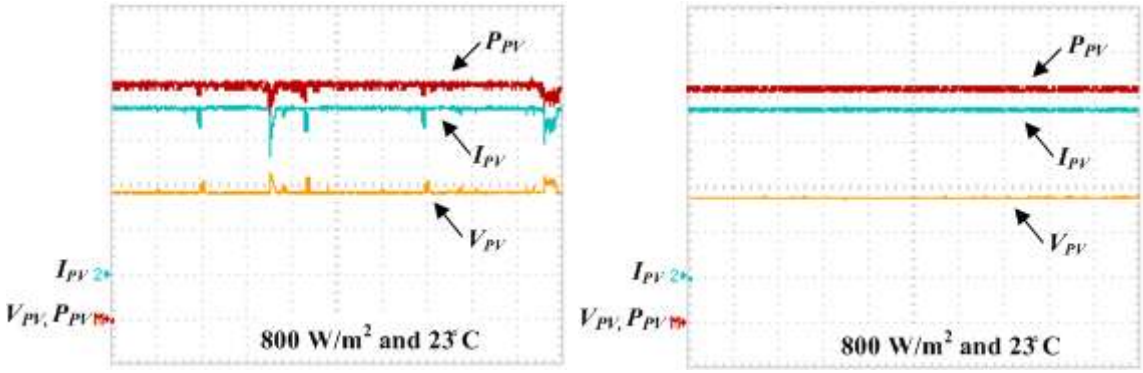

1 s/div, ch1: 5 V/div, ch2: 2 A/div, chM: 20 VA/div (a)

1 s/div, ch1: 5 V/div, ch2: 2 A/div, chM: 20 VA/div (b)

Figure 4.9. Experimental results of (a) conventional technique adopting $\Delta P/\Delta V$ step and (b) proposed division-free technique with ΔP step, using KD135X-UPU panel under stable conditions (800 W/m^2 and 23℃).

ii. Sudden changing irradiance conditions

In order to compare the transient performance of both techniques under sudden changes, a step change in irradiance is created. This is not practical with roof-mounted PV panels as their surrounding environmental conditions are uncontrollable. Thus, a PV module simulator can replace the actual PV panel or a lower-cost way of simulating *I-V* and *P-V* curves similar in nature to those generated by a PV panel is presented in [4.34]. The latter presents a simplified circuit employing a variable resistance (R_{ss}) in series with a variable voltage DC power supply and the MPP tracker (boost converter) is connected at its output. This circuit produces a *P-V* curve that exhibits a peak point for the tracker to lock on.

For PV sources, when the PV cell temperature changes, the open-circuit voltage changes significantly while as the solar irradiance varies the short-circuit current changes proportionally with a slight change in V_{oc}. Hence, the cell temperature change is simulated, in the system presented in [4.34], by varying the DC supply voltage while maintaining the series resistance constant. The irradiance change can be simulated by changing the circuit current via the variable series resistance while keeping the DC source voltage constant.

A simplified PV simulating circuit is employed, as shown in Figure 4.10 (a). This circuit emulates the PV source when exposed to sudden step change in irradiance. It consists of a DC power supply with constant voltage of 28 V and two parallel resistances of 3.2 Ω each to represent R_{ss}. When the switch S is on, the two resistances are in parallel

and R_{ss} is 1.6 Ω and this gives a *P-V* curve of almost 120W peak power. When S is opened, R_{ss} becomes 3.2 Ω which results in a step decrease in the current *I* producing a different *P-V* curve with reduced peak power level (about 60 W) as shown in Figure 4.10 (b).

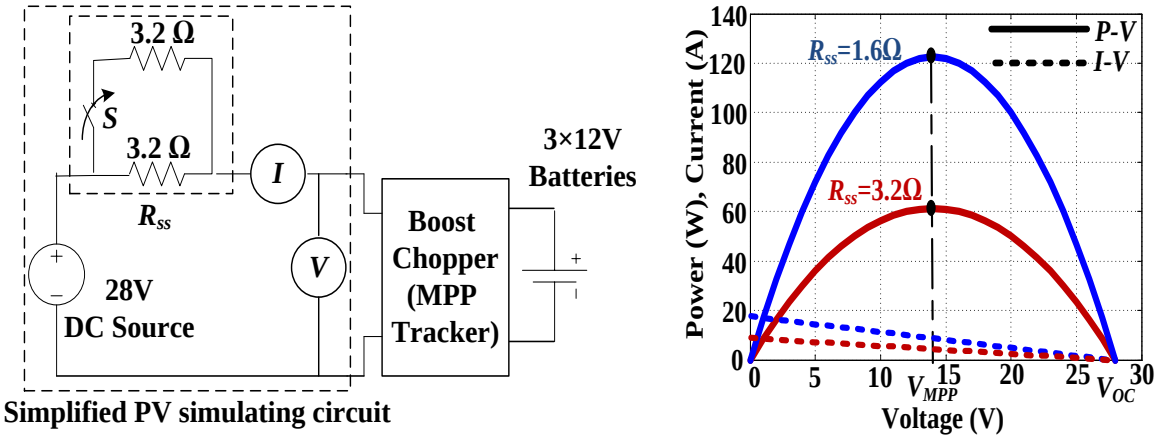

(a) (b)

Figure 4.10. Low-cost PV panel emulating circuit's (a) schematic diagram and (b) *P-V*, *I-V* curves for two different values of R_{ss} (corresponding to two different power levels).

Figure 4.11 parts (a), and (b) show the steady-state and transient performance of the conventional $\Delta P/\Delta V$-based and the proposed division-free ΔP-based Inc.Cond. techniques respectively under a step change in the PV simulator power level (from 120W to 60W). The conventional step-size exhibits more steady-state power oscillation than that produced by the proposed step-size. When focusing on their transient response during the sudden change (Figure 4.11 parts (c) and (d)), the conventional step-size shows slower response with a settling time t_s= 60 ms which is four times the settling time experienced by the proposed variable step (t_s=15 ms).

The experimental rig for the considered system is illustrated in Figure 4.12. A KD135SX PV panel is used for performance investigation under stable environmental conditions with the results shown in Figure 4.9. The low-cost PV emulating circuit is used for performance investigation under varying irradiance conditions with the results shown in fig 4.11.

It's worth noting that the tracked PV power shows considerably higher ripples in case of the PV emulating circuit than that in case of the actual PV panel. This owes to the flattened region around the MPP of the former circuit *P-V* curve (Figure 4.10 (b)) when compared to the relatively sharper MPP region of the actual PV curve (Figure 4.8). This results in more

operating points of PV power close in value to that of the MPP which in turn causes more steady-state PV power oscillations around the MPP in case of the PV simulating circuit.

However, experimental results, presented in this subsection, substantiate that the steady-state performance of the proposed step-size outperforms that of the conventional step-size during stable and changing conditions. Also the proposed step shows better transient response during sudden irradiance changes.

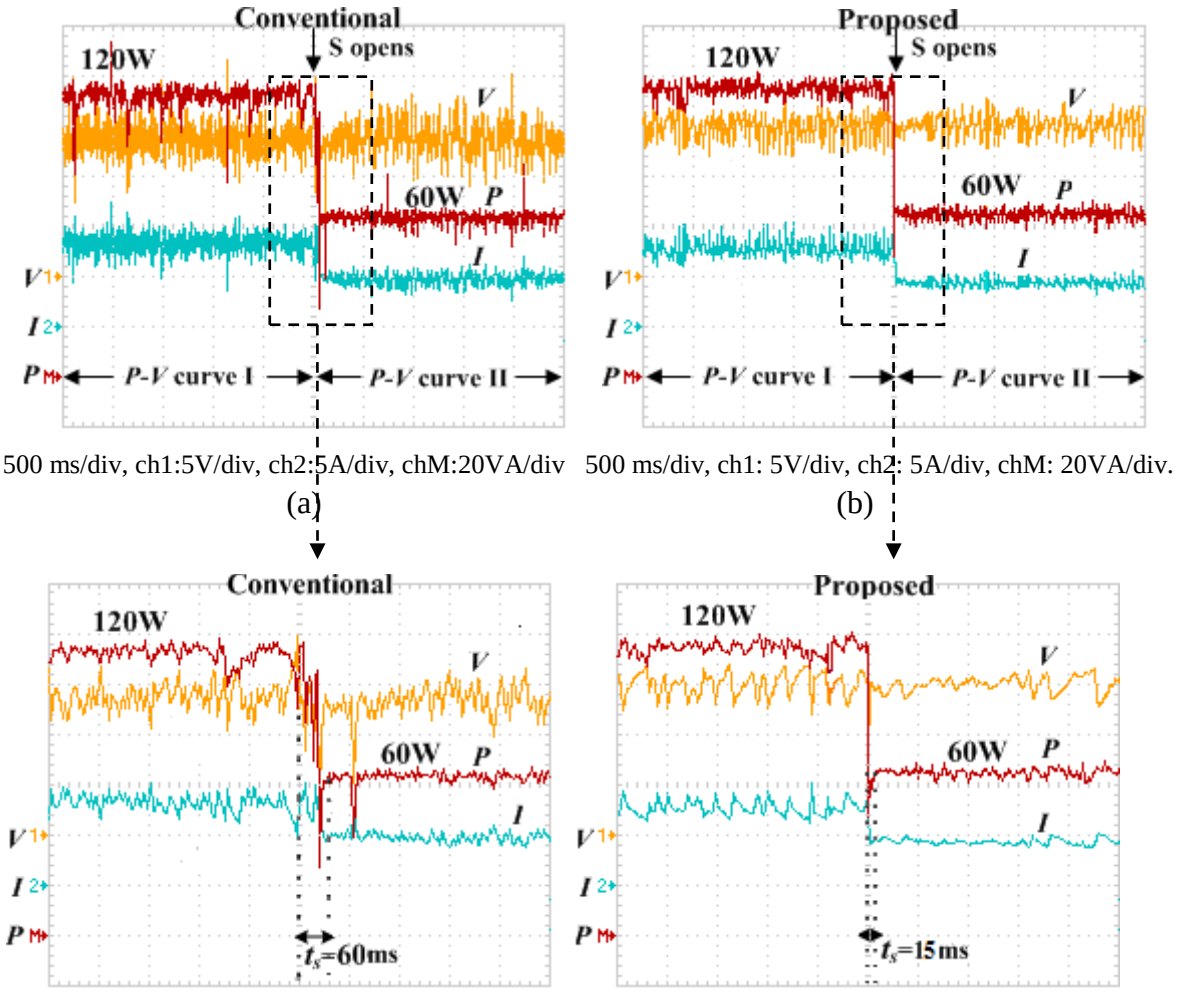

500 ms/div, ch1:5V/div, ch2:5A/div, chM:20VA/div (a)

500 ms/div, ch1: 5V/div, ch2: 5A/div, chM: 20VA/div. (b)

100 ms/div, ch1:5V/div, ch2:5A/div, chM:20VA/div (c)

100 ms/div, ch1: 5V/div, ch2: 5A/div, chM: 20VA/div. (d)

Figure 4.11. Experimental results, using low-cost PV simulating circuit under a step change in power level for: (a) conventional technique adopting $\Delta P/\Delta V$ step, (b) proposed division-free technique with ΔP step, (c) zoom of Figure 4.11(a), and (d) zoom of Figure 4.11(b).

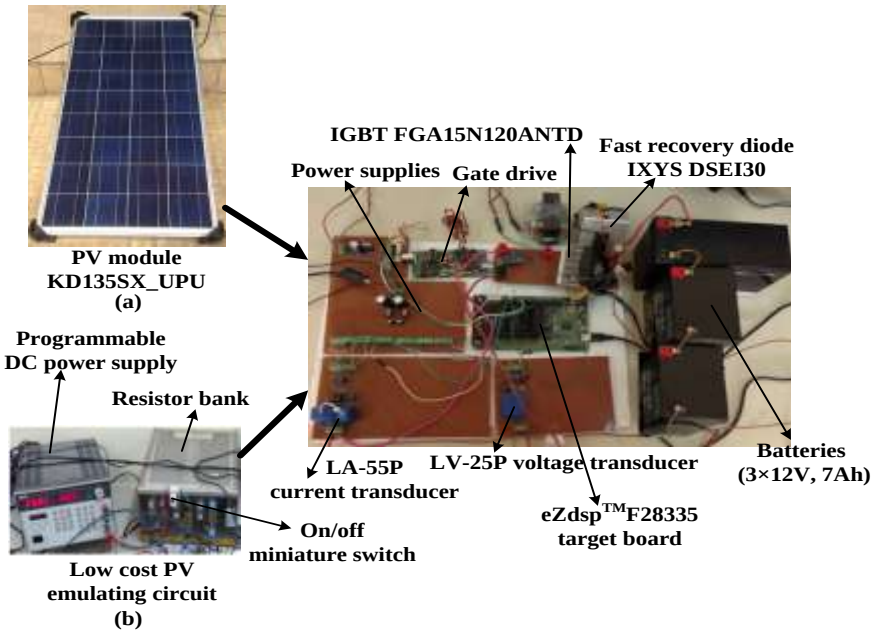

Figure 4.12. Test rig photograph when applying DSP TMS320F28335 using (a) KD135SX PV panel and (b) low cost PV emulating circuit.

4.6.2 Experimental implementation using low-cost Atmega 328 microcontroller

Merits of division elimination, from the Inc.Cond. algorithm, mainly lie in simplifying its structure and enhancing its performance, enabling it to be implemented by low cost microcontrollers. To clarify this, an experimental rig employing an Arduino Uno board, based on the low cost 8-bit Atmega 328 16-bit microcontroller, is assessed. The rig allows real-time comparison between the conventional Inc.Cond. technique featuring several division computations and $\Delta P/\Delta V$ step-size, and the proposed division-free IncCond. method, adopting the ΔP step-size. This assessment is carried out using the PV simulating circuit, considered in the previous subsection, and at the same power level changes.

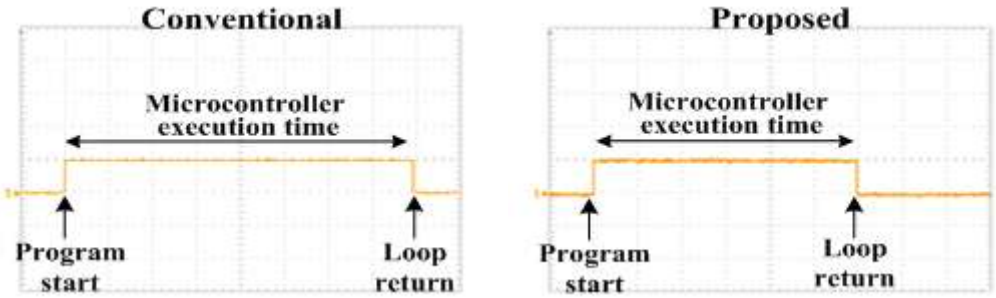

50 µs/div (a) 50 µs/div (b)

Figure 4.13. Program execution time for (a) conventional division-included Inc.Cond. technique adopting $\Delta P/\Delta V$ step, (b) proposed division-free technique adopting ΔP step.

For effective implementation using low-cost microcontrollers, the execution time of both the conventional and the proposed techniques, has to be measured in order to choose the most convenient sampling time. This is calculated by programming a pilot pin to toggle during program execution, triggering a digital output. Figure 4.13 (a) shows the maximum program execution time for the conventional technique which is 400µs while Figure 4.13 (b) shows that of the proposed technique is 300µs. Elimination of division calculations from the proposed algorithm, decreases the execution time and consequently simplifies microcontroller operation.

However, for a valid comparison, a 450µs sampling time is chosen for both techniques (to exceed the larger execution time of the conventional algorithm). Figure 4.14 parts (a) and (b) show the performance of the conventional and the proposed Inc.Cond. techniques respectively, under the step decrease in the PV simulator power level (from 120W to 60W). The $\Delta P/\Delta V$ step applied in the conventional scheme exhibits more steady-state power oscillation around the MPP than that produced by the proposed ΔP step-size employed in the modified scheme. When zooming in on both schemes transient response during the step-change, as shown in Figure 4.14 parts (c) and (d), the conventional step-size shows slower response with a settling time (t_s) of 400 ms which is four times that of the settling time experienced by the proposed step, t_s=100 ms.

Thus, for the same sampling time, the proposed technique shows better performance due to employing ΔP-based step-size. However, since this division-free technique exhibits less processing time (300µs), its performance can be retested at a sampling time of 350µs which is less than that adopted in the previous test case. This improves the sampling rate which improves system response during changes. Figure 4.15 (a) shows the proposed scheme's performance during the step decrease in power level with a sampling time of 350µs. A zoom into this step-change is seen in Figure 4.15 (b). The settling time (t_s) of the proposed scheme, in this case, is 40ms which is less than half that exhibited by the same scheme with a 450µs sampling time (Figure 4.14(d)).

Table 4.4. summarises the settling time executed by the conventional and proposed MPPT techniques under the step power change using DSP TMS320F28335 and Atmega 328 implemented in a Arduino-Uno board.

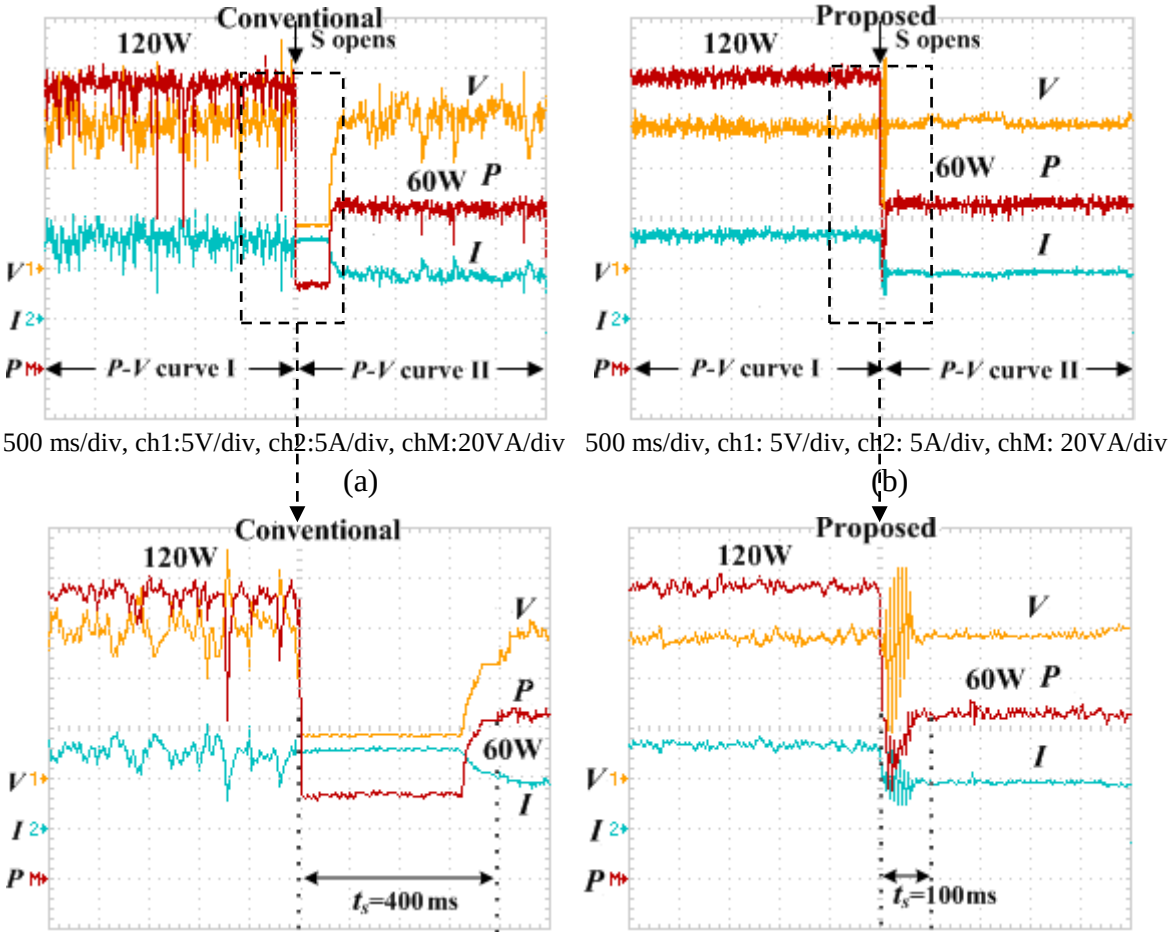

Figure 4.14. Step change experimental results at $T_{sampling}$=450μs for (a) conventional technique adopting $\Delta P/\Delta V$ step, (b) proposed division-free technique adopting ΔP step, (c) zoom of Figure 4.14(a), and (d) zoom of Figure 4.14(b).

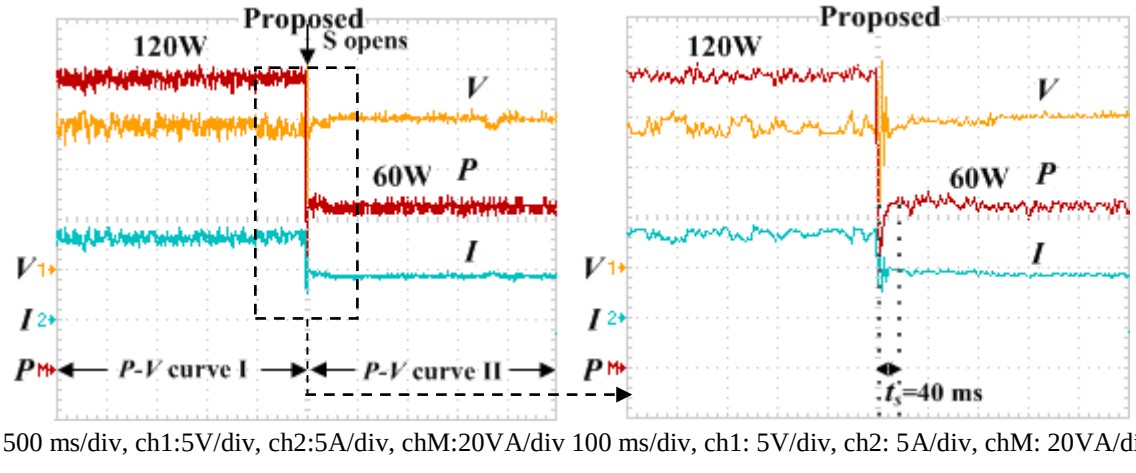

Figure 4.15. Step change experimental results at $T_{sampling}$=350μs for (a) proposed division-free technique adopting ΔP step and (b) zoom of Figure 4.15(a).

Table 4.4. Settling time of the considered techniques during the power step change

Controller / MPPT Technique	**DSP TMS320F28335**	**Atmega 328** $T_{sampling}$=450μs	**Atmega 328** $T_{sampling}$=350μs
Conventional Inc.Cond. MPPT (division-included algorithm adopting $\Delta P/\Delta V$ step)	60 ms	400 ms	not applicable
Proposed Inc.Cond. MPPT (division-free algorithm adopting ΔP step)	15 ms	100 ms	40 ms

In summary, the experimental results in this subsection, verify that the proposed step-size enhances system steady-state and transient performance during changes. The division computation elimination reduces the program execution time, enabling the user to improve the sampling rate which further enhances the technique's response during transients. The test rig for the Arduino-based system is shown in Figure 4.16.

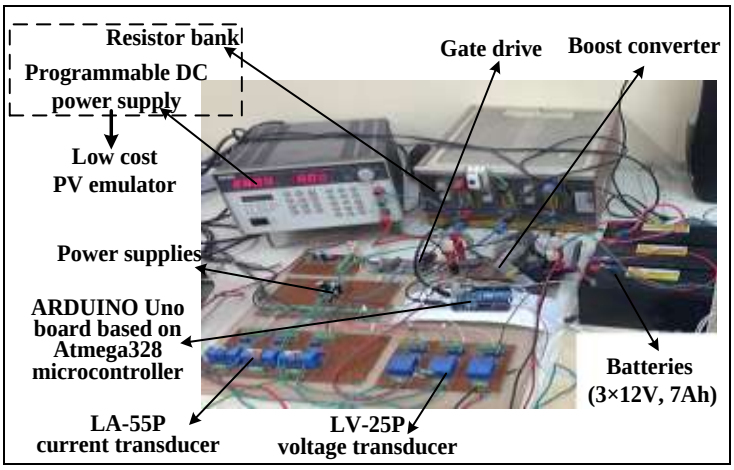

Figure 4.16. Test rig photograph when applying Arduino-UNO board.

The proposed MPPT technique, implemented by Atmega 328 microcontroller**,** is compared with other experimental prototypes presented in recent publications, as shown in Table 4.5. When compared with low-price microcontroller prototypes [4.24, 4.31, and 4.40], the proposed prototype gives faster MPPT during sudden changes. Prototypes of faster response [4.6, 4.30, and 4.39] employ much more expensive microcontrollers than that used in the proposed research. Hence, being implemented by low-cost 8-bit Atmega 328 microcontroller, the proposed division-free algorithm, with the modified step-size, achieves the best compromise between MPPT dynamic performance and employed microcontroller cost. Consequently, its functionality is substantiated, offering an economical efficient solution for stand-alone PV MPPT.

Table 4.5. Comparison between the proposed technique, implemented by Atmega 328 microcontroller**,** and experimental prototypes presented in recent publications

Work, Publication year	**Power rating**	**Converter type**	**Switching frequency**	**MPPT Technique**	**Hardware Programmed platform**	**Tracking speed**	**Controller price**
[4.30] (2014)	80W	buck	100 kHz	Inc.Cond.	FPGA XC3S400	2.5 ms	$38.5
[4.6] (2013)	200 W	boost	50 kHz	P&O-based on PI controller	DSP TMS320F240	20 ms	$25.64
[4.35] (2012)	240W	buck-boost	50 kHz	Improved PSO	DSP TMS320F240	40 ms	$25.64
[4.36] (2014)	800W	boost	----------	Zero-oscillation adaptive step P&O	Microcontroller TI C2000	1s	$24
[4.17] (2012)	1080W	buck	10 kHz	P&O	DSP TMS320F2812	0.5s	$23.32
[4.29] (2013)	1080W	Buck	10 kHz	Inc.Cond.	DSP TMS320F2812	0.5s	$23.32
[4.37] (2011)	20W	buck	100 kHz	Load-current based MPPT	DSP TMS320F28335	80 ms	$21.17
[4.9] (2011)	54 W	boost	25 kHz	PI–based P&O	DSP TMS320F28335	1s	$21.17
[4.38] (2012)	150W	buck	----------	Fuzzy -based P&O	DSP TMS320F28335	1.5 s	$21.17
[4.39] (2014)	210W	boost	----------	Adaptive P&O fuzzy MPPT	DSP TMS320F28335	20 ms	$21.17
[4.28] (2011)	110W	boost	50 kHz	Inc.Cond.	Microcontroller C515C	0.5 s	$19.6
[4.24] (2014)	40W	DC/DC converter	10 kHz	TS fuzzy-based Inc.Cond.	Embedded controller dsPIC33FJ128MC802	2s	$4.46
[4.31] (2015)	85W	sepic	20kHz	Load line-based MPPT	Microcontroller PIC18F4520	0.2s	$4.26
[4.40] (2013)	250W	boost	40 kHz	Power increment-based Inc.Cond.	Embedded controller dsPIC33FJ06GS202	5 s	$3.95
Proposed	**130W**	**boost**	**15 kHz**	**Modified step-size division-free Inc.Cond.**	**Microcontroller Atmega328**	**40 ms**	**$2.00**

----------: not mentioned, controller prices are from [4.41, 4.42].

4.7 Summary

This research aims at combining the advantages of simple algorithm structure and uncomplicated converter control together with improved steady-state and transient system performance, in one MPPT technique. Hence, an Inc.Cond. algorithm is modified featuring elimination of any division calculations, thus simplifying technique implementation. A new variable step-size is proposed which only depends on the PV power change (ΔP), thus eliminating its division by the PV voltage change (ΔV). The proposed step-size minimizes steady-state power oscillation around the MPP and effectively improves MPPT dynamics during sudden changes. This proposed variable-step technique directly controls converter switching without closed loop controllers, hence minimizing control complexity. This

results in a division-free variable-step technique which does not only have the merits of enhanced steady-state and transient performance but also shows simplified implementation and control structure. Hence, processing real-time is reduced enabling the proposed technique to be implemented in low-cost microcontrollers which decreases system costs.

However, it should be noted that the performance of this proposed technique has not been tested under very low irradiance levels or partial shading conditions.

References

[4.1] C. Hua and C. Shen, "Study of Maximum Power Tracking Techniques and Control of DC/DC Converters for Photovoltaic Power System", in Proc. IEEE Power Electronics Specialists Conference (PESC), 1998, pp 86-93.

[4.2] D.W. Hart, Power Electronics Handbook. McGraw Hill, 2011.

[4.3] D.P. Hohm and M. E. Ropp, "Comparative Study of Maximum Power Point Tracking Algorithms", Progress in Photovoltaics: Research and Applications, Vol. 11, No.1, 2003, pp. 47–62.

[4.4] T. Esram, P.L. Chapman, "Comparison of Photovoltaic Array Maximum Power Point Tracking Techniques", IEEE Trans. Energy Conversion, Vol. 22, No. 2, June 2007, pp. 439-449.

[4.5] B. Subudhi, and R. Pradhan, "A Comparative Study on Maximum Power Point Tracking Techniques for Photovoltaic Power Systems", IEEE Trans. Sustainable Energy, Vol. 4, No. 1, January 2013, pp. 89-98.

[4.6] M. A. Gomes de Brito, et al, "Evaluation of the Main MPPT Techniques for Photovoltaic Applications", IEEE Trans. Industrial Electronics, Vol. 60, No. 3, March 2013, pp. 1156-1167.

[4.7] F. Liu, et al, "Comparison of P&O and Hill Climbing MPPT Methods for Grid-connected PV Converter," in Proc. IEEE Conference on Industrial Electronics and Applications (ICIEA), June 2008, pp.804-807.

[4.8] M. G. Villalva, and F. E. Ruppert, "Analysis and Simulation of the P&O MPPT Algorithm using a Linearized PV Array Model", in Proc. IEEE Industrial Electronics Conference (IECON), November 2009, pp. 231-236.

[4.9] A. Abdelsalam, et al, "High Performance Adaptive Perturb and Observe MPPT Technique for Photovoltaic-based Microgrids", IEEE Trans. Power Electronics, Vol. 26, No. 4, April 2011, pp. 1010 – 1021.

[4.10] K. S. Tang, et al, "An Optimal Fuzzy PID Controller", IEEE Trans. Industrial Electronics, Vol. 48, No. 4, August 2001, pp. 757 – 765.

[4.11] J. Zhang, N. Wang, and S. Wang., “Developed Method of Tuning PID Controllers with Fuzzy Rules for Integrating Processes”, in Proc. IEEE American Control Conference (ACC), 2004, pp. 1109-1114.

[4.12] K. Sinthipsomboon, W. Pongaen, and P. Pratumsuwan, "A Hybrid of Fuzzy and Fuzzy Self-tuning PID Controller for Servo Electro-hydraulic System", in Proc. IEEE Conference on Industrial Electronics and Applications, 2011, pp. 220-225.

[4.13] D. Sera, et al, " On the Perturb-and-Observe and Incremental Conductance MPPT Methods for PV Systems", IEEE Journal of Photovoltaics, Vol. 3, No. 3, July 2013, pp. 1070- 1078.

[4.14] R. Faranda, and S. Leva, "Energy Comparison of MPPT Techniques for PV Systems", WSEAS Trans. Power Systems, Vol. 3, No. 6, June 2008, pp 446-455.

[4.15] V. M. Pacheco, et al, "Stand-alone Photovoltaic Energy Storage System with Maximum Power Point Tracking", in Proc. IEEE Applied Power Electronics Conference (APEC), 2003 , pp. 97 – 102.

[4.16] A. Ingegnoli, and A. Iannopollo, "A Maximum Power Point Tracking Algorithm for Stand-alone Photovoltaic Systems Controlled by Low Computational Power Devices," in Proc. IEEE Mediterranean Electrotechnical Conference (MELECON), 2010, pp.1522 – 1527.

[4.17] H. Aghazadeh, H. M. Kojabadi, and A. S. Yazdankhah, "Stand-alone PV Generation System with Maximum Power Point Tracking", in Proc. Environment and Electrical Engineering International Conference (EEEIC), 2010, pp.549 – 552.

[4.18] M. Elgendy, B. Zahawi, and D. J. Atkinson, "Assessment of Perturb and Observe MPPT Algorithm Implementation Techniques for PV Pumping Applications", IEEE Trans. Sustainable Energy, Vol. 3, No. 1, January 2012, pp. 21-33.

[4.19] X. Zhang, et al, "The Analysis of Power Loss Caused by the Truncation Error of MPPT Algorithms," IEEE Symposium on Power Electronics for Distributed Generation Systems (PEDG), June 2010, pp.7-11.

[4.20] G. Azevedo, et al, "Evaluation of Maximum Power Point Tracking Methods for Grid-connected Photovoltaic Systems", in Proc. IEEE Power Electronics Specialists Conference (PESC) 2008, pp 1456-1462.

[4.21] G. Spiazzi, et al, "Low Complexity MPPT Techniques for PV Module Converters," in Proc. IEEE International Power Electronics Conference (IPEC), 2010, pp.2074-2081.

[4.22] S. Qin, et al, "Comparative Analysis of Incremental Conductance and Perturb-and-Observation Methods to Implement MPPT in Photovoltaic System," in Proc. IEEE International Conference on Electrical and Control Engineering (ICECE), September 2011, pp. 5792-5795.

[4.23] M. Adly, M. Ibrahim, and H. El Sherif, "Comparative Study of Improved Energy Generation Maximization Techniques for Photovoltaic Systems," in Proc. IEEE Asia-Pacific Power and Energy Engineering Conference (APPEEC),2012, pp. 1-5.

[4.24] P. Sekhar, and S. Mishra, "Takagi–Sugeno Fuzzy-based Incremental Conductance Algorithm for Maximum Power Point Tracking of a Photovoltaic Generating Sstem", IET Renewable Power Generation, Vol. 8, No. 8, 2014, pp. 900–914.

[4.25] B. Liu, et al, "Analysis and Improvement of Maximum Power Point Tracking Algorithm Based on Incremental Conductance Method for Photovoltaic Array", in Proc. IEEE International Conference on Power Electronics and Drive Systems (PEDS) , 2007, pp. 637-641.

[4.26] F. Liu, et al, "A Variable Step Size INC MPPT Method for PV Systems," IEEE Trans. Industrial Electronics, Vol. 55, No. 7, July 2008, pp. 2622-2628.

[4.27] D. Menniti, et al, "An Incremental Conductance Method with Variable Step Size for MPPT: Design and Implementation," in Proc. IEEE International Conference on Electrical Power Quality and Utilization (EPQU), September 2009, pp.1-5.

[4.28] Q. Mei, et al, "A Novel Improved Variable Step-size Incremental-Resistance MPPT Method for PV Systems," IEEE Trans. Industrial Electronics, Vol. 58, No. 6, June 2011, pp. 2427-2434.

[4.29] M. A. Elgendy, B. Zahawi, and D. J. Atkinson, "Assessment of the Incremental Conductance Maximum Power Point Tracking Algorithm," IEEE Trans. on Sustainable Energy, Vol. 4, No. 1, January 2013, pp. 108- 117.

[4.30] R. Faraji, A. Rouholamini, H. R. Naji, R. Fadaeinedjad, M. R. Chavoshian, "FPGA-based Real Time Incremental Conductance Maximum Power Point Tracking Controller for Photovoltaic Systems", IET Power Electronics, Vol. 7, No. 5, 2014, pp. 1294–1304.

[4.31] T. K. Soon and S. Mekhilef, "A Fast-converging MPPT Technique for Photovoltaic System under Fast-varying Solar Irradiation and Load Resistance," IEEE Trans. Industrial Informatics, Vol. 11, No. 1, February 2015, pp. 176-186.

[4.32] A. N. Ridge, G. A. Amaratunga, "Photovoltaic Maximum Power Point Tracking for Mobile Applications", Electronics Letters, Vol. 46,No.22, 2010, pp.1520-1521.

[4.33] W. Ping, et al, "An Improved MPPT Algorithm Based on Traditional Incremental Conductance Method," in Proc. IEEE International Conference on Power Electronics Systems and Applications (PESA), June 2011, pp. 1-4.

[4.34] A. K. Mukerjee and N. Dasgupta, "DC Power Supply used as Photovoltaic Simulator for Testing MPPT Algorithms", Renewable Energy, Vol. 32, No. 4, 2007, pp. 587–592.

[4.35] K. Ishaque, et al, "An Improved Particle Swarm Optimization (PSO)–based MPPT for PV with Reduced Steady-state Oscillation", IEEE Trans. Power Electronics, Vol. 27, No. 8, August 2012, pp. 3627- 3638.

[4.36] F. Paz, and M. Ordonez, "Zero Oscillation and Irradiance Slope Tracking for Photovoltaic MPPT", IEEE Trans. Industrial Electronics, Vol. 61, No. 11, November 2014, pp. 6138- 6147.

[4.37] Y. Jiang, J. Qahouq, T. Haskew, "Adaptive-step-size with Adaptive-perturbation-frequency Digital MPPT Controller for a Single-sensor Photovoltaic Solar System", IEEE Trans. Power Electronics, Vol. 28, No. 99, 2011, pp. 3195–3205.

[4.38] A. Al Nabulsi, and R. Dhaouadi, "Efficiency Optimization of a DSP-based Standalone PV System using Fuzzy Logic and Dual-MPPT Control", IEEE Trans. Industrial Informatics, Vol. 8, No. 3, 2012, pp. 573–584.

[4.39] M. M. Zainuri1, et al, "Development of Adaptive Perturb and Observe-fuzzy Control Maximum Power Point Tracking for Photovoltaic Boost DC–DC Converter", IET Renewable Power Generation, Vol. 8, No. 2, 2014, pp. 183–194.

[4.40] G. C. Hsieh, *et al*, "Photovoltaic Power-increment-aided incremental-conductance MPPT with Two-phased Tracking", IEEE Trans. Power Electronics, Vol. 28, No. 6, 2013, pp. 2895–2911.

[4.41] Website: www.farnell.com

[4.42] Website: www.parts.arrow.com

Chapter Five

Novel Sensorless Control Technique for Single-phase Two-stage Grid-connected Photovoltaic Systems

For low-power (< 10 kW) applications, PVs are usually connected to the AC grid through a single-phase voltage-source inverter (VSI) at voltage level of 110/220V [5.1]. The two-stage PV topology employs a DC/DC converter stage before the VSI stage, for decoupling and voltage boosting purposes [5.2]. Conventionally, the first DC/DC chopper stage achieves PV MPPT while the second inverter stage is used to deliver the PV power to the electric grid [5.3]. Normally, the VSI stage features two control loops; outer DC-link voltage control loop and inner grid current control loop. Measurements of PV voltage and current are required to detect the PV power and achieve MPPT. Furthermore, sensing DC-link voltage is mandatory for the outer DC-link voltage control loop and measuring grid voltage and current is essential for the inner grid current control loop. This requires a number of sensors that add to systems' cost and size.

Sensorless control techniques have been proposed to reduce these measurements through mitigation of PV voltage and/or PV current sensors and in turn reduce cost [5.4-9]. Most of these techniques are based on the sensorless MPPT control scheme [5.10] which relies on the fact that as the DC-link voltage is kept constant by the controller action at steady-state, the PV generated power and the regenerative power to the grid side should be in balance [5.11]. This force the grid current’s amplitude to be proportional to the PV generated power. Thus, varying the chopper duty cycle, to maximize the line current amplitude, results in PV MPPT without the need of PV sensors [5.10]. However, overall system response deteriorates in comparison with that of the conventional method which directly detects the PV power through dedicated sensors. This can be related that the response of this sensorless MPPT process mainly depends on the response of the inverter DC-link voltage control loop and in turn on its grid current loop whereas, in the conventional control technique, the MPPT is achieved independent of the inverter control loops [5.12].

In this chapter, a new DC-link voltage sensorless technique is proposed for single-phase two-stage grid-tied PV string system. Matching conventional control techniques, the proposed scheme still requires PV sensors to directly calculate the PV power and achieve

MPPT via the first chopper stage. Hence, the MPPT process is achieved independent of the inverter loops, limiting system response degradation. However, in the second inverter stage, the proposed technique employs only the grid current control loop and mitigates the voltage control loop thus eliminating the high DC-link voltage sensor. Hence, system cost and footprint are reduced and control complexity is minimized. Furthermore, the removal of the DC-link voltage loop PI controller enhances system stability and improves its dynamic response during sudden environmental changes. Simulation and experimental results verify the effectiveness of the proposed scheme at different DC-link voltage levels and confirm its superior performance, compared to the conventional scheme, under varying irradiance conditions.

5.1 System under investigation

The considered system is a 1.5 kW, 220 V, 50 Hz single-phase two-stage grid-connected PV system as shown in Figure 5.1. The first stage consists of a boost converter responsible for the MPPT process, PV voltage level amplification, and decoupling between the PV source and the DC-link. The second stage features a current-controlled voltage source inverter (VSI) to achieve PV-grid interface. The PV source, in this paper, is a string configuration which consists of ten KD135SX_UPU PV modules connected in series.

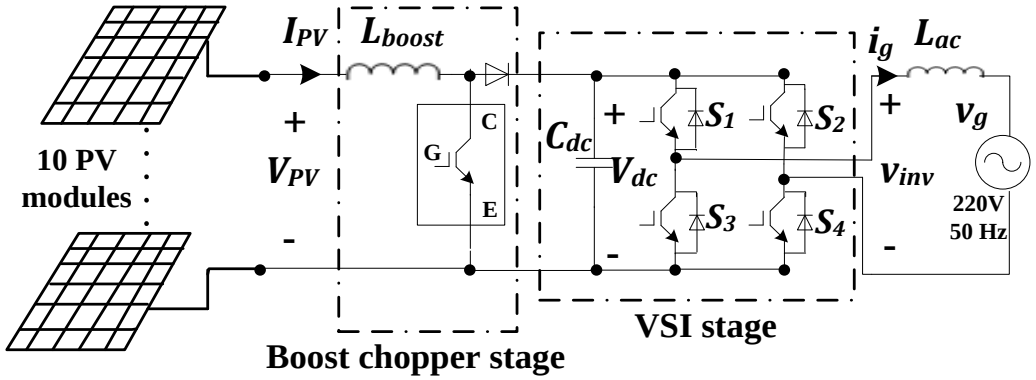

Figure 5.1. PV-grid connected system under investigation.

5.1.1 DC/DC boost converter design

In this work, the applied step up DC/DC converter is a single-phase single-switch boost chopper [5.13]. In its continuous conduction mode, it amplifies the PV input voltage level with a gain given as:

$$G_{boost} = \frac{V_{o/p}}{V_{i/p}} = \frac{V_{dc}}{V_{PV}} = \frac{1}{1 - D_{boost}} \tag{5.1}$$

where V_{PV} is the PV string voltage, V_{dc} is the DC-link mean voltage and D_{boost} is the chopper duty ratio. The inductance of the boost converter (L_{boost}) is determined by selecting acceptable current ripple (Δi_L) passing through it from (5.2):

$$\Delta i_L = \frac{D_{boost} V_{PV}}{f_{sw(b)} L_{boost}} = \frac{D_{boost}(1 - D_{boost}) V_{dc}}{f_{sw(b)} L_{boost}} \tag{5.2}$$

where $f_{sw(b)}$ is the switching frequency of the boost converter.

5.1.2 Decoupling capacitor selection

The VSI DC-link capacitor (C_{dc}) must be properly sized to limit DC-link voltage ripple to a desired level in order to prevent over-voltage on the DC-bus and minimize the ripples' impact on grid current quality. Meanwhile, C_{dc} should be kept as small as possible since it is the main limiting factor of inverter lifetime [5.2].

As discussed in chapter three (subsection 3.3.2), C_{dc} buffers the VSI DC-link voltage ripple resulting from grid power pulsations at double the line frequency ($P_g \cos 2\omega t$). Hence, DC-link energy ripple result from grid pulsations as follows [5.14]:

$$\frac{1}{2} C_{dc}(V_{dcmax}^2 - V_{dcmin}^2) = \int_{\frac{-T}{4}}^{\frac{T}{4}} P_g \cos 2\omega t \, dt \tag{5.3}$$

where V_{dcmax} and $V_{dcmin}$are the maximum and minimum values around the average DC-link voltage respectively, P_g is the average active power injected into the grid, and ω is the line angular frequency in rad/s. After manipulation, (5.4) results:

$$\therefore \frac{1}{2} C_{dc}(V_{dcmax} + V_{dcmin})(V_{dcmax} - V_{dcmin}) = \frac{P_g}{2\omega} \int_{\frac{-2\pi}{4}}^{\frac{2\pi}{4}} \cos 2\omega t \, d(2\omega t) \tag{5.4}$$

$$\therefore \; C_{dc} V_{dc} \Delta v_{dcp-p} = \frac{P_g}{2\omega} \int_{-\frac{\pi}{2}}^{\frac{\pi}{2}} \cos 2\omega t \, d(2\omega t) \tag{5.5}$$

where $\Delta v_{dcp\text{-}p}$ is the peak to peak DC voltage ripple. Let $2\omega t = \theta$

$$\therefore \; C_{dc} V_{dc} \Delta v_{dcp-p} = \frac{P_g}{2\omega} \int_{\frac{-\pi}{2}}^{\frac{\pi}{2}} \cos\theta \, d\theta \tag{5.6}$$

Hence, the DC-link capacitor that limits DC-voltage ripple to a desired value can be calculated by solving the integration of (5.6) which results in (5.7) [5.14, 5.15],

$$C_{dc} = \frac{P_g}{\omega V_{dc} \Delta v_{dcp-p}} = \frac{P_g}{2\omega V_{dc} \Delta v_{dc}} \tag{5.7}$$

where Δv_{dc} is the amplitude of the DC-link voltage ripple

5.1.3 Full bridge voltage source inverter (VSI)

The second stage involves a current controlled full-bridge single-phase VSI operating with sinusoidal pulse width modulation (SPWM) featuring carrier frequency of 15 kHz. The inverter output filter inductor (L_{ac}) is designed so as to limit the magnitude of the switching harmonics in grid current. For high switching frequency and near-unity power factor operation, the inverter output voltage is approximately equal to the grid voltage and the modulation index amplitude (m_a) is given by [5.16, 5.17]:

$$m_a = \frac{\hat{V}_g}{V_{dc}} \tag{5.8}$$

where $\hat{V}_g$ is the grid voltage amplitude.

For single-phase inverters, V_{dc} level is determined such that $m_a \leq 1$ so as to achieve acceptable total harmonic distortion in the grid current ($THDi$) [5.16]. Hence, L_{ac} is calculated from (5.9) as follows [5.17]:

$$\Delta I_g = \frac{V_{dc}}{2 f_{sw(i)} L_{ac}} \frac{1}{2\sqrt{3}} \sqrt{\frac{1}{2} m_a^2 - \frac{8}{3\pi} m_a^3 + \frac{3}{8} m_a^4} \tag{5.9}$$

where ΔI_g is the rms ripple component of the grid current and $f_{sw(i)}$ is the switching frequency of the inverter. ΔI_g can be calculated from (5.10) [5.17]:

$$THDi = \frac{\Delta I_g}{I_{g(1)}} \times 100 \leq THDi\ (required) \tag{5.10}$$

where $I_{g(1)}$ is the rms value of fundamental frequency component of the grid current.

Hence, for V_{dc} =400 V, $f_{sw(b)}$ =$f_{sw(i)}$ =15 kHz, the system parameters are designed according to the previous equations and their values are shown in Table 5.1;

Table 5.1. Parameters of the 1.5 kW, 220V, 50Hz investigated system

$\boldsymbol{L_{boost}}$	4 mH, for Δi_L=1.64 A
$\boldsymbol{m_a}$	0.778, for V_{dc}=400 V
$\boldsymbol{C_{dc}}$	300 µF, for Δv_{dc}= ±4.5%
$\boldsymbol{L_{ac}}$	4 mH, for $THDi$=4%

5.1.4 Applied Pulse Width Modulation Scheme

The VSI produces modulated AC output voltage from a constant or controlled DC voltage source by generating the appropriate gating signals for the inverter switches via a pulse width modulation (PWM) technique. Several PWM techniques can be applied for three-phase VSIs such as; sinusoidal PWM, triple harmonic injection into modulating waveform, space-vector modulation, and selective harmonic elimination [5.16, 5.18]. Techniques involving triplen injection are not applicable to single phase systems.

For single-phase full bridge VSIs, the modulating technique should ensure that either the top or the bottom switch of each leg is on at any instant, in order to avoid short circuits across the dc bus. Bipolar and unipolar SPWM techniques are widely used [5.16]. The former allows the AC output voltage waveform to feature only two values, which are the input voltage and its negative value. On the other hand, the unipolar technique forces the AC output voltage waveform to instantaneously take one of three values; the input voltage, its negative value and zero. Although both techniques produce sinusoidal AC voltage, the unipolar modulating technique has the advantage of eliminating even harmonics from its output voltage. Hence, smaller filtering components are required and high-quality voltage and current waveforms are obtained when using this technique for modulating VSIs than when applying the bipolar approach for similar switching frequency [5.16].

For its mentioned merits, unipolar SPWM technique is applied for the considered VSI in this work. Figure 5.2 shows the carrier and the references waveforms, along with the switching patterns for one reference period (0.02 s). The reference with the solid straight line is responsible for the switches of the first leg, while the dashed line reference is responsible for the other leg switches and is shifted by 180◦. Each of the ten regions, shown in Figure 5.2, represents one carrier frequency period (0.002 s). Table 5.2 shows the switch combination for each of the ten regions. When switches (S_1, S_4) are on, positive output voltage occurs while negative voltage is produced for simultaneous on-state S_2, and S_3 switches. Finally, when either the inverter top switches or the bottom switches are both on, a short-circuit occurs at the VSI output resulting in zero output voltage.

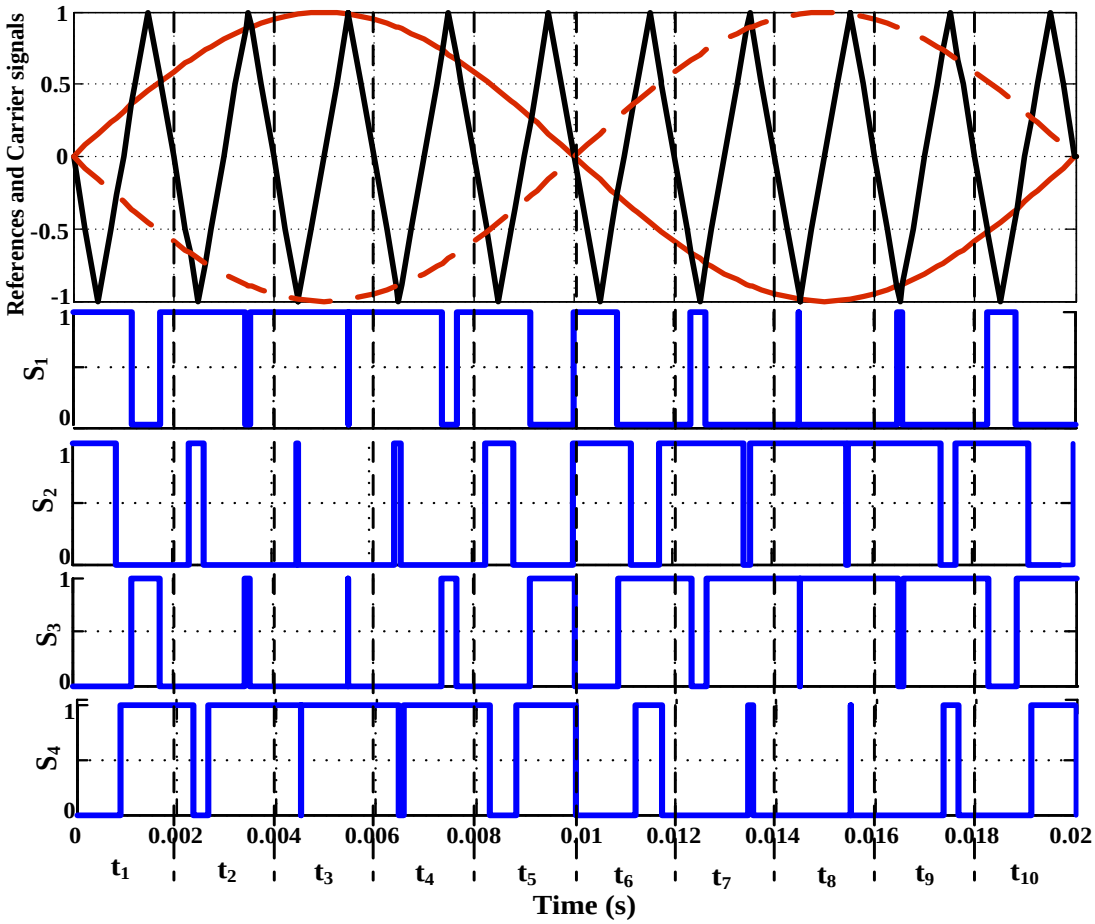

Figure 5.2. Applied VSI PWM scheme and switching sequence for one fundamental frequency cycle.

Table 5.2: VSI switching combination sequence

Region	Combination Sequence
t_1	(S_1-S_2) (S_1-S_4) (S_3-S_4) (S_1-S_4)
t_2	(S_1-S_2) (S_1-S_4) (S_3-S_4) (S_1-S_4)
t_3	(S_1-S_2) (S_1-S_4) (S_3-S_4) (S_1-S_4)
t_4	(S_1-S_2) (S_1-S_4) (S_3-S_4) (S_1-S_4)
t_5	(S_1-S_2) (S_1-S_4) (S_3-S_4)
t_6	(S_1-S_2) (S_2-S_3) (S_3-S_4) (S_2-S_3)
t_7	(S_1-S_2) (S_2-S_3) (S_3-S_4) (S_2-S_3)
t_8	(S_1-S_2) (S_2-S_3) (S_3-S_4) (S_2-S_3)
t_9	(S_1-S_2) (S_2-S_3) (S_3-S_4) (S_2-S_3)
t_{10}	(S_1-S_2) (S_2-S_3) (S_3-S_4)

5.2 Power Balance at VSI DC-Link

Neglecting AC inductor losses, equation (5.11) represents the power balance at the VSI DC-link [5.14, 5.19 and 5.20], as illustrated in Figure 5.3.

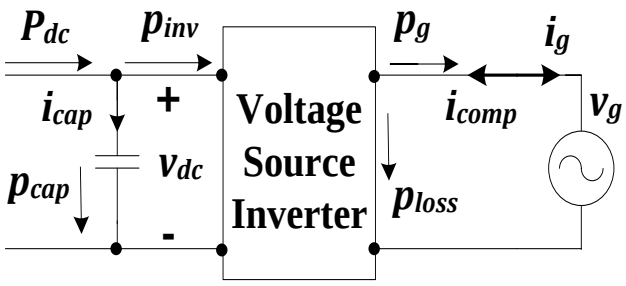

Figure 5.3. Power flow at the DC and AC sides of the PV VSI.

$$P_{dc} = p_{inv} + p_{cap} \tag{5.11}$$

where

P_{dc} is input power to the DC-link,

p_{inv} is instantaneous power supplied to inverter, and

p_{cap} is instantaneous power in the DC capacitor.

$$p_{cap} = v_{dc} C_{dc} \frac{dv_{dc}}{dt} \tag{5.12}$$

where v_{dc} is the instantaneous values of the DC-link voltage.

Assuming the AC line current (i_g) is sinusoidal and in-phase with the AC grid voltage (v_g), equation (5.13) results for a lossless inverter.

$$p_{inv} = p_g = P_g(1 - \cos(2\omega t)) \tag{5.13}$$

Thus, by substituting (5.12) and (5.13) in (5.11), equation (5.14) results:

$$P_{dc} = P_g(1 - \cos(2\omega t)) + v_{dc} C_{dc} \frac{dv_{dc}}{dt} \tag{5.14}$$

From equation (5.14), the DC-link capacitor should instantaneously buffer grid power ripple of twice the AC mains frequency, in order to minimise DC-link voltage ripple [5.21]. However, (5.14) does not account for converter losses ($p_{conv\text{-}loss}$) which include turn-on, turn-off and conduction losses of converter switches as well as losses in the DC capacitor equivalent series resistance [5.22]. These introduce error into the power balance equation that results in a steady-state error in the DC-link voltage. Thus, they must be taken into account as follows [5.19]:

$$P_{dc} = P_g(1 - cos(2\omega t)) + C_{dc} v_{dc} \frac{dv_{dc}}{dt} + p_{conv-loss} \tag{5.15}$$

In order to satisfy the power balance equation at the inverter DC-link, the DC-link voltage should be kept constant at a certain predetermined level to guarantee power flow from the PV source to the utility. Hence, a control strategy is mandatory to achieve DC-link voltage regulation and PV-grid interface.

5.3 Control Techniques for grid–connected PV Converters

PV-grid interface is commonly achieved, for the considered system, using conventional DC-link voltage sensored control technique [5.14, 5.23, and 5.24]. However, in this thesis, a DC-link voltage sensorless technique is proposed to realize this interface. It depends on the fact that if the entire PV maximum power is forced to flow to the grid, then power balance at the inverter DC-link will be satisfied and the DC-link voltage will stabilize by nature without the need of outer DC-link voltage control loop. Control schemes of both techniques are modelled, analyzed and their performance is compared to validate the proposed scheme effectiveness.

5.3.1 Conventional Control Technique

The conventional control scheme is shown in Figure 5.4. Boost chopper switching is directly controlled using the modified variable step-size Inc.Cond. MPPT technique, presented in chapter four. Hence, PV maximum power is efficiently extracted at variable conditions. On the other hand, DC-link voltage regulation as well as grid coupling are achieved using current controlled VSI that inhibits two control loops; the outer DC-link voltage control loop and the inner grid current control loop.

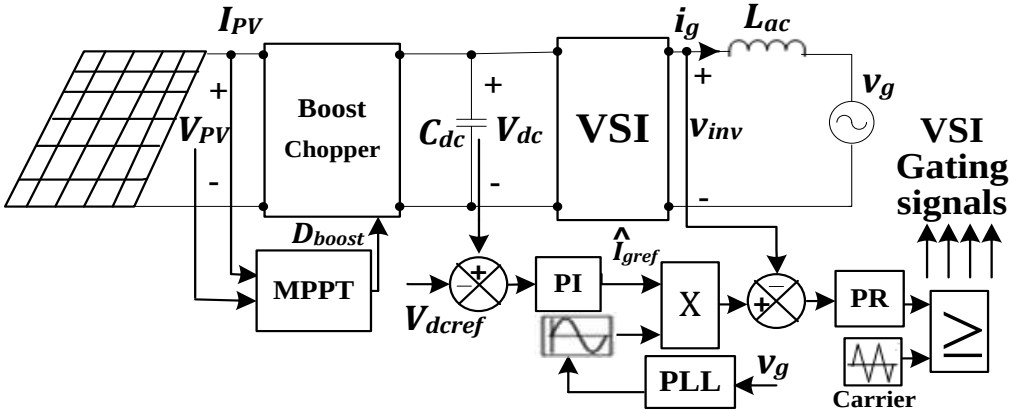

Figure 5.4. Conventional technique control scheme.

i. Inner grid current control loop

To achieve PV-grid interface, the inverter is required to output a sinusoidal grid current with acceptable THD and near-unity power factor. Thus, the output of the DC-link voltage controller, which represents the reference grid current amplitude, is multiplied by a sinusoidal unit vector which is obtained from a phase-locked loop (PLL) synchronized with the grid voltage. Then, the inner current loop controller forces the grid current to match this sinusoidal reference. The block diagram of the inner grid current control loop is shown in Figure 5.5 (a).

The most common types of controllers used for the inner current control loop are; proportional-integral (PI) with feed forward and proportional-resonant (PR) controllers [5.25-30]. However, PR controllers' performance outweighs that of the traditional PI ones, when regulating sinusoidal signals [5.25, 5.26, 5.28 and 5.30]. The former have the ability to remove the current's magnitude and phase angle steady-state errors without the need of voltage feed forward unlike traditional PI controllers. Thus, an ideal PR controller is applied for the inner grid current control loop with a gain given as [5.27-29];

$$G_{PR}(s) = K_{P-r} + K_{I-r}\frac{s}{s^2 + {\omega_r}^2} \tag{5.16}$$

where K_{P-r} is proportional part gain, K_{I-r} is the resonant part gain and ω_r is the resonant frequency of the controller. The desired sinusoidal signal's frequency is chosen as the resonance frequency, which is the grid line angular frequency in this case.

The PR controller gains are designed achieving high gain (almost 50 dB) at a bandwidth (of about 4 rad/s) around the resonant frequency as shown in the Bode plots in Figure 5.5 (b), which minimizes the sensitivity of the controller to slight grid frequency variations. However, it should be remarked that if severe grid frequency variations are registered in the utility network, non-ideal PR controllers [5.31, 5.32] or damped resonant controllers [5.33, 5.34] can be used to give a wider bandwidth around the resonant frequency.

The converter operates at high switching frequency, so the PWM block can be represented by a simple gain [5.14, 5.23].

$$K_{PWMv} = \frac{V_{dc}}{\hat{V}_{tri}} \tag{5.17}$$

where $\hat{V}_{tri}$ is the amplitude of the triangular carrier signal

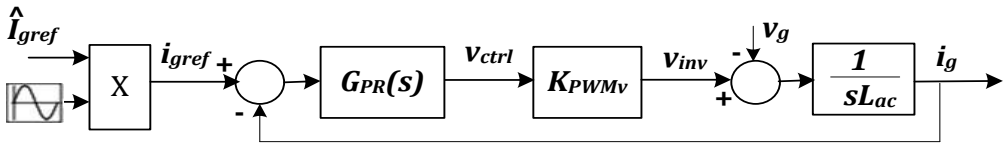

(a)

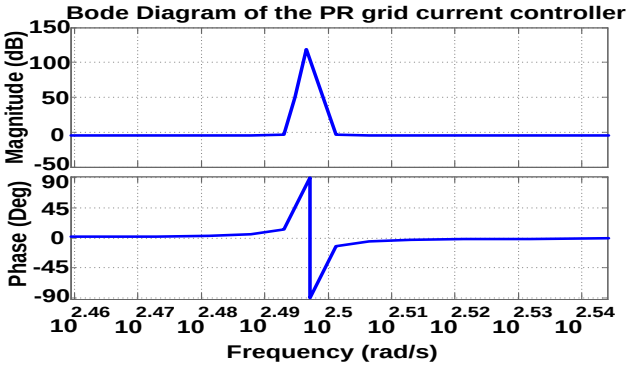

(b)

Figure 5.5. Inner grid current control loop of conventional technique (a) block diagram and (b) Bode plots of grid current loop PR controller.

ii. Outer DC-link voltage control loop

This loop is responsible for DC-link voltage regulation by adjusting $\hat{I}_{gref}$ which is the amplitude of the sinusoidal reference grid current that must be in-phase with the grid voltage (v_g). The amplitude ($\hat{I}_{gref}$) represents the active component of the reference grid current which indicates the instantaneous amount of power available at the DC side of the inverter (p_{inv}) [5.19]. By accurately adjusting this current amplitude and using a fast grid current controller, the power at the inverter DC side is transferred to grid. Thus, power balance at the DC-link is achieved which makes V_{dc} stabilizes at the required level. However, in order to compensate for system losses given in (5.15) (that is, inverter losses and energy required by C_{dc} to keep V_{dc} at a certain level), grid power decreases that is, a decrease in $\hat{I}_{gref}$occurs.

The block diagram of the outer DC-link voltage control loop is shown in Figure 5.6 (a). The implemented voltage controller can be a simple proportional controller [5.23] or a proportional-integral (PI) one [5.14] to minimize the DC-link voltage steady-state error. The latter is used and it is represented by the gain $G_{PI}(S)$ where K_{P-i} and K_{I-i} are proportional and integral gains of the DC-link voltage PI controller respectively:

$$G_{PI}(s) = K_{P-i} + \frac{K_{I-i}}{s} \tag{5.18}$$

Basically, K_{P-i} determines the dynamics of the system in terms of bandwidth, phase and gain margin while K_{I-i} eliminates the steady-state error. These gains must be precisely designed for a low cross-over frequency (10-20 Hz) in order to attenuate the magnitude of the double line-frequency DC voltage ripple. Thus, oscillations in grid current reference are limited. Otherwise, grid current THD may exceed the limit and a larger DC capacitor is required, to overcome these oscillations, which in turn reduces the inverter life-time.

To illustrate this issue, the PI gains are first designed with initial values computed from Ziegler-Nichols method followed by successive tuning aiming at achieving grid current THD within IEEE Std. 519 [5.35]. Hence, the outer loop controller gains are selected as; K_{P-i}=0.01 and K_{I-i}=0.5 giving a cross-over frequency of almost 20Hz as shown in the Bode plots in Figure 5.6 (b). In this case, the system shows minimal grid current THD however at the cost of slower response during changes. If K_{P-i} is increased to 0.1 to enlarge its effect versus the integral gain and in turn fasten system response, grid current THD breaks the IEEE harmonics limits [5.35], as shown in Figure 5.6(c).

The inner grid current control loop, with a bandwidth of a few kHz and unity feedback, can be represented by a unity gain at the low frequency range considered for the voltage control loop [5.14] as shown in Figure 5.6(a). The relationship between variations in the fundamental grid current magnitude and the mean DC-link voltage can be calculated using the average power balance equation (5.19), neglecting converter losses [5.14].

$$P_{dc} = P_g + \frac{d\left[\frac{1}{2}C_{dc}V_{dc}^2\right]}{dt} \tag{5.19}$$

For simplified sensitivity analysis, when studying relationship and correlation between certain system variables, other variables of least contribution and effect, on the studied variables, can be partially eliminated [5.36]. Hence, for determining the impact of the grid current magnitude variation on the average DC-link voltage, one neglects P_{dc} [5.14].

$$\therefore \frac{d\left[\frac{1}{2}C_{dc}V_{dc}^2\right]}{dt} = -P_g \tag{5.20}$$

$$\frac{d\left[\frac{1}{2}C_{dc}V_{dc}^2\right]}{dt} = -\frac{\hat{V}_g\hat{I}_g}{2} \tag{5.21}$$

where $\hat{V}_g$is the grid voltage amplitude, $\hat{I}_g$is the injected grid current amplitude. Applying small perturbations around the operating point leads to:

$$\frac{d\left[\frac{1}{2}C_{dc}(V_{dc}+v_{dc-pert})^2\right]}{dt} = -\frac{\hat{V}_g(\hat{I}_g+\hat{\imath}_{g-pert})}{2} \tag{5.22}$$

where $v_{dc-pert}$, and $\hat{\imath}_{g-pert}$ are the small perturbations applied around the mean DC-link voltage and the grid current amplitude respectively. Neglecting steady-state values and square of small perturbations,

$$\frac{d\left[\frac{1}{2}C_{dc}2V_{dc}v_{dc-pert}\right]}{dt} = -\frac{\hat{V}_g\hat{\imath}_{g-pert}}{2} \tag{5.23}$$

Hence, (5.24) can be concluded as [5.14];

$$C_{dc}V_{dc}sV_{dc}(s) = -\frac{\hat{V}_g\hat{I}_g(s)}{2} \tag{5.24}$$

And

$$\frac{V_{dc}(s)}{\hat{I}_g(s)} = -\frac{\hat{V}_g}{2sC_{dc}V_{dc}} \tag{5.25}$$

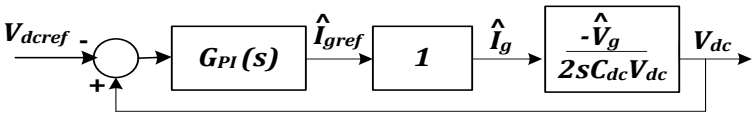

(a)

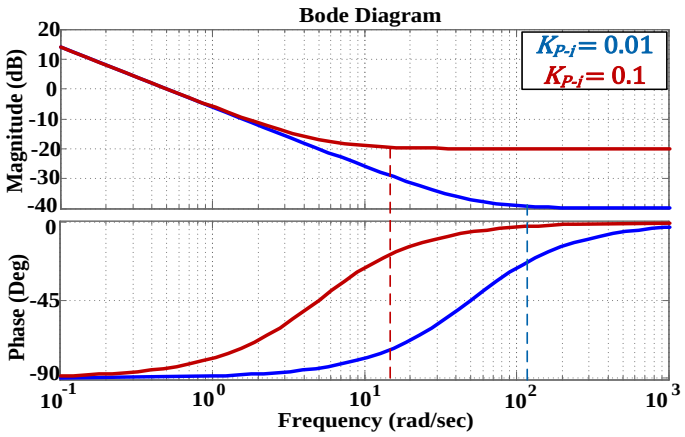

(b)

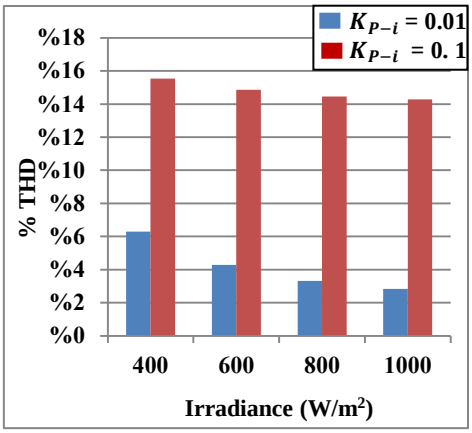

(c)

Figure 5.6. Outer DC-link voltage control loop of the conventional scheme; (a) block diagram (b) Bode plots of voltage loop PI controller, and (c) grid current THD at different irradiance levels for 2 values of (K_{P-i}) applied in the DC-link voltage PI controller.

The system, under investigation, is simulated using the conventional DC-link voltage sensored technique. The steady-state performance (regarding *THDi* and grid power losses) is presented for four V_{dc} values at different irradiance levels as shown in Figure 5.7.

For V_{dc}=300V that is, m_a>1, *THDi* increases beyond limits [5.35] while for V_{dc}= 320 V, 400V and 500V that is, m_a<1, *THDi* is within standards as shown in Figure 5.7(a). Moreover, for the same radiation (that is same P_{PV}), as V_{dc} increases, system losses increase, thus imposing more losses on grid power as shown in Figure 5.7 (b). Although the least power loss occur at V_{dc}=300 volt, this corresponds to m_a>1 resulting in *THDi* beyond the grid current's standard harmonics limitations. Therefore, for the considered system, the best compromise between utility power losses and grid current *THDi* occurs at V_{dc}=320V where $m_a \approx 1$.

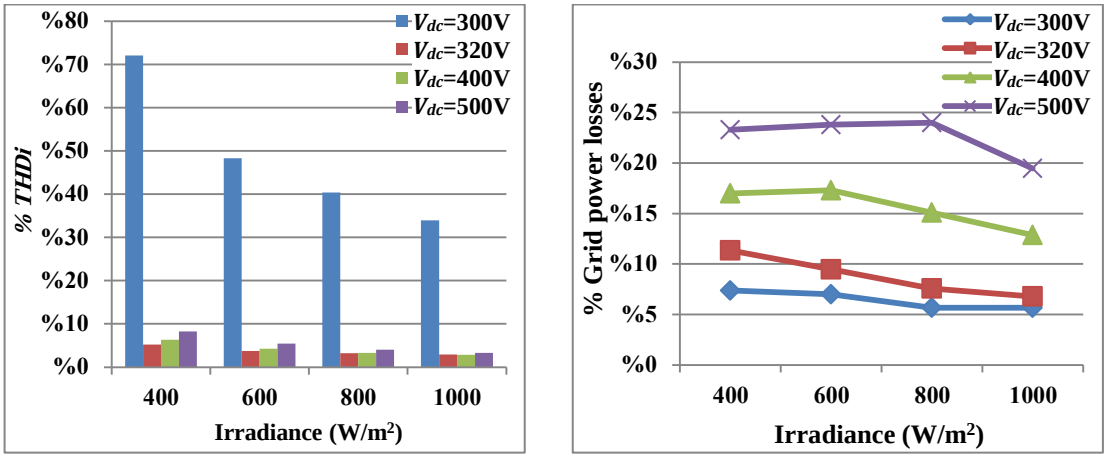

(a) (b)

Figure 5.7. Conventional control technique steady-state results at different irradiance levels for four DC-link voltage values regarding (a) grid current THD and (b) power losses imposed on grid as percentage of the relative PV power at the current irradiance level.

5.3.2 Proposed DC-link Voltage Sensorless Control Technique

In the proposed technique, MPPT is achieved, similarly as in the conventional technique, by sensing the PV voltage and current to be utilized by the modified variable-step incremental conductance algorithm which directly controls the boost converter switching. However, the proposed technique involves only one control loop in the second inverter stage which is the grid current control loop, thus mitigating the inverter outer DC-link voltage control loop with its PI controller which in turn simplifies the overall control scheme. Moreover, the high DC-link voltage sensor is no longer required, reducing the system footprint and cost. The proposed control scheme is shown in Figure 5.8.

The reference grid current amplitude ($\hat{I}_{gref}$) must be properly adjusted to transfer the inverter power to the grid. Thus, power balance at the DC-link is achieved and V_{dc} stabilizes at the required level. In the conventional technique, DC-link voltage regulation

and $\hat{I}_{gref}$ adjustment are achieved using the DC-link voltage controller as explained in the previous subsection. Alternatively, in the proposed method, the DC-link voltage is stabilized and $\hat{I}_{gref}$ is adjusted without the need of an outer DC-link voltage control loop.

In the proposed control technique, the PV voltage and current are sensed to achieve MPPT. Depending on the tracked maximum PV power, the amplitude of the reference grid current is adjusted. The grid current controller forces the inverter to produce a sinusoidal current with a magnitude matching that of the reference current which corresponds to the tracked maximum PV power. Thus, PV maximum power is forced to flow to the inverter AC side satisfying the power balance at the inverter DC-link hence forcing the DC-link voltage to stabilize by nature at a certain level without the need of a voltage controller.

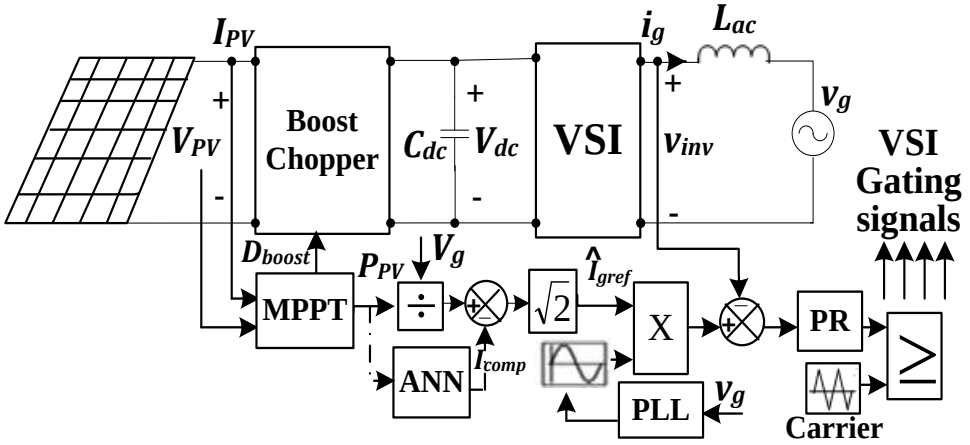

Figure 5.8. Control scheme of the proposed DC-link voltage sensorless technique.

i. Without system losses compensation

The proposed control technique, when adjusting$\hat{I}_{gref}$, must guarantee that the tracked PV maximum power is transferred to the grid so that power balance is achieved at inverter DC-link and V_{dc} stabilizes by nature without the need of DC-link voltage controller. Hence, $\hat{I}_{gref}$is determined by dividing PV maximum power at certain environmental condition (P_{PV}) by grid voltage rms value (V_g), as shown in (5.26). This amplitude is then multiplied by the sine template of the grid voltage derived from PLL. The grid current PR controller, similar to the one implemented in the conventional control technique (with the same gains), forces the inverter to produce a sinusoidal grid current that matches this reference. The uncompensated grid current control loop is shown in Figure 5.9 (a).

$$\hat{I}_{gref}(uncomp) = \sqrt{2}\frac{P_{PV}}{V_g} \tag{5.26}$$

However, this uncompensated scheme doesn't take into account system losses which include converters losses and the energy required by C_{dc} to keep V_{dc} at a predetermined level that ensures that $m_a \leq 1$. Thus, a disturbance in the power balance at DC-link occurs and the DC-link voltage is expected to reach a value less than the grid voltage amplitude ($\hat{V}_g$) which means that the modulation index (m_a) is more than 1, imposing harmonics in the grid current beyond acceptable limits as will be demonstrated at this subsection end

ii. With system losses compensation

System losses must be taken into account to guarantee power balance at inverter DC-link. However, due to the absence of DC-link voltage control loop in the proposed technique, there must be an alternative way to compensate for these losses. Since these losses decrease the active grid power, then the grid current in turn decreases. Thus, $\hat{I}_{gref}$ must be readjusted by a compensating component as shown in (5.27):

$$\hat{I}_{gref}(comp) = \sqrt{2}\left(\frac{P_{PV}}{V_g} - I_{comp}\right) \tag{5.27}$$

where I_{comp} is the rms value of the compensating current (i_{comp}).

This current represents the decrease in grid current amplitude, and in turn the decrease in grid active power to compensate for system losses. Thus, power balance is ensured, achieving DC-link voltage stabilization. According to I_{comp} value, V_{dc} can be kept at a level that ensures that $m_a \leq 1$ which results in acceptable grid current THD. The proposed compensated grid current control loop is shown in Figure 5.9 (b).

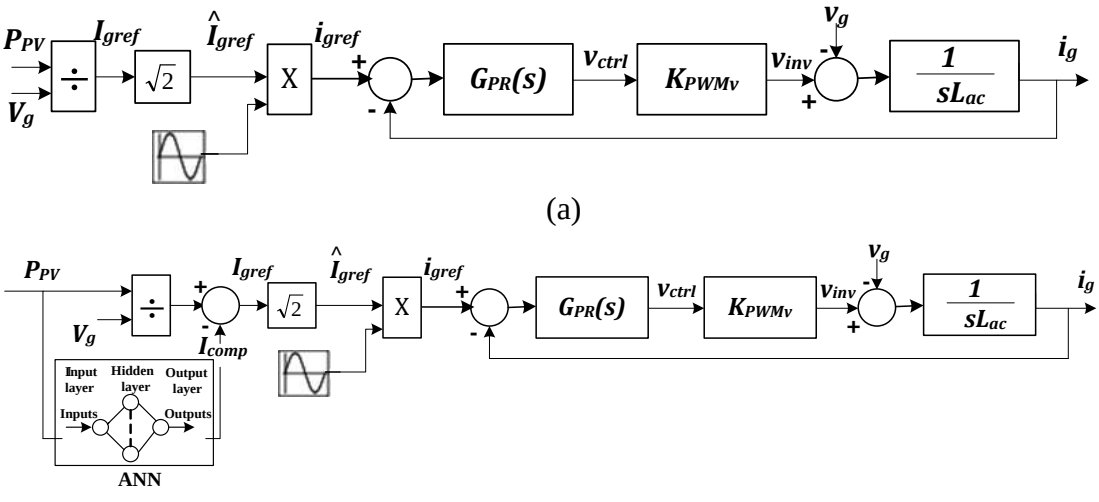

Figure 5.9. Block diagram of (a) uncompensated grid current control loop and (b) compensated grid current control loop; employed for the proposed sensorless technique.

At certain V_{dc}, as P_{PV} increases, system losses increase which in turn requires the increase of I_{comp} to compensate for these losses. Thus, for constant V_{dc}, I_{comp} depends on P_{PV} and varies proportionally with it however in a non-linear form. Moreover, as V_{dc} increases, for constant P_{PV}, system losses again increase which results in an increase in I_{comp}. Figure 5.10 shows the non-linear relation between P_{PV} and I_{comp} at two different V_{dc} values for the investigated system. It can be noticed that at V_{dc}=320V (that is, m_a≈1), I_{comp} has lower value which decreases system losses imposed on grid.

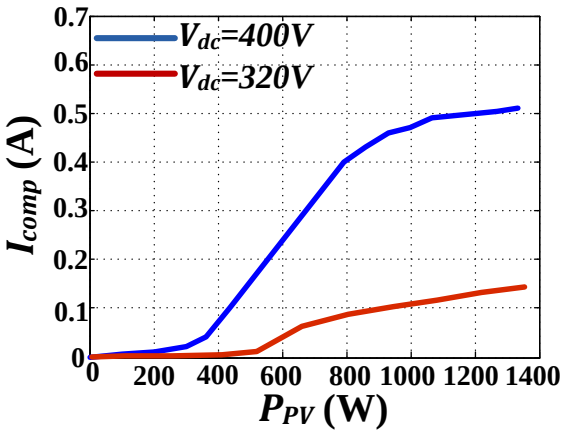

Figure 5.10. P_{PV} -I_{comp} mapping for V_{dc} of 320V and 400V.

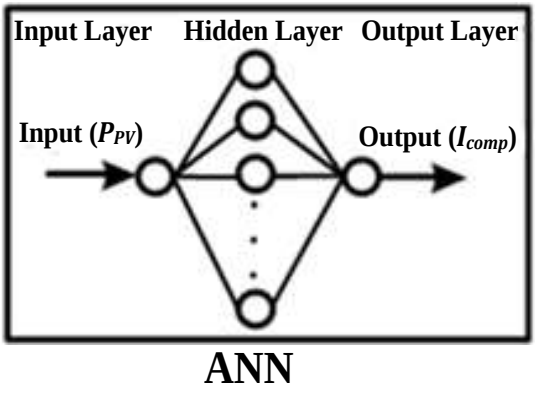

Figure 5.11. Configuration of the proposed ANN for P_{PV} -I_{comp} mapping implementation.

Hence, mapping between P_{PV} and I_{comp}, at a predetermined V_{dc} level, is system-dependent and mandatory in order to achieve the proposed DC-link voltage sensorless scheme. The P_{PV}-I_{comp} mapping can be implemented using a simple look-up table as shown in Appendix D.2.2.

However, for more precise mapping and better system performance, a simple feed-forward back-propagation artificial neural network (ANN) is proposed featuring an input layer, a hidden layer and an output layer as shown in Figure 5.11. The input represents the

PV power while the output layer gives the corresponding compensating current required to stabilize V_{dc} at a predetermined level. The applied hidden layer features 10 sigmoid neurons. The links between the nodes are all weighted. Successful fitting between P_{PV} and I_{comp} depends on the hidden layer and how well the ANN is trained to optimize these weights [5.37]. The utilized ANN is off-line trained and optimized to give almost zero mean square error for the studied case.

The system, under investigation, is simulated using the proposed DC-link voltage sensorless technique. Steady-state results (regarding grid current THD and grid power losses) are presented at variable irradiance levels, for the uncompensated scheme as well as the compensated scheme for two DC-link voltage levels, as shown in Figure 5.12.

Regarding the uncompensated scheme, since system losses compensation is not taken into account, V_{dc} will reach about 305V which is less than $\hat{V}_g$ (311V) as explained before. Although, this will decrease the grid average power losses due to V_{dc} decrease, harmonics level in the grid current will exceed the permitted level according to IEEE Std. 519 as $m_a > 1$. Considering the compensated scheme, the system performance is almost similar to that acquired by the conventional DC-link voltage sensored technique regarding the *THDi* and grid power losses for the same operating conditions. Consequently, for the proposed technique with the compensated scheme, the best compromise between the *THDi* and utility power losses occurs at V_{dc}=320V same as for the conventional scheme. This proves the validity and feasibility of the proposed DC-link sensorless technique with the proposed system losses compensation scheme.

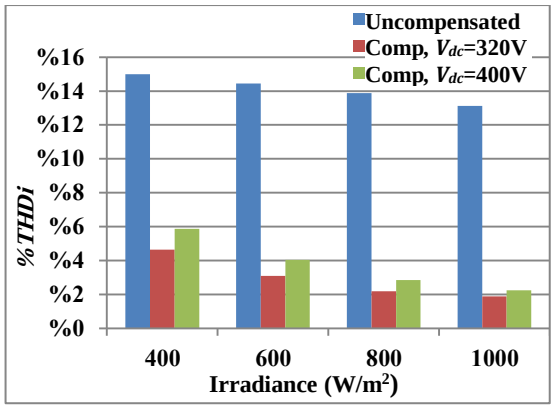

(a)

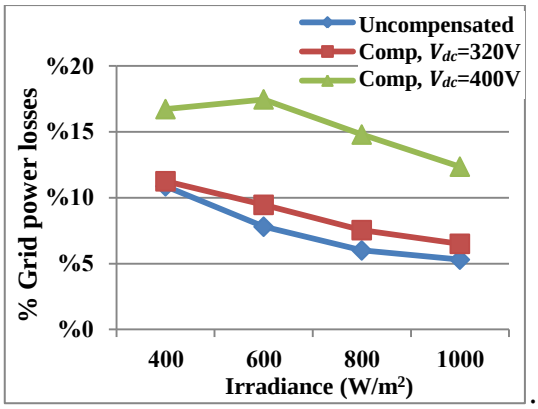

(b)

Figure 5.12. Proposed technique steady-state results at different irradiance levels for uncompensated and compensated schemes at DC-link voltage of 320V and 400V regarding (a) *THDi* and (b) grid power losses as percentage of the relative PV power at the current irradiance level.

5.4 Simulation Results Analysis

Regarding the two control techniques' performance at different values of DC-link voltage, it's concluded that at a certain DC-link voltage value (V_{dc}=320V), the best compromise between utility power losses and grid current THD is achieved. Hence, the investigated system, presented in section 5.1, is simulated for both techniques using MATLAB/Simulink at V_{dc}=320V.

In this work, the transient and steady-state performance of the conventional scheme is compared to that of the proposed one, under two step changes in irradiance; from 1000 W/m^2 to 600 W/m^2 at 6s then from 600 W/m^2 to 800 W/m^2 at 9s. Performance parameters regarding simulation results are given in Table 5.3. Figure 5.13 parts (a) and (b) show that both techniques succeed to extract the maximum PV power at various irradiance levels. Moreover, both schemes are capable of adjusting the DC-link voltage at 320V during different irradiance levels as shown in Figure 5.14 parts (a) and (b). However, grid powers, achieved by both schemes, experience losses as shown in Figure 5.15 parts (a) and (b), due to system losses compensation. Figure 5.16 parts (a) and (b) show the grid current experienced by both techniques during irradiance changes.

At start-up (Figure 5.14(c), Figure 5.15(c) and Figure 5.16(c)), V_{dc} overshoot in the conventional technique is about 1.6 times that of the proposed one, thus C_{dc} of the former must handle this voltage increase. On the other hand, V_{dc} adjustment takes longer time, in the proposed scheme, which increases transient power losses. However, once the required V_{dc} level is reached, the proposed scheme shows faster transient response during irradiance changes owing to DC-link voltage PI controller elimination.

The latter can be shown as follows; during the first step change in irradiance, at t=6s, irradiance decreases from 1000 W/m^2 to 600 W/m^2, thus P_{PV} decreases causing a transient decrease in V_{dc} till it is regulated to 320V. Analyzing Figure 5.14(d), Figure 5.15(d) and Figure 5.16(d), the conventional scheme shows slower response by about 0.3s. Furthermore, during the conventional scheme's longer transient period, V_{dc} decreases to an average value of 300V (6.3% V_{dc} undershoot) that is, m_a >1, thus *THDi* will go beyond acceptable limits (= 31.42 %). On the other hand, the proposed technique shows better response with settling time (t_s) of 0.1s and transient decrease in V_{dc} to 310 V that is, $m_a \approx 1$. Hence, its *THDi* is within limits (6.3%) during proposed scheme's transient period. During the second step change at t= 9 s, irradiance increases from 600 W/m^2 to 800 W/m^2, thus P_{PV}

increases causing transient increase in V_{dc}. Considering Figure 5.14(e), Figure 5.15(e) and Figure 5.16(e), the conventional scheme exhibits settling time of about 0.2s to reach its steady-state and experiences transient V_{dc} increase to 360 V (12.5% V_{dc} overshoot). On the contrary, during this step change, the proposed scheme shows faster response with t_s of almost 0.07s and experiences nearly non significant V_{dc} overshoot during its transient period.

Steady-state grid currents versus grid voltages for both techniques at the three considered irradiance levels are shown in Figure 5.17. It's clear that both techniques show near-unity power factor. Steady-state results, including peak-peak DC-link voltage ripple, THD and power factor of grid current, and utility power losses for both schemes, are listed in Table 5.3. Both schemes show almost the same steady-state performance which proves the proposed technique validity and effectiveness.

Table 5.3. Transient and steady-state performance parameters of the conventional and proposed schemes regarding simulation results

Irradiance (W/m^2)	**Control technique**	**Transient for V_{dc}**		**Steady-state**			
		Over/Under Shoot	***$t_{settling}$* (s)**	***Δv_{dc}(p-p)* (V)**	***Power losses* (W)**	***THDi***	***Phase shift***
Start-up at 1000	Conventional	+ 68.75 %	0.4	50	90	3%	1^o
	Proposed	+ 43.75%	4	50	90	2%	0^o
From 1000 to 600	Conventional	- 6.25%	0.4	30	75	3.8%	0.8^o
	Proposed	- 3.13%	0.1	30	75	3%	0.1^o
From 600 to 800	Conventional	+ 12.5 %	0.2	40	80	3.2%	1^o
	Proposed	+1.5%	0.07	40	80	2.2%	0^o

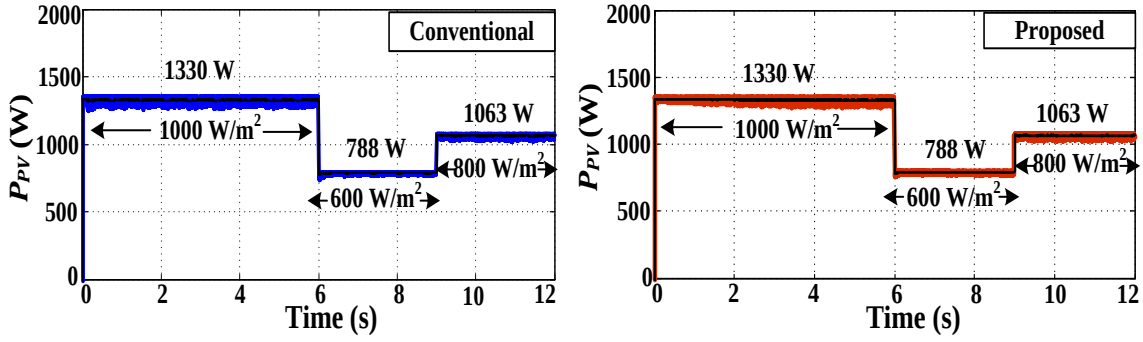

(a) (b)

Figure 5.13. PV maximum power, at the considered varying irradiance conditions, acquired by (a) conventional technique and (b) proposed technique.

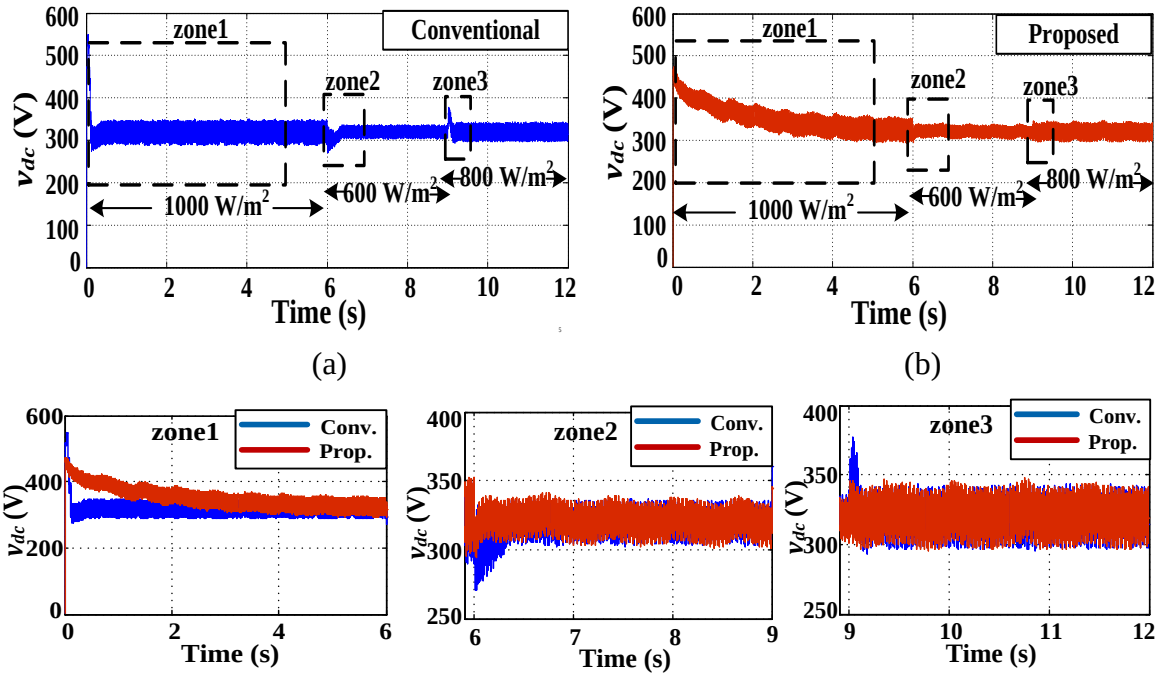

Figure 5.14. DC-link voltage, at the considered varying irradiance conditions, acquired by (a) conventional technique, (b) proposed technique, with a magnified view for each zone at (c)1000 W/m^2, (d) 600W/m^2, and (e) 800 W/m^2.

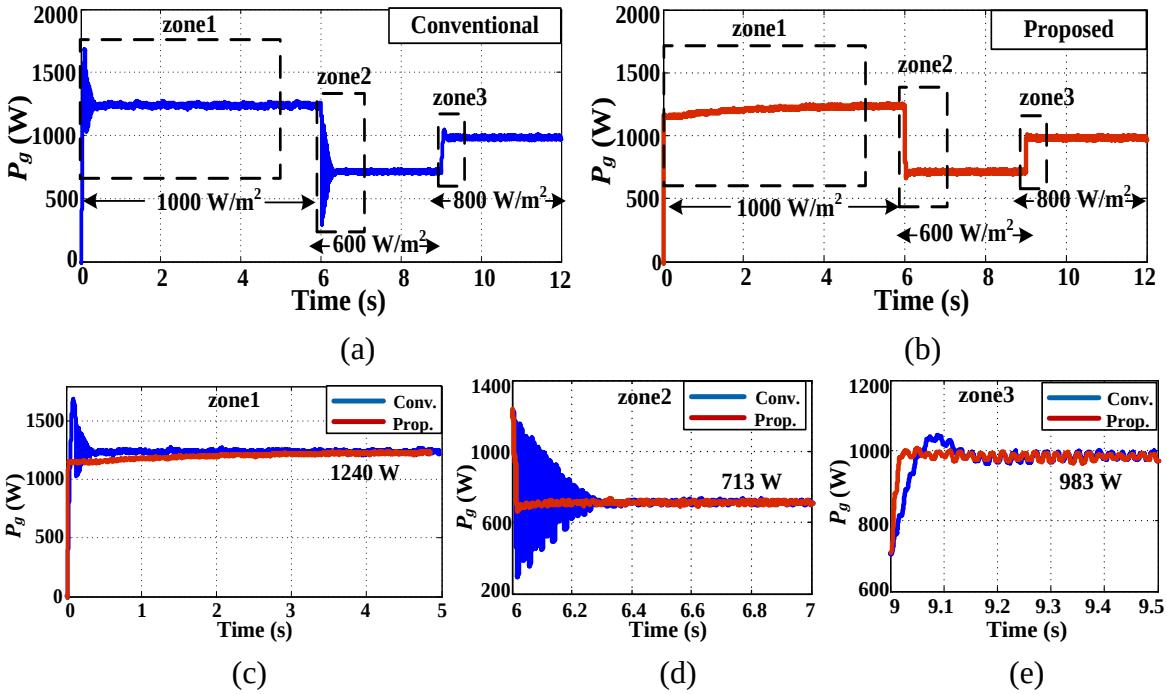

Figure 5.15. Average grid power, at the considered varying irradiance conditions, acquired by (a) conventional technique, (b) proposed technique, with a magnified view for each zone at (c) 1000 W/m^2, (d) 600W/m^2, and (e) 800 W/m^2.

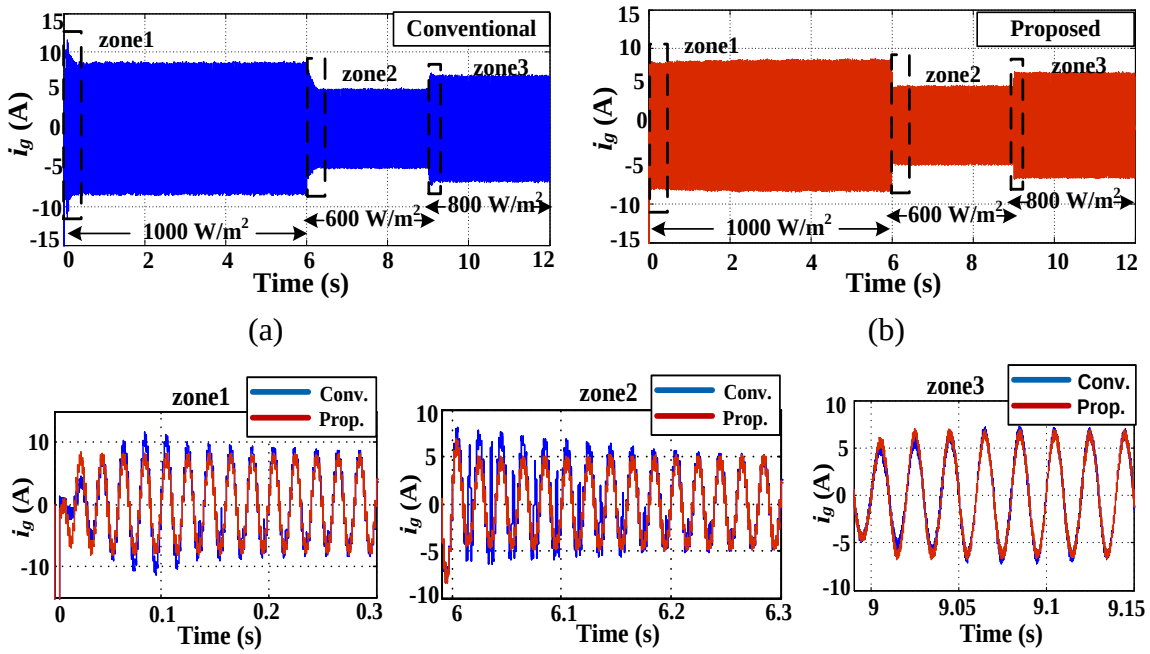

Figure 5.16. Grid current, at the considered varying irradiance conditions, acquired by (a) conventional technique, (b) proposed technique, with a magnified view for each zone at (c) operation start-up, (d) first step change, and (e) second step change.

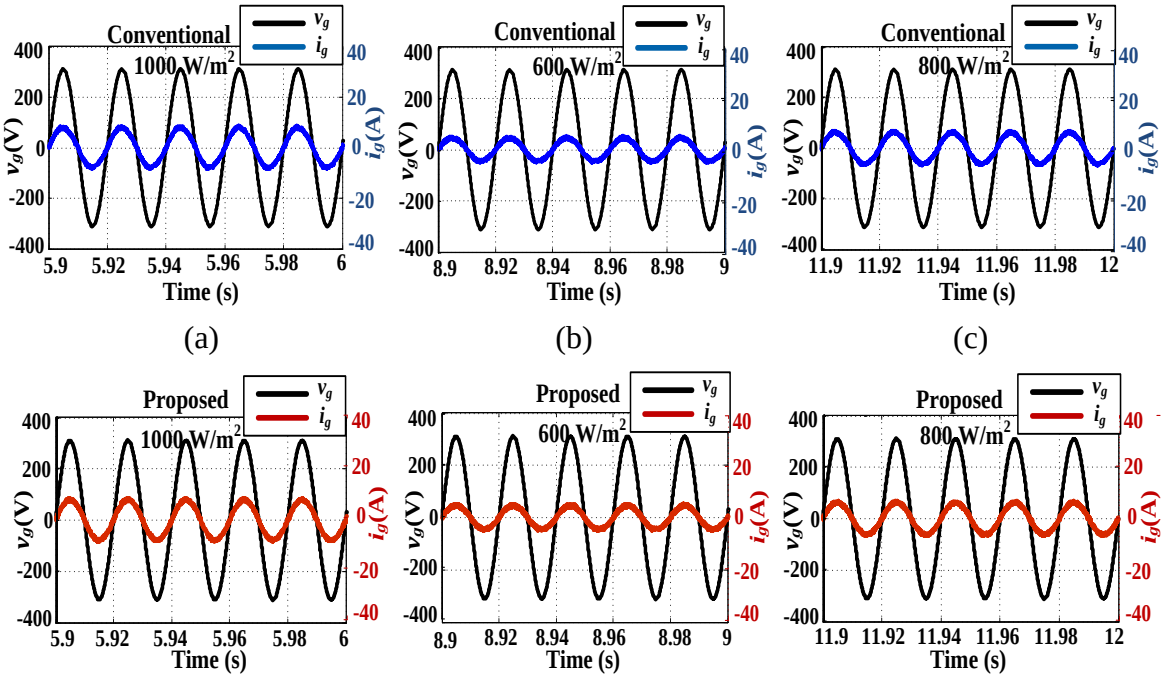

Figure 5.17. Steady-state grid current versus grid voltage for conventional technique at (a) 1000 W/m^2, (b) 600W/m^2 and (c) 800W/m^2 and for proposed technique at (d) 1000 W/m^2, (e) 600W/m^2, and (f) 800W/m^2.

In order to verify the capability of the proposed technique to perform well at different values of DC-link voltage, both techniques are readjusted to perform at V_{dc} = 400 V under the same two step changes in irradiance. Figure 5.18 shows that both scheme succeeded to stabilize the DC-link voltage at the required level yet the proposed technique shows better transient response during irradiance changes. However, as previously discussed, increasing the DC-link voltage to 400 V, yields to more losses on the grid than that acquired at V_{dc}= 320 V as shown in Figure 5.19.

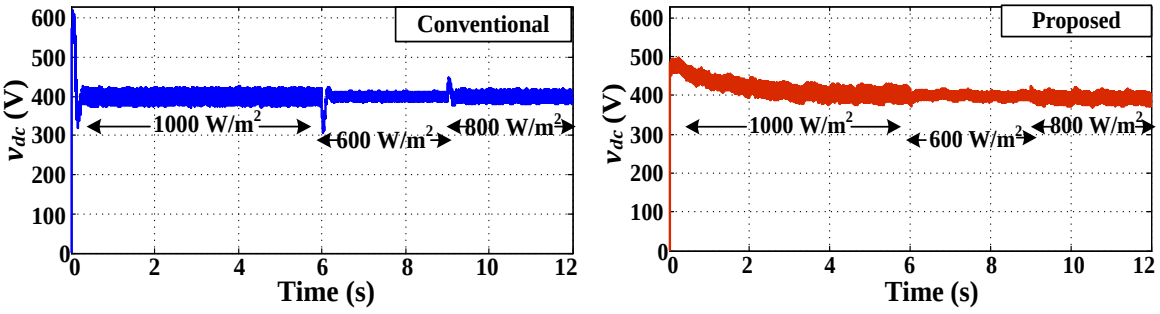

(a) (b)

Figure 5.18. DC-link voltage at three different irradiance levels acquired by (a) conventional technique and (b) proposed techniques.

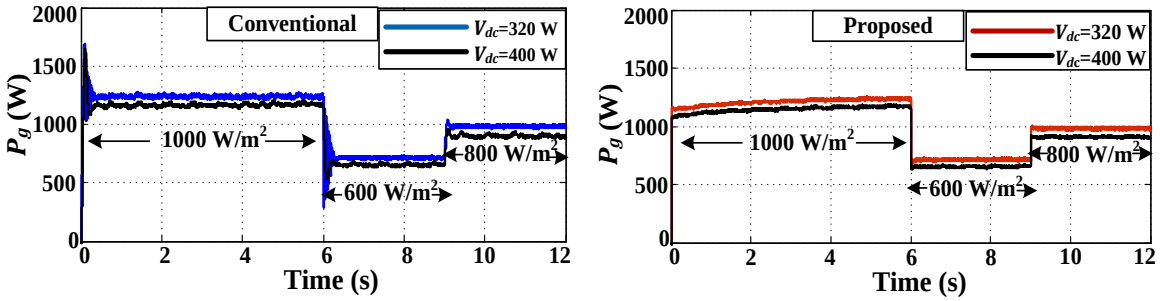

(a) (b)

Figure 5.19. Average grid power at V_{dc}=320 V and V_{dc}=400 V at variable irradiance levels for (a) conventional technique and (b) proposed technique.

5.5 Experimental Implementation

An experimental setup, for the system under investigation, is implemented in order to hold a practical comparison between the proposed sensorless technique and the conventional one. For fair comparison, it's mandatory to test these techniques under controlled environmental conditions. This ensures similar environmental conditions for both techniques when the tests are carried out. Furthermore, it enables the achievement of a step-change in environmental conditions to compare the transient performance of both techniques. However, this is inapplicable for rooftop mounted PV panels as they are unable

to reproduce similar *I-V* and *P-V* curves due to the randomly fluctuating environmental conditions. Hence, the PV emulating circuit, employed in chapter four, section 4.6, is utilized again in the experimental prototype considered in this chapter.

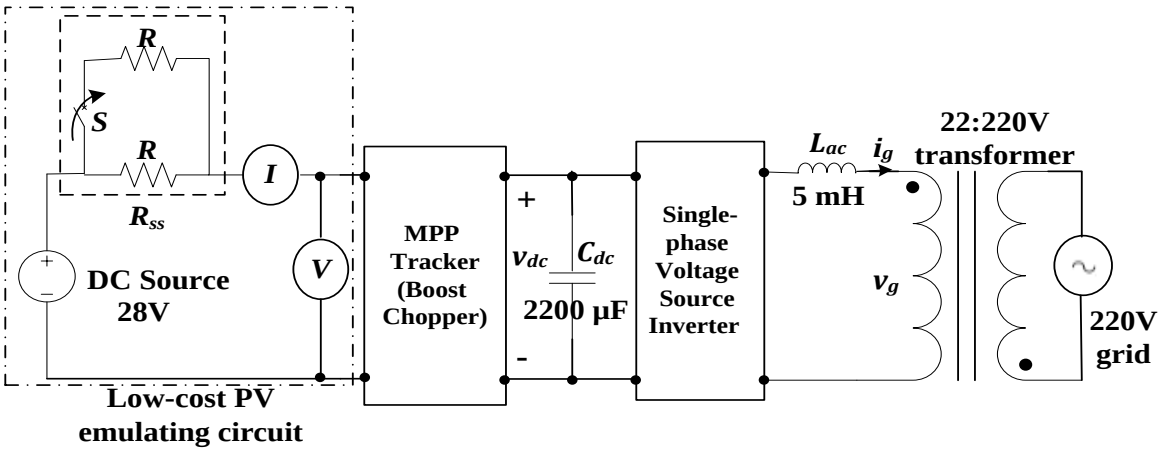

(a)

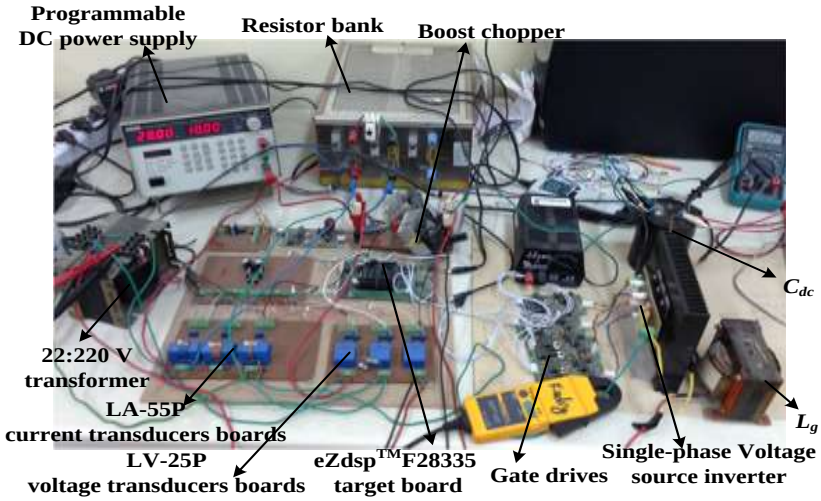

(b)

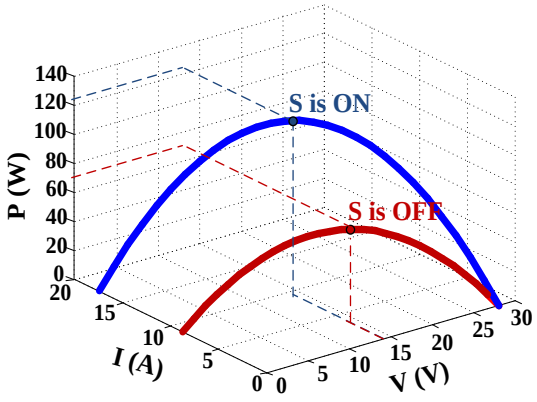

(c)

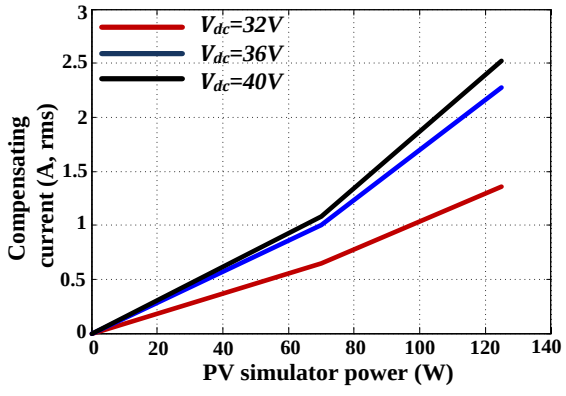

(d)

Figure 5.20. Experimental setup (a) schematic diagram, (b) test rig photography (c) *P-I-V* curves of PV simulating circuit for two different values of R_{ss}, and (d) $P_{PV\ simulator}$ - I_{comp} mapping for different V_{dc} levels.

Figure 5.20 (a) shows the schematic diagram of the experimental rig while Figure 5.20 (b) shows the implemented test rig photography. Figure 5.20 (c) demonstrates the emulating circuit *P-I-V* curves at two different conditions. Tracking of the PV simulating circuit maximum power is carried out by the first boost chopper stage which is followed by the second VSI stage to achieve coupling with the grid. Both stages have f_{sw} =15 kHz.

The maximum tracked PV power as well as the MPP voltage (V_{MPP}), achieved by the practical PV simulating circuit, are almost one tenth those achieved by the PV string presented in simulation work,. Hence, in the experimental work, the DC-link voltage will be divided by ten and a 22:220 V transformer is introduced to emulate the grid as shown in Figure 5.20 parts (a) and (b). For similar DC-link voltage ripple percentage; the experimental DC-link voltage ripple will again be one tenth its value in simulation. According to equation (5.7), this requires a large practical DC-link capacitor (ten times its value in simulation) as shown in Figure 5.20(a). This large capacitor will unfortunately cause an additional delay in the conventional technique dynamic response during changes which is already delayed due to the time lag imposed by the DC-link voltage PI controller. This will be demonstrated in the following experimental results.

In order to compare between the performances of both techniques, the DC-link voltage must be adjusted at the same level in both cases. Thus, the techniques' responses, at three different levels of V_{dc} (32V, 36V and 40V), are analyzed to settle on the most convenient V_{dc} value to work at. The latter is done at two power levels; low power level ($P_{PV\text{-}simulator}$ =70 W) and high power level ($P_{PV\text{-}simulator}$=126 W). The system is working first at the low power level then a step-change to the high power level occurs. This is followed by a second step-change to the low power level again. Figure 5.20 (d) shows the mapping between the PV simulator power and compensating current for the three considered V_{dc} levels. This pattern is used by the sensorless technique in order to determine the reference grid current amplitude as shown in Appendix D.2.2 where the experimentally implemented algorithms of the conventional and proposed techniques are presented.

Figure 5.21 shows the DC-link voltage adjusted by both schemes at the three considered levels. Although both techniques can successfully adjust V_{dc} at the required level, the conventional technique shows slower response.

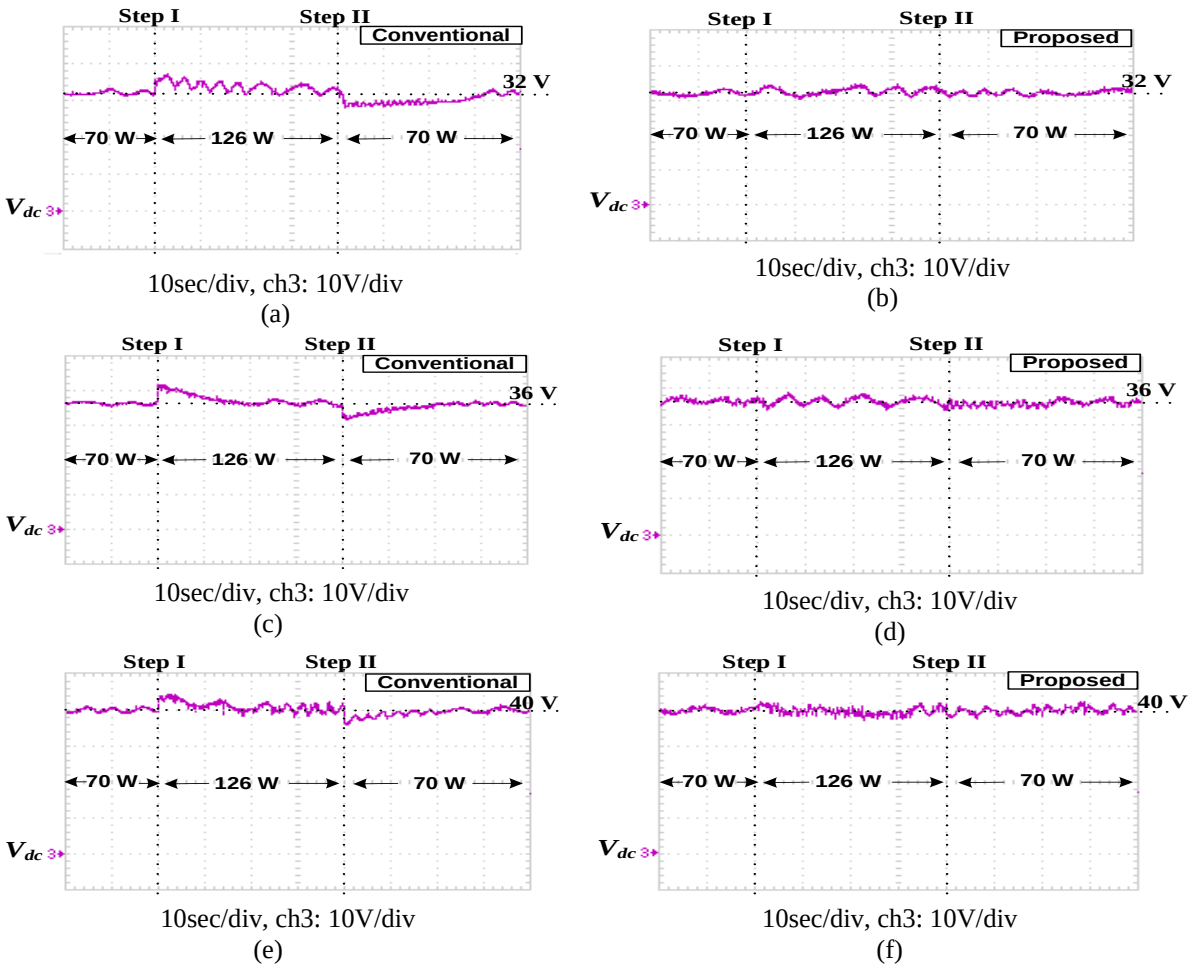

Figure 5.21. DC-link voltage at three different levels adjusted by (a), (c), (e) conventional technique and (b), (d), (f) proposed sensorless technique.

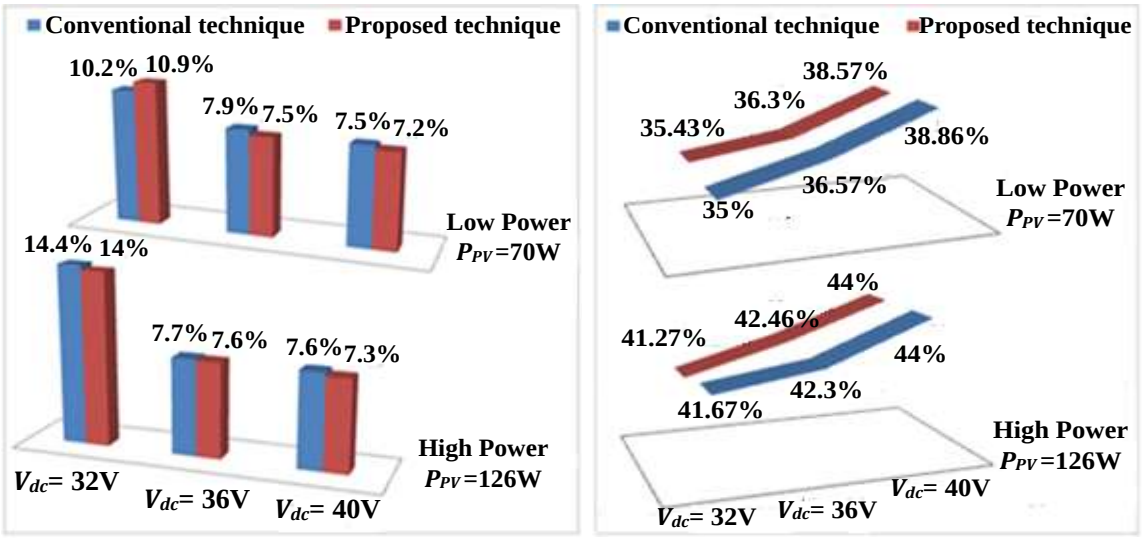

Figure 5.22. Comparison between conventional and proposed scheme regarding (a) THD of grid current and (b) system power losses as percentage of the current PV power level.

FFT analysis is applied to compare the steady-state *THDi* of both techniques at the two considered power levels as shown in Figure 5.22(a). Furthermore, grid power losses are calculated at both power levels for different values of V_{dc} when applying both schemes as shown in Figure 5.22(b). Considering these two figures, it can be concluded that both techniques give almost similar steady-state results at a certain V_{dc} level. However, increasing the DC-link voltage improves *THDi* yet imposes more losses on the utility. Hence, the most appropriate DC voltage to work at is V_{dc}=36 V as it compromises between grid current power quality and power losses imposed on grid.

Both techniques' practical results are presented and analyzed at V_{dc}=36 V and under the two step-changes in the input power from the PV emulator (first from 70W to 126W, then from 126W to 70W). Figure 5.23 zooms into the DC-link voltage adjusted by both techniques at 36 V at both step-changes. During the first step-change, the conventional technique is slower to stabilize V_{dc} ($t_{settling}$=16s) and experiences an overshoot of about 5V (13.9%) which increases the transient grid losses. During the second step-change, similarly, the conventional scheme shows poorer transient response with settling time of about 18s and V_{dc} undershoot of almost 4V (11.11%). The latter would affect *THDi* during this transient period. On the other hand, the proposed technique shows fast transient response during both step changes.

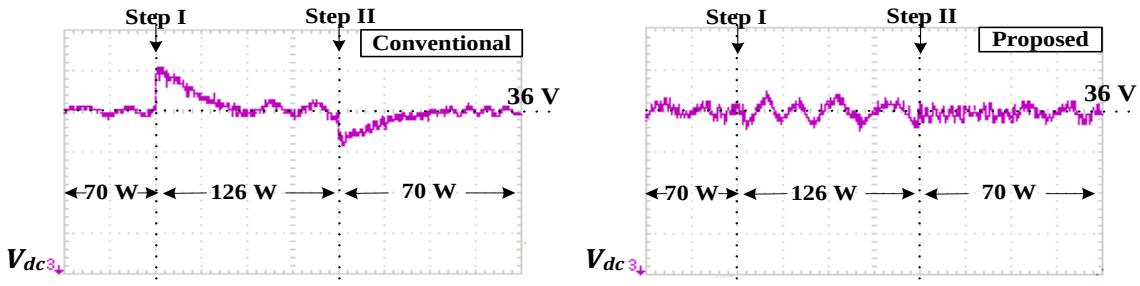

10s/div, ch3: 5V/div (a)

10s/div, ch3: 5V/div (b)

Figure 5.23. DC-link voltage response, during PV emulator power step changes, acquired by (a) conventional technique and (b) proposed technique.

For more detailed analysis to practical results, a focus, within the steady-state operation of both schemes, is presented at both power levels. In addition, a zoom into the two step changes is applied to compare between the transient performances of both techniques. This can be explained as follows;

During the two step changes, both the conventional and the proposed control techniques, are capable of extracting PV simulator maximum power at both power levels

as shown in Figure 5.24 parts (a) and (b), and Figure 5.25 parts (a) and (b). However, the conventional scheme takes much longer time to stabilize V_{dc} at 36V as demonstrated before. During the first step change (from low to high power level), the conventional scheme exhibits a V_{dc} increase to 40V (overshoot of 11.11%) as shown in Figure 5.24(c) then takes almost 16 s to stabilize V_{dc} at 36V. This causes a decrease in the grid power, during this transient period, of about 3% than its steady-state value at high power level (73W) as shown in Figure 5.24(e). This transient decrease in grid power occurs in order to compensate for energy required by C_{dc} to achieve the transient V_{dc} increase to 40V. During the second step change (from high to low power level), the conventional technique experiences V_{dc} decrease to 32 V (undershoot of 11.11%) as shown in Figure 5.24(d) and takes almost 18s to stabilize V_{dc} at 36V. This, in turn, increases the grid power, during this transient period, of about 2.5% than its steady-state value at low power level (44.4W) as shown in Figure 5.24(f). However, during this transient period, the grid current suffers from high *THDi* beyond the acceptable limits (of about 9%) due to the decrease of DC-link voltage to 32 V. On the other hand, during both step changes, the proposed technique, immediately adjusts the DC-link voltage to its required value (36V) as shown in Figure 5.25 parts(c) and (d) and sustains the grid power to its steady-state value during high power level (73W) and during low power level (44.5W) as shown in Figure 5.25 parts (e) and (f). During the second step-change, unlike the conventional technique, the proposed scheme exhibits transient grid current of 7% THD.

At steady-state, both schemes succeed in extracting PV simulator maximum power at low PV power level (70W) as shown in Figure 5.26(a) and Figure 5.27(a) and at high PV power level (126W) as shown in Figure 5.26(b) and Figure 5.27(b). Similarly, both techniques are capable of adjusting the steady-state DC-link voltage at 36 V during both power levels as shown in Figure 5.26 parts (c) and (d) and Figure 5.27 parts (c) and (d). At the grid side, the steady-state grid powers achieved by both techniques are similar during low grid power level (about 44.5W) as shown in Figure 5.26(e) and Figure 5.27(e) as well as at high grid power level (about 73W) as shown in Figure 5.26(f) and Figure 5.27(f). Finally, Figure 5.28 parts (a) and (b), and Figure 5.29 parts (a) and (b) show that both schemes achieve near-unity power factor at both power levels and that their exhibited grid power oscillates around double the line frequency (100 Hz).

	Conventional technique	Proposed Sensorless Technique
During step changes	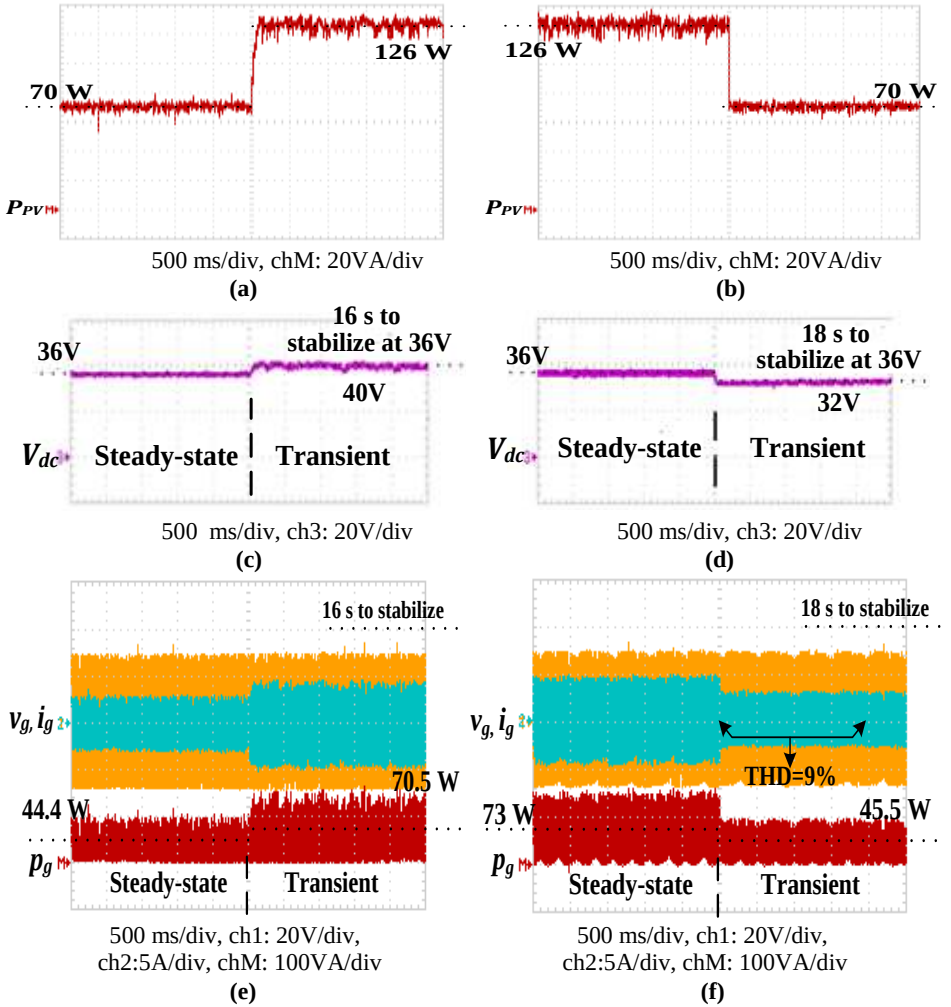	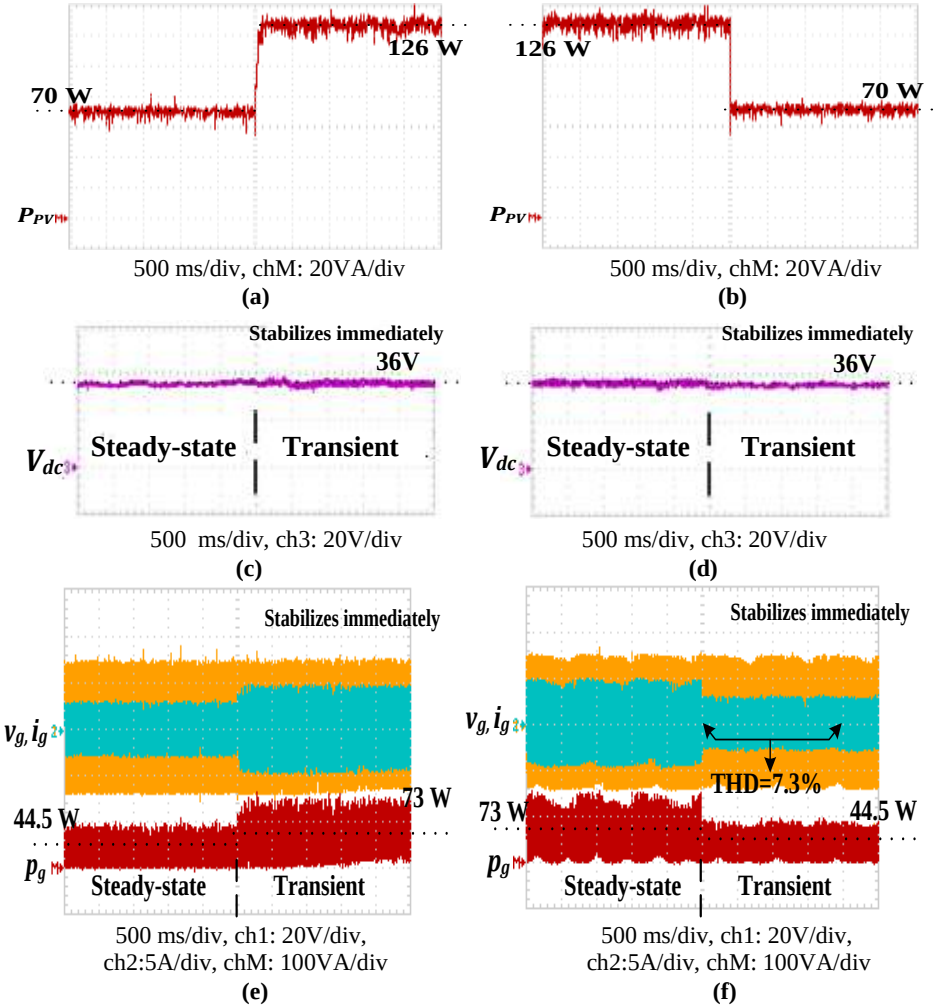

Figure 5.24. Conventional technique performance during step changes: PV power; DC-link voltage; grid voltage, current, and power at (a), (c), (e) step change I and (b), (d), (f) step change II.

Figure 5.25. Proposed technique performance during step changes: PV power; DC-link voltage; grid voltage, current, and power at (a), (c), (e) step change I and (b), (d), (f) step change II.

During Steady-state

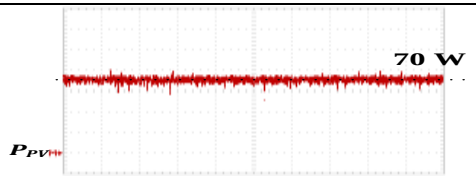

500 ms/div, chM: 20VA/div

(a)

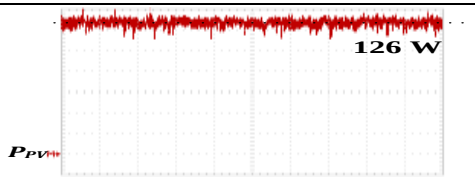

500 ms/div, chM: 20VA/div

(b)

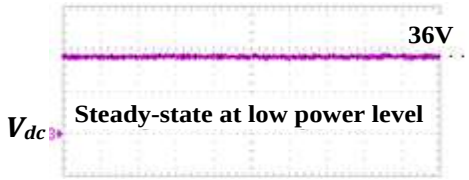

500 ms/div, ch3: 20V/div

(c)

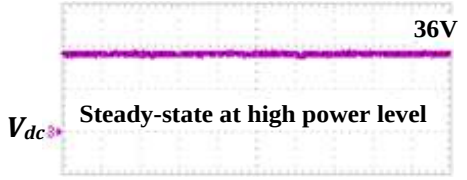

500 ms/div, ch3: 20V/div

(d)

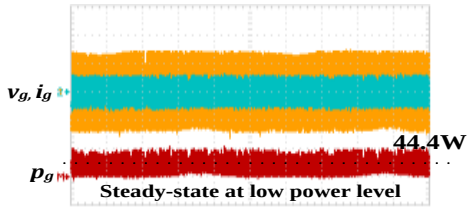

500 ms/div, ch1: 20V/div,
ch2:5A/div, chM: 100VA/div

(e)

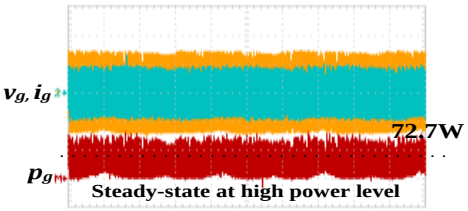

500 ms/div, ch1: 20V/div,
ch2:5A/div, chM: 100VA/div

(f)

Figure 5.26: Conventional technique steady-state performance: PV power; DC-link voltage; grid voltage, current, and power at (a), (c), (e) low power level and (b), (d), (f) high power level.

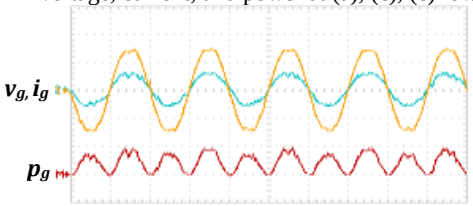

10 ms/div, ch1: 20V/div,
ch2:5A/div, chM: 100VA/div

(a)

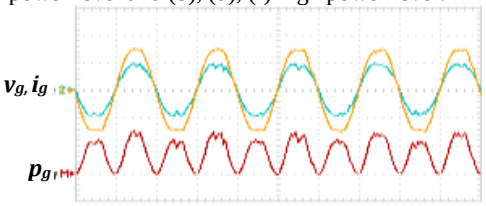

10 ms/div, ch1: 20V/div,
ch2:5A/div, chM: 100VA/div

(b)

Figure 5.28. Magnified view of conventional technique's steady-state grid voltage, current, and power at (a) low power level and (b) high power level.

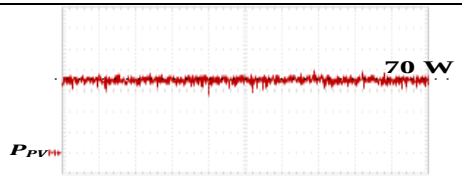

500 ms/div, chM: 20VA/div

(a)

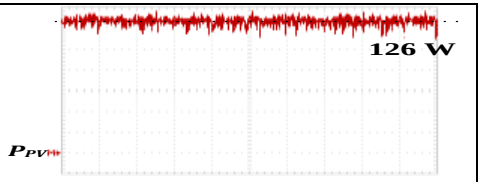

500 ms/div, chM: 20VA/div

(b)

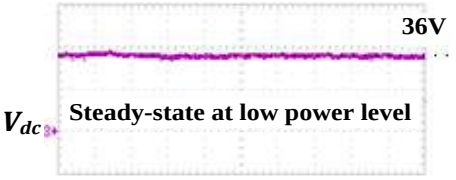

500 ms/div, ch3: 20V/div

(c)

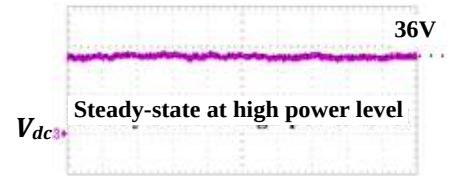

500 ms/div, ch3: 20V/div

(d)

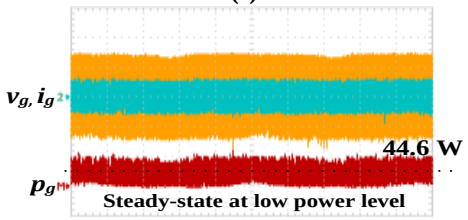

500 ms/div, ch1: 20V/div,
ch2:5A/div, chM: 100VA/div

(e)

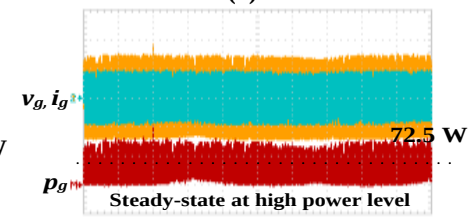

500 ms/div, ch1: 20V/div,
ch2:5A/div, chM: 100VA/div

(f)

Figure 5.27: Proposed technique steady-state performance: PV power; DC-link voltage; grid voltage, current, and power at (a), (c), (e) low power level and (b), (d), (f) high power level.

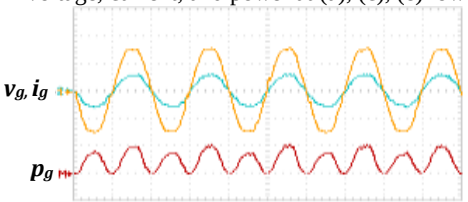

10 ms/div, ch1: 20V/div,
ch2:5A/div, chM: 100VA/div

(a)

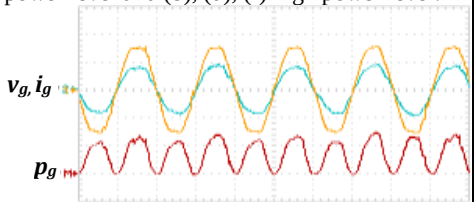

10 ms/div, ch1: 20V/div,
ch2:5A/div, chM: 100VA/div

(b)

Figure 5.29. Magnified view of proposed technique's steady-state grid voltage, current, and power at (a) low power level and (b) high power level.

5.6 Summary

In this chapter, a novel DC-link voltage sensorless control technique is proposed for the grid interface of single-phase two-stage PV converters. This new technique eliminates the need of the VSI outer DC-link voltage control loop. Alternatively, a new reference grid current generation method is presented to transfer the PV power to the grid. Thus, power balance is achieved at the DC-link and the DC voltage stabilizes at a predetermined level. Consequently, system implementation is simplified and the control scheme complexity is minimized. Furthermore, the absence of the DC-link high voltage sensor reduces the system footprint and cost. Simulation and experimental results of both, the conventional and the proposed sensorless techniques, verify the latter's superiority regarding transient response during irradiance changes. This is a consequent improvement due to the elimination of the DC-link voltage loop PI controller with its lagging effect. Both techniques show close steady-state performance when operating at similar conditions which in turn validates the proposed principle.

However, it should be noted that the proposed sensorless control technique still has its limitations. It needs periodic system training and mapping between the tracked PV power and system losses. Moreover, it has not been tested during grid faults where it can show degraded performance or even malfunction in comparison to the conventional technique. The latter is more robust as it controls the DC-link voltage using a closed loop PI controller. Finally, inverter switches protection, especially in case of DC capacitor failures, is an issue to be considered since the DC-link voltage is not measured in the proposed sensorless technique.

References

[5.1] S. Chowdhury, S. P. Chowdhury and P. Crossley, Microgrids and Active Distribution Networks, IET Renewable Energy Series 6, Institution of Engineering and Technology, London, 2009.

[5.2] S. B. Kjaer, J. K. Pedersen, and F. Blaabjerg," A Review of Single-phase Grid-connected Inverters for Photovoltaic Modules", IEEE Trans. Industry Applications, Vol. 41, No. 5, 2005, pp.1292-1306.

[5.3] E. Romero-Ca Daval, et al, "Grid-Connected Photovoltaic Plants: An Alternative Energy Source, Replacing Conventional Sources", IEEE Industrial Electronics Magazine, Vol. 9, No. 1, March 2015, pp. 18-32.

[5.4] M. Matsui, T. Kitano, and X. Dehong, "A Simple Maximum Photovoltaic Power Tracking Technique Utilizing System Inherent Limit Cycle Phenomena", in Proc. IEEE Industry Applications Conference, 2003.

[5.5] C. Meza, et al, "Boost-buck Inverter Variable Structure Control for Grid-connected Photovoltaic Systems with Sensorless MPPT" in Proc. IEEE International Symposium on Industrial Electronics (ISIE), 2005, pp. 657 – 662.

[5.6] N. A. Rahim, J. Selvaraj, Krismadinata, "Hysteresis Current Control and Sensorless MPPT for Grid-connected Photovoltaic Systems", in Proc. IEEE International Symposium on Industrial Electronics (ISIE), 2007, pp. 572-577.

[5.7] S. Park, et al, "Hardware Implementation of Optimization Technique Based Sensorless MPPT Method for Grid-connected PV Generation System," in Proc. IEEE International Conference on Electrical Machines and Systems (ICEMS), 2009, pp.1-6.

[5.8] B. Yang, et al, "Design and Analysis of a Grid-connected Photovoltaic Power System," IEEE Trans. Power Electronics, Vol. 25, No. 4, 2010, pp. 992-1000.

[5.9] Y. Kim et al, "Sensorless Current Balancing and MPPT Control for Photovoltaic AC Module Type Interleaved Flyback Inverter ", in Proc. IEEE Power Electronics and Motion Control Conf. (IPEMC), vol. 2, pp. 1363 – 1367, June 2012.

[5.10] T. Kitano, M. Matsui, and D. Xu, "A Maximum Power Point Tracking Control Scheme for PV System Based on Power Equilibrium and its System Design", IEEJ Trans. Industry Applications, Vol.121, No.12, 2001, pp.1263-1269.

[5.11] M. Matsui, "A New Maximum Photovoltaic Power Tracking Control Scheme Based on Power Equilibrium at DC Link", in Proc. IEEE Industry Applications Conference, 1999, pp. 804 – 809.

[5.12] T. Kitano, M. Matsui, and D. Xu, "Power Sensor-less MPPT Control Scheme Utilizing Power Balance at DC Link –system Design to Ensure Stability and Response", in Proc. IEEE Industrial Electronics Society Conference (IECON), 2001, pp. 1309-1314.

[5.13] D.W. Hart, Power Electronics Handbook. McGraw Hill, 2011.

[5.14] N. A. Ninad and L. A. C. Lopes, "Operation of Single-phase Grid-connected Inverters with Large DC Bus Voltage Ripple", in Proc. IEEE Electrical Power Conference (EPC), 2007, pp. 172-176.

[5.15] S. V. Araújo, P. Zacharias, and R. Mallwitz, "Highly Efficient Single-phase Transformerless Inverters for Grid-connected Photovoltaic Systems ", IEEE Trans. Industrial Electronics, Vol. 57, No. 9, Sep. 2010, pp. 3118-3128.

[5.16] M. H. Rashid, Power Electronics Handbook, Butterworth-Hinemann, 2011.

[5.17] B. Farhangi, and S. Farhangi, "Comparison of Z-source and Boost-buck Inverter Topologies as a Single Phase Transformer-less Photovoltaic Grid-connected Power Conditioner", in Proc. IEEE Power Electronics Specialists Conference (PESC), 2006 , pp.1-6.

[5.18] B. W. Williams, Principles and Elements of Power Electronics. Devices, Drivers, Applications, and Passive Components, 2nd edition, Barry W. Williams, 2006.

[5.19] A. Kotsopoulos, J. L. Duarte, and M. A. M. Hendrix, "Predictive DC Voltage Control of Single-phase PV Inverters with Small DC Link Capacitance", in Proc. IEEE International Symposium on Industrial Electronics, 2003, pp. 793 – 797.

[5.20] L. Yin, et al, "An Improved DC-Link Voltage Fast Control Scheme for a PWM Rectifier-Inverter System," IEEE Trans. Industry Applications, Vol. 50, No. 1, 2014, pp. 462-473.

[5.21] Y. M. Chen, C. H. Chang, and H. C. Wu, "DC-link Capacitor Selections for the Single-phase Grid-connected PV System", in Proc. International Power Electronics and Drive Systems Conference (PEDS), 2009, pp. 72 – 77.

[5.22] E. P. Wiechmann, et al, "On the Efficiency of Voltage Source and Current Source Inverters for High-power Drives", IEEE Trans Industrial Electronics, Vol. 55, No. 4, April 2008, pp. 1771-1782.

[5.23] R. J. Wai and W. H. Wang, "Grid-connected Photovoltaic Generation System," IEEE Trans. on Circuits and Systems, Vol. 55, No. 3, April 2008, pp 953- 964.

[5.24] N. Femia, et al, "A Technique for Improving P&O MPPT Performances of Double-stage Grid-connected Photovoltaic Systems", IEEE Trans. Industrial Electronics, Vol. 56, No. 11, November 2009, pp. 4473-4482.

[5.25] D. Zammit, C. Staines, and M. Apap, "Comparison between PI and PR Current Controllers in Grid Connected PV Inverters," International Journal of Electrical, Robotics, Electronics and Communications Engineering, Vol. 8, No. 2, 2014, pp. 217-222.

[5.26] M. Ciobotaru, R. Theodorescu and F. Blaabjerg, "Control of Single-stage Single-phase PV Inverter," in Proc. European Power Electronics Conference, 2005, pp. 1-10.

[5.27] A. Timbus, et al," Evaluation of Current Controllers for Distributed Power Generation Systems", IEEE Trans. Power Electronics, Vol. 24, No. 3, March 2009, pp. 654-662.

[5.28] B. Song, Y. Kim, H. Cha, and H. Lee, "Current Harmonic Minimization of a Grid-connected Photovoltaic 500kW Three-phase Inverter Using PR Control", in Proc. IEEE Energy Conversion Congress and Exposition, 2011, pp.1063-1068.

[5.29] R. A. Mastromauro, M. Liserre, and A. D. Aquila, "Control Issues in Single-stage Photovoltaic Systems: MPPT, Current and Voltage Control", IEEE Trans. on Industrial Informatics, Vol. 8, No. 2, May 2012, pp. 241-254.

[5.30] F. Blaabjerg, et al, "Overview of Control and Grid Synchronization for Distributed Power Generation Systems", IEEE Trans. Industrial Electronics, Vol. 53, No. 5, October 2006, pp. 1398-1409.

[5.31] R. Teodorescu, et al, "Proportional-resonant Controllers and Filters for Grid-connected Voltage-source Converters", in Proc. IEE Electric Power Applications, Vol. 153, No. 5, September 2006, pp. 750-762.

[5.32] R. Chattopadhyay, A. De, S. Bhattacharya, "Comparison of PR controller and damped PR controller for grid current control of LCL filter based grid-tied inverter under frequency variation and grid distortion", in Proc. IEEE Energy Conversion Congress and Exposition (ECCE), 2014, pp. 3634 – 3641.

[5.33] M. Castilla, et al, "Control Design Guidelines for Single-phase Grid-connected Photovoltaic Inverters with Damped Resonant Harmonic Compensators", IEEE Trans. Industrial Electronics, Vol. 56, No. 11, November 2009, pp. 4492-4501.

[5.34] M. Castilla, et al, "Reduction of Current Harmonic Distortion in Three-Phase Grid-Connected Photovoltaic Inverters via Resonant Current Control", IEEE Trans. Industrial Electronics, Vol. 60, No. 4, April 2013, pp. 1464-1471.

[5.35] IEEE, “IEEE Recommended Practices and Requirements for Harmonic Control in Electric Power Systems,” IEEE Std. 519-1992.

[5.36] K. K. Benke, K. E. Lowell, and A. J. Hamilton, "Parameter Uncertainty, Sensitivity Analysis and Prediction Error in a Water-balance Hydrological Model", Mathematical and Computer Modelling, Vol. 47, No. 11–12, 2008, pp. 1134–1149.

[5.37] C.M. Bishop, Neural Networks for Pattern Recognition. Oxford University Press, New York, 1995.

Chapter Six

Single-phase Single-stage Grid-tied Current Source Inverter for Photovoltaic Applications

Modular integrated converter (MIC) technology connects a PV module to grid through a single DC/AC inverter achieving functions of PV MPPT altogether with PV-grid interfacing, thereby reducing system footprint and enhancing conversion efficiency [6.1]. However, for such a single-stage topology using a conventional H-bridge VSI, a step-up transformer or additional circuits and elements are needed for voltage boosting, which in turn adds bulk and cost to the system, and increases losses [6.1, 6.2]. For single-phase systems, a large electrolytic capacitor is required at VSI DC-side, thus limiting its lifetime and affecting system reliability as well as increasing converter weight, size and cost [6.3].

To overcome VSI voltage buck properties and the required large electrolytic DC capacitor, a single-phase VSI can be replaced by a single-phase current source inverter (CSI) [6.4-10]. The latter is highly competitive with its inherent voltage boost functionality, short-circuit proof properties, and has higher reliability [6.11]. However, its input DC current inherently contains even harmonics which affect PV MPPT, reduce the PV lifetime, and when modulated by the PWM signal produce odd-order harmonics on the grid side [6.5].

Conventionally, to suppress these DC-side harmonics, a large DC inductor is incorporated, however at the cost of a bulky system which is practically inconvenient. Various techniques have been proposed to eliminate CSI DC-side harmonics without the need of a large inductor. Hardware solutions are proposed in [6.9, 6.10]. In [6.9] an additional doubled-tuned parallel resonant circuit is placed on the DC-link inductor in order to eliminate DC-side second and fourth order harmonics. However, these extra passive elements add to system size, cost, losses and design complexity. Furthermore, it may affect system reliability. In [6.10] an active buffer (power decoupling circuit) is added between the DC-link inductor and the CSI yet at the cost of a higher component count and more system losses. Hence, control solutions are preferred in this research. Specially-designed feedback current controllers are proposed in [6.4, 6.5, and 6.8] to eliminate the DC-side harmonics without the need of a bulky inductor. In [6.4], pulse amplitude modulation (PAM) is applied where the carrier signal is varied with the DC-link second-

order harmonic component to eliminate its effect on the AC grid current. Analogue-based active nonlinear pulse width modulation (NPWM) has been proposed in [6.5] to improve AC-side harmonic mitigation. In [6.8], the third-order harmonic grid current is cancelled by employing a harmonic canceller-based proportional resonant controller tuned at that harmonic order.

In this chapter, a single-phase single-stage PV grid-connected system is considered. Modelling, design and analysis of the applied CSI are presented altogether with its proposed control loops and enhanced PWM technique. Furthermore, the CSI DC-link inductor is reduced, while grid current harmonics are minimized using a cascaded proportional resonant (CPR) controller in the grid current control loop. This controller is associated with harmonic compensator units tuned at low-order grid current harmonics to be selectively eliminated. System performance using reduced DC-link inductance is investigated when applying a conventional PR controller and then retested with the proposed CPR controller. Simulation results as well as experimental results for both cases are compared to verify the effectiveness of the proposed controller on grid current quality.

6.1 System under investigation

The considered 300W single-phase single-stage grid-connected PV system is shown in Figure 6.1. It consists of a H-bridge CSI with four IGBT's (S1-S4) and four fast recovery diodes (D1-D4), each diode is connected in series with an IGBT switch for reverse blocking capability. The inverter AC side is connected to the 110V, 50Hz grid through a CL low-pass filter, in the form of series L_f and shunt C_f. The inverter input is connected to an ASE-285-DGF/17 PV module, with the datasheet presented in Appendix B, through the DC-link inductor L_{dc}.

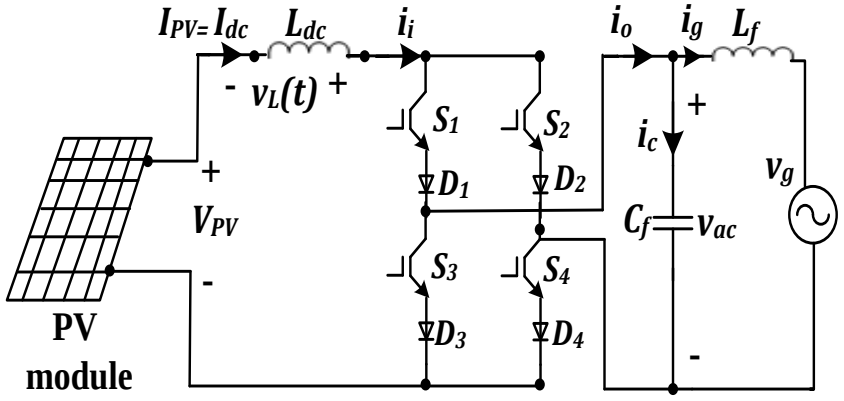

Figure 6.1. PV-grid connected system under investigation.

6.1.1 Applied Pulse Width Modulation scheme

In order to provide a continuous path for the DC-side current, at least one top switch in either arm and one bottom switch must be turned ON during every switching period. The most common technique for single phase CSI switching, introduced in late 90's [6.4] and recently enhanced [6.5, 6.7], relies on a sinusoidal pulse width modulation (SPWM) base. The constraint of DC-link current continuity is solved by maintaining the upper switches ON for half the fundamental cycle and the lower switches are sinusoidally modulated. However, this technique suffers from unsymmetrical utilization of the upper and lower semiconductors, unequal losses distribution and low carrier frequency utilization. Work introduced in [6.12] solves this problem by proposing an on-line PWM generation technique for single phase CSIs, which is a modified version of the three-phase CSI on-line generation technique based on duality theory. The proposed technique achieves equal distribution of the shoot-through pulses and uniform losses distribution among the inverter's semiconductor devices, however at the cost of a more complex design and implementation.

Conventional SPWM techniques applied for single-phase VSIs include bipolar and unipolar techniques [6.13]. As previously explained, the former allows the AC output voltage waveform to feature only two values, which are the input voltage and its negative. The unipolar technique forces the AC output voltage waveform to instantaneously take one of three values; the input voltage, its negative and zero value. Hence, when being applied to single-phase CSI switching, unipolar SPWM does not allow a continuous path for DC current in its state when either its tops switches or bottom ones are both on. In contrast, bipolar SPWM can guarantee DC current continuity when being utilized for single-phase CSI switching and achieves uniform switching distribution among semiconductor devices. However, the overlap time is insufficient to energize the DC-link inductor, which results in increased THD. Hence, a modified carrier based SPWM technique, which consists of two carriers and one reference, is proposed in [6.9]. This switching technique can provide sufficient short-circuit current after every active switching action, thus grid current THD is reduced. Furthermore, equal pulses distribution among the CSI switches is achieved yet with simple implementation.

For all its merits, the PWM technique presented in [6.9] is considered in this research. However, since a TMS320F28335 DSP is applied in the practical implementation, with its

inherited PWM block in the MATLAB/Simulink library, it will be difficult to apply two carriers as proposed in [6.9]. Hence, this chapter proposes another realization for the modified SPWM technique where similar gating signals, to those produced in [6.9], are achieved however with one carrier and two references. The SPWM technique applied in this chapter, for single-phase CSI switching, can be presented as follows; Figure 6.2 shows the carrier and the references waveforms, along with the switching patterns for one reference period, 0.02s. The reference with the solid straight line is responsible for gating the upper switches, while the dashed line reference is responsible for the lower switches and is shifted by 180°. Figure 6.2 is divided into ten regions ($t_1 - t_{10}$), and each represents one carrier frequency period, 0.002s. Table 6.1 shows the switch combination for each of the ten regions. The applied PWM operates in two modes, a conductive mode and a null mode, and the switching action of each switch is equally distributed during each fundamental period.

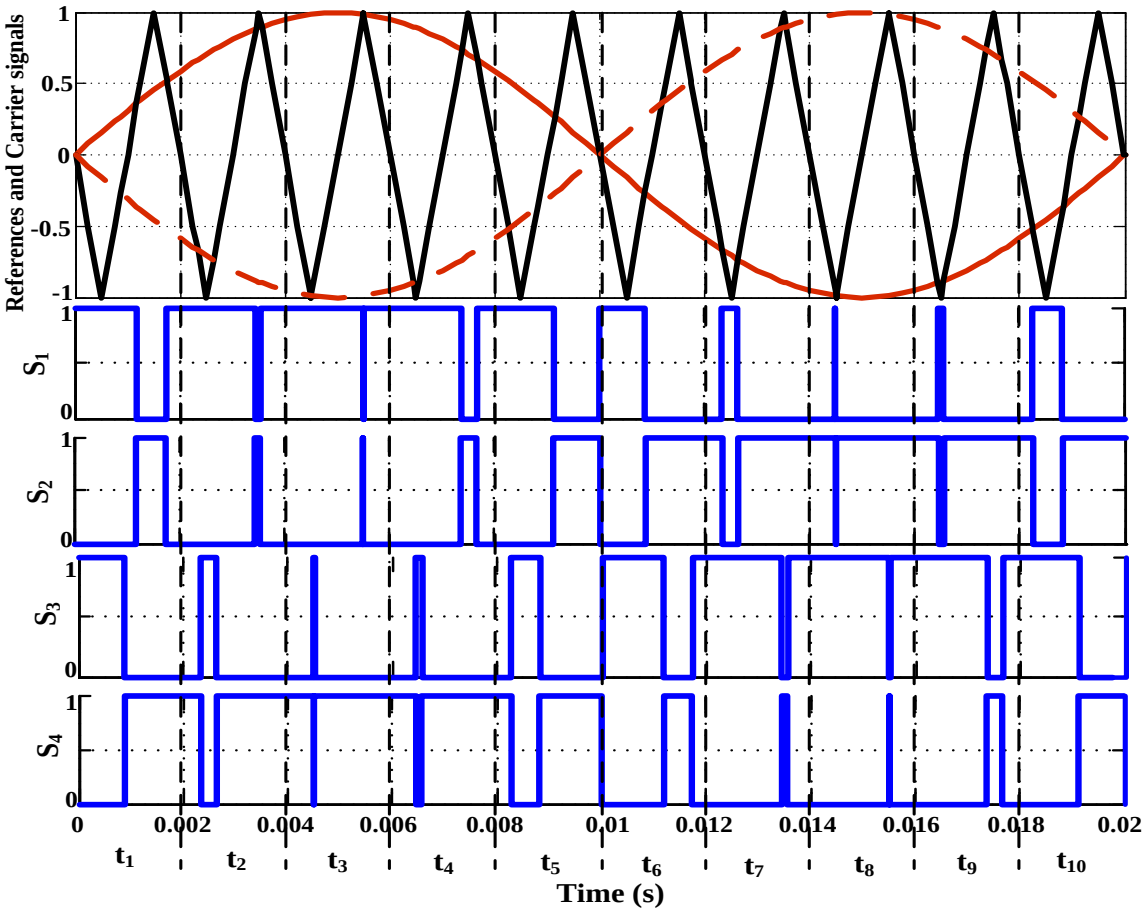

Figure 6.2. Applied CSI PWM scheme and switching sequence for one fundamental frequency cycle.

Table 6.1: CSI switching combination sequence

Region	Combination Sequence
$\mathbf{t_1}$	(S_1-S_3) (S_1-S_4) (S_2-S_4) (S_1-S_4)
$\mathbf{t_2}$	(S_1-S_3) (S_1-S_4) (S_2-S_4) (S_1-S_4)
$\mathbf{t_3}$	(S_1-S_3) (S_1-S_4) (S_2-S_4) (S_1-S_4)
$\mathbf{t_4}$	(S_1-S_3) (S_1-S_4) (S_2-S_4) (S_1-S_4)
$\mathbf{t_5}$	(S_1-S_3) (S_1-S_4) (S_2-S_4)
$\mathbf{t_6}$	(S_1-S_3) (S_2-S_3) (S_2-S_4) (S_2-S_3)
$\mathbf{t_7}$	(S_1-S_3) (S_2-S_3) (S_2-S_4) (S_2-S_3)
$\mathbf{t_8}$	(S_1-S_3) (S_2-S_3) (S_2-S_4) (S_2-S_3)
$\mathbf{t_9}$	(S_1-S_3) (S_2-S_3) (S_2-S_4) (S_2-S_3)
$\mathbf{t_{10}}$	(S_1-S_3) (S_2-S_3) (S_2-S_4)

6.1.2 System Modelling

For a grid-connected PV system using a CSI, the relationship between the PV output voltage and the grid voltage is derived as follows [6.9].

For a unity power factor:

$$p_g = \hat{V}_g \hat{I}_g sin^2 \omega t = \frac{\hat{V}_g \hat{I}_g}{2}(1 - \cos 2\omega t) \tag{6.1}$$

where p_g is the instantaneous active power injected into the grid assuming unity power factor, $\hat{V}_g$ is the grid voltage amplitude, $\hat{I}_g$ is the injected grid current amplitude, and ω is the line angular frequency in rad/s.

By neglecting system losses, the PV output power is equal to the average part of the grid power

$$V_{PV} I_{PV} = \frac{\hat{V}_g \hat{I}_g}{2} \tag{6.2}$$

where V_{PV} and I_{PV} are the PV output voltage and current. The grid current is equal to the PV output current multiplied by the inverter modulating amplitude *M*.

$$\hat{I}_g = M I_{PV} \tag{6.3}$$

Substituting (6.2) into (6.3), the equation describing the relationship between the PV output voltage and the grid voltage is:

$$V_{PV} = \frac{M \hat{V}_g}{2} \tag{6.4}$$

Therefore, in order to interface the PV system to the grid using a CSI, the PV voltage should not exceed half the grid peak voltage.

From (6.1) the grid power consists of two components; the DC component (average grid power) and the AC component (grid power oscillating at double the line frequency). The latter is reflected at the CSI DC-side resulting in oscillating power at the DC-link inductor as follows [6.5];

$$v_L(t)I_{PV} = -\frac{\hat{V}_g\hat{I}_g}{2}\cos 2\omega t = -V_{PV}I_{PV}\cos 2\omega t \tag{6.5}$$

where $v_L(t)$is the instantaneous voltage across L_{dc} as shown in Figure 6.1. Then;

$$v_L(t) = -V_{PV}\cos 2\omega t = -\frac{M\hat{V}_g}{2}\cos 2\omega t \tag{6.6}$$

This in turn results in PV current ripple denoted as $i_L(t)$

$$i_L(t) = -\frac{1}{L_{dc}}\int_0^t v_L(t)dt = \frac{M\hat{V}_g}{4\omega L_{dc}}\sin 2\omega t \tag{6.7}$$

Then

$$i_i(t) = I_{PV} + i_L(t) = \frac{2P_{PV}}{M\hat{V}_g} + \frac{M\hat{V}_g}{4\omega L_{dc}}\sin 2\omega t \tag{6.8}$$

where $i_i(t)$ is the instantaneous inverter input current in which second-order harmonics appear. Since the CSI is modulated with a SPWM function *m(t)*, the instantaneous inverter output current is [6.5];

$$i_0(t) = m(t)i_i(t) = M\sin\omega t\left(\frac{2P_{PV}}{M\hat{V}_g} + \frac{M\hat{V}_g}{4\omega L_{dc}}\sin 2\omega t\right) \tag{6.9}$$

$$i_0(t) = \frac{2P_{PV}}{\hat{V}_g}\sin\omega t + \frac{M^2\hat{V}_g}{4\omega L_{dc}}\sin\omega t\sin 2\omega t \tag{6.10}$$

$$i_0(t) = \frac{2P_{PV}}{\hat{V}_g}\sin\omega t + \frac{M^2\hat{V}_g}{8\omega L_{dc}}\cos\omega t - \frac{M^2\hat{V}_g}{8\omega L_{dc}}\cos 3\omega t \tag{6.11}$$

Hence, a third order harmonic component is introduced into the inverter output current (i_0) due to the second order harmonics in the inverter input current (i_i). In order to mitigate the latter, single-phase grid-tied PV CSIs usually feature a large inductor in their DC-link.

6.1.3 Parameters Design

Design steps of the CL filter placed at the CSI AC side, is presented, then the selection criteria of the CSI DC-link inductor are illustrated.

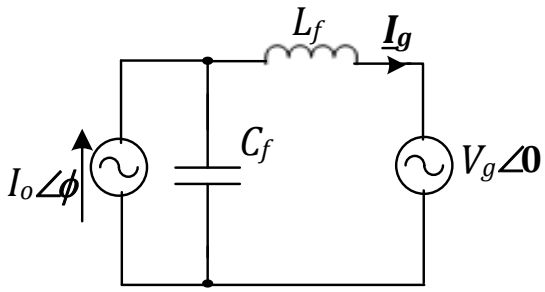

Figure 6.3. Equivalent circuit of the CSI AC output connected to the grid [6.5].

i. AC filter

The CSI AC side filter attenuates high frequency harmonics associated with the switching frequency and it sidebands. The CSI near sinusoidal output voltage is achieved owing to the inverter output capacitor bank (C_f). A sinusoidal output current can be realized, when applying the CSI sinusoidal voltage to the grid voltage, through the interface AC inductor (L_f) [6.11].

For this filter design [6.5], consider the equivalent circuit of the CSI output to the grid shown in Figure 6.3. Assume that the fundamental component of the CSI output current (I_{o1}) is at an angle ϕ with respect to grid voltage. The output phasor grid current ($\underline{\boldsymbol{I_g}}$) can be calculated using superposition as follows;

- First consider the $I_{o1}\angle\phi$ source,

$$\therefore \underline{\boldsymbol{I_{g1}}} = \frac{-\frac{I_{o1}\angle\phi}{\omega C_f}}{\omega L_f - \frac{1}{\omega C_f}} \tag{6.12}$$

- Then consider the $V_g\angle 0^o$ source**,**

$$\therefore \underline{\boldsymbol{I_{g2}}} = \frac{V_g\angle 90^o}{\omega L_f - \frac{1}{\omega C_f}} \tag{6.13}$$

$$\therefore \underline{\boldsymbol{I_g}} = \underline{\boldsymbol{I_{g1}}} + \underline{\boldsymbol{I_{g2}}} = \frac{-\frac{I_{o1}\angle\phi}{\omega C_f} + V_g\angle 90^o}{\omega L_f - \frac{1}{\omega C_f}} \tag{6.14}$$

To achieve unity power factor, the imaginary part of $\underline{\boldsymbol{I_g}}$ should equal zero. Hence

$$-\frac{I_{o1}\sin\phi}{\omega C_f}+V_g=0 \tag{6.15}$$

Then

$$\sin\phi=\frac{V_g\omega C_f}{I_{o1}} \tag{6.16}$$

and

$$I_g=\frac{I_{o1}}{1-\omega^2 L_f C_f}\cos\phi \tag{6.17}$$

where I_{o1}, V_g, and I_g are the rms values of the CSI fundamental output current, grid voltage and grid current respectively.

From (6.16), it can be concluded that;

$$\cos^2\phi=1-\frac{{V_g}^2\omega^2{C_f}^2}{{I_{o1}}^2} \tag{6.18}$$

Moreover, the AC output filter is designed so that I_g=I_{o1}, then from (6.17)

$$\cos\phi=1-\omega^2 L_f C_f \tag{6.19}$$

Hence, from (6.18) and (6.19)

$$\left(1-\omega^2 L_f C_f\right)^2=1-\frac{{V_g}^2\omega^2{C_f}^2}{{I_{o1}}^2}=1-\frac{{V_g}^4\omega^2{C_f}^2}{{P_{PV}}^2} \tag{6.20}$$

The AC filter is designed so that the inductor reactance is *x* times the capacitor reactance at the CSI switching frequency$f_{sw(i)}$, then

$$\omega_{sw}L_f=x\frac{1}{\omega_{sw}C_f}\qquad\Rightarrow\qquad L_f=x\frac{1}{{\omega_{sw}}^2 C_f} \tag{6.21}$$

where $\omega_{sw}=2\pi f_{sw(i)}$. By substituting (6.21) into (6.20)

$$C_f=\frac{P_{PV}}{{V_g}^2\omega}\sqrt{\frac{x\omega^2}{\omega_{sw}^2}\left(2-\frac{x\omega^2}{\omega_{sw}^2}\right)} \tag{6.22}$$

Using (6.21) and (6.22), $L_f$and C_f are designed based on the selected values of *x* and ω_{sw} [6.5].

ii. DC-link inductor

The CSI DC-link inductor is implemented to mitigate low-order harmonics introduced by the grid at the DC-link. Also it provides a steady DC current to the inverter. It is sized to keep the DC-link current fluctuations within specified limits in the same way the DC-link capacitor is designed in case of VSI to keep the DC voltage ripple within specified margins [6.14, 6.15].

As discussed in chapter three (subsection 3.3.2), L_{dc} buffers the CSI DC-link current ripple resulting from grid power pulsations at double the line frequency ($P_g \cos 2\omega t$). Hence, DC-link energy ripple results from grid pulsation as follows;

$$\frac{1}{2}L_{dc}(I_{dcmax}^2 - I_{dcmin}^2) = \int_{\frac{-T}{4}}^{\frac{T}{4}} P_g \cos 2\omega t \, dt \tag{6.23}$$

where I_{dcmax} and $I_{dcmin}$are the maximum and minimum values of the average DC-link current respectively, and P_g is the average value of the active power injected into the grid.

After manipulations, (6.24) results:

$$\therefore \frac{1}{2}L_{dc}(I_{dcmax} + I_{dcmin})(I_{dcmax} - I_{dcmin}) = \frac{P_g}{2\omega}\int_{\frac{-2\pi}{4}}^{\frac{2\pi}{4}} \cos 2\omega t \, d(2\omega t) \tag{6.24}$$

$$\therefore \; L_{dc}I_{dc}\Delta i_{dcp-p} = \frac{P_g}{2\omega}\int_{\frac{-\pi}{2}}^{\frac{\pi}{2}} \cos 2\omega t \, d(2\omega t) \tag{6.25}$$

where $\Delta i_{dcp\text{-}p}$ is the peak to peak DC current ripple. Let $2\omega t=\theta$

$$\therefore \; L_{dc}I_{dc}\Delta i_{dcp-p} = \frac{P_g}{2\omega}\int_{\frac{-\pi}{2}}^{\frac{\pi}{2}} \cos\theta \, d\theta \tag{6.26}$$

The DC-link inductor that limits DC-current ripple to a desired value can be calculated by integrating (6.26) which results in (6.27) [6.6],

$$L_{dc} = \frac{P_g}{\omega I_{dc}\Delta i_{dcp-p}} = \frac{P_{PV}}{2\omega I_{dc}\Delta i_{dc}} \tag{6.27}$$

where Δi_{dc} is the amplitude of the DC current ripple.

Hence, the considered system parameters are designed according to the previous equations and their values are shown in Table 6.2.

Table 6.2. Parameters of the 300W, 110V, 50Hz investigated system

$\boldsymbol{L_{dc}}$	150 mH, for Δi_{dcp-p}=0.33 A, and 50 mH, for Δi_{dcp-p}=1 A
$\boldsymbol{C_f, L_f}$	25 µF and 3 mH for $f_{sw(i)}$ =15 kHz

6.2 Proposed control scheme

The proposed control scheme, which achieves single-stage PV-grid interfacing via a single-phase CSI, is demonstrated as follows;

6.2.1 CSI Control Loops

For the considered single-stage grid-tied PV system, there is only one DC/AC conversion stage in which a single-phase PWM CSI is employed. The CSI should track the maximum PV power and interface the PV module to the grid. In order to achieve the latter, two control loops are used; an outer DC-link current control loop, which regulates the DC-link current to a value that ensures MPPT, and an inner grid current control loop for PV-grid interfacing. Figure 6.4 (a) shows the proposed control scheme.

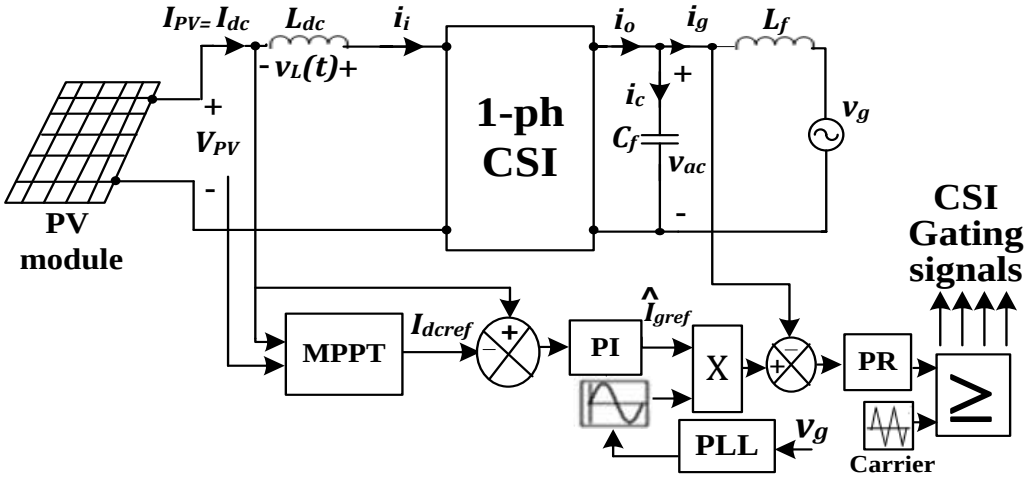

(a)

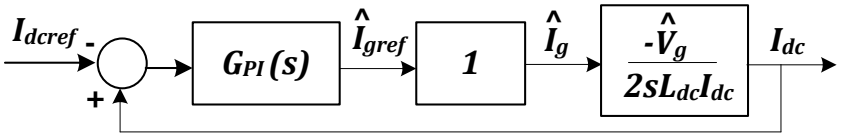

(b)

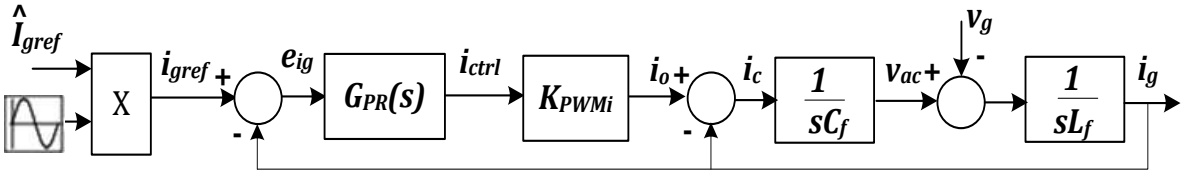

(c)

Figure 6.4. Control scheme for the applied single-phase single-stage grid-tied PV CSI (a) schematic diagram, (b) outer DC-link control loop, and (c) inner grid current loop.

i. Outer DC-link current control loop

This loop is responsible for forcing the CSI DC-link current I_{dc} (which is the PV current I_{PV}) to match a reference value, I_{dcref}. This reference value corresponds to the PV current at which the PV module supplies its maximum power (I_{MPP}). Hence, I_{dcref} is determined by an MPPT algorithm in order to extract PV module maximum power. For enhanced performance and simple implementation, the modified variable step-size Inc.Cond. technique, presented in Chapter four, is used.

The extracted PV power should be transferred to the grid; hence the output of this control loop determines the amplitude of the sinusoidal reference grid current. This reference amplitude $\hat{I}_{gref}$ represents the reference grid current's active component which indicates the power amount available at the CSI DC-side. By accurately adjusting $\hat{I}_{gref}$ and using a fast grid current controller, the power at the inverter DC-side is transferred to grid.

The block diagram of the outer DC-link current control loop is shown in Figure 6.4 (b). This loop implements a simple proportional-integral (PI) controller to minimize the DC-link current steady-state error. This controller is represented by the gain $G_{PI}(S)$ where K_{P-i} and K_{I-i} are the controller proportional and integral gains respectively:

$$G_{PI}(s) = K_{P-i} + \frac{K_{I-i}}{s} \tag{6.28}$$

The DC-link current controller gains are designed for a low cross-over frequency in order to attenuate the magnitude of the double line-frequency DC current ripple. Hence, as demonstrated in [6.15], the inner grid current control loop, with a bandwidth of a few kHz and unity feedback, can be represented by a unity gain at the low frequency range considered for the outer DC-link current control loop as shown in Figure 6.4(b).

The relationship between variations in the fundamental grid current magnitude and the average DC-link current can be calculated using the average power balance equation (6.29), neglecting converter and filter losses.

$$P_{PV} = P_g + \frac{d\left[\frac{1}{2}L_{dc}I_{dc}^2\right]}{dt} \tag{6.29}$$

For simplified sensitive analysis, when studying the relationship and correlation between certain system variables, other variables of less contribution and effect on the studied variables, can be partially eliminated. Hence, in order to determine the impact of grid current magnitude variation on the average DC-link current, one neglects P_{PV} [6.15].

$$\therefore \frac{d\left[\frac{1}{2}L_{dc}I_{dc}^2\right]}{dt} = -P_g \tag{6.30}$$

$$\frac{d\left[\frac{1}{2}L_{dc}I_{dc}^2\right]}{dt} = -\frac{\hat{V}_g\hat{I}_g}{2} \tag{6.31}$$

Applying small perturbations around the operating point leads to:

$$\frac{d\left[\frac{1}{2}L_{dc}(I_{dc} + i_{dc-pert})^2\right]}{dt} = -\frac{\hat{V}_g(\hat{I}_g + \hat{\imath}_{g-pert})}{2} \tag{6.32}$$

where $i_{dc-pert}$, and $\hat{\imath}_{g-pert}$ are the small perturbations applied around the mean DC-link current and the grid current amplitude respectively. Neglecting steady-state values and square of small perturbations,

$$\frac{d\left[\frac{1}{2}L_{dc}2\ I_{dc}\ i_{dc-pert}\right]}{dt} = -\frac{\hat{V}_g\hat{\imath}_{g-pert}}{2} \tag{6.33}$$

Hence,

$$L_{dc}I_{dc}sI_{dc}(s) = -\frac{\hat{V}_g\hat{I}_g(s)}{2} \tag{6.34}$$

$$\therefore \frac{I_{dc}(s)}{\hat{I}_g(s)} = -\frac{\hat{V}_g}{2sL_{dc}I_{dc}} \tag{6.35}$$

ii. Inner grid current control loop

To achieve grid interface, the inverter should output a sinusoidal grid current with acceptable THD and near-unity power factor. Thus, the output of the DC current controller, which represents the reference grid current amplitude, is multiplied by a sinusoidal unit vector which is obtained from a phase-locked loop (PLL) synchronized to the grid voltage. Then, the inner current loop controller forces the grid current to match this sinusoidal reference. The block diagram of the inner grid current control loop is shown in Figure 6.4 (c). Since the CSI operates at relatively high switching frequency, the PWM block can be represented by a simple gain, as demonstrated in [6.15, 6.16];

$$K_{PWMi} = \frac{I_{dc}}{\hat{I}_{tri}} \tag{6.36}$$

where $\hat{I}_{tri}$ is the amplitude of the triangular carrier signal.

Since the grid current is a time-varying control variable, conventional PI controllers encounter difficulties in removing the steady-state error [6.17, 6.18]. Hence, either

proportional-integral (PI) controllers with feed-forward should be employed or proportional-resonant (PR) controllers. The latter have gained popularity in the last decade due to their ability to eliminate the magnitude and phase angle steady-state errors when regulating sinusoidal signals without the need of voltage feed forward [6.19, 6.20]. Hence, the proportional resonant controller is employed for current control of grid-connected PV VSIs [6.21] and CSIs [6.9] with the ideal transfer function given as;

$$G_{PR}(s) = K_{P-r} + K_{I-r}\frac{s}{s^2 + {\omega_r}^2} \tag{6.37}$$

where K_{P-r} is proportional part gain, K_{I-r} is the resonant part gain, and ω_r is the resonant frequency of the controller. The desired sinusoidal signal's frequency is chosen as the resonance frequency, which is the grid line angular frequency in this case.

6.2.2 Proposed harmonic compensator

Since the fundamental PR controller acts on a narrow band around its resonant frequency ω, the implementation of a harmonic compensator for low-order harmonics is possible without affecting the PR controller behaviour and dynamics [6.22, 6.23]. Hence, besides single frequency compensation, selective harmonic compensation can also be achieved by cascading several resonant blocks tuned to resonate at the desired low-order harmonic frequencies to be compensated. This makes this controller suitable for grid-tied systems minimizing its line current low-order harmonics which result from DC-link even harmonics. The transfer function of the harmonic compensator is given by;

$$G_{HC}(s) = \sum_{H=3,5,\ldots,n} K_{(I-r)H}\frac{s}{s^2 + (\omega H)^2} \tag{6.38}$$

where H is the harmonic order to be compensated and $K_{(I-r)H}$ represents the individual resonant gain, which must be tuned for minimizing harmonics at the related frequency.

Ideal PR controllers with harmonic compensators are common with VSIs [6.21, 6.24-26], however they not widely used with the CSI. In this research, a harmonic compensator is designed to cancel low-order harmonics as they are the most prominent harmonics in a typical CSI output current spectrum. This allows the use of lower DC-link inductance without degrading grid current quality. The control block diagram of the proposed controller is shown in Figure 6.5. $K_{(I\text{-}r)n}$ is the resonant gain at nth harmonic order designed to limit grid current harmonics at its related frequency.

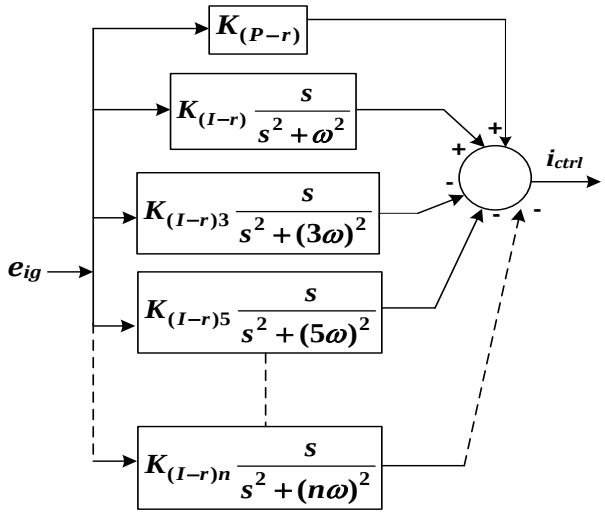

Figure 6.5. Proposed cascaded harmonic compensator block diagram.

6.3 Simulation results

The investigated single-phase single-stage grid-tied PV system, presented in section 6.1, is simulated using MATLAB/Simulink. First, system performance is studied for L_{dc} =150 mH when applying a conventional PR controller (CPRC) in the grid current loop. Then, L_{dc} is reduced to 50mH and the latter is repeated once when applying conventional PR control (CPRC) and again when applying the proposed cascaded harmonic compensator (PCHC). In this research, a step change in irradiance; from 1000 W/m^2 to 700 W/m^2 is applied at t= 3s to study system performance at different power levels.

System response for L_{dc} =150 mH using CPRC, in grid current loop, is shown in Figure 6.6. Figure 6.6 parts (a) and (b) show the PV current (DC-link current) and the maximum tracked PV power respectively at the considered irradiance levels (1000 and 700 W/m^2). Figure 6.6 parts (c) and (d) show the grid current and average grid power respectively. The large DC-link inductor experiences minimal PV power ripple which will be reflected in the grid current THD. At operation start, t_s=0.185s while at the irradiance step change, the PV maximum power is tracked after 0.025s. The large size DC-link inductor shows relatively slower tracking response compared to that with 50 mH L_{dc} as will be demonstrated later. Moreover, the large DC-link inductor, together with its series resistance, creates power losses with system efficiencies of 86%, and 89% at 1000 and 700 W/m^2 respectively. Figures 6.7 and 6.8 zoom into the system response where Figure 6.7 parts (a) and (b) show the effect of the CSI C_f in achieving almost sinusoidal inverter output voltage at 1000 and 700 W/m^2 respectively. Figure 6.8 parts (a) and (b) show near unity power factor at both irradiance levels. Finally, Figure 6.8 parts (c) and (d) show the exerted grid currents with

their associated fast Fourier analysis (FFT) at both power levels. The high value of L_{dc} result in grid current THDs of 4.22% and 4.9% at 1000 and 700 W/m^2 respectively; within IEEE Std. 519 [6.27].

System performances for L_{dc} =50 mH using CPRC and PCHC are shown in figs. 6.9 and 6.10 respectively. Figure 6.9 parts (a) , (b), (c), and (d) show DC-link current, maximum PV power, grid current, and average grid power respectively when applying CPRC while Figure 6.10 parts (a) , (b), (c), and (d) show those associated with PCHC, respectively. Reducing the DC-link inductor to its one third results in higher steady-state PV power oscillation which result in less average PV power than for L_{dc}=150 mH. However, lower losses are experienced by L_{dc}=50 mH resulting in enhanced system efficiencies of 92%, and 94% at 1000 and 700 W/m^2 respectively in case of CPRC as well as in the case of PCHC. This results in more average power delivered at the grid than in case of L_{dc}=150 mH. Moreover, reducing L_{dc} results in a faster dynamic response when applying both controllers (At operation start, t_s=0.055s while at the irradiance step change, the PV maximum power is tracked after 0.015s).

Figures 6.11 and 6.12, 6.13 and 6.14 zoom into the system response when applying CPRC and PCHC. Figures 6.11 parts (a) and (b) show the almost sinusoidal inverter output voltage at 1000 and 700 W/m^2 respectively, in the case of CPRC while Figure 6.12 parts (a) and (b) show those for PCHC. Figure 6.13 parts (a) and (b) show the near unity power factor achieved at both irradiance levels in the case of CPRC while Figure 6.14 parts (a) and (b) show those for PCHC. However, the higher PV power oscillation in case of L_{dc}=50 mH, results in distorted grid current when applying conventional PR control as shown in Figure 6.13 parts (c) and (d) with THDs beyond standards [6.27] (9.4% and 12.57% at 1000 and 700 W/m^2 respectively). When studying FFT analysis in the case of CPRC, the main cause of high grid current THD is the third order harmonic component (8.9% and 12.25% at 1000 and 700 W/m^2 respectively). Hence, a PR controller is designed with a cascaded harmonic compensator tuned at the third harmonic order to minimize harmonics at this frequency (150 Hz). The impact of the PCHC is shown in Figure 6.14 parts (c) and (d) where grid current third order harmonics are reduced to 1.83% and 2.33% at 1000 and 700 W/m^2 respectively which result in a minimized grid current THD (3.19% and 3.93% at 1000 and 700 W/m^2 respectively) which is even better than with L_{dc}=150 mH. Table 6.3 summarizes the performance parameters of the simulated systems, for all cases.

Simulation results show that more PV power oscillation is experienced, when reducing the DC-link inductor, but system efficiency and dynamic performance are enhanced. However, a harmonic compensator must be used in the inner grid current control loop to mitigate low-order harmonics found in grid current as a result of higher PV power ripple.

Bode plots of the PR controller proposed in the simulation study, with its cascaded third-order harmonic compensator, are shown in Figure 6.15 versus the Bode plots of the conventional PR controller. There are resonant peaks at only the selected filtering frequencies; the fundamental in case of CPRC and the fundamental and 150 Hz in the PCHC case. Since the third harmonic is to be extracted from the grid current waveform, its resonant block is subtracted from fundamental PR block as shown in Figure 6.5. The latter explains why the phase angle, at the third harmonic order, reverses its direction compared to that of the fundamental, fig 6.15 (b).

Table 6.3: Performance parameters of system applied in simulation work

Case	Irradiance	Settling time (s)	PV Power (W)	Grid Power (W)	Efficiency
L_{dc}= 150 mH CPRC	1000 W/m^2	0.185	284.8	245	86%
	700 W/m^2	0.025	195	174	89%
L_{dc}= 50 mH CPRC	1000 W/m^2	0.055	282	260	92%
	700 W/m^2	0.015	186	175	94%
L_{dc}= 50 mH PCHC	1000 W/m^2	0.055	282.5	260	92%
	700 W/m^2	0.015	188	177	94%

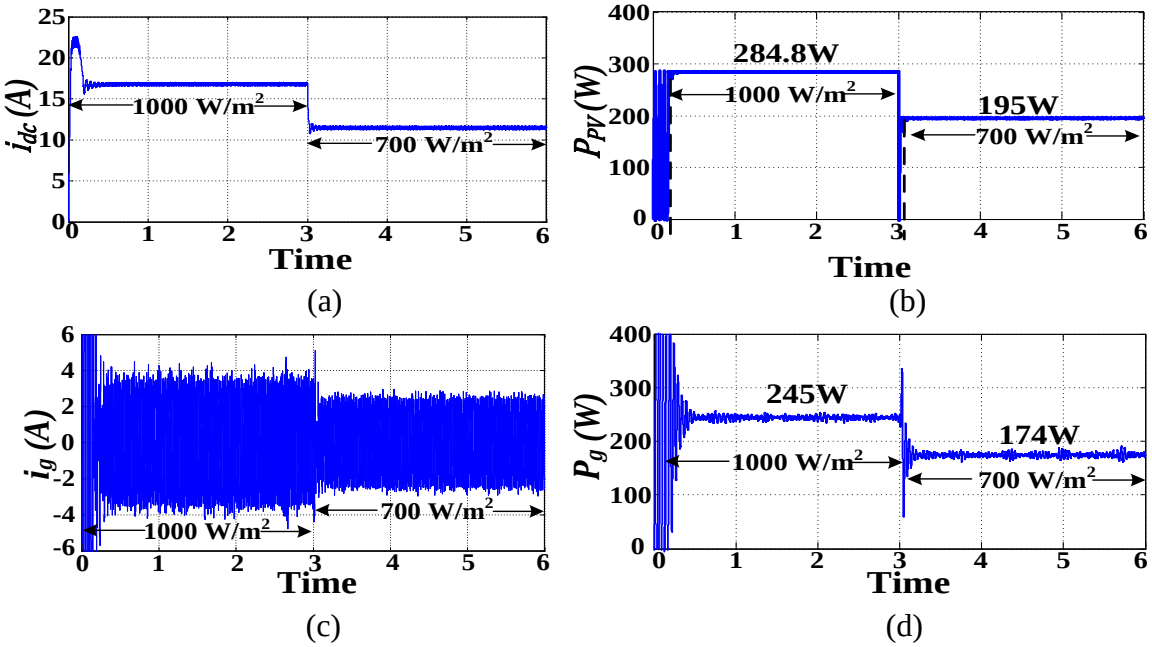

Figure 6.6. System performance with CPRC and L_{dc} = 150 mH; (a) DC-link current, (b) PV power, (c) grid current, and (d) average grid power.

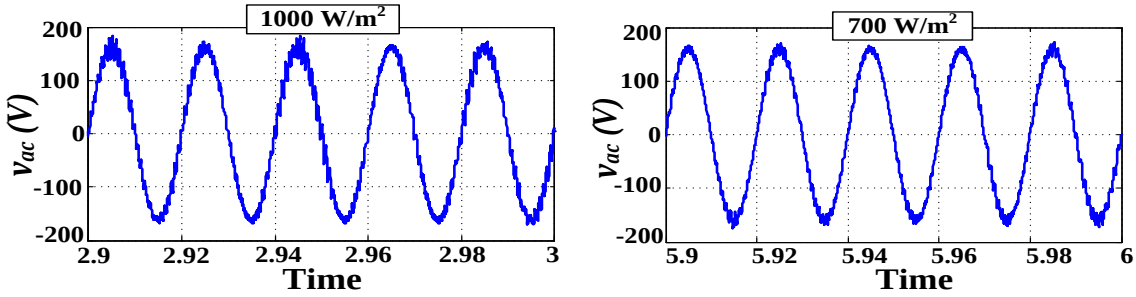

(a) (b)

Figure 6.7. Zoom into CSI output voltage applying CPRC and L_{dc} = 150 mH at (a) 1000 W/m^2, and (b) 700 W/m^2.

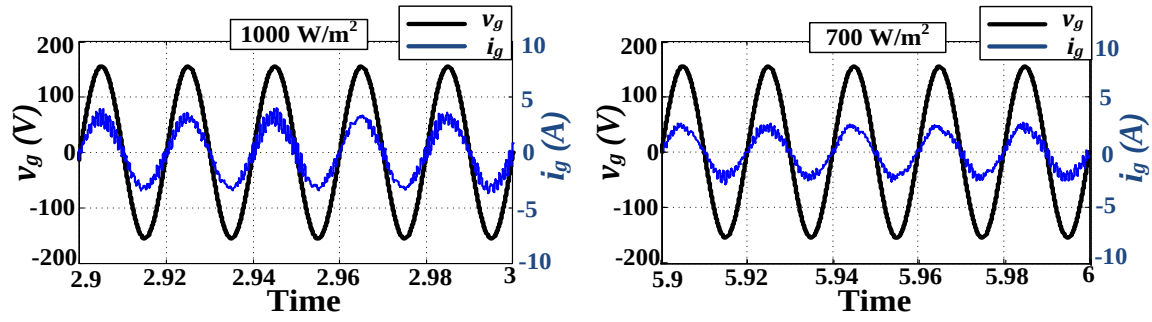

(a) (b)

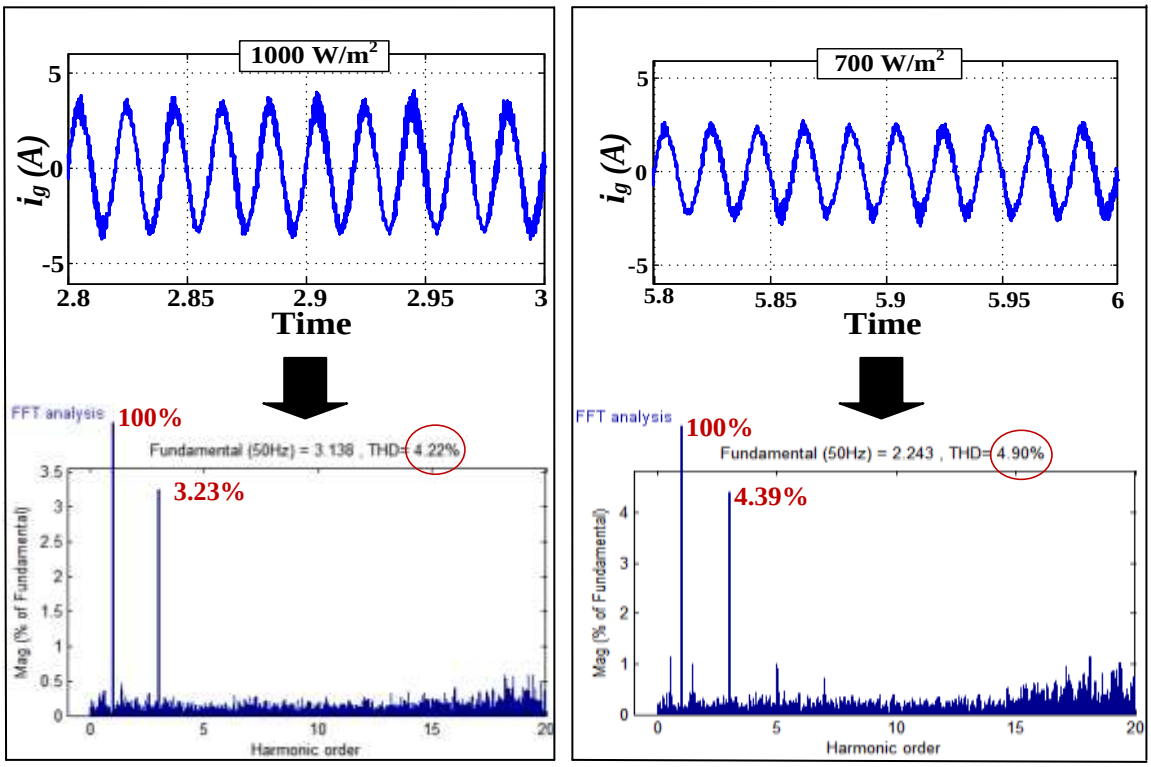

(c) (d)

Figure 6.8. Zoom into system performance applying CPRC and L_{dc} = 150 mH; grid voltage versus grid current, and grid current with its FFT analysis at (a), (c) 1000 W/m^2, and (b), (d) 700 W/m^2.

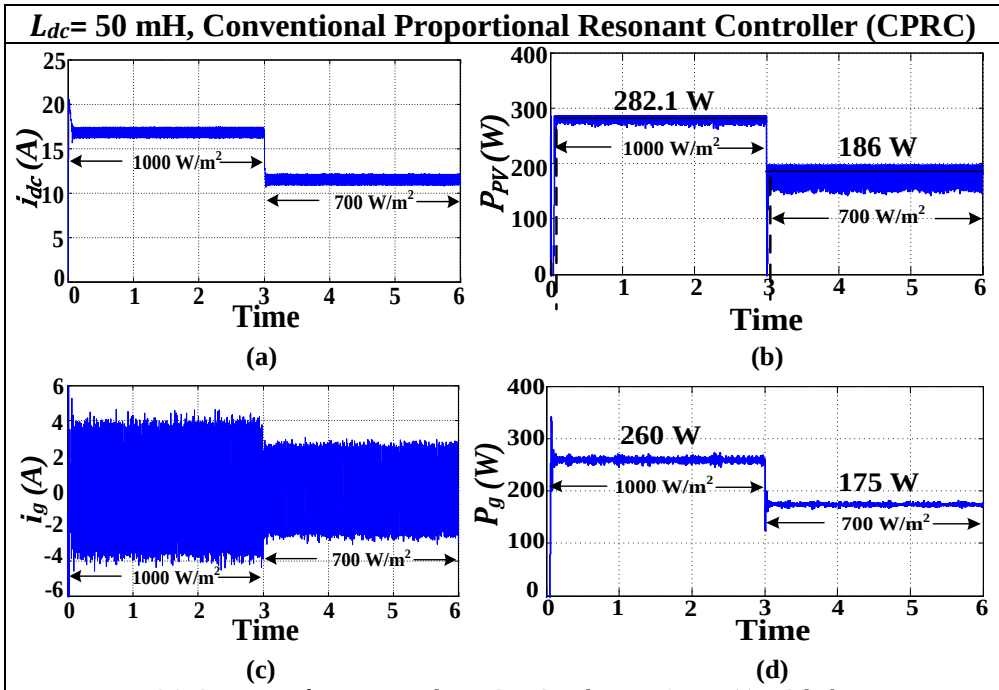

Figure 6.9. System performance applying CPRC and L_{dc} = 50 mH; (a) DC-link current, (b) PV power, (c) grid current, and (d) average grid power.

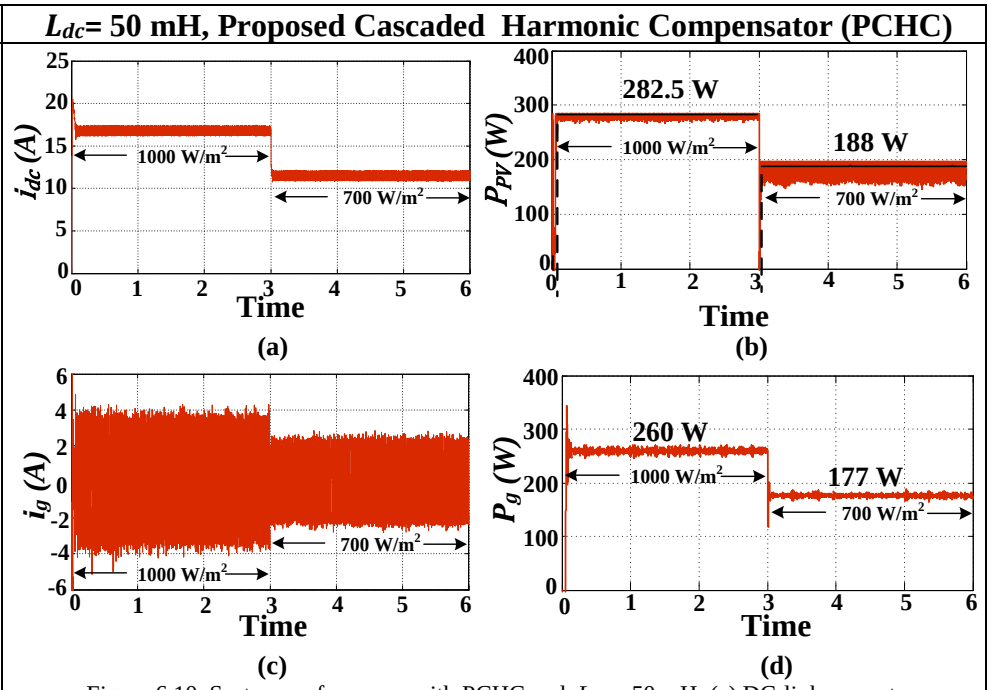

Figure 6.10. System performance with PCHC and L_{dc} = 50 mH; (a) DC-link current, (b) PV power, (c) grid current, and (d) average grid power.

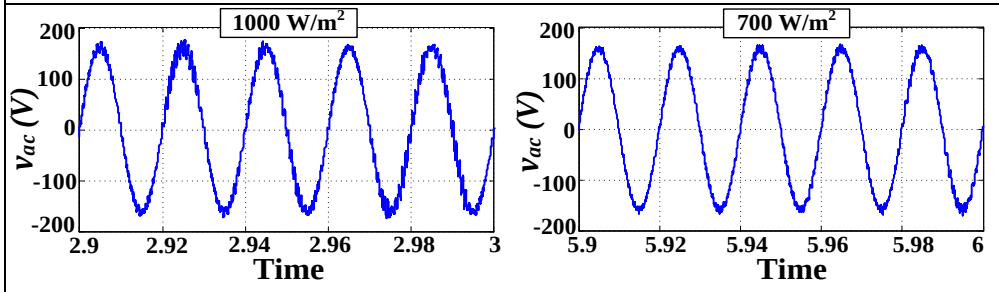

Figure 6.11. Zoom into CSI output voltage applying CPRC and L_{dc} = 50 mH at; (a) 1000 W/m^2 and (b) 700 W/m^2.

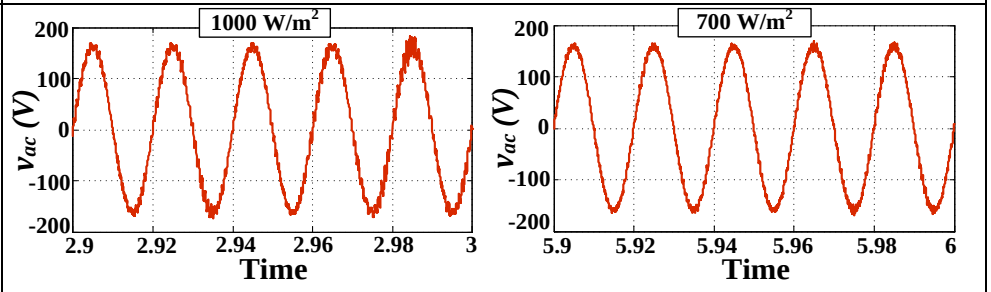

Figure 6.12. Zoom into CSI output voltage applying PCHC and L_{dc} = 50 mH at; (a) 1000 W/m^2 and (b) 700 W/m^2.

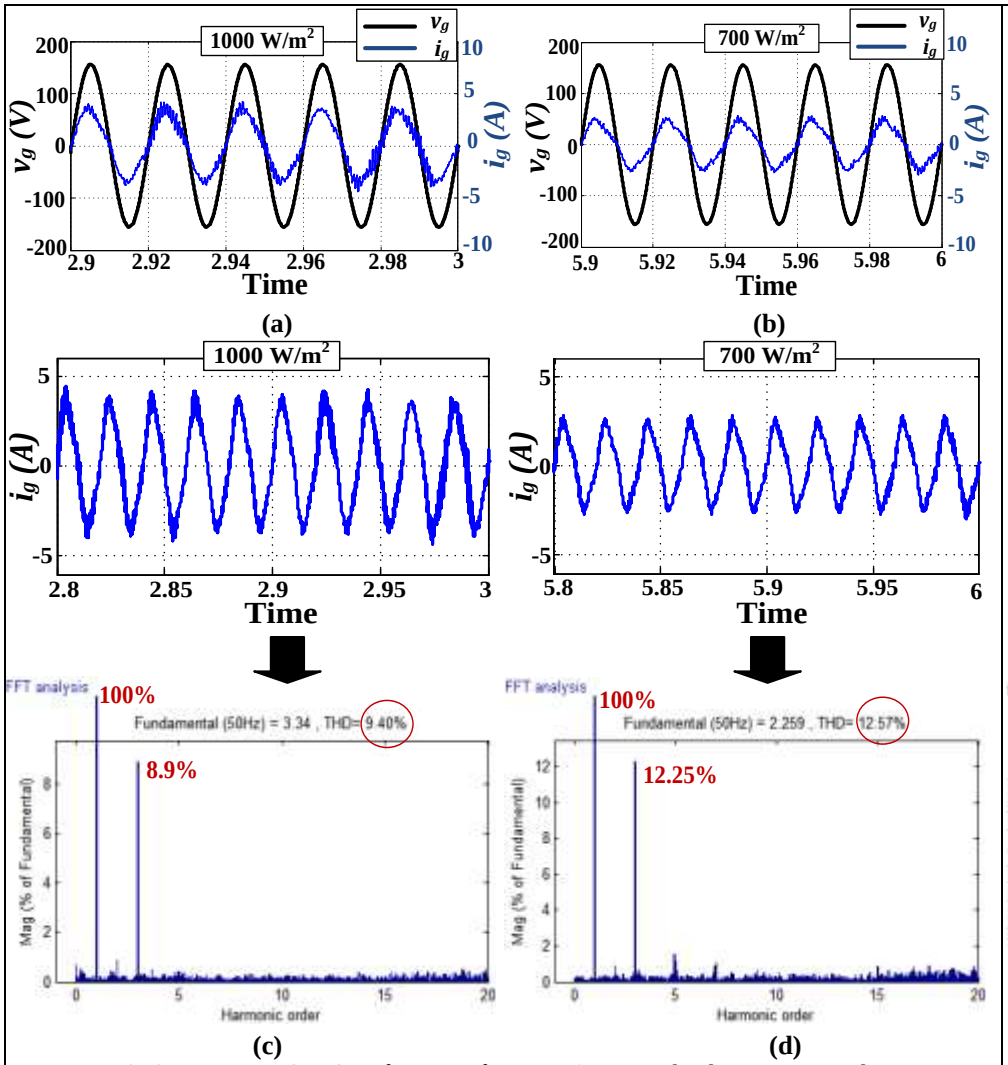

Figure 6.13. Zoom into CPRC performance for L_{dc}= 50 mH; grid voltage versus grid current, and grid current with its FFT analysis at (a), (c) 1000 W/m^2, and (b), (d) 700 W/m^2.

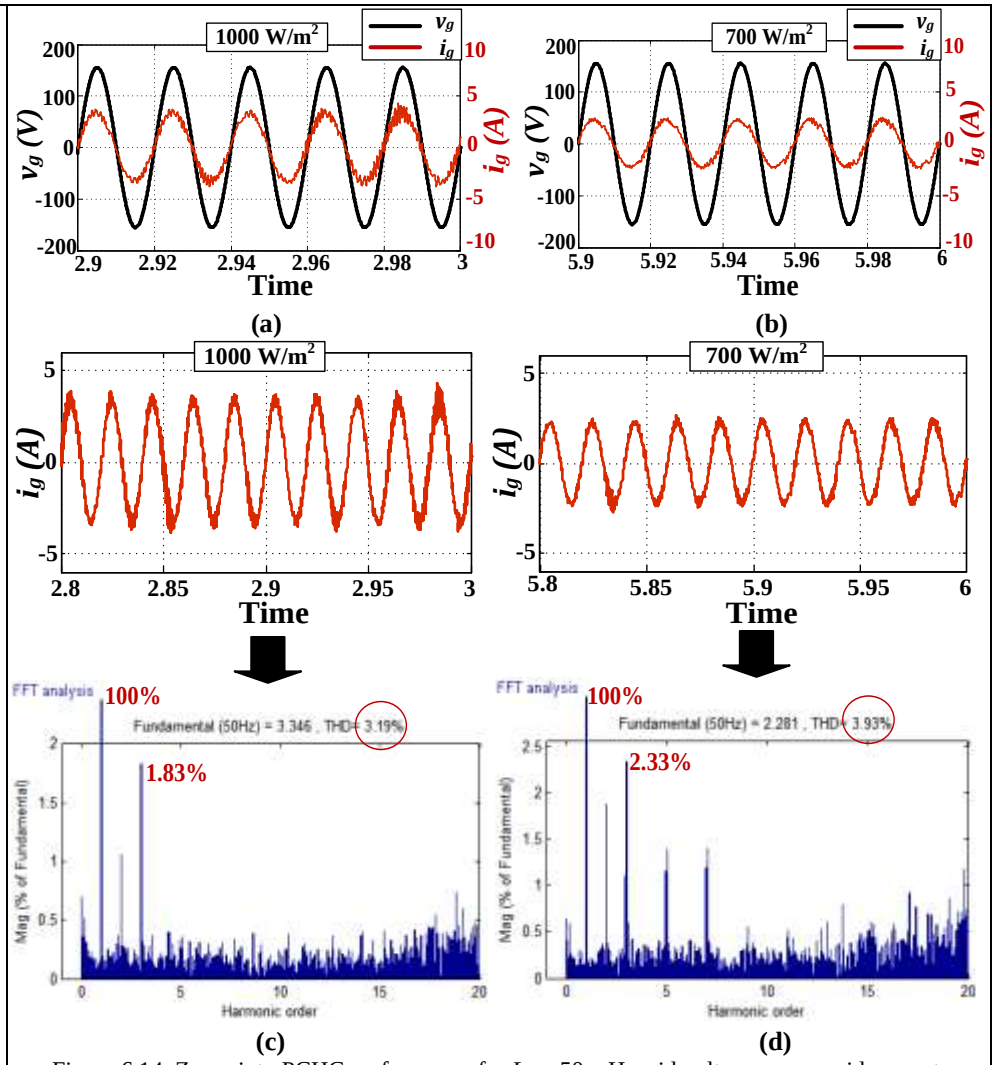

Figure 6.14. Zoom into PCHC performance for L_{dc}= 50 mH; grid voltage versus grid current, and grid current with its FFT analysis at (a), (c) 1000 W/m^2, and (b), (d) 700 W/m^2.

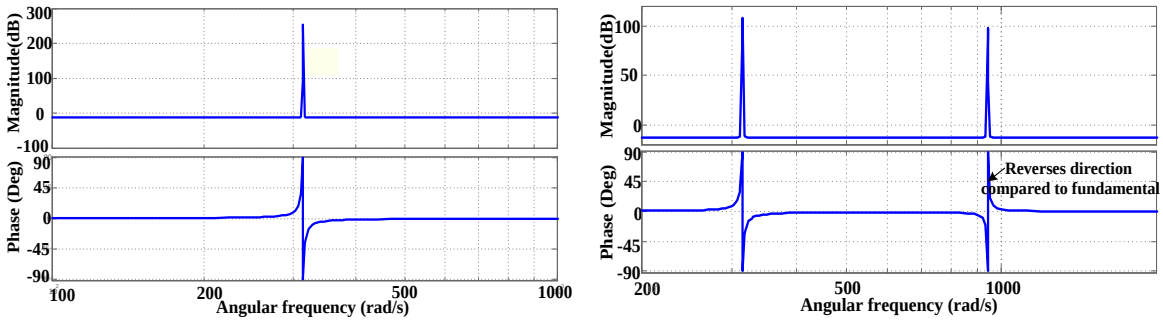

(a) (b)

Figure 6.15. Bode plots for (a) CPRC, (b) PCHC applied in the simulations.

6.4 Experimental results

The effectiveness of the proposed cascaded harmonic compensator (PCHC), associated with a single-phase single-stage grid-tied CSI, is verified experimentally when compared to the conventional proportional resonant controller (CPRC). However, to hold a valid practical comparison, it is mandatory for both controllers to be tested under similar conditions. Hence, a low-cost simulating circuit is used to emulate PV system operation, with the schematic diagram shown in Figure 6.16 (a) and the *V-I-P* curve shown in Figure 6.16(b). A PWM modulated CSI, with $f_{sw(i)}$=15 kHz, is connected to the PV emulator output to boost the output voltage, track the maximum power point, and interface the PV system to the grid. A single-phase autotransformer is utilized to emulate the power grid while a TMS320F28335 DSP is used to generate the PWM signals and realize the proposed feedback loop controllers. The test rig photograph is shown in Figure 6.16 (c) and the implemented algorithms are shown in Appendix D.2.3.

Both the proposed and the conventional PR controllers are tested for L_{dc}= 150 mH under a step decrease in the PV simulator power (from 67.5W to 47W) by opening the switch 'S'. Figure 6.17 parts (a) and (b) show voltage, current and power at the CSI DC-side and grid side respectively in the case of CPRC while Figure 6.18 parts (a) and (b) show those of PCHC. Both controllers allow the CSI to successfully track the PV maximum power at both power levels, and both have the same conversion efficiency.

Figures 6.19, 6.20, 6.21 and 6.22 zoom into the system response when applying CPRC and PCHC. Figure 6.19 parts (a) and (b) show the near sinusoidal inverter output voltage at the higher and lower power levels respectively with CPRC while Figure 6.20 parts (a) and (b) show those for PCHC. Figure 6.21 parts (a) and (b) show the near unity power factor achieved at both power levels with CPRC while Figure 6.22 parts (a) and (b) show those in PCHC case. However, Figure 6.21 parts (c) and (d) show the distorted grid current

experienced by the conventional PR control with a THD beyond IEEE 519 standards (12.26% and 12.97% at higher and lower power levels respectively). When studying grid current FFT analysis in the case of CPRC, the third and fifth order components are the most dominant harmonics in grid current waveform spectrum (10.7% and 4% at higher power level and 11.3% and 5% at lower level for the third and fifth harmonics respectively). Hence, a PR controller is designed with a cascaded harmonic compensator tuned at 150 and 250 Hz in order to minimize harmonics at these frequencies. The impact of the PCHC is shown in Figure 6.22 parts (c) and (d) where the grid current third order harmonic is reduced to 3.4% and 3.7% and the fifth order harmonic is reduced to 2.5% and 3% at the higher and lower power levels respectively. This result in a minimized grid current THD of 5.2% and 5.8% at both levels respectively. Hence, the effectiveness of the PCHC is verified experimentally.

Bode plots of the conventional PR controller are shown in Figure 6.23 versus the Bode plots of the PR controller proposed in for the experimentation, with its cascaded third and fifth-order harmonic compensator units.

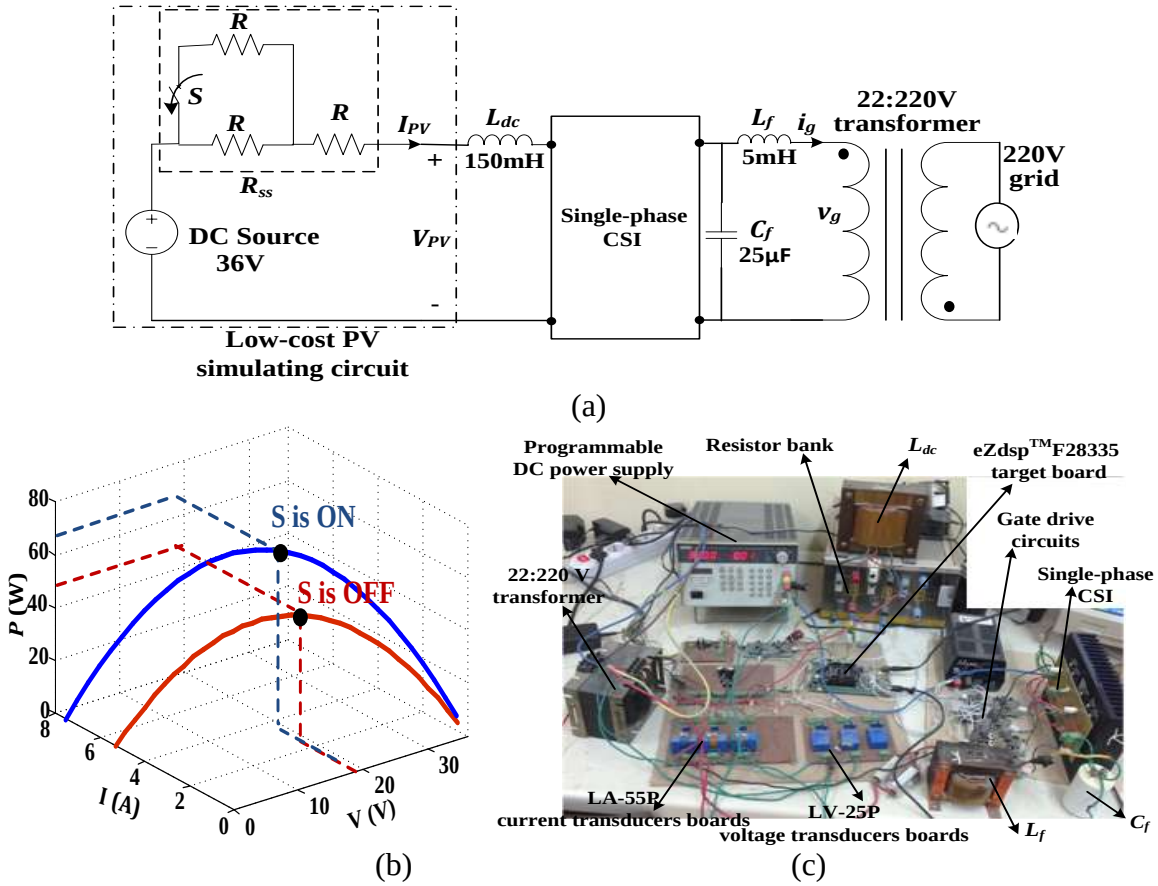

Figure 6.16. Experimental setup (a) schematic diagram, (b) *P-I-V* curves of PV emulator under two power levels, and (c) test rig photography.

L_{dc}= 150mH, Conventional Proportional Resonant Controller (CPRC)	L_{dc}= 150mH, Proposed Cascaded Harmonic Compensator (PCHC)

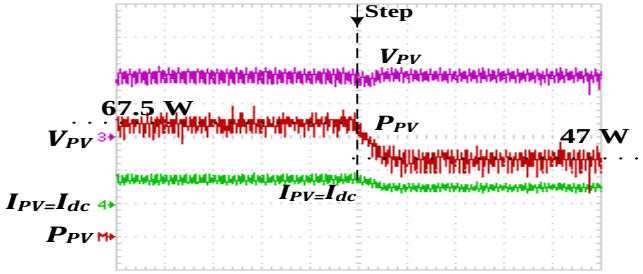

100 ms/div, ch3:10V/div, ch4:5A/div, chM: 20VA/div

(a)

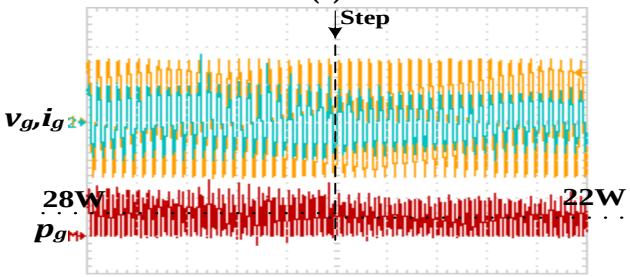

100 ms/div, ch1:20V/div, ch2:2A/div, chM: 50VA/div

(b)

Figure 6.17. System performance applying CPRC (a) PV voltage, current and power and (b) grid voltage, current and power.

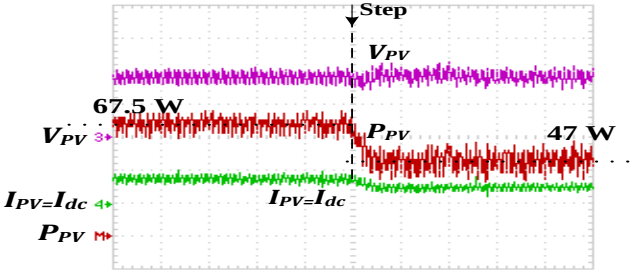

100 ms/div, ch3:10V/div, ch4:5A/div, chM: 20VA/div

(a)

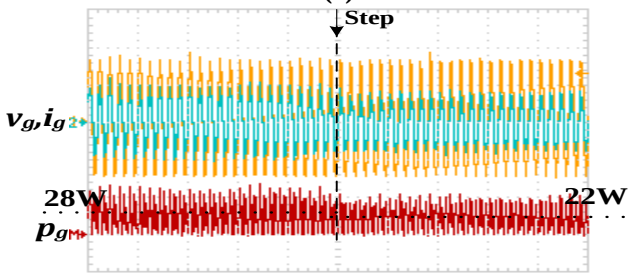

100 ms/div, ch1:20V/div, ch2:2A/div, chM: 50VA/div

(b)

Figure 6.18. System performance applying PCHC (a) PV voltage, current and power and (b) grid voltage, current and power.

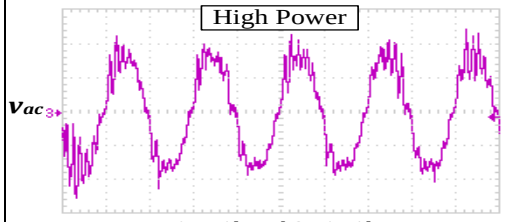

10 ms/div, ch3:20V/div

(a)

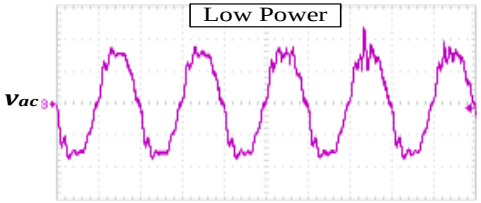

10 ms/div, ch3:20V/div

(b)

Figure 6.19. Zoom into CSI output voltage using CPRC at; (a) high power level and (b) low power level.

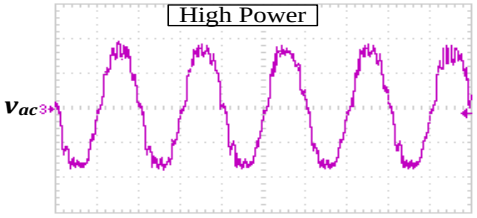

10 ms/div, ch3:20V/div

(a)

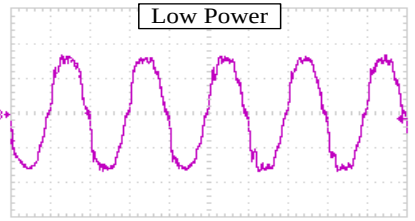

10 ms/div, ch3:20V/div

(b)

Figure 6.20. Zoom into CSI output voltage using PCHC at; (a) high power level and (b) low power level.

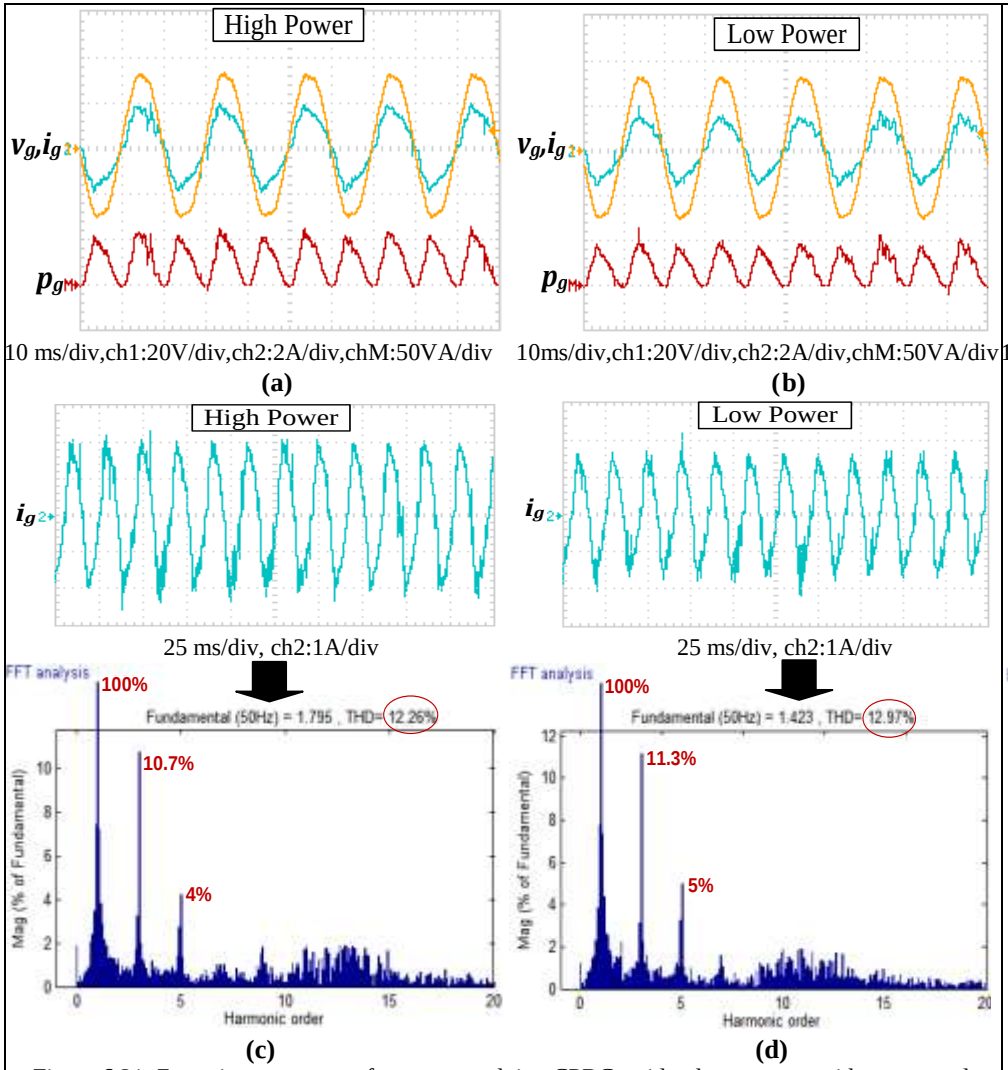

Figure 6.21. Zoom into system performance applying CPRC; grid voltage versus grid current and power, and grid current with its FFT analysis at (a), (c) high power level, and (b), (d) low power level.

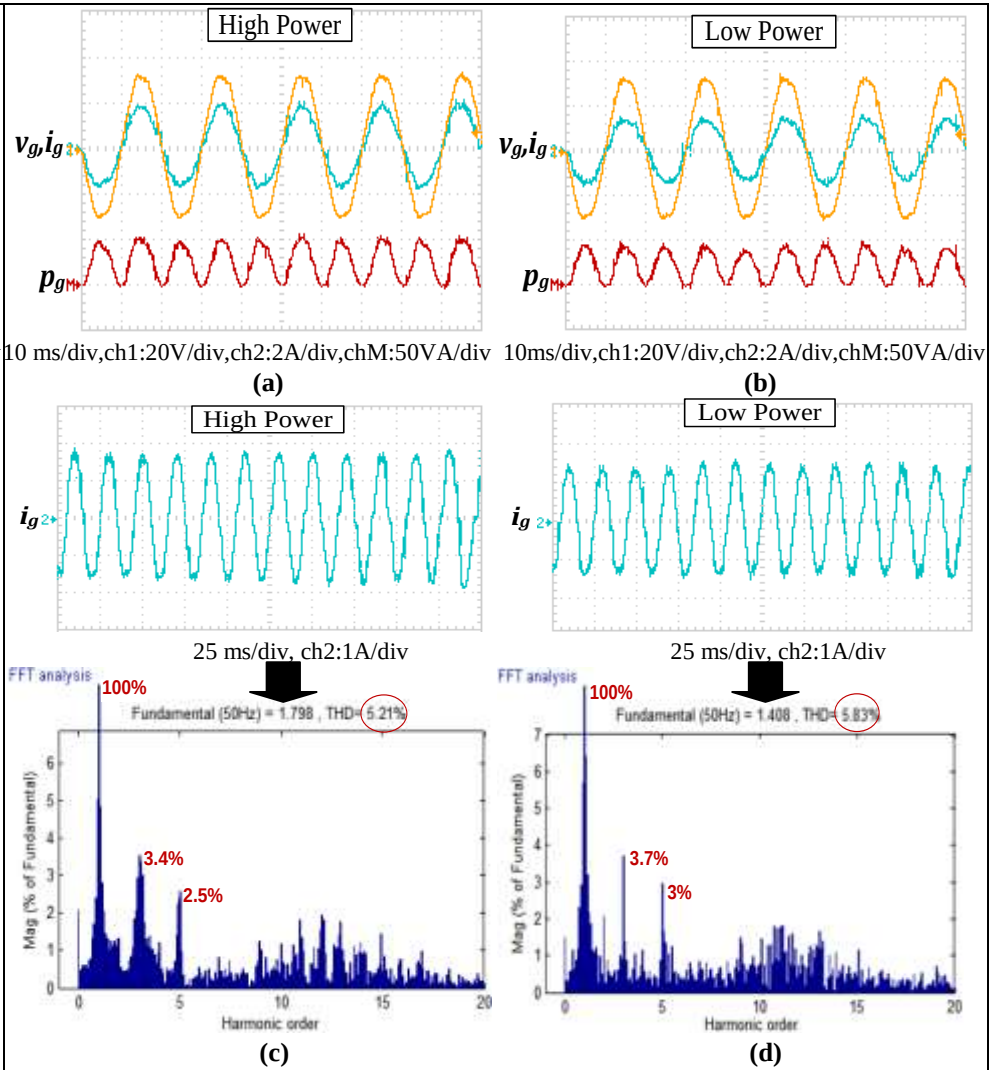

Figure 6.22. Zoom into system performance applying PCHC; grid voltage versus grid current and power, and grid current with its FFT analysis at (a), (c) high power level, and (b), (d) low power level.

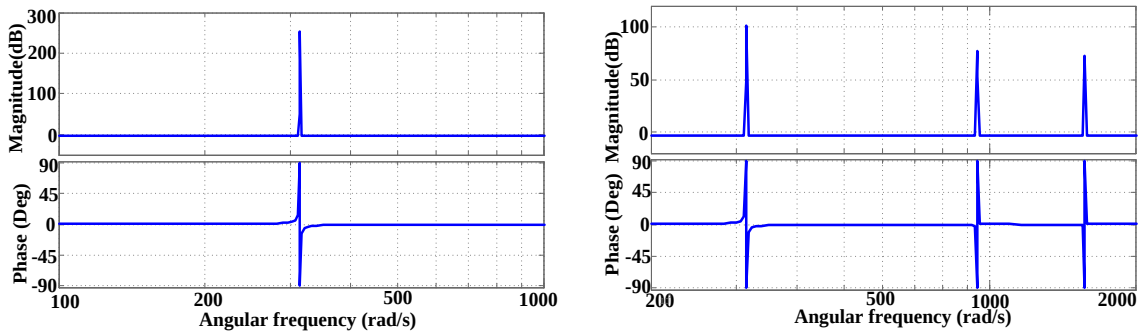

(a) (b)

Figure 6.23. Bode plots for (a) CPRC and (b) PCHC applied in the experimentation.

6.5 Summary

Modelling and design of a single-phase single-stage grid-tied PV CSI was presented in this chapter together with its enhanced PWM switching technique and proposed control loops. Reducing the CSI DC-link inductor reduces system cost and size. Also it improves system dynamic response, decreases losses and enhances efficiency as verified by the simulation results. However, this occurs at the cost of increased PV power oscillation and more even harmonics in the DC-link current. This is reflected at the grid side in the form of low-order odd harmonics resulting in a distorted grid current. To overcome this, the performance of the conventional PR controller, applied in the inverter inner grid current loop, is modified by adding cascaded resonant control units (cascaded harmonic compensator) tuned at the grid current low-order harmonics. Hence, these are selectively eliminated and the grid current quality is improved to meet IEEE519 standards. The feasibility and effectiveness of the proposed cascaded PR controller have been established by simulation and practically.

However, the presented system may show considerably decreased efficiency at very low irradiance levels owing to the low power density of the CSI with losses experienced in its DC-link inductor. Moreover, under severe variation in the irradiance level, the proposed controller may show degraded performance since its parameters are designed at certain conditions and far away from these conditions, the controller may need tuning.

References

[6.1] S. B. Kjaer, J. K. Pedersen, and F. Blaabjerg, "A Review of Single-phase Grid Connected Inverters for Photovoltaic Modules", IEEE Trans. Industry Applications, Vol. 41, No. 5, 2005, pp.1292-1306.

[6.2] Y. Zhou, et al, "Coupled-inductor Single-stage Boost Inverter for Grid-connected Photovoltaic System", IET Power Electronics, Vol. 7, No. 2, 2014, pp. 259–270.

[6.3] Y. M. Chen, C. H. Chang, and H. C. Wu, "DC-link Capacitor Selections for the Single-phase Grid-connected PV System", in Proc. IEEE International Power Electronics and Drive Systems Conference (PEDS), 2009, pp. 72 – 77.

[6.4] K. Hirachi, et al, "Pulse Area Modulation Control Implementation for Single-phase Current Source-fed Inverter for Solar Photovoltaic Power Conditioner," in Proc. IEEE Power Electronic Drives and Energy Systems for Industrial Growth Conference,1998, pp. 677-682.

[6.5] R. T. H. Li, H. S. H. Chung, and T. K. M. Chan, " An Active Modulation Technique for Single-Phase Grid-Connected CSI", IEEE Trans. on Power Electronics, Vol. 22, No. 4, July 2007, pp. 1373-1382

[6.6] G. Ertasgin, et al, "Analysis and Design of Energy Storage for Current-Source 1-ph Grid-Connected PV Inverters", in Proc. IEEE Applied Power Electronics Conference and Exposition (APEC), 2008, pp. 1229-1234.

[6.7] H. Komurcugil, "Steady-state Analysis and Passivity-based Control of Single-phase PWM Current-source Inverters", IEEE Trans. on Industrial Electronics, Vol. 57, No. 3, March 2010, pp. 1026-1030.

[6.8] A. Darwish, et al, “Single phase Grid-connected Current Source Inverter: Mitigation of Oscillating Power Effect on the Grid Current”, in Proc. IET Conf. Renewable Power Generation, September 2011, pp. 1–7.

[6.9] B. N. Alajmi, et al, " Single-Phase Single-Stage Transformer less Grid-Connected PV System", IEEE Trans. on Power Electronics, Vol. 28, No. 6, June 2013, pp. 2664-2676.

[6.10] Y. Ohnuma, K. Orikawa, and J. Itoh, "A Single-Phase Current-Source PV Inverter With Power Decoupling Capability Using an Active Buffer", IEEE Trans. Industry Applications, Vol. 51, No. 1, 2015, pp. 531-538.

[6.11] B.Wu, High-power Converters and AC Drives Handbook, John Wiley & Sons Inc., 2006.

[6.12] A. K. Abdelsalam, et al, "Simplified Generic On-line PWM Technique for Single Phase Grid Connected Current Source Inverters", in Proc. IEEE Applied Power Electronics Conference and Exposition (APEC), 2012, pp. 1398-1403.

[6.13] M.H. Rashid, Power Electronics Handbook, Butterworth-Hinemann, 2011.

[6.14] S. V. Araújo, P. Zacharias, and R. Mallwitz, "Highly Efficient Single-phase Transformerless Inverters for Grid-connected Photovoltaic Systems", IEEE Trans. Industrial Electronics, Vol. 57, No. 9, September 2010, pp. 3118-3128.

[6.15] N. A. Ninad and L. A. C. Lopes, "Operation of Single-phase Grid-connected Inverters with Large DC Bus Voltage Ripple", in Proc. IEEE Electrical Power Conference (EPC), 2007, pp. 172-176.

[6.16] R. J. Wai and W. H. Wang, "Grid-connected Photovoltaic Generation System", IEEE Trans. on Circuits and Systems, Vol. 55, No. 3, pp. 953- 964, April 2008.

[6.17] M. Ciobotaru, R. Teodorescu and F. Blaabjerg, "Control of Single-stage Single-phase PV Inverter", in Proc. IEEE European Power Electronics and Applications Conference (EPE), 2005, pp.1-10.

[6.18] D. Zammit, C. Spiteri Staines, and M. Apap, "Comparison between PI and PR Current Controllers in Grid Connected PV Inverters", International Journal of Electrical, Robotics, Electronics and Communications Engineering, Vol. 8, No. 2, 2014, pp. 217-222.

[6.19] S. Fukuda and T. Yoda, “A Novel Current-tracking Method for Active Filters Based on a Sinusoidal Internal Model”, IEEE Trans. Industrial Electronics, Vol. 37, No. 3, 2001, pp. 888–895.

[6.20] X. Yuan, et al, “Stationary-frame Generalized Integrators for Current Control of Active Power Filters with Zero Steady-state Error for Current Harmonics of Concern under Unbalanced and Distorted Operating Conditions”, IEEE Trans. Industrial Applications, Vol. 38, No. 2, 2002, pp. 523–532.

[6.21] R. A. Mastromauro, M. Liserre, and A. D. Aquila, "Control Issues in Single-stage Photovoltaic Systems: MPPT, Current and Voltage Control", IEEE Trans. on Industrial Informatics, Vol. 8, No. 2, May 2012, pp. 241-254.

[6.22] R. Teodorescu and F. Blaabjerg, "Proportional-resonant Controllers. A New Breed of Controllers Suitable for Grid-connected Voltage-source Converters", in Proc. OPTIM 2004, pp. 9–14.

[6.23] R. Teodorescu, et al, "Proportional-resonant Controllers and Filters for Grid-connected Voltage-source Converters", in Proc. IEE Electric Power Applications, Vol. 153, No. 5, September 2006, pp. 750-762.

[6.24] R. Teodorescu, et al, " A New Control Structure for Grid-Connected LCL PV Inverters with Zero Steady-State Error and Selective Harmonic Compensation", in Proc. IEEE Applied Power Electronics Conference and Exposition (APEC), 2004, pp. 580-589.

[6.25] M. Ciobotaru, et al, "PV Inverter Simulation using MATLAB/Simulink Graphical Environment and PLECS Blockset", in Proc. IEEE Industrial Electronics Conference (IECON), 2006, pp. 5313 – 5318.

[6.26] A. Timbus, et al, "Evaluation of Current Controllers for Distributed Power Generation Systems", IEEE Trans. Power Electronics, Vol. 24, No. 3, 2009, pp. 654-662.

[6.27] IEEE, "IEEE Recommended Practices and Requirements for Harmonic Control in Electric Power System", IEEE Std. 519-1992.

Chapter Seven

Conclusions

7.1 General conclusion

Photovoltaic (PV) energy is gaining increased attention, among different renewable energy resources, for its capabilities of direct electric energy conversion, minimal environmental impact, low operation cost, and flexibility in size. With no machinery or noise, PV modules have proven to be reliable maintenance-free sources convenient in distributed generation, and many stand-alone applications.

However, PV modules non-linear behaviour and dependency on environmental conditions are a challenge facing the PV sector's penetration into the energy market. Hence, PV maximum power point tracking (MPPT) is mandatory to maximize PV system efficiency. A MPPT technique's performance and implementation complexity depend mainly on the algorithm structure, adopted step-size and the nature of the applied converter control scheme. Directly generating the converter duty ratio shows the simplest control scheme however at the cost of high power oscillation around the MPP. Thus, the applied step-size should be enhanced to eliminate this oscillation. The algorithm structure mainly affects the microcontroller choice. MPPT algorithms, with minimal computational burden, are efficiently implemented by low-cost microcontrollers which in turn reduces system costs.

PV sources are increasingly being connected to utility grids for best utilization of their produced electric power. For successful grid interfacing of a PV source, requirements of MPPT, voltage level transformation according to the available PV source voltage, and DC/AC conversion are mandatory. A number of grid-tied PV inverter configurations exist to achieve this interface. A single-phase two-stage topology employs a DC/DC converter stage before the voltage source inverter (VSI) stage, for decoupling and voltage boosting purposes. The first stage achieves MPPT while the second VSI stage features two control loops; outer DC-link voltage control loop and inner grid current control loop. Hence, measurements of PV voltage and current are required to detect the PV power and achieve MPPT. Sensing the DC-bus voltage is mandatory for the VSI outer control loop and measuring grid voltage and current is essential for the VSI inner control loop. This requires many sensors which add to system cost and size. Hence, sensorless control techniques are

considered a good solution for the two-stage topology in order to reduce the number of measurements and sensors and in turn decrease system footprint and cost.

Single-stage grid-tied PV topologies employ a single DC/AC inverter to achieve functions of MPPT together with PV-grid interfacing, thus reducing system stage count and size, and increasing conversion efficiency. However, with such a topology, an H-bridge VSI must be followed by a step-up transformer which adds bulk, cost and losses. But current source inverters (CSIs) are highly competitive with their inherent voltage boost functionality, intrinsic short-circuit proof, and higher reliability. However, the input DC current of single-phase CSIs inherently contains even harmonics which affect PV MPPT, reduce PV lifetime, and when modulated by PWM signals produce odd-order harmonics on the grid side. Conventionally, to suppress these DC-side harmonics, a costly bulky inductor is used in the CSI DC-link. In order to use a smaller size inductor, harmonic compensator units can be added to the applied proportional resonant grid current controller, minimizing grid current harmonics.

7.2 Author's contribution

The contributions of this thesis are presented mainly in chapters four, five and six and can be summarized in a number of points as follows:

- Three different control schemes were studied to control DC/DC converter switching applied to PV MPPT. This includes a direct control scheme, closed loop control with classical PI controllers then using adaptive fuzzy-tuned PI controllers.
- A modified Inc.Cond. technique was proposed featuring elimination of its division computations, a modified variable-step and direct converter control scheme. High steady-state power oscillation, resulting from the direct control scheme, is minimized by the enhanced performance of the proposed variable step which depends solely on PV power change. The proposed technique does not only have the merits of superior steady-state and transient performance but also offers simple implementation and control structure enabling it to be implemented in low-cost microcontrollers.
- The proposed MPPT technique, practically implemented in a low-cost Atmega 328 microcontroller**,** was compared with some experimental prototypes presented in recent publications. It was concluded that the proposed technique achieves the best compromise between MPPT performance and the employed microcontroller cost.

However, the proposed technique has not been tested under very low irradiance levels or partial shading conditions where its performance may differ.

- A novel DC-link voltage sensorless control technique was proposed for single-phase two-stage grid-connected PV string system, eliminating the need of a VSI DC-link voltage control loop. This reduces system footprint, cost, control complexity, and number of required sensors along with enhancing dynamic performance at transients. However, the proposed sensorless technique was not tested during grid faults or DC-link capacitor failure where it can show degraded performance and limitations in the inverter switches' protection when compared to the robust conventional technique.
- A single-phase, single-stage CSI-based photovoltaic system for grid connection was proposed. A control scheme and an enhanced sinusoidal modulating technique were proposed for the CSI to achieve the functions of MPPT and grid-interfacing. However, the presented system may show considerably decreased efficiency at low irradiance levels owing to the low power density of the CSI with high losses experienced in its bulky DC-link inductor.
- To allow a non-bulky smoothing inductor at the considered CSI DC-link, a cascaded proportional resonant controller was used, in the grid current control loop. This is a PR controller associated with harmonic compensator units tuned at the grid current low order harmonics to be selectively mitigated. Hence, grid current quality and system efficiency are simultaneously improved.

7.3 Suggestion for future research

The research performed in this thesis addresses some PV system challenges related to maximum power point tracking under varying weather conditions, grid-interfacing topologies for the PV system and power quality issues. Suggestions for future research are:

- A PV module has a single maximum power point, at any given irradiance and cell temperature. However, in case of partial shading, it is possible to have multiple local maxima, but overall there is still only one true MPP. Thus, PV MPPT, during partial shading conditions, is an important issue that should be addressed. Hence, the modified Inc.Cond. technique should be tested under these conditions and its performance should be enhanced to cope with such cases.
- The proposed sensorless control technique, applied in the two-stage PV grid-tied system, should be tested during grid faults to investigate its performance and suggest

enhancements. Moreover, a DC-link voltage limitation mechanism should be addressed to protect inverter switches during capacitor failures.

- In this thesis, ideal proportional resonant controllers are employed in the grid current control loops of the grid-connected VSI and CSI. However, for severe grid frequency variations, non ideal PR controller can be considered to give wider bandwidth around the resonant frequency.
- In case of severe environmental changes, adaptively-tuned cascaded PR controllers should be considered in the grid current control loop of single-phase single-stage CSIs with non-bulky DC-link inductors. Hence, the controller gains are continuously adjusted, with varying conditions, to maintain minimum grid current harmonics.
- Grid-tied PV systems encounter some challenges such as islanding and fault-ride-through issues that can be studied.
- Grid interfacing options of PV, through three-phase systems and cascaded multilevel inverters, can be investigated for high power PV applications.

Appendix A: Current Harmonic Limits in IEEE Std. 519-1992

Table I: Current Harmonic Limits

Maximum Harmonic Current Distortion in % of I_L						
Individual Harmonic Order (Odd Harmonics)						
I_{SC} / I_L	<11	11≤h<17	17≤h<23	23≤h<35	35≤h	TDD
<20*	4.0	2.0	1.5	0.6	0.3	5.0
20<50	7.0	3.5	2.5	1.0	0.5	8.0
50<100	10.0	4.5	4.0	1.5	0.7	12.0
100<1000	12.0	5.5	5.0	2.0	1.0	15.0
>1000	15.0	7.0	6.0	2.5	1.4	20.0
Even harmonics are limited to 25% of the harmonic limits, TDD refers to Total Demand Distortion and is based the average maximum demand current at the fundamental frequency, taken at PCC.						
*All power generation equipment is limited to these values of current distortion regardless of I_{SC}, I_L.						
I_{SC} = Maximum short current at the PCC I_L = Maximum demand load current (fundamental) at the PCC h = Harmonic number						

Appendix B: Specifications of the Applied PV Modules

KD135SX_UPU modules are used in chapter four and five whereas an ASE-285-DGF/17 module is used in chapter six.

Table B.1. KD135SX_UPU module specifications at standard test conditions

Nominal Short Circuit Current ($I_{SC\text{-}n}$)	8.37	A
Nominal Open Circuit Voltage ($V_{OC\text{-}n}$)	22.1	V
Maximum Power Current ($I_{MPP\text{-}e}$)	7.63	A
Maximum Power Voltage ($V_{MPP\text{-}e}$)	17.7	V
Maximum Output Power ($P_{MPP\text{-}e}$)	135	W
Temperature Coefficient of I_{SC} (K_I)	$5.02e^{-3}$	$A/^oC$
Temperature Coefficient of V_{OC} (K_V)	$-8e^{-2}$	$V/^oC$
Series Cells (N_s)	36	----

Table B.2. ASE-285-DGF/17 module specifications at standard test conditions

Nominal Short Circuit Current ($I_{SC\text{-}n}$)	18.4	A
Nominal Open Circuit Voltage ($V_{OC\text{-}n}$)	20	V
Maximum Power Current ($I_{MPP\text{-}e}$)	16.8	A
Maximum Power Voltage ($V_{MPP\text{-}e}$)	17	V
Maximum Output Power ($P_{MPP\text{-}e}$)	285	W
Temperature Coefficient of I_{SC} (K_I)	$18.4e^{-3}$	$A/^oC$
Temperature Coefficient of V_{OC} (K_V)	$-7.6e^{-2}$	$V/^oC$
Series Cells (N_s)	216	------

New Release
Greater Field Performance

http://www.wholesalesolar.com/solar-panels.html

KYOCERA

135 WATT

HIGH EFFICIENCY MULTICRYSTAL
PHOTOVOLTAIC MODULE

KD135SX-UPU

NEC 2008 Compliant
UL1703, Class C
CLASS I, DIV II

c UL us

CUTTING EDGE TECHNOLOGY

As a pioneer with 35 years in solar, Kyocera demonstrates leadership in the development of solar energy products. Kyocera's *Kaizen* Philosophy, commitment to continuous improvement, is shown by repeatedly achieving world record cell efficiencies.

Kyocera Quality Built In:

- New frame technology allows for end mounting under 2400 Pa (50 psf) or wind speeds of 130 mph (ASTM E1830) and traditional mounting under 5400 Pa (113 psf) to support increased snow load
- UV stabilized, aesthetically pleasing black anodized frame
- Supported by all major mounting structure manufacturers
- Easily accessible grounding points on all four corners for fast installation
- Proven junction box technology

Kyocera manufactures and assembles solar cells and modules at its own worldwide production sites using a true vertical integration process. This superior approach gives Kyocera complete control over every step of the manufacturing process, producing modules with the industry's tightest power tolerance, promising high quality and efficiency.

- Built-In Quality for Off-Grid Applications
- Proven Superior Field Performance
- Tight Power Tolerance
- 20 Year Warranty
- 5 Year Workmanship Warranty

SOLAR by KYOCERA

KD135SX-UPU

http://www.wholesalesolar.com/solar-panels.html

ELECTRICAL CHARACTERISTICS

Current-Voltage characteristics of Photovoltaic Module KD135SX-UPU at various cell temperatures

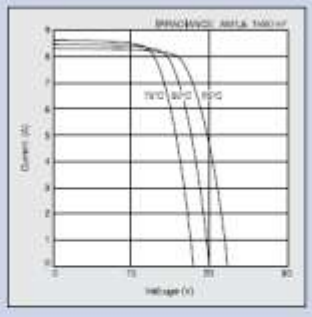

Current-Voltage characteristics of Photovoltaic Module KD135SX-UPU at various Irradiance levels

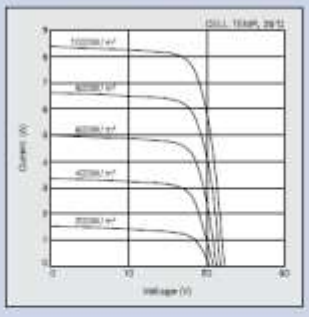

SPECIFICATIONS

■ Physical Specifications

Unit : mm (in.)

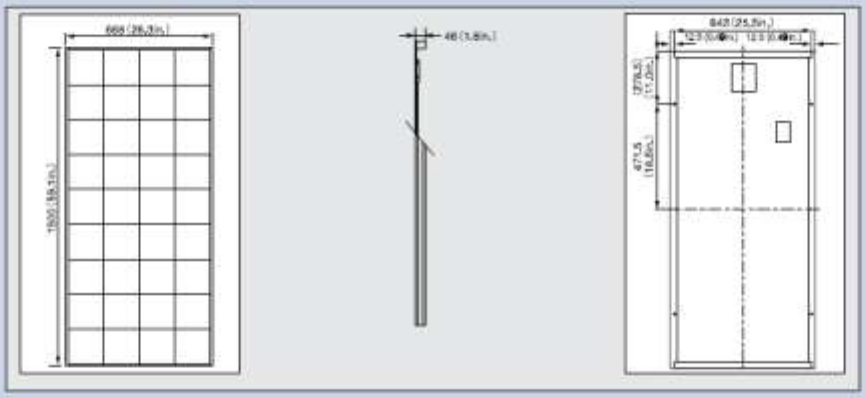

■ Specifications

■ Electrical Performance under Standard Test Conditions (*STC)	
Maximum Power (Pmax)	135W (+5%/–5%)
Maximum Power Voltage (Vmpp)	17.7V
Maximum Power Current (Impp)	7.63A
Open Circuit Voltage (Voc)	22.1V
Short Circuit Current (Isc)	8.37A
Max System Voltage	600V
Temperature Coefficient of Voc	-8.0×10^{-3} V/°C
Temperature Coefficient of Isc	5.02×10^{-3} A/°C

*STC : Irradiance 1000W/m², AM1.5 spectrum, cell temperature 25°

■ Electrical Performance at 800W/m², *NOCT, AM1.5	
Maximum Power (Pmax)	95W
Maximum Power Voltage (Vmpp)	15.7V
Maximum Power Current (Impp)	6.10A
Open Circuit Voltage (Voc)	20.0V
Short Circuit Current (Isc)	6.79A

*NOCT (Nominal Operating Cell Temperature) 47.8°C

■ Cells	
Number per Module	36
■ Module Characteristics	
Length x Width x Depth	[illegible]
Weight	12.5kg(27.5lbs.)
■ Junction Box Characteristics	
Length x Width x Depth	[illegible]
IP Code	IP65
■ Others	
*Operating Temperature	–40°–90°C
Maximum Fuse	15A

*The temperature is based on cell temperature

ISO 9001 and ISO 14001 Certified and Registered

KYOCERA

www.kyocerasolar.com
800-223-9580 toll free 800-523-2329 fax

UL Class A Fire Rated

A·S·E

World's Most Powerful Battery Charging Photovoltaic Module with ASE's Crystal Clean™ EFG Cell Technology

ASE-300-DGF/17

ASE-300-DGF/17 connection box with bypass diodes. Module – module wiring with MC®-plug.

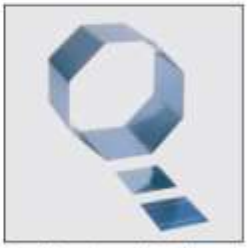

Crystalline octagonal Si tubes are drawn from the melt. There are no losses due to sawing.

Designation:
DG = Double Glass
F = Frame
/17 = Nominal Voltage at STC

The ASE-300-DGF/17 is ASE's low-voltage, large-area module typically used in systems charging 12, 24 and 48 volt batteries. The ASE 300 has been a power workhorse across the world serving everything from telecommunication sites to remote homes. Four of these modules in series create the perfect 1 kW/48 volt building block for grid-connected home systems with emergency battery back up. People who want a power system that they can depend on choose the ASE-300-DGF/17. Give your PV system the ASE 300 advantage.

Design Advantage

The size, power and completeness in this module make designing and installing a system a breeze.

Reliability Advantage

- Our advanced proprietary encapsulation system overcomes the decline in module performance associated with degradation of traditional EVA encapsulant.
- Weather barrier system on both the front and back of the module protects against tear, penetration, fire, electrical-conductance, delamination, and moisture.
- Our patented no-lead high reliability soldering system ensures long life, while making the module environmentally benign for disposal or recycling.

Quality Advantage

ASE Americas' quality program is focused on meeting or exceeding expected performance and reducing system losses:

- Each module is individually tested under ASE Americas' calibrated solar simulator.
- Module-module wiring losses are included in the rating.
- Each of the 216 crystalline silicon cells is inspected and power matched.

Installation Advantage

We designed the ASE-300-DG/17 to save time and cost:

- Large area requires fewer interconnects and structural members.
- Module-module wiring is incorporated in the module.
- Wiring comes neatly clipped inside module frame – no need to secure wiring in the field.
- Unique ASE quick-connects reduce source circuit wiring time to minutes.

Certification Advantage

- To provide our customers with the highest level of confidence, the ASE-300-DG/17 is independently IEEE 1262 and IEC 1215 certified. It is UL (Underwriters Laboratories) listed with the only Class A fire rating in the industry.

Available Versions

The standard power rating is 285 watts at STC with versions at 300 watts and 265 watts also available. We offer a variety of wiring/connector options. Modules without frames are also available.

ASE Core Advantage

ASE's patented EFG process (Edge-defined Film-fed Growth) produces silicon octagons of correct thickness and width. Energy, hazardous waste and material intensive wafer sawing is replaced by highly efficient advanced laser cutting.

ASE-300-DGF/17

ASE-300-DGF/17

Electrical data

The electrical data applies to standard test conditions (STC):
Irradience at the module level of 1,000 W/m² with spectrum AM 1.5 and a cell temperature of 25° C.

Power (max.)	P_p (watts)	285.0 W	300.0 W	265.0 W
Voltage at maximum-power point	V_p (volts)	17.0 V	17.2 V	16.8 V
Current at maximum-power point	I_p (amps)	16.8 A	17.4 A	15.8 A
Open-circuit voltage	V_{oc} (volts)	20.0 V	20.0 V	20.0 V
Short-circuit current	I_{sc} (amps)	18.4 A	19.1 A	17.3 A

The quoted technical data refer to the usual series cell configuration.
The rated power may only vary by ± 4% and all other electrical parameters by ±10%.
NOCT-value (800 W/m², 20° C, 1m/sec.): 45° C.

Dimensions and weights

Length mm (in)	1,892.3 (74.5")
Width mm (in)	1,282.7 (50.5")
Weight kg (lbs)	46.6 ± 2 kg (107 ± 5 lbs)
Area	2.43 sq meters (26.13 ft sq)

Characteristic data

Solar cells per module	216
Type of solar cell	Multi-crystalline solar cells (EFG process), 10x10 cm²
Connections	10 AWG with Pig-Tails or Quick-Connects Modules come with 2 integrated bypass diodes

Cell temperature coefficients

Power	T_K (P_p)	- 0.47 % / °C
Open-circuit voltage	T_K (V_{oc})	- 0.38 % / °C
Short-circuit current	T_K (I_{sc})	+ 0.10 % / °C

Limits

Max. system voltage	600 V_{DC} U.S.
Operating module temperature	-40...+90° C
Tested wind resistance	Wind speed of 192 km/h (120 mph)

The right is reserved to make technical modifications.

For detailed product drawings and specifications please contact your distributor or our office.

Certifications and Warranty

The ASE-300-DGF/17 has been independently certified to IEC 1215 and IEEE 1262, UL 1703 (Class A Fire rating).
The ASE-300-DGF/17 comes with a 20 year power warranty (see terms and conditions for details).

Current/voltage characteristics with dependence on irradiance and module-temperature.

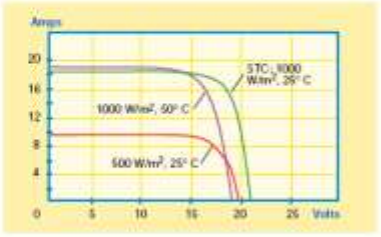

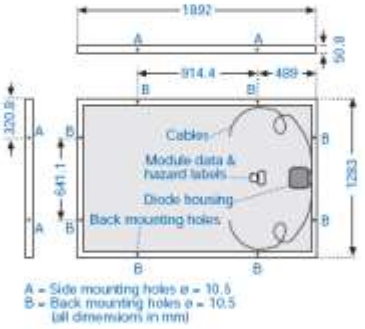

A = Side mounting holes ø = 10.5
B = Back mounting holes ø = 10.5
(all dimensions in mm)

ASE Americas, Inc.
4 Suburban Park Drive
Billerica, MA 01821-3980 USA
Phone 800-977-0777
978-667-5900
Fax 978-663-2868
www.asepv.com e-mail: sales@asepv.com

Photovoltaics from your specialist dealer:

Appendix C: Hardware and Software Environment Introduction

In this section, hardware elements and the simulation package software are introduced.

C.1 Hardware Structure

In this thesis, three practical test-rigs are implemented. The first verifies the modified Inc.Cond. MPPT technique, in chapter four, using DSP TMS320F28335 and ARDUINO-Uno board, based on a low-cost Atmega328 microcontroller. The second test rig investigates the single-phase two-stage grid-connected PV system, discussed in chapter five, which uses a boost chopper followed by a single-phase VSI. Finally, the third rig tests the single-phase single-stage CSI-based grid-tied PV system investigated in chapter six. Hardware elements of each test rig are shown below.

1. First test rig;
    - KD135SX PV panel/ Low-cost PV emulating circuit
    - eZdspTM F28335 board/ARDUINO-Uno board
    - Boost converter
    - Gate drive circuit
    - Current and voltage measuring circuits
    - DC power supply ($\pm$12V for V and I measuring circuits and +5 for gate drive)
    - 3 lead-acid 12 V, 7Ah batteries
2. Second test rig
    - Low-cost PV emulating circuit
    - eZdspTM F28335 board
    - Boost converter
    - Single-phase H-bridge VSI with input DC-link capacitor and output AC L filter
    - Gate drive circuits
    - Current and voltage measuring circuits
    - DC power supply ($\pm$12V for V and I measuring circuits and +5 for gate drive)
    - A 22: 220 V grid coupling transformer

3. Third test rig

- Low-cost PV emulating circuit
- eZdspTM F28335 board
- Single-phase CSI with input DC-link inductor and output AC C-L filter
- Gate drive circuits
- Current and voltage measuring circuits
- DC power supply (±12V for V and I measuring circuits and +5 for gate drive)
- A 22: 220 V grid coupling transformer

C.1.1 PV emulating circuit

This circuit consists of a 35V/10A programmable DC power supply in series with a resistance bank as shown in Figure C.1

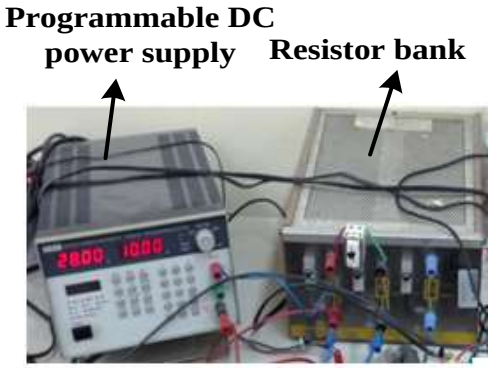

Figure C.1. Low-cost PV emulating circuit

C.1.2 Microcontroller

During practical evaluation, the control strategy is implemented using an embedded controller which is considered the heart of the control system. The controller must have features such as processer speed, storage memory, and programming simplicity. Two microcontrollers are used in this thesis; 32-bit microcontroller TMS320F28335 and its experimenter eZdspTM F28335 board and low-cost Atmega328 microcontroller on an Arduino-Uno board. The main task of the microcontroller is to generate the switching pattern driving the switches of the applied power electronic converter according to the software algorithm of the proposed system.

i. eZdspTM F28335 board

The applied Texas Instruments 32-bit microcontroller TMS320F28335 experimenter board (eZdspTM F28335 board) is shown in Figure (C.2). The eZdsp™ F28335 is a stand-alone card-allowing developers to evaluate the TMS320F28335 digital signal controller (DSC) to determine if it meets their application requirements [C.1]. The module is an excellent platform to develop and run software for the TMS320F28335 processor. To simplify code development and shorten debugging time, a C2000 Code Composer Studio™ driver is provided. In addition, an onboard JTAG connector provides interface to emulators, with assembly language and 'C' high level language debug.

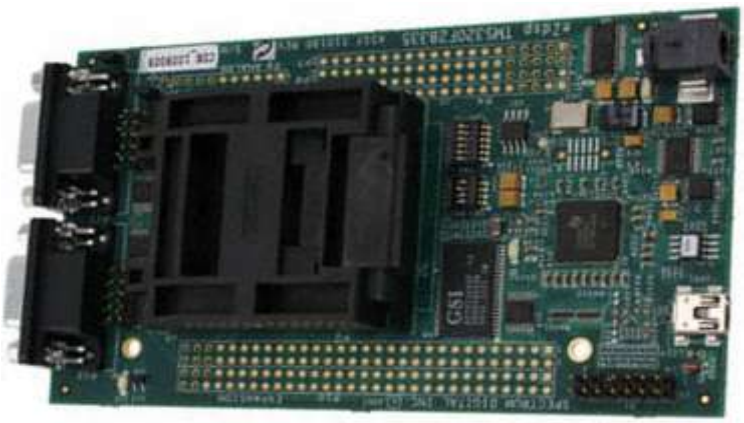

Figure C.2. eZdspTM F28335 board

Features [C.2];

- TMS320F28335 Digital Signal Controller
  - ✓ On chip 32-bit floating point unit
  - ✓ 150 MHz operating speed
  - ✓ Protected in a socket
- Memories
  - ✓ 68K bytes on-chip RAM
  - ✓ 512K bytes on-chip Flash memory
  - ✓ 256K bytes off-chip SRAM memory
- Analogue to digital (A/D) conversion
  - ✓ On chip 12-bit Analog to Digital (A/D) converter with 16 input channel
  - ✓ 80-ns Conversion Rate

- ✓ 2 x 8 Channel Input Multiplexer
- ✓ Two Sample-and-Hold
- ✓ Single/Simultaneous Conversions
- ✓ Internal or External Reference

- Multiple Expansion Connectors (analog, I/O) with Up to 18 PWM (ePWM) Outputs
- Timers
  - ✓ Three 32-Bit CPU Timers
  - ✓ Up to 8 32-Bit Timers
  - ✓ Up to 9 16-Bit Timers (including 6 for ePWMs)
- Input clock of 30 MHz
- I/O Voltage 3.3 V
- 5-volt operation with supplied AC adapter
- On board RS-232 connector with line driver
- On board CAN 2.0 interface with line driver and connector
- On board embedded USB JTAG Controller
- On board IEEE 1149.1 JTAG emulation connector

ii. Arduino-UNO board

The Arduino-UNO is a microcontroller board based on the ATmega328 as shown in Figure C.3 [C.3]. It contains everything needed to support the microcontroller; simply connect it to a computer with a USB cable or power it with an AC-to-DC adapter or battery to get started.

Figure C.3. Arduino-UNO board

Features [C.4];

- ATmega328 microcontroller
  - ✓ AVR® 8-Bit Microcontroller
  - ✓ 20 MHz operating speed
- Memories
  - ✓ 32 KB Flash Memory
  - ✓ 2 KB SRAM 2 KB
  - ✓ 1 KB EEPROM 1 KB
- Analogue to digital (A/D) conversion
  - ✓ 10-bit Resolution
  - ✓ 6 Multiplexed Single Ended Input Channels
  - ✓ 13 - 260 μs Conversion Time
  - ✓ 0 - V_{CC} ADC Input Voltage Range
  - ✓ Free Running or Single Conversion Mode
  - ✓ Interrupt on ADC Conversion Complete
- 14 digital input/output pins (of which 6 can be used as PWM outputs)
- Timers
  - ✓ Two 8-bit Timer/Counters with Separate Prescaler and Compare Mode
  - ✓ One 16-bit Timer/Counter with Separate Prescaler, Compare Mode, and Capture Mode
- A 16 MHz crystal oscillator
- Operating Voltage 5V
- Input Voltage (recommended) 7-12V
- Input Voltage (limits) 6-20V
- A USB connection
- A power jack
- An ICSP header
- A reset button

C.1.3 Power electronic converters

In this thesis, three power electronic converters are used; a DC/DC boost converter in the first and second test rigs for MPPT, a single-phase H-bridge VSI in the second test rig for the PV-grid interface and a single-phase CSI in the third test rig for MPPT and PV-grid interfacing.

i. Boost DC/DC converter

This chopper, as shown in Figure C.4, is composed of a current filtering inductor, an IGBT, a fast recovery diode, a group of heat sinks and a filtering capacitor. The parameters of the boost chopper items are listed in Table C-1.

Table C.1. The boost chopper specifications

Input boost capacitor	1000 μF, 35V
Boost chopper inductor	2.33 mH, 0.5 Ω
Ultrafast IGBT (FGA15N120ANTD) [C.5]	1200 V, 45 A
Fast recovery diode (IXYS DSEI30) [C.6]	1000V, 30A
Switching Frequency	15 kHz

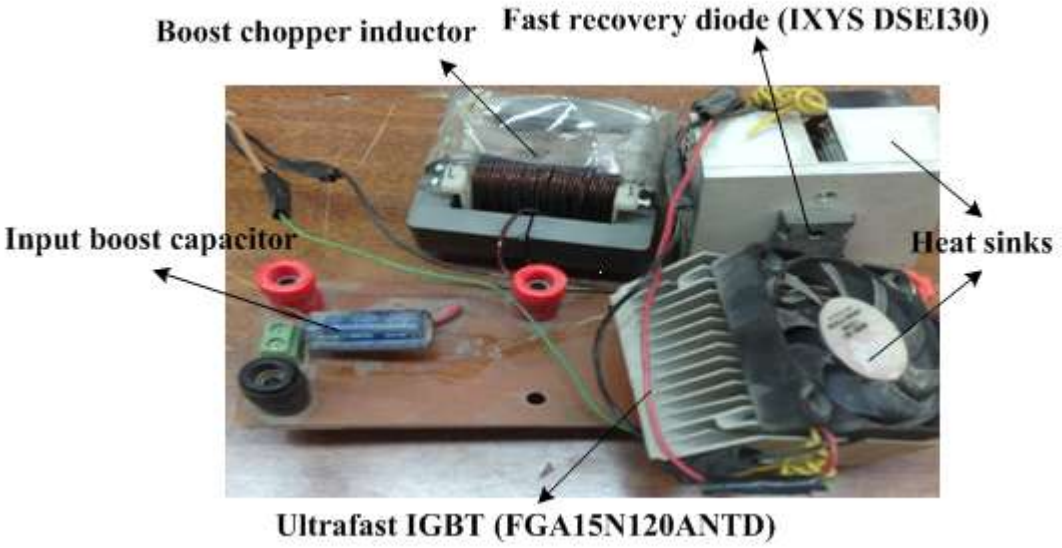

Figure C.4. Boost chopper circuit

ii. Single-phase VSI

The applied single-phase full-bridge voltage source inverter consists of four IGBT switches (S_1-S_4) as shown in Figure C.5(a). For the VSI operation, a 2200μF capacitor, shown in Figure C.5 (b), is utilized at the inverter input to maintain the DC-link voltage constant. A 5mH filtering inductor, shown in Figure C.5 (c), is used at the inverter output for grid current smoothing. VSI parameters are listed in Table C.2.

Table C.2. The applied single-phase VSI specifications

DC-link capacitor	2200μF , 450V
Ultrafast IGBT (FGA15N120ANTD) [C.5]	1200 V, 45 A
PWM carrier Frequency	15 kHz

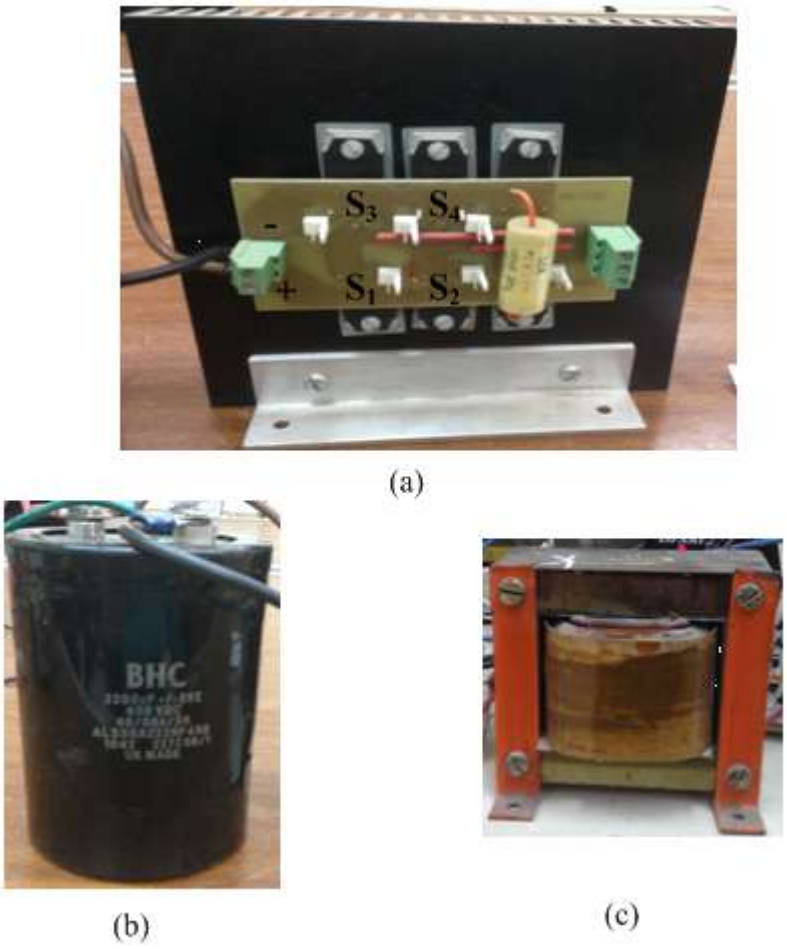

(a)

(b)

(c)

Figure C.5 (a) Single-phase full-bridge VSI, (b) DC-link capacitor, (c) AC filter inductor

iii. Single-phase CSI

The applied single-phase full-bridge CSI, shown in Figure C.6(a), consists of four IGBTs (S_1-S_4) and four diodes (D_1-D_4), each diode is connected in series with an IGBT switch for reverse blocking capability. For the CSI operation, a 150mH inductor, shown in Figure C.6 (b), is utilized at the inverter input to maintain the DC-link current constant. A 25μF, 5mH CL ac power filter, shown in Figure C.6(c), is used at the inverter output. CSI parameters are listed in Table C.3.

Table C.3. The applied single-phase VSI specifications

DC-link inductor	150mH , 0.8Ω
Ultrafast IGBT (FGA15N120ANTD) [C.5]	1200 V, 45 A
Fast recovery diode (IXYS DSEI30) [C.6]	1000V, 30A
PWM carrier Frequency	15 kHz

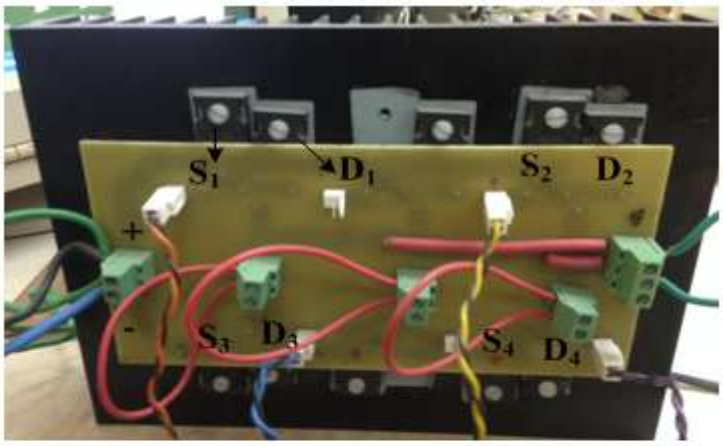

(a)

(b)

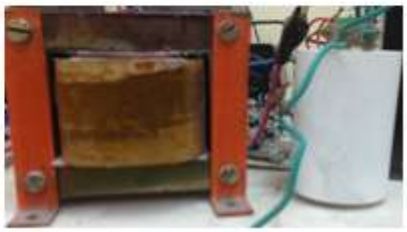

(c)

Figure C.6 (a) Single-phase full-bridge CSI, (b) DC-link inductor, and (c) CL AC filter

C.1.4 Transducer Boards

Currents and voltage sensing is required to provide the feedback signals to the controller. These are achieved using current and voltage transducer boards.

i. Current Sensing

For the three test rigs, the PV output current is needed for the maximum power point tracker. For the second and third rigs, the grid current is required for the inner grid current loop. The Hall effect current sensor devices LEM (LA-55P) were used. Table C-4 shows their parameters. This type of sensor has the advantage of isolating the sensing signal and is easy to implement. The sensing range of the Hall Effect current sensor varies between 0A to 50A, and the frequency range varies between 0 Hz to 200 kHz [C.7]. For proper operation, the output of the transducer is amplified through a signal conditioning circuit and fed to the control circuit. Figure C.7 shows the schematic diagram of the current transducer along with the signal conditioning circuit while Figure C.8 shows the current transducer board.

Table C.4. The current transducer nominal parameter values

Primary Nominal current	50 (rms) A
Primary current (measuring range)	0 to ± 70 A
Current output	1 mA/A
Frequency range	DC to 200 kHz
di/dt	> 200 A/μs

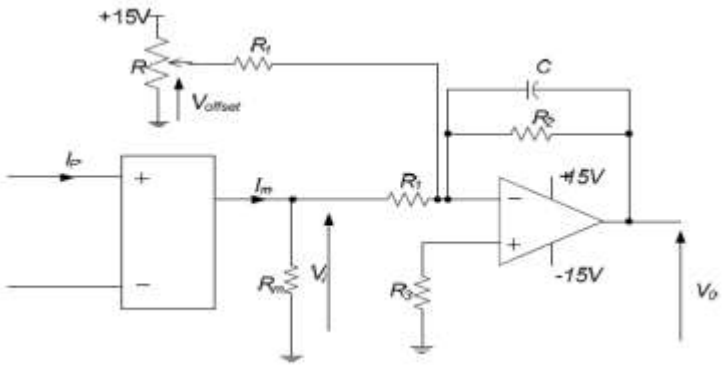

Figure C.7. Current transducer circuit diagram.

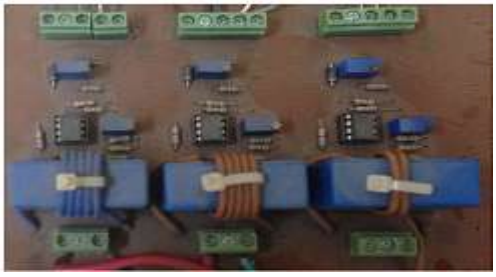

Figure C.8. Current transducer board.

ii. Voltage measuring

In the three test rigs, the PV output voltage needs to be measured for the maximum power point tracker. For the second rig, the VSI DC-link voltage is required for the outer DC-link voltage loop of the conventional control technique. The second and third rigs require sensing the grid voltage to obtain its sine-template as required by the inner grid current control loop.

Hall Effect voltage sensor devices LEM (LV25-P) were used to measure the AC and DC signals with a galvanic isolation between the primary circuit (high voltage) and the secondary circuit (electronic circuit). Table C.5 shows the nominal parameters of the transducer used. This sensor can sense a range up to 500 V and a high frequency bandwidth, but dependent on the series connected external resistor in the primary circuit of the transducer [C.8]. The transducer output is fed to the control circuit via a signal conditioning circuit. Figure C.9 shows the schematic diagram of the voltage transducer along with the signal conditioning circuit while the voltage transducer board is shown in Figure C.10.

Table C.5. The voltage transducer nominal values

Primary nominal current	10 (rms) mA
Primary current (measuring range)	0… ± 14 mA
Primary nominal voltage	10... 500 V
Bandwidth	Drop resistor dependent
Accuracy	± 0.9 %

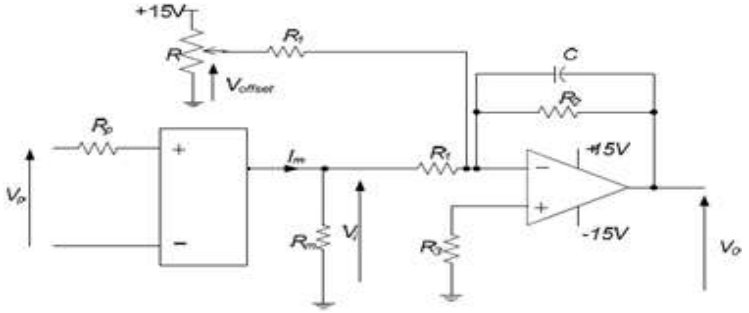

Figure C.9. Voltage transducer circuit diagram.

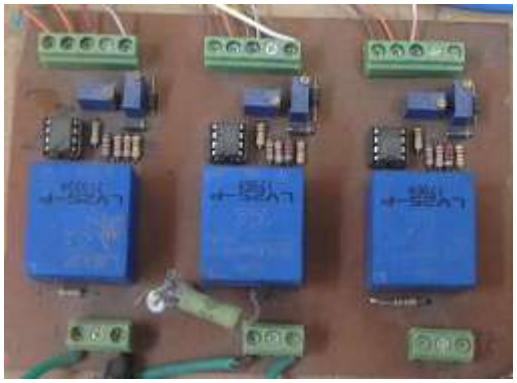

Figure C.10. Voltage transducer board.

C.1.5 Gate drive circuit

Normally, the maximum current that can be sunk by the control circuit is in the range of milli-amperes, while the gate terminal of the IGBT may require a large instantaneous spike of current to enable the fast charging of the gate capacitance and hence the turn on of the switch. Therefore, gate drive circuits are required to source enough current for the switches. Moreover, they offer galvanic isolation between the controller and the IGBT gate by means of two transformers. One transformer is for transmitting power from the low side circuit and the other is for transmitting the gate drive signal.

The photo of the gate drive used in the three test rigs is shown in Figure C-11. Table C-6 shows the gate drive circuit parameters.

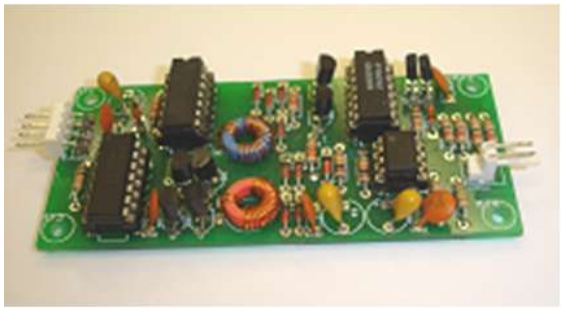

Figure C.11. Gate drive circuit

Table C.6. Gate drive circuit parameters

Supply voltage (max)	5.25 V
$t_{d\,on}$ (typ.)	60 ns
$t_{d\,off}$ (typ.)	60 ns
Drive signal frequency (max)	75 kHz
Output voltages	0, 15 V
Output current	± 3 A

C.2 Software development structure

In order to validate the proposed MPPT technique and the PV grid connected systems, practical implementation is required. Also, the simulation package software is important to test the proposed systems before practical implementation. MATLAB/SIMULINK simulation is used to investigate the proposed control algorithms performance.

C.2.1 Simulation analysis program

For the software analysis program, MATLAB® [7.10] and SIMULINK® v7.5 from Mathworks are utilized.

C.2.2 DSP software

After collecting the measurement data inside the TMS320F28335 microcontroller, the program starts execution according to the specific written algorithm. However, to simplify code development and shorten debugging time, a C2000 Code Composer Studio^{TM} driver is provided. This increases the controller flexibility and its ability for rapid prototyping, using model based programming via Simulink under MATLAB. Hence, this controller is considered a powerful flexible tool for various control applications. An onboard JTAG connector is supplied, providing interface to emulators, with assembly language and 'C' high level language debug.

The eZdspTM F28335 board includes the following software features;

- eZdsp™ F28335 Code Composer Studio DSK Tools. (Includes 'C' compiler, Assembler, Linker, Debugger)
- Texas Instruments' F28335 header files and example software
- Texas Instruments' Flash APIs to support the F28335
- Compatible with Windows 2000, XP
- Compatible with SDFlash programming utility from Spectrum Digital

The DSP used with the proposed system requires a PC. The PC is used to build the MATLAB/Simulink program, convert it to C code, then debug, compile and download the code to the TMS320F28335 microcontroller throughout the USB port. The specifications of the used PC are CoreTM2 Duo microprocessor, and 2 GB RAM.

MATLAB/Simulink programs and codes, for the practical implementation of the proposed algorithms, are shown in appendix D

C.2.3 Arduino software

For programming the microcontrollers, the Arduino platform provides an integrated development environment (IDE) based on the Processing project, which includes support for C and C++ programming languages. The IDE software makes it easy to write code and upload it to the board. It runs on Windows, Mac OS X, and Linux. Software written using Arduino are called sketches. These sketches are written in the text editor and saved with the file extension .ino.

Similarly, A PC is required to write, debug, compile and download the Ardunio code to the ATmega328. The specifications of the used PC are CoreTM2 Duo microprocessor, and 2 GB RAM.

Arduino codes, for the conventional and modified Inc.Cond. MPPT techniques, are given in appendix D

References

[C.1] Spectrum Digital, Inc., "eZdspTM F28335: Technical reference", 2007.

[C.2] Texas Instruments, "TMS320F28335, TMS320F28334, TMS320F28332, TMS320F28235, TMS320F28234, TMS320F28232 Digital Signal Controllers (DSCs): Data Manual"

[C.3] "Arduino UNO",
Available: http://www.oz1edr.dk/Arduino%20Uno/Arduino%20UNO.pdf

[C.4] ATmega328, Atmel, "8-bit Microcontroller with 4/8/16/32K In-System Programmable Flash".

[C.5] Fairchild Semiconductor, FGA15N120ANTD1200V NPT Trench IGBT.

[C.6] IXYS, DSEI 30, Fast Recovery Epitaxial Diode (FRED).

[C.7] Current transducer, LEM, “LTA 100-P/SP1/CE - STROMWANDLER 100A”.

[C.8] Voltage transducer, LEM, “LV25-P - SPANNUNGSWANDLER PCB MTG”.

Appendix D: Programs Codes for Different Control Algorithm

D.1. MATLAB m-files for developing a PV single diode model

D.1.1 Iterative process for R_s and R_P calculation

```
clear
clc
To=298;
Go=1000;
Vocn=22.1;
Iscn=8.37;
Vmp=17.7;
Imp=7.63;
a=1.25;
Ns=36;
Kv=-0.08;
Ki=0.00502;
Bcons=1.3806503*10^(-23);
q=1.60217646*10^(-19);
M=ceil(Vocn)
Vt=Ns*To*Bcons/q;
C=exp(Vocn/(a*Vt));
I0=Iscn/(C-1);
i=1;
error(1)=2;
Rs(1)=0;
Rp(1)=(Vmp/(Iscn-Imp))-((Vocn-Vmp)/Imp)
while (error(i)>0.1)
    Ipvn(i)=Iscn*(Rs(i)+Rp(i))/Rp(i);
    D(i)=exp((Vmp+Imp*Rs(i))/(Vt*a));
    E(i)=(Vmp*Ipvn(i)-Vmp*I0*D(i)+Vmp*I0-Vmp*Imp);
    Rp(i+1)=Vmp*(Vmp+Imp*Rs(i))/E(i);
    V(i,1)=0;
    I(i,1)=Iscn;
    P(i,1)=0
    for j=1:(100*M)
        F(i,j)=exp((V(i,j)+Rs(i)*I(i,j))/(Vt*a));
        I(i,j+1)=Ipvn(i)-I0*(F(i,j)-1)-((V(i,j)+Rs(i)*I(i,j))/Rp(i+1));
        V(i,j+1)=V(i,j)+0.01;
        P(i,j+1)=V(i,j+1)*I(i,j+1);
    end
    Pmax(i)=max(P(i,:));
    error(i+1)=abs(Pmax(i)-(Vmp*Imp));
    Rs(i+1)=Rs(i)+0.035;
    i=i+1;
end
Rs
Rp
Pmax
```

D.1.2 PV curves adjustment and plotting

```
clear
clc
T=273+0;
G=1000;
Rs=0.18;
Rp=63;
Vocn=22.1;
Iscn=8.37;
Vmp=17.7;
Imp=7.63;
a=1.25;
Ns=36;
Kv=-0.08;
Ki=0.00502;
Bcons=1.3806503*10^(-23);
q=1.60217646*10^(-19);
Voc=Vocn+Kv*(T-298);
Isc=(Iscn+Ki*(T-298))*G/1000;
M=ceil(Voc);
Vt=Ns*T*Bcons/q;
C=exp((Vocn+(Kv*(T-298)))/(a*Vt));
I0=(Iscn+(Ki*(T-298)))/(C-1);
Ipvn=Iscn*(Rs+Rp)/Rp;
Ipv=(Ipvn+Ki*(T-298))*G/1000;
V(1)=0;
I(1)=Isc;
P(1)=0;
for j=1:(100*M)
F(j)=exp((V(j)+Rs*I(j))/(Vt*a));
I(j+1)=Ipv-I0*(F(j)-1)-((V(j)+Rs*I(j))/Rp);
V(j+1)=V(j)+0.01;
P(j+1)=V(j+1)*I(j+1);
end
plot(V,I*10)
hold on
plot(V,P)
```

D.2. MATLAB/Simulink programs for algorithms implemented by DSP TMS320F28335

D.2.1 Inc.Cond. MPPT techniques for the first test rig

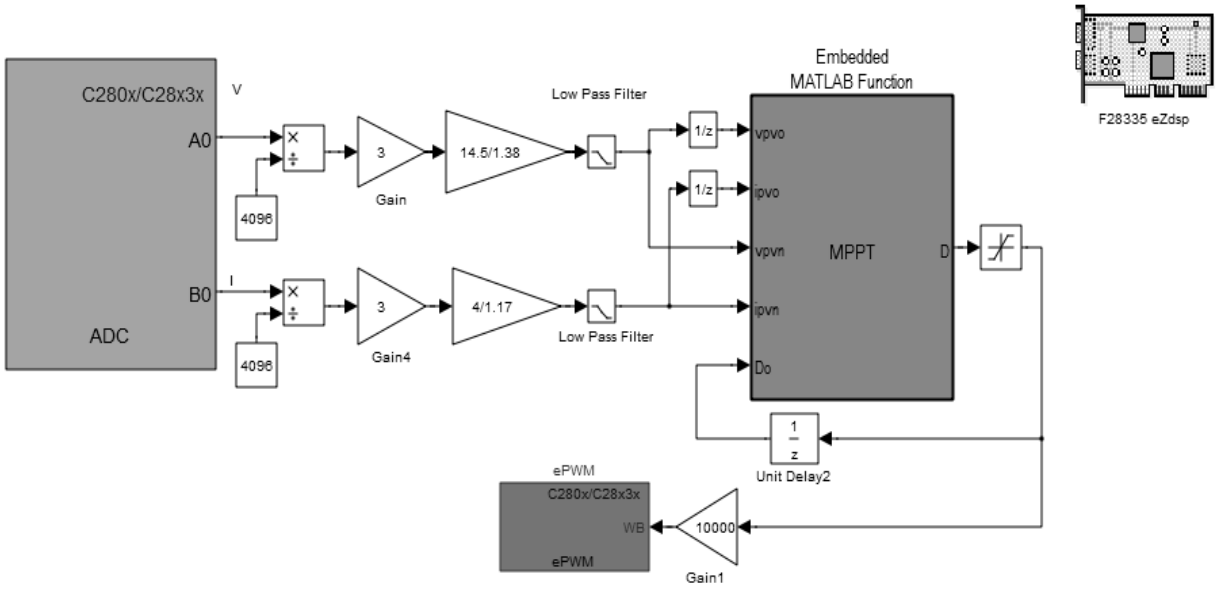

Conventional Inc.Cond. MPPT technique

```
function D = MPPT(vpvo,ipvo,vpvn,ipvn,Do)
    po=ipvo*vpvo;
    pn=vpvn*ipvn;
    dp=pn-po;
    dv=vpvn-vpvo;
    di=ipvn-ipvo;
    D=0.5;
    N=0.0001;
if (dv<0.005) && (dv>0)
    dv=0.005;
end
if (dv<0) && (dv>-0.005)
    dv=-0.005;
end
if (vpvn<0.005)
    vpvn=0.005;
end
step=abs(dp/dv);
X=(di/dv);
Y=(ipvn/vpvn);
Z=X+Y;
if (Z>0)
   D=Do+(N*step);
end
if (Z<0)
   D=Do-(N*step);
end
end
```

Proposed Inc.Cond. MPPT technique

```
function D = MPPT(vpvo,ipvo,vpvn,ipvn,Do)
    po=ipvo*vpvo;
    pn=vpvn*ipvn;
    dp=pn-po;
    dv=vpvn-vpvo;
    di=ipvn-ipvo;
    D=0.5;
    N=0.0013;
end
step=abs(dp);
X=(vpvn*di);
Y=(ipvn*dv);
Z=X+Y;
if (Z>0 && dv>0) || (Z<0 && dv<0)
   D=Do+(N*step);
end
if (Z>0 && dv<0)||(Z<0 && dv>0)
   D=Do-(N*step);
end
end
```

D.2.2 Control techniques of the two-stage grid-tied PV system used in the second test rig

i. Conventional control technique

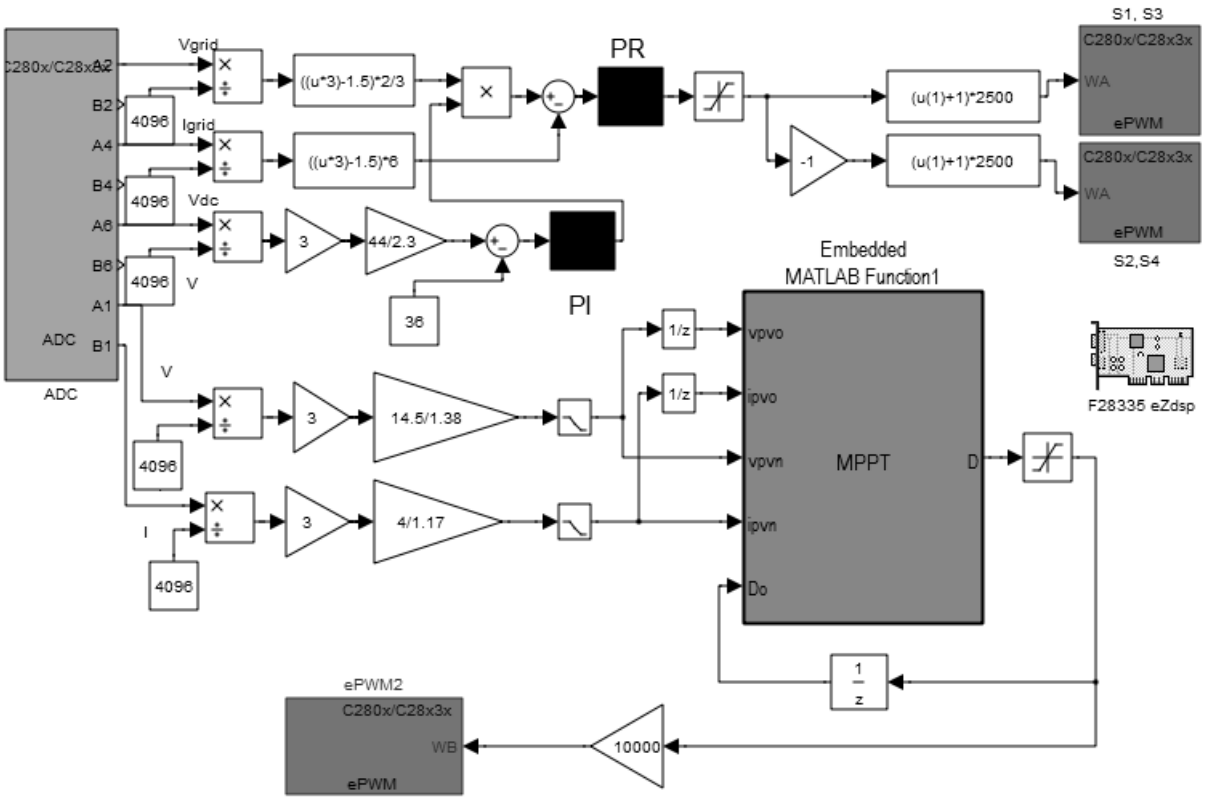

ii. Sensorless control technique

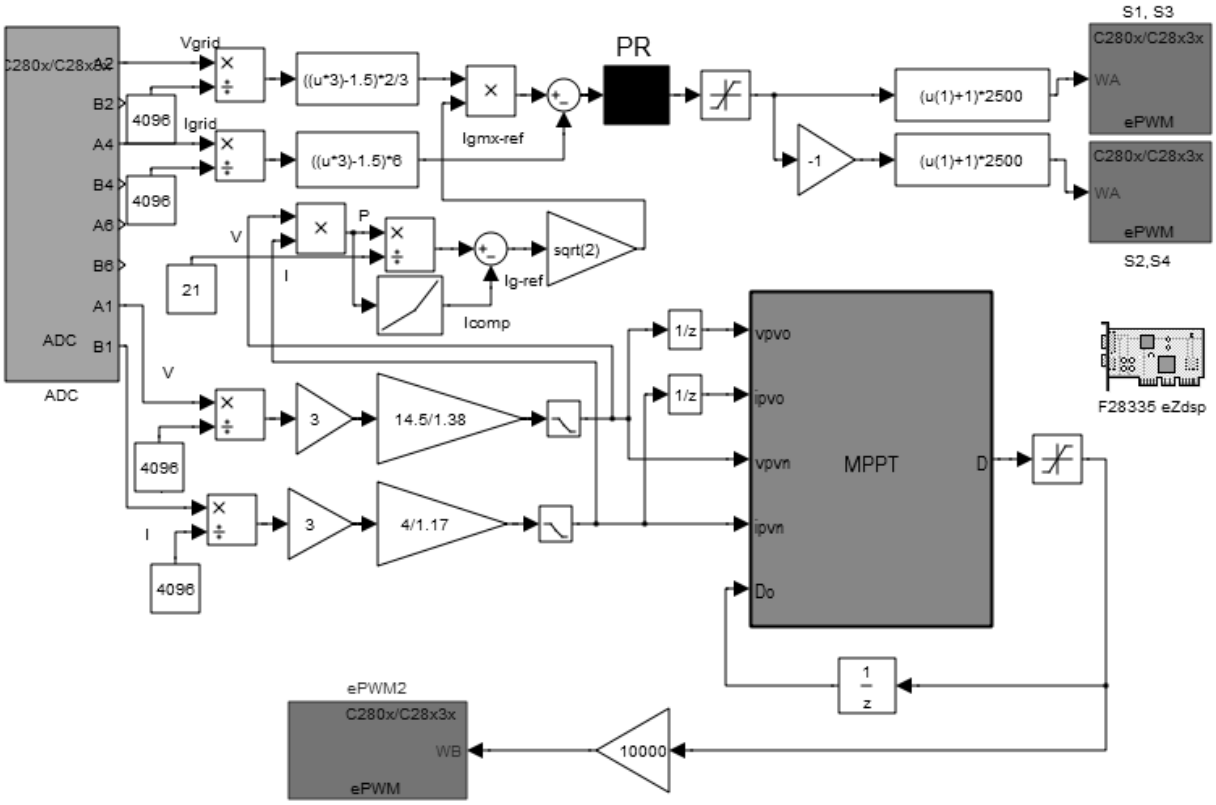

D.2.3 Control of the single-stage grid-tied PV system applied in the third test rig

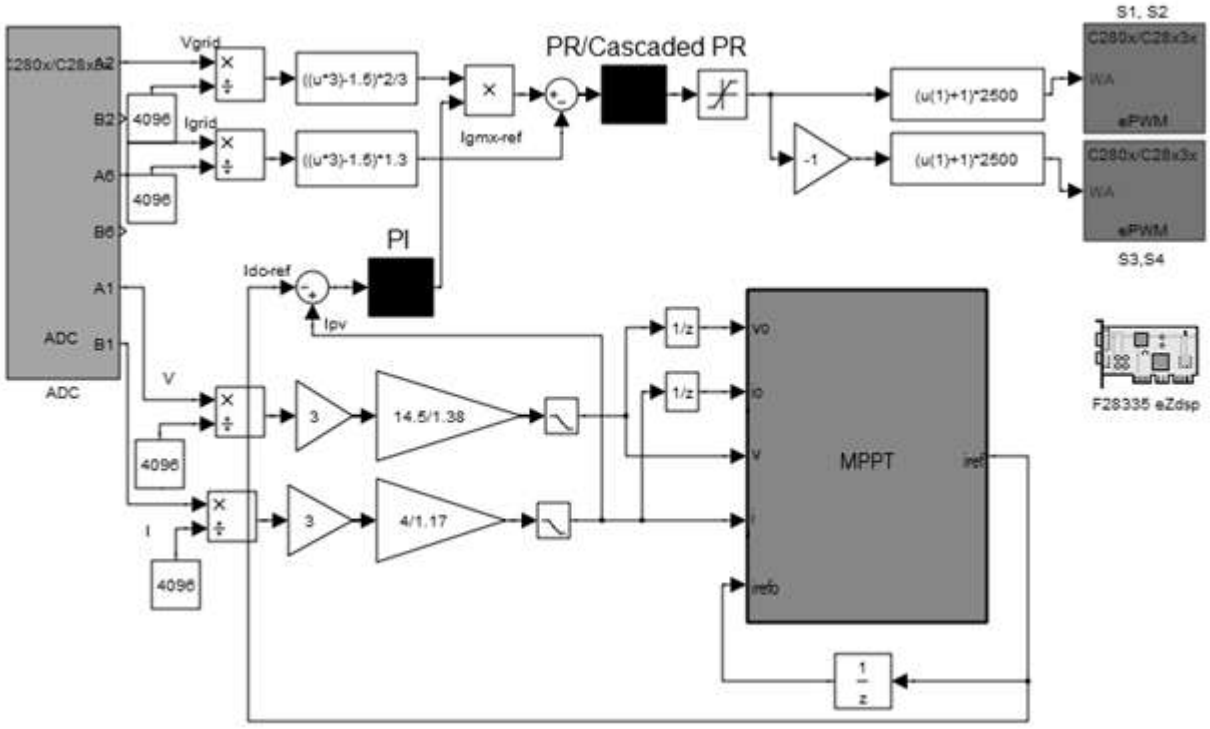

MPPT Technique producing I_{dc}

```
function iref= MPPT(vo,io,v,i,irefo)
iref=5;
dv=v-vo;
di=i-io;
P=v*i;
Po=vo*io;
dP=P-Po;
step=dP;
N=0.0015;
if (v*di+i*dv)==0
       iref=irefo;
end
if ((v*di+i*dv)>0) && (dv>0)
       iref=irefo-N*abs(step);
end
if ((v*di+i*dv)<0) && (dv<0)
       iref=irefo-N*abs(step);
end
if ((v*di+i*dv)>0) && (dv<0)
       iref=irefo+N*abs(step);
end
if ((v*di+i*dv)<0) && (dv>0)
       iref=irefo+N*abs(step);
end
end
```

PR controller

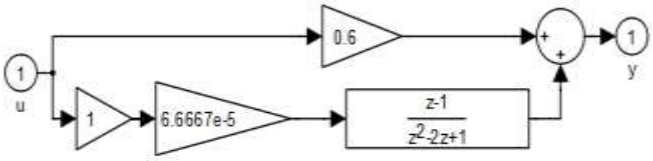

Cascaded PR controller

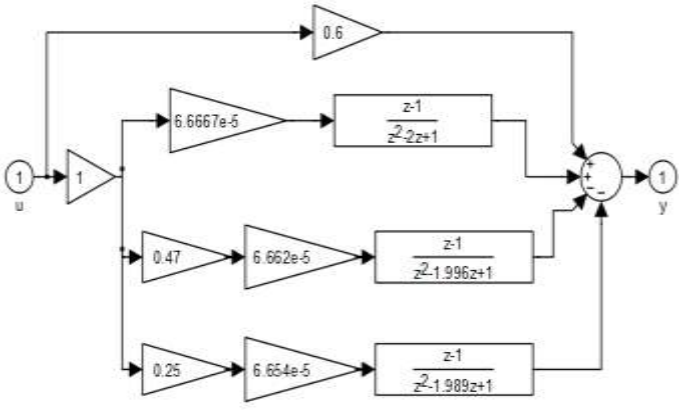

D.3 Arduino code for the Inc.Cond. MPPT techniques

D.3.1 Conventional Inc.Cond. MPPT technique

```
#include <PWM.h>    //Library used to output high frequency PWM on PWM PINS
#include <TimerOne.h>  //Library used to enable regular interrupts

const unsigned int Ts=450;
const unsigned char PWM_PIN=3;
const unsigned int FREQ=15000;
const unsigned char V_pin=A0;
const unsigned char I_pin=A1;
const unsigned int FILTER_FREQ=100;
const unsigned int Tsf=1000;
const float
FILTER_CONST=((2*PI*FILTER_FREQ)*Tsf/1000000.0)/(1+(2*PI*FILTER_FREQ)*Tsf/1
000000.0);
float dV0=0.003;
float V0=0.003;
float V;
float I;
float Vf;
float If;
float ADC_to_Vsig=0.00488759;
float Vsig_Offset_V=0;
float Vsig_Offset_I=0;
float Vsig_to_V=10.51;
float Vsig_to_I=3.42;
float k=0.5;
float N=0.0005;
float Vo;
float Io;
float Po;
float P;
float dV;
float dI;
float dP;
float st;
float kf;
float X;
float Y;
float Z;
void setup()
{
bitSet(ADCSRA,ADPS2);
bitClear(ADCSRA,ADPS1);
bitClear(ADCSRA,ADPS0);
pinMode(2,OUTPUT);
pinMode(4,OUTPUT);
InitTimersSafe();
SetPinFrequencySafe(PWM_PIN,FREQ);
Timer1.initialize(Ts);
Timer1.attachInterrupt(program);
};
```

```
void loop()
{
};
void program()
{
bitSet(PORTD,2);
Vf=((analogRead(V_pin)*ADC_to_Vsig)-Vsig_Offset_V)*Vsig_to_V;
If=((analogRead(I_pin)*ADC_to_Vsig)-Vsig_Offset_I)*Vsig_to_I;
V=Vf*FILTER_CONST+(1-FILTER_CONST)*V;
I=If*FILTER_CONST+(1-FILTER_CONST)*I;
Po=Vo*Io;
P=V*I;
dV=V-Vo;
dI=I-Io;
dP=P-Po;
if ((dV<dV0)&&(dV>0))
dV=dV0;
if ((dV<0)&&(dV>dV0))
dV=-dV0;
if (V<V0)
V=V0;
st=abs(dP/dV);
X=dI/dV;
Y=I/V;
Z=X+Y;
if (Z>0)
k=k-(N*st);
else if (Z<0)
k=k+(N*st);
Vo=V;
Io=I;
kf=k;
if (kf>0.999)
kf=0.999;
else if (kf<0.0001)
kf=0.0001;
pwmWrite(PWM_PIN,kf*255);
bitClear(PORTD,2);
};
```

D.3.2 Proposed Inc.Cond. MPPT technique

```
#include <PWM.h>    //Library used to output high frequency PWM on PWM PINS
#include <TimerOne.h>  //Library used to enable regular interrupts

const unsigned int Ts=450;
const unsigned char PWM_PIN=3;
const unsigned int FREQ=15000;
const unsigned char V_pin=A0;
const unsigned char I_pin=A1;
const unsigned int FILTER_FREQ=100;
const unsigned int Tsf=1000;
const float
FILTER_CONST=((2*PI*FILTER_FREQ)*Tsf/1000000.0)/(1+(2*PI*FILTER_FREQ)*Tsf/1
000000.0);
float V;
float I;
float Vf;
float If;
float ADC_to_Vsig=0.00488759;
float Vsig_Offset_V=0;
float Vsig_Offset_I=0;
float Vsig_to_V=10.51;
float Vsig_to_I=3.42;
float k=0.5;
float N=0.01;
float Vo;
float Io;
float Po;
float P;
float dV;
float dI;
float dP;
float st;
float kf;
float X;
float Y;
float Z;
void setup()
{
bitSet(ADCSRA,ADPS2);
bitClear(ADCSRA,ADPS1);
bitClear(ADCSRA,ADPS0);
pinMode(2,OUTPUT);
pinMode(4,OUTPUT);
InitTimersSafe();
SetPinFrequencySafe(PWM_PIN,FREQ);
Timer1.initialize(Ts);
Timer1.attachInterrupt(program);
};
void loop()
{

};
```

```
void program()
{
bitSet(PORTD,2);
Vf=((analogRead(V_pin)*ADC_to_Vsig)-Vsig_Offset_V)*Vsig_to_V;
If=((analogRead(I_pin)*ADC_to_Vsig)-Vsig_Offset_I)*Vsig_to_I;
V=Vf*FILTER_CONST+(1-FILTER_CONST)*V;
I=If*FILTER_CONST+(1-FILTER_CONST)*I;
Po=Vo*Io;
P=V*I;
dV=V-Vo;
dI=I-Io;
dP=P-Po;
st=abs(dP);
X=V*dI;
Y=I*dV;
Z=X+Y;
if (((Z>0) && (dV>0))||((Z<0) && (dV<0)))
k=k-N*st;
if (((Z>0) && (dV<0))||((Z<0) && (dV>0)))
k=k+N*st;
Vo=V;
Io=I;
kf=k;
if (kf>0.999)
kf=0.999;
else if (kf<0.0001)
kf=0.0001;
pwmWrite(PWM_PIN,kf*255);
bitClear(PORTD,2);
};
```

Appendix E: List of Figures and Tables

List of Figures

List of Tables

Appendix F: Summary of Relevant Published Work by the Author

[1] A. Abdelsalam, Ahmed Helal, Nahla Zakzouk and B.W.Williams, "PV Maximum Power Point Tracking under Rapidly Changing Irradiance: Control Scheme Investigation " in Proc. International Renewable Energy Congress (IREC), 2012.

Abstract- In this paper, the maximum power point tracking (MPPT) issue, in standalone photovoltaic (PV) systems, is considered. Various control schemes are investigated under varying irradiance conditions. Directly controlling the MPP converter shows good transient performance, yet with the highest steady-state power oscillations at the MPP. On the contrary, closed-loop control, using a classical PI controller, produces low steady-state power oscillations, but exhibits the worst transient performance. Thus, this paper proposes an adaptive fuzzy-tuned PI controller to compromise between the steady-state and transient performance during sudden changes. Simulation results show that the proposed controller can achieve the least power oscillations as well as the fastest dynamic performance and the same overshoot achieved by the direct-control model. All the previous schemes use variable-step Incremental Conductance (IncCond.) MPPT method. However, in order to study the impact of the applied MPPT algorithm on the system response, an open-loop fuzzy-logic MPPT technique is presented and compared with the IncCond. model adopting the adaptive controller. The performance of the fuzzy-based MPPT model outweighs the latter regarding the transient overshoot and has a relatively simpler structure. However, it's slower to reach the MPP and experiences more steady-state power oscillations especially with severe changes.

[2] N.E. Zakzouk, A.K. Abdelsalam, A.A. Helal and B. W. Williams, "Modified Variable-step Incremental Conductance Maximum Power Point Tracking Technique for Photovoltaic Systems'', in Proc. IEEE Industrial Electronics Society Conference, IECON 2013, pp. 1741 – 1748.

Abstract- Among various photovoltaic (PV) maximum power point tracking (MPPT) techniques, variable-step incremental conductance (Inc.Cond.) method is widely employed with the merits of high tracking accuracy and fast convergence speed. Yet, mathematical division computations are mandatory for the algorithm's structure which in turn adds more

complexity to its implementation. Moreover, conventional variable step, depending on the change of the array power with respect to the array voltage, encounters steady-state oscillations and dynamic problems especially under sudden irradiance changes. This paper proposes a modified variable-step Inc.Cond. MPPT technique featuring division-free algorithm, simplified implementation, and enhanced transient performance with minimal steady-state power oscillations around the MPP. Simulation and experimental results are presented for concept realization and performance evaluation.

[3] N.E. Zakzouk, A.K. Abdelsalam, A.A. Helal and B. W. Williams, "DC-link Voltage Sensorless Control Technique for Single-phase Two-stage Photovoltaic Grid-connected System'', in Proc. IEEE International Energy Conference (ENERGYCON), 2014, pp. 58 - 64

Abstract- Control techniques, applied to single-phase two-stage grid-connected photovoltaic (PV) systems, mainly achieve functions of maximum power point tracking (MPPT), voltage adjustment at inverter DC-link, and grid current control. Conventional control techniques require measurements of PV voltage and current, DC-link voltage, and grid voltage and current. Commonly, sensorless techniques are proposed to simplify system implementation and decrease its entire size and cost. However, most focus on eliminating PV voltage and/or current sensors. In this paper, a sensorless technique is proposed which keeps PV sensors, but eliminates the expensive high DC-link voltage sensor by mitigating the inverter DC-link voltage control loop. Alternatively, voltage regulation at inverter DC-link is achieved through power balance guarantee at this link. Hence, control complexity is minimized and system stability is enhanced. Moreover, the entire system implementation is simplified and its dynamic response is improved during sudden irradiance changes. Simulation work is carried out to verify the effectiveness of the proposed technique when compared to the conventional one regarding their transient and steady-state performance under varying irradiance conditions.